DTIC
ELECTE
APR 2 0 1995
C

THEORY AND SIMULATION OF ELECTROSTATIC WAVE TURBULENCE IN THE SPACE SHUTTLE-INDUCED PLASMA ENVIRONMENT

David R. Rivas
Daniel E. Hastings

Massachusetts Institute of Technology
Department of Aeronautics & Astronautics
77 Massachusetts Avenue
Cambridge, MA 02139

30 September 1994

Final Report
3 January 1990-30 September 1994

19950419 079

" This technical report has been reviewed and is approved for publication "

David L. Cooke

DAVID L. COOKE
Contract Manager

Charles P. Pike

CHARLES P. PIKE
Branch Chief

REPORT DOCUMENTATION PAGE

1. AGENCY USE ONLY (Leave blank)	2. REPORT DATE 30 September 1994	3. REPORT TYPE AND DATES COVERED Final (3 Jan 1990 – 30 Sept. 1994)

4. TITLE AND SUBTITLE

Theory and Simulation of Electrostatic Wave Turbulence in the Space Shuttle-Induced Plasma Environment

5. FUNDING NUMBERS

PE 62101F
PR 7601 TA 30 WU CJ

Contract F19628-90-K-0021

6. AUTHOR(S)

Daniel E. Hastings
David R. Rivas

7. PERFORMING ORGANIZATION NAME(S) AND ADDRESS(ES)

Massachusetts Institute of Technology
Department of Aeronautics & Astronautics
77 Massachusetts Avenue
Cambridge, MA 02139

8. PERFORMING ORGANIZATION REPORT NUMBER

9. SPONSORING/MONITORING AGENCY NAME(S) AND ADDRESS(ES)

Phillips Laboratory
29 Randolph Road
Hanscom AFB, MA 01731-3010

Contract Manager: David Cooke/WSSI

10. SPONSORING/MONITORING AGENCY REPORT NUMBER

PL-TR-95-2021

11. SUPPLEMENTARY NOTES

12a. DISTRIBUTION/AVAILABILITY STATEMENT

Approved for public release; distribution unlimited

12b. DISTRIBUTION CODE

13. ABSTRACT (Maximum 200 words)

One of the important observations of the Plasma Diagnostic Package (PDP) experiments that were designed to probe the environment around the shuttle was the high degree of electrostatic turbulence in the ambient plasma compared to what has been observed from similar instruments flown on unmanned spacecraft. It is shown that the turbulence is caused by a process which involves the outgassing of water vapor from the shuttle orbiter, the subsequent collisional charge exchange of these water neutral molecules with ionospheric oxygen ions for form "pick-up" water ions, and the excitation of the beam-arc plasma instability. This is a new instability which is driven by the interaction of the beam-arc (i.e., asymmetric ring) velocity distribution function of the contaminating water ions with the background ionospheric plasma.

14. SUBJECT TERMS

Electrostatic wave turbulence
Space shuttle-induced plasma environment
Plasma diagnostic package (PDP)

15. NUMBER OF PAGES

312

16. PRICE CODE

17. SECURITY CLASSIFICATION OF REPORT	18. SECURITY CLASSIFICATION OF THIS PAGE	19. SECURITY CLASSIFICATION OF ABSTRACT	20. LIMITATION OF ABSTRACT
Unclassified	Unclassified	Unclassified	SAR

Contents

iv

Chapter 1

Introduction

1.1 Observations of Plasma Waves in the Space Shuttle Orbital Environment

One of the major effects observed in the plasma experiments of the STS-3, Spacelab-2 and other shuttle missions was the higher degree of turbulence in the ambient plasma compared to what was observed from similar instruments flown on unmanned vehicles [Shawhan et al., 1984; Murphy et al., 1986; Hwang et al., 1987; Gurnett et al., 1988]. During extended periods of the STS-3 and Spacelab-2 flights, a small subsatellite called Plasma Diagnostic Package (PDP) was released from the shuttle to probe the plasma environment around the shuttle. Both experiments showed very similar results concerning plasma waves [Reasoner et al., 1986; Murphy et al., 1986; Cairns and Gurnett, 1991a,b] (see Chapter 2 for a detailed description and qualitative interpretation of the results of the PDP plasma wave experiments). The PDP detected intense broadband electrostatic turbulence in the environment around the shuttle at frequencies extending from a few Hz to about the lower hybrid frequency (~ 8 kHz). The broadband electrostatic noise had intensities ranging from 1 to 5 mV/m and was observed all the way to distances of 400 meters from the shuttle (i.e. the largest separation distance between the shuttle and the PDP). The highest intensities were seen in the region downstream of the shuttle and along the magnetic field lines passing near the shuttle. The electron density fluctuations were as large as tens of percent

1

at the lowest frequencies (below 6 Hz) and substantially above ambient level up to about the lower hybrid frequency. Antenna interference patterns observed in the PDP wideband data showed that the wavelengths of the turbulence were very short, in the range from 2 to 4 meters [Feng et al., 1993].

The effects of various chemical releases from the shuttle on its environment were also detected with the PDP. The PDP data showed that during water dumps the broadband electrostatic noise was enhanced mostly at frequencies below about 3 kHz and the plasma density fluctuations $\Delta N/N$ increased by 5-6 times [Pickett et al., 1985; Pickett et al., 1989]. It thus seemed that the effect of water dumps was not to generate the noise but merely to amplify it. Thruster firings also stimulated the electrostatic noise with similar intensity increases in the spectrum [Gurnett et al., 1988; Cairns and Gurnett, 1991a,b; Machuzak et al., 1993]. These observations that show a strong increase in the turbulence level near the shuttle during periods in which liquid water was released and/or of high thruster activity provide strong evidence that the turbulence is caused by an interaction of the ionosphere with gaseous emissions from the shuttle. Specifically, the general scenario envisaged for the shuttle's interaction with the ionospheric plasma involves the outgassing of water vapor from the shuttle orbiter, the subsequent collisional charge exchange of these water neutral molecules with ionospheric oxygen ions to form "pick-up" water ions, the generation of plasma waves by the water ions and subsequent plasma heating [Cairns, 1990; Cairns and Gurnett, 1991a,b; Rivas and Hastings, 1992]. This situation is thus similar in many respects to the interaction of a comet with the solar wind [Scarf et al., 1986; Grard et al., 1986].

1.2 Importance of the Plasma Waves of the Space Shuttle Environment

A good understanding of the nature of the shuttle environment plasma wave turbulence is important for the design of future Low Earth Orbit (LEO) missions involving orbital platforms subject to outgassing, such as the space shuttle or the proposed space station, which have a requirement that the background of plasma waves driven by

2

outgassed pickup ions be minimized. This requirement for minimal levels of platform-associated plasma waves is a natural one for missions focused on either natural iono-spheric plasma waves or active space plasma experiments involving plasma waves as either a diagnostic tool or the focus of the research. Therefore, if the physics of the platform-associated plasma waves are known some design strategies may be found to partially or completely eliminate the wave turbulence.

Furthermore, turbulence can significantly affect the evolution of the contaminant plasma cloud produced by outgassing from the LEO platform or spacecraft (e.g., space shuttle, space station) and thus alter the design plasma parameters near the space-craft. The observed waves are likely to be in the strong turbulence regime since they produce large density fluctuations, of the order of 25% [Gurnett et al., 1988; Pickett et al., 1989]. This strong turbulence should induce anomalous transport processes in the contaminant plasma cloud surrounding the spacecraft. In particular, it could readily enhance the transport of charged particles across the magnetic field and re-duce the electrical conductivity along the magnetic field by one order of magnitude or more [e.g., Ichimaru, 1973]. Consequently, the plasma turbulence may dramatically change the predictions of the plasma cloud evolution so far calculated by only using classical transport theory for the study of data from previous missions and the design of future missions [e.g., Hastings and Gatsonis, 1989; Eccles et al., 1989; Gatsonis and Hastings, 1991].

1.3   General Outline of this Thesis

This thesis concerns itself with an interpretation of the PDP shuttle environment wave data through theoretical and computer simulation models. In the remainder of this chapter we make a critical analysis of the various mechanisms suggested to be the source of the shuttle environment waves. We show that the mechanism that is the most consistent with the observed wave properties indicates that the waves are driven by a two-stream type instability from the interaction of the pickup water ions with the ionospheric plasma.

In Chapter 2, we give a detailed, consistent description and, when possible, a

3

qualitative interpretation of the major characteristics of the PDP wave data.

In Chapter 3, we analyze in detail the non-Maxwellian pickup water ion distribution function, which is expected to have the free energy for driving the shuttle environment waves. We determine analytically that this distribution function is a beam-arc (i.e. asymmetric ring) in velocity space having different characteristics in the various regions of the shuttle environment.

In Chapter 4, we develop the linear theory of the instability that is driven by the interaction of the beam-arc distribution of water ions with the background Maxwellian ionospheric plasma. This is a new instability and we call it the beam-arc plasma instability. The results of the linear analysis show that this instability has unique properties that can explain various characteristics of the observed waves and that it is the major source of the shuttle environment turbulence. However, the linear theory is unable to explain certain properties of the observed waves thus indicanting the need for a nonlinear analysis of the instability.

In Chapter 5, we develop a PIC code simulation of the beam-arc plasma instability to study the nonlinear regime of the instability. This involves a careful analysis and testing of the simulation design for accurately modeling the stochastic nature of the spectrum of this instability. In addition, we develop the quasilinear theory of the instability and derive simple analytical models to explain the physical processes observed in the simulations. The results again show that the beam-arc plasma instability has unique properties, different to those of the closely related beam plasma and ring plasma instabilities.

In Chapter 6, we interpret the PDP wave data by using the results of the beam-arc plasma instability simulations for the plasma parameters and distributions predicted for various regions of the shuttle environment. Most of the major features of the PDP wave data are interpreted including the wave spectra of various regions of the shuttle environment and the source regions of the waves. This interpretation constitutes significant progress in the understanding of the nature of the shuttle environment waves.

Finally, in Chapter 7 we give a summary of the results and point out the major

areas that need future work. We also give recommendations on how to partially or completely eliminate the waves from the shuttle environment.

1.4 Analysis of Theories Suggested for Explaining the Space Shuttle Environment Turbulence

Various authors [Siskind et al., 1984; Pickett et al., 1985; Gurnett et al., 1988; Pickett et al., 1989] who have studied the PDP data from the STS-3 and/or Spacelab-2 shuttle flights have noted that the intense electrostatic noise observed in the plasma near the shuttle appears to be caused by an interaction of gases emitted from the shuttle with the surrounding ionosphere. They have argued that the shuttle environment turbulence is likely to be closely related to a variety of other situations in which intense broadband electric field noise is produced by a neutral gas interacting with a rapidly moving plasma. These situations include (1) the intense electric field noise associated with cesium ion releases in the earth's ionosphere [Kintner et al., 1980], (2) the intense electrostatic noise observed during the AMPTE lithium ion releases [Gurnett et al., 1985; 1986], (3) the electric field noise observed by Voyager 1 in the vicinity of Titan [Gurnett et al., 1981], and (4) the electrostatic noise observed during the flybys of the gaseous envelopes of the comets Giacobini-Zinner and Halley [Scarf et al., 1986; Grard et al., 1986]. In this section we make a critical analysis which shows that the mechanisms or instabilities responsible for generating broadband electrostatic noise in these other situations cannot be directly applied to the case of the shuttle. We also critically analyze other theories suggested for explaining the shuttle environment electrostatic noise and propose one which is more consistent with the observed properties of this wave turbulence.

1.4.1 The Ion Beam-Plasma Instability Hypothesis

During the Active Magnetospheric Particle Tracer Explorers (AMPTE) solar wind lithium release on September 11, 1984 and again on September 20, 1984, an intense burst of electrostatic noise was observed near the upstream edge of the lithium ion

cloud [Gurnett et al., 1985; 1986]. A stability analysis using realistic parameters shows that the electrostatic noise can be accounted for by the ion beam-plasma instability [Fried and Wong, 1966] caused by the solar wind proton beam streaming through the nearly stationary lithium cloud [Gurnett et al., 1986].

Comparisons with measurements of the earth's bow shock by the IMP6 and ISEE 1 spacecraft show that the spectrum and overall features of the noise in the AMPTE releases are very similar to the electrostatic noise observed at the earth's bow shock [Rodriguez and Gurnett, 1975]. In fact, the ion beam-plasma instability is also the mechanism responsible for the electrostatic noise in the earth's bow shock. In this case, the electrostatic noise is closely correlated with the onset of ions reflected from the bow shock [Rodriguez and Gurnett, 1975]. These reflections produce an ion beam-plasma interaction that is very similar to the interaction that occurs as the solar wind protons stream through a stationary AMPTE ion cloud. The growth rate of this instability is largest when the ion cloud density and solar wind proton density are similar, which explains why the noise only occurs near the outer edge of the AMPTE ion cloud [Gurnett et al., 1986]. Furthermore, the similarity of the AMPTE releases noise to the noise in the earth's bow shock suggests that a shock may exist in the solar wind plasma flow upstream of the AMPTE ion cloud [Gurnett et al., 1986].

Now, let us consider the broadband electrostatic noise observed in the shuttle's outgassed water cloud. In this case, the ion beam-plasma instability appears to be a likely candidate to explain the broadband electrostatic noise because of the drift, along the magnetic field, of the pickup water ions relative to the background (mostly) oxygen ionospheric ions [Pickett et al., 1989]. However, the PDP data shows that the shuttle environment electrostatic noise reaches its highest intensities when the water cloud is moving nearly or exactly perpendicular to the magnetic field [Cairns and Gurnett, 1991a], which is when the ion beam-plasma instability would have zero growth rates [Pickett et al., 1989]. Moreover, it can be shown, by using Fried and Wong's [1966] linear theory results for the ion beam-plasma instability, that this instability would only account for a narrow band of frequencies near ~ 800 Hz of the broadband electrostatic noise observed with the PDP. Therefore, this instability is

unlikely to be the mechanism that drives the shuttle environment turbulence.

1.4.2 The Secondary Ion Streams Hypothesis

Stone et al. [1986] have argued that possible interaction between measured secondary, high inclination ion streams [Stone et al., 1983; 1986] and the ambient plasma could generate broadband electrostatic noise such as that observed by the wave instruments on the PDP. In this case the ion beam-plasma instability would be the mechanism responsible for the noise. However, we have found that the wavevector directions predicted by this theory (i.e. parallel to the magnetic field) are inconsistent with those observed with the PDP, which are mostly perpendicular to the magnetic field. Moreover, the ion streams were observed only near the shuttle whereas the electrostatic noise was also observed a few hundred meters away from the shuttle. Therefore, this mechanism suggested by Stone et al. [1986] is unlikely to be the source of the observed turbulence.

More recently, Hwang et al. [1987] have developed a theory for the shuttle environment waves involving ion acoustic and ion-ion acoustic instabilities driven by the secondary ion streams observed in the near vicinity of the shuttle [Stone et al., 1983; 1986]. Cairns and Gurnett [1991b], however, have shown that this theory is inconsistent with the frequency distribution and wave vector orientations of the observed waves. In addition, Hwang et al.'s instabilities are suppressed for more nominal values of the shuttle environment plasma parameters. Therefore, mechanisms involving the secondary ion streams are unlikely to be the source of the shuttle environment turbulence.

1.4.3 The CIV Hypothesis

Papadopoulos [1984] has argued that the anomalous glow observed near the shuttle surfaces and the near zone waves can be attributed to a combination of beam plasma discharge and critical ionization phenomena. In particular, while the shuttle velocity ($\sim$ 8 km/sec) is below the critical ionization velocity, which for oxygen is 12.7 km/sec, specular reflection of a small fraction (2-3%) of ambient ions from a shuttle

surface forms an ion beam with velocity near 16 km/sec making up for the energy deficit in the critical ionization velocity phenomenon. The instability mechanism in this case is the modified-two-stream instability [Krall and Liewer, 1971]. Although Papadopoulos' theory predicts wave activity more or less consistent with the properties of the observed electrostatic noise, it could only account for the noise observed very near the shuttle vehicle surfaces (where ram ions are reflected forming an ion beam). This theory could not explain the noise detected a few hundreds of meters away from the orbiter. Moreover, Cairns and Gurnett [1991b] have pointed out that this theory has severe theoretical problems since efficient reflection of low energy ions (ram energy of the order 5 eV) off metallic or ceramic surfaces should not occur. The majority of such ions should be reflected as neutrals and the ion reflection yield (and corresponding relative beam density) should be almost invariably much less than 1%. On the other hand, as we shall discuss later, pickup water ions streaming through the background ionospheric ions with relative densities of the order of 10 % may drive the same type of (and even stronger) instability throughout the orbiter's outgassed cloud. We therefore conclude that Papadopoulos' theory is not viable for explaining the shuttle environment turbulence.

1.4.4   The Giacobini-Zinner and Halley's Comet Hypothesis

The plasma wave instrument on the International Cometary Explorer (ICE) detected broadband electrostatic waves in the region extending from just beyond the visible coma of the Giacobini-Zinner comet to within 2 million kilometers of the nucleus [Scarf et al., 1986]. Although, the wave instrument detected turbulence structures with familiar bow shock characteristics that were well correlated with observations of localized electron heating phenomena, the noise appears to be associated with heavy ion pickup [Scarf et al., 1986]. Due to ionization processes (charge exchange, photoionization) that occur in the comet's tail, the tail ions have a distribution function which is of the peaked loss-cone type. Various authors [e.g., Wu and Davidson, 1972; Scarf et al., 1986] have shown that this nonequilibrium distribution function can excite electrostatic as well as electromagnetic instabilities that could be attributed to

8

the observed turbulence. A similar explanation was given for the Halley's comet tail turbulence [Grard et al., 1986].

Likewise, in preliminary interpretations of the shuttle cloud turbulence, various authors [Siskind et al., 1984; Pickett et al., 1985; Gurnett et al., 1988; Pickett et al., 1989] have suggested that the pickup water ions should have ringlike distributions [Pickett et al., 1985] (which was confirmed by Paterson and Frank [1989] observations) that could generate the electrostatic noise. In this case, the likely candidate for generating the noise would be the Ott-Farley instability [Ott and Farley, 1975], driven by the ringlike distribution of pickup ions. However, using an analysis of this instability for the shuttle plasma parameters, Pickett et al. [1989] have argued that this instability would only account for the intense turbulence observed at frequencies from about 1 kHz to 10 kHz, of the order of the lower hybrid frequency. Thus, to them this mechanism seemed to be inconsistent with the noise observed at frequencies well below 1 kHz. On the other hand, they have suggested that if the Ott-Farley instability is the primary agent responsible for the observed broadband noise, it would appear that an inverse cascading of the wave energy, from small wavelengths (i.e. high frequency) to large wavelengths (i.e. low frequency), takes place in the non-linear regime, so that most of the noise energy is finally concentrated at the largest wavelength allowed by the system, i.e., by the "size" of the water cloud. That is, small-scale "whirls" would continuously coalesce into large-scale whirls, all the way to the size of the cloud. Therefore, at that stage in the interpretation of the shuttle cloud turbulence a nonlinear instability analysis seemed to be necessary to give some support to this hypothesis.

1.4.5 The Doppler-Shifted Lower Hybrid Waves Hypothesis

Let us now point out that the above critical analyses of the hypotheses are actually a description of what was the state of the art in the interpretation of the shuttle environment electrostatic noise when we started the work for this thesis, in the Fall of 1990. It should be noted that back then the mechanism that generates the electrostatic

noise in the shuttle environment was still somewhat mysterious.

More recently, Cairns and Gurnett [1991a,b] have made detailed observational analyses of the PDP data from the Spacelab-2 mission. In addition, they have reconsidered the mechanism which involves the ringlike distributions of pickup water ions for generating the noise (see previous section). They have concluded that ring plasma type instabilities, which are of the family of the Ott-Farley instability [Ott and Farley, 1975], should indeed generate the turbulence. As noted above, the characteristic frequencies of this instability are of the order the lower hybrid frequency (1-10 kHz). Cairns and Gurnett have shown that there should not actually be a major difficulty in explaining the lower frequency waves, observed with the PDP, with this instability since in order to interpret the PDP data the frequencies predicted with the linear theory have to be Doppler-shifted to the frame of the PDP. They have shown that the Doppler-shifted frequencies of the lower hybrid waves driven by ring plasma instabilities (and also beam plasma instabilities) should extend from a few Hz to about the lower hybrid frequency and thus should be in agreement with the frequency ranges of the observed waves. However, they have found a major disagreement between the frequencies where the growth rates peaked and the peaks of the PDP frequency spectra. Moreover, various other major features of the observed waves could not be explained by their ring plasma and beam plasma instability analyses. Nevertheless, their more detailed analyses gave more support to the hypothesis that the shuttle environment waves should be driven by the ringlike distribution functions of pickup water ions.

In our case, after analyzing all the mechanisms criticized in the above sections and considering various other possible mechanisms, we found, simultaneously and independently, similar linear theory results to those of Cairns and Gurnett [1991a,b]. However, since Cairns and Gurnett's [1991a,b] results were published first and were more complete, they deserve most of the credit for those results.

In this thesis, we reconsider the interaction of the ringlike distributions of the pickup water ions with the background ionospheric plasma, based on the partial agreement of Cairns and Gurnett's [1991a,b] results with the PDP data and on our preliminary analysis which shows similar results. We first develop models of the

10

beam-arc (i.e. asymmetric ring) distributions of pickup water ions for various regions of the shuttle environment and then use these models in instability analyses. Unlike Cairns and Gurnett [1991a,b] who only used rings and beams to model the pickup water ion distributions, by using our predicted beam-arc models we will find ourselves dealing with a new instability with unique properties, different to those of the beam plasma and ring plasma instabilities. We will develop the linear theory and PIC code simulation of this new instability for the plasma parameters and distributions predicted for various regions of the shuttle environment. The results of the simulation along with an analysis of the convection of waves will allow us to interpret the major properties of the waves observed with the PDP.

Chapter 2

The Plasma Diagnostic Package (PDP) Wave Data: Description and Qualitative Interpretation

This chapter focuses on the description and qualitative interpretation of plasma waves observed during the Spacelab-2 mission. The Spacelab-2 mission was launched on 29 July 1985 into a nearly circular, low inclination orbit with an altitude of about 320 km and an inclination of 49.5 degrees. One major objective of the Spacelab-2 mission was to investigate the shuttle-ionospheric plasma interaction at distances up to about 400 m from the orbiter. This study involved a small free-flying spacecraft, the Plasma Diagnostic Package or PDP spacecraft [Shawhan, 1982; Kurth and Frank, 1989], that was released from the shuttle to explore the plasma environment around the shuttle in the so-called "free-flight" mission. During the 6-hour free flight phase of the mission, the PDP completed 2 fly-arounds of the shuttle at distances up to 400 meters. In addition to the fly-arounds, a series of wake transits were performed to survey the wake region directly downstream from the shuttle.

In another phase of the Spacelab 2 mission the PDP probed the shuttle's environment while attached to the spacecraft on the RMS arm (distances less than about 10 meters). While the PDP was on the RMS arm the shuttle performed a roll maneuver (the XPOP roll) designed to allow investigation of the broadband near zone waves as a function of phase relative to the orbiter's velocity vector. The PDP spacecraft carried a full complement of particle and field instruments. Reviews of the instrument,

the PDP spacecraft, and the observations are given by Shawhan [1982] and Kurth and Frank [1990].

The Spacelab-2 mission PDP wave data has been provided to us by Dr. Iver Cairns and Ms. Jolene Pickett of the Department of Physics and Astronomy of the University of Iowa in the form of written reports. The PDP wave data from the Spacelab-2 mission and the OSS-1 shuttle flight have also been published in over 20 journal articles. In this chapter we make a review of this literature and give a qualitative interpretation of the data by identifying the possible observed physical phenomena. Although sometimes contradictory, we also refer to the qualitative interpretations found in the literature. In the next chapters we shall refer frequently to the PDP data description and discussion of this chapter; a summary of this chapter is presented in Section 7.1. In addition, we will find that most of the data presented here will be successfully interpretated using the instability theory and simulation developed in this thesis.

2.1 Observations of Waves During the Free-Flight Mission

In this section we will show that many of the variations in amplitude and spectral properties of the plasma waves from 31 Hz to 31 kHz observed well away from the shuttle during the free-flight mission , the so-called "mushroom" spectral features (illustrated schematically in Figure 2-1), can be understood in terms of the variation of the angle between the orbiter's velocity vector relative to the plasma and the magnetic field vector, the so called $V_\parallel/V_T$ effect.

2.1.1 The PDP Data of the Free-Flight Mission

The data presented here are from the Helios subsystem of the plasma wave instrument on the PDP spacecraft [Shawhan, 1982; Gurnett et al., 1988] and were obtained during the free-flight portion of the Spacelab-2 mission. The Helios instrument provides electric field measurements from 31.1 Hz to 178 kHz using 16 logarithmically spaced channels, four per frequency decade. The frequency bandwidths are nominally ±15

% below 1 kHz and ± 7.5 % above 1 kHz. A double sphere antenna with a sphere separation of 3.89 meters is used for detecting the electric fields during free-flight. Each channel provides a data point every 1.6 seconds; only the peak signal during each measurement interval is used.

The PDP data description given in this section (Section 2.1.1) is mostly a summary of Cairns and Gurnett's [1991a] detailed observational characterization of the PDP free flight mission data. It is therefore implied that the credit of all the results presented in this section belongs to Cairns and Gurnett [1991a] unless otherwise indicated.

Figure 2-2 shows Helios data in a spectrogram format with wave amplitude color coded. The white curve at about 8 kHz shows the lower hybrid frequency computed using the square root of the electron to oxygen ion mass ratio times the electron gyrofrequency. There are three effects which complicate the interpretation of the data. First is the modulation at the spacecraft spin period of 13.6 seconds, most visible as a periodic blue spike in the spectrogram near 20 kHz. This modulation does not correspond to natural waves (the modulation period would be half the spacecraft spin period in this case), but to some unidentified source of spacecraft-associated interference. This effect leads to spurious signals during times of relatively low wave levels. The second interference effect is the impulsive production of intense waves by the orbiter's thrusters. These thruster signals are the yellow (typically) spikes which are most intense at low frequencies but extend up to about the lower hybrid frequency. Illustrative examples of these thruster signals, visible throughout this time period, occur at 0025:42, 0026:28, and 0037:40(time format hour-minute: second). Not all thruster firings result in intense, impulsive signals: the diffuse, relative weak, broadband (up to f_{LH}) enhancement shown in Figure 2-2 from 0025:00 to about 0025:30 (but which starts at 0024:48) does correspond in time with almost continuous thruster firings from 0024:48 to 0025:05, and is almost certainly a thruster signal. Some thruster firings also produce no observable wave signals at the PDP spacecraft. All wave signals were therefore carefully checked against the record of firings to eliminate thruster-associated waves from further consideration. No water

dumps [e.g., Pickett et al., 1989] occurred during the PDP free-flight mission. The third interference effect is that of the Fast Pulse Electron Generator (FPEG) electron beam experiment, visible as the intense red signals from about 0046:00 to 0047:00 in figure 2-2, with intense signals at all frequencies up to about 20 kHz together with signals near the electron gyrofrequency (not shown) [Gurnett et al., 1986; Farell et al., 1988].

The feature of interest in this section is the "mushroom" spectral feature in Figure 2-2: the top of the mushroom is formed by the lower hybrid frequency waves, while the base is the triangular shape emission which starts at low frequencies and extends up to the lower hybrid frequency near the mushroom's center. This feature is illustrated schematically in Figure 2-1. This mushroom shaped feature also corresponds to a significant and smooth (punctuated by thruster firings) enhancement in the intensity of the low frequency waves by a factor of order 10. The time record of thruster firings shows that the smoothly varying mushroom feature is not due to the effects of thruster firings. For instance, the smooth enhanced wave levels (light yellow color) for the period 0038:00 to 0039:07 near the center of the mushroom feature are not associated with thruster firings: no thruster firings occurred from 0037:58 until 0039:07. Correspondingly, all the impulsive yellow and red signals in the data either correspond directly to the times of thruster firings or are associated with the modulated spacecraft interference pattern discussed above.

In Figure 2-2 the lower hybrid frequency waves show little evidence of change over the time period of the mushroom, except for frequency changes corresponding solely to variations in the magnetic field amplitude. Therefore, the primary characteristics of interest are the increase in the frequency bandwidth of the triangle-shaped features (up to the lower hybrid frequency) and the smooth increase in amplitude of the low frequency waves near the mushroom's apex. During the time period of Figure 2-2, the first "station-keeping" period, the PDP spacecraft is located in the wake region downstream from the shuttle and remains almost stationary relative to the shuttle's plasma wake (coordinates X', Y_P and Z'; see Figure 2-3), as shown in Figure 2-4. Wake transit occur near 0028:40, 0031:45 and 0041:15 with no accompanying changes

in the plasma waves. This time period does, however, coincide with a transition from positive to negative values for $V_\parallel$. We define the quantities $V_\parallel$, $V_\perp$ and V_T as the components of the orbiter's velocity vector (relative to the ionospheric plasma) parallel and perpendicular to the magnetic field and the orbiter's speed, respectively. The quantity $V_\parallel/V_T$ passes through zero near 0037:00, coinciding with the maximum intensities of the low frequency waves and the apex of the "mushroom" spectral feature. This feature in the plasma waves therefore apparently corresponds to variations in the quantity $V_\parallel/V_T$ and not to plasma waves associated purely with the orbiter's plasma wake.

Figure 2-5 shows the variation in the quantity $V_\parallel/V_T$ during the free-flight mission, giving the times of further predicted mushroom spectral features, the PDP's position relative to the orbiter at these times, and times of wake transits. Stylized mushroom features on the figure indicate where mushroom spectral features were indeed observed. In each case when the PDP was in the downstream region mushroom spectral features were indeed observed to be centered near times when $V_\parallel/V_T = 0$, although the event near 0128 is somewhat problematical. While many of these mushroom features occur within a few minutes of transits of the center of the orbiter's wake, the events near 0037 and 0515 and the many wake transits not accompanied by mushroom features show that mushroom features are not associated with the orbiter's plasma wake. These mushroom spectral features are usually not as well defined as the in the station-keeping period of Figure 2-2; most mushroom features occur while the PDP is moving significantly relative to the orbiter. The deviations from the idealized mushroom shape are interpreted in terms of PDP motion and spatial variations of the wave spectrum for a given value of $V_\parallel/V_T$.

Therefore, these data are consistent with mushroom spectral features (1) occurring in conjunction with the variations in $V_\parallel/V_T$, and (2) not being associated with specific plasma structures in the orbiter's plasma wake.

2.1.2 Interpretation of the Free-Flight Mission Observations

The interpretation of the PDP data presented in this section (Section 2.1.2) is mostly a summary of Cairns and Gurnett's [1991a] interpretation of the PDP free flight mission data. It is therefore implied that the credit of all the results given in this section belongs to Cairns and Gurnett [1991a] unless otherwise indicated.

The data analysis, described in the previous section, shows that the so-called "mushroom" spectral features of plasma waves found downstream of the space shuttle orbiter during the Spacelab-2 mission are strongly correlated with the parameter $V_{\parallel}/V_T$: in particular the maximum amplitude, frequency bandwidth, and apex of a mushroom occurs near where $V_{\parallel}$ goes through zero and the orbiter's velocity vector perpendicular to the ionospheric magnetic field. Cairns and Gurnett [1991a] argue that this correlation between mushroom spectral features and $V_{\parallel}/V_T$ has a natural interpretation in terms of the optimum conditions for wave growth driven by pick-up water ions and the time available for evolution of the wave spectrum. Consider the growth of localized wavepackets with sizes small compared with the water cloud (and water ion trail) and group velocities that lie in the $X_P - Y_P$ plane and are small compared with the plasma flow velocity (this orientation of the group velocities is assumed since the argument below indicates that group velocities significantly out of the $X_P - Y_P$ plane are inconsistent with the occurrence of the mushroom apexes near $V_{\parallel} = 0$). These wavepackets then move essentially with the background plasma through the water ion trail. When the orbiter moves perpendicular to the magnetic field, water ions produced by charge-exchange of outgassed water molecules move in the same plane (the $X_P - Y_P$ plane) and have the same gyrocenter velocity as the ionospheric plasma and the convected wavepackets of plasma waves. Therefore, in this case maximum path lengths for the growing waves, the maximum time for evolution of the wave spectrum, and the symmetry axis for the mushroom feature at $V_{\parallel} = 0$, can be envisaged. In contrast, when the orbiter velocity has a significant component along the magnetic field, the pick-up ions and the ionospheric plasma (and wavepackets) move in different planes with significantly different gyrocenter velocities. The finite

17

sizes of the orbiter's water cloud and water ion trail then imply a significant limitation of the path length available for growth of the waves. For instance, in a time equal to one ion cyclotron period a convected wave packet and a pick-up water ion suffer a separation of order 250 cos α meters along the magnetic field, where α is the angle between the magnetic field and the plasma flow velocity, and a periodic separation of order 40 meters in the $X_P - Y_P$ plane due to the water ion gyromotion. In contrast, the characteristic scale of the water molecule cloud is of order 10 - 100 meters in the high density region of the cloud which might be expected to be source region for the water ions driving the waves (i.e., pick-up ion number densities in excess of 1%) [Paterson and Frank, 1989; Cairns, 1990], and the data analysis described below predicts wavelengths of order 1 - 2 meters. These strong spatial inhomogeneities in the water ion distribution function and number density imply considerable spatial variations in the dispersion relations of locally generated waves (as found in the linear and nonlinear theories developed in the next chapters) and thus significant effects of convection. There is therefore considerable scope for limitation of wave growth due to the different motions of the background plasma, plasma waves and pick-up ions. Cairns and Gurnett [1991a] emphasize that the existence of the observed $V_{\parallel}/V_T$ effect is strong evidence that the waves are driven by water pick-up ions.

In conclusion, the two simple models for the source region of the plasma waves forming the mushroom spectral features are: the waves are (1) generated throughout the region containing water ions produced from the orbiter's water cloud(this region might be referred to as the shuttle's water ion trail), or (2) generated within the Near Zone region of the orbiter and convected downstreams. These models are not mutually incompatible and both are plausibly consistent with the observed $V_{\parallel}/V_T$ effect.

2.1.3 Observations of Interference Patterns During the Free-Flight Mission

Interference or "fingerprint" patterns in frequency-time spectrograms are a well-known space plasma wave phenomena. They are caused by electrostatic waves with

wavelengths short compared to the antenna length [Temerin, 1979; Fuselier and Gurnett, 1984; Feng et al., 1992]. Typically, a periodic pattern of constructive and destructive interference is produced by the spin-related rotation of the antenna in the wave field. For "fingerprint" patterns to be observed, two conditions must be met: (1) the Doppler shift of the waves (in the moving frame from which they are observed) has to be quite large compared to the rest frame wave frequency, and (2) waves with different wavelengths must propagate in almost the same direction. The frequency-time spectrum in the wideband data can then be regarded as the wavenumber (or wavelength) - time spectrum. An example of an interference pattern observed in the PDP data is shown in Figure 2-6. Analysis of interference patterns allows a determination of the wavelength, the plasma rest frame frequency, the direction of propagation, the power spectrum, and in some cases the location of the source.

The PDP data description given in this section (Section 2.1.3) is mostly a summary of Feng et al. [1993] analysis of the interference patterns in the PDP data. It is therefore implied that the credit of all the results presented in this section belongs to Feng et al. [1993] unless otherwise indicated.

During the 6-hour free flight mission, interference patterns were observed more than 20 times when the PDP was on the downstream side of the shuttle. These interference patterns were in the 0 to 10 kHz and the 10 to 20 kHz electric field wideband data from the wideband receiver connected to the 3.98 meters double-sphere electric antenna. They have different characteristics in the two frequency bands. In the 10 to 20 kHz frequency band the U-shaped interference pattern always opens upward. An example of this type of interference pattern is shown in Figure 2-6. In the 0 to 10 kHz frequency band, the U-shaped interference patterns always opens downward. An example of this type of interference pattern is shown in Figure 2-7. The interference patterns are symmetric about the lower hybrid frequency, which is typically about to 6 to 9 kHz.

For the events in Figures 2-6 and 2-7, the lower hybrid frequency is 8.2 kHz and 6.5 kHz, respectively. The interference patterns in the 0 to 10 kHz band are seen to correspond to lower hybrid waves that are Doppler-shifted to lower frequencies

(i.e., propagating upstream) while the interference patterns in the 10 to 20 kHz band correspond to lower hybrid waves that are Doppler-shifted to higher frequencies (i.e., propagating downstream).

The wavevector direction in the X'-Y' plane can be determined from the PDP antenna orientation at the center of the U-shaped interference pattern and the direction (up or down) of the U-shape. In Figure 2-10 the wavevector and magnetic field directions for the lower hybrid-wave interference patterns are plotted along the PDP trajectory in the X'-Y' plane. The magnetic field direction is shown with a short arrow while the wave vector direction is shown with a long arrow. Wavevectors pointing downstream correspond to interference patterns observed in the 10 to 20 kHz band, and wavevector pointing upstream correspond to interference patterns observed in the 0-10 kHz band. The plotted events all occur between 0124 UT and 0441 UT on August 1, 1985. Several similar interference patterns occurred either both before and after this time period and when the PDP remained about 90 meters directly downstream from the shuttle and moved little with respect to the shuttle during this period. However, these wavevector directions are not shown in Figure 2-10. All of these events were measured downstream from the magnetic field lines connected to the shuttle. Feng et al. [1993] argue that this relationship suggests that the waves are produced by an interaction that takes place along magnetic field lines linked to the shuttle.

As can be seen from Figure 2-10, the wavevectors are in all cases almost perpendicular to the magnetic field (in the X'-Y' plane). For most of the cases, the measured angles with respect to the magnetic field are within the range $80 - 90^o$, with a $\pm5^o$ error. Large wave normal angles, near 90°, are in identifying characteristic of lower hybrid waves. Furthermore, the dispersion relation in the rest frame deduced from the interference patterns shows that this is the case. The dispersion relation for the waves near 0038 UT is shown in Figure 2-8. The rest frame wave frequencies are very close to and a little above the lower hybrid frequency, w_{LHR}. The dispersion relation has also been computed for the 0128 and 0200 UT events where interference patterns are clearly present. They have characteristics similar to those shown in Figure 2-8.

From now on we refer to these interference patterns as lower hybrid-type interference patterns. Figure 2-9 shows the best fit power spectrum for the 0038 UT event. The best fit is obtained when the standard deviation in wavevector directions in the X'-Y' plane is assumed to be about 5°. The range of the wavelengths for the lower hybrid waves is about 1 to 4 meters, with the intensity peaking near 2 meters.

Comparing Figure 2-10 with Figure 2 of Gurnett et al. [1988], which showed the strong noise region observed by the PDP broadband receiver, Feng et al. [1993] find that the lower hybrid-type interference patterns are strongly associated with high plasma wave intensities. Most of the interference patterns are observed in the regions (dark dots in Figure 2 from Gurnett et al. [1988]) where the broadband shuttle-induced wave field exceeds 1 mV/m, clearly enhanced near the lower hybrid frequency. Furthermore, the locations of the lower hybrid-type interference patterns can be divided into two groups. The first group, which includes most events, was observed in the shuttle wake region when the PDP was about 100 meters downstream from the shuttle (0030 to 0130 UT and 0350 to 0455 UT), and about 250 meters downstream from the shuttle (0255 to 0312 UT). The second group, which includes the 0200 UT event (see Figure 2-7), was observed when the PDP was approaching magnetic conjunction from the downstream direction (i.e., in the region directly downstream of the magnetic field lines through the shuttle). Both upward and downward Doppler shifts (corresponding to downstreams and upstream propagation) were observed in each group of events.

An interesting new phenomenon observed in association with the lower hybrid waves of the wideband data is the occurrence of asymmetric or "tilted" interference patterns, e.g. the 0310 UT event (not shown, see figure 7 of Feng et al., 1993). These patterns differ from the others in that their vertical axes of symmetry, which passes through the center of the U shape, is slightly tilted. Tilted interference patterns correspond to waves propagating in various (but not that different) directions and not quite in the same directions like for the other patterns. The 0310 event is from a series of lower hybrid-type interference patterns that was observed from 0250 to 0310 UT when the PDP was completing the last wake crossing well downstream from

the shuttle. However, only the last one near 0310 UT was clearly asymmetric. This event occurred just after the PDP had crossed the wake region. The position of the PDP along the y'-axis had increased to about 140 meters in the shuttle rest frame. "Tilted" interference patterns were also observed at 0150 UT, 0200 UT, and 0325 UT. The "tilted" interference patterns all occurred when the PDP had relatively large Y position in the shuttle rest frame. Considering that the magnetic field is usually oriented somewhat out of the X'-Y' plane (20 to 30°), the PDP was not directly downstream from the shuttle at these times. The interpretation of these asymmetric interference patterns will be discussed in detail in the next chapters.

2.2   Observations of the Near Zone Waves

In addition to the free flight mission, which we have discussed in detail in the previous sections, the PDP spacecraft performed another type of investigation into the shuttle's interaction with the ionosphere during the Spacelab-2 mission. The PDP probed the shuttle's environment both while flying free of the shuttle (the so-called "free-flight" mission) out to distances of order 400 meters and while attached to the spacecraft on the RMS arm (distances less than about 10 meters). While the PDP was on the RMS arm the shuttle performed a roll maneuver (the XPOP roll) designed to allow investigation of the broadband near zone waves as a function of phase relative to the orbiter's velocity vector. The free-flight mission included two complete fly-arounds of the shuttle orbiter, and included two pairs of transitions from the region downstream of the shuttle (defined by the orbiter's velocity relative to the ionospheric plasma) to the upstream region, as discussed in the previous sections.

This section focuses on the observation of plasma waves in the very near vicinity (within 10 meters) of the space shuttle during the Spacelab-2 mission. The observational data presented are from the XPOP roll period and from one upstream-downstream transition during the free-flight period. These data allow demonstration of the control of the amplitude and spectral characteristics of the near zone waves by the angle between the orbiter's velocity vector and the magnetic field direction, the so-called $V_\parallel/V_\perp$ effect, analogous to the results described in the previous section for

some waves during the free-flight mission.

The PDP data description given in this section (Section 2.2) is mostly a summary of Cairns and Gurnett's [1991b] detailed observational characterization of the PDP near zone wave data. It is therefore implied that the credit of all the results presented in this section belongs to Cairns and Gurnett [1991b] unless otherwise indicated.

2.2.1   Observations of the Near Zone Waves During the XPOP Roll

The results presented in this section are from the Helios and MFR (Medium Frequency Receiver) subsystems of the plasma wave receiver on the PDP spacecraft [Shawhan, 1982; Gurnett et al., 1988]. As we have already mentioned above, the Helios instrument measures narrowband electric field signals from 31.1 Hz to 178 kHz using 16 logarithmically spaced channels, four per frequency decade. The frequency bandwidths are nominally ± 15 % below 1 kHz and ± 7.5 % above 1 kHz. Eight additional higher frequency channels from 311 kHz to 17.8 MHz constitute the MFR subsystem. A double sphere antenna is used with these instruments. The sphere separation (and effective antenna length) is 1.15 meters while on the RMS arm (e.g., during the XPOP roll) and 3.89 meters during the free-flight mission. The diameter of each sphere is 10 cm. Each channel provides a data point each 1.6 seconds; both peak and average signals during each measurement interval are recorded. Only the average values are presented here.

The geometry of the XPOP roll is described in Figure 2-11. The PDP spacecraft is attached to the RMS arm, and remains in the same position (but in various orientations) relative to the orbiter during the XPOP roll. At about 0134 thruster firings induce the orbiter to roll around the X_{OBAS} axis, corresponding to the nose-tail axis of the orbiter, with the orbiter oriented so that the X_{OBAS} axis is essentially perpendicular to the shuttle's orbital motion around the Earth. Accordingly, the orbiter rotates about an axis perpendicular to the ram velocity direction. This rotation is designed to move the PDP into the orbiter's wake region and upstream region at a constant distance and position relative to the orbiter. The rotation rate is 0.933

degrees per second, corresponding to one wake transit about every six minutes.

The upper panel in Figure 2-12 shows a spectrogram formed from Helios and MFR data with spectral density (in $V^2 m^{-2} Hz^{-1}$) color-coded for the time period of the XPOP roll during the Spacelab-2 mission: 0134 - 0240, Day 212, 1985. The lower black curve is the lower hybrid frequency computed as the product of the square root of the electron to (oxygen) ion mass ratio times the electron gyrofrequency (upper black curve). For comparison, nominal plasma parameters for the XPOP roll period, including the oxygen ion plasma frequency and gyrofrequency, are given in Table 2.1. The data invariably show the highest spectral densities at low frequencies below 1 kHz, and the lowest spectral densities at high frequencies of order 100 kHz and above. Many depletion features are visible in the data, including the event near 0140:00 (HHMM:SS) and the periodic events marked with arrows at 0148:40, 0154:40 etc. (note that for simplicity in some of the figures we use the notation HH:MM). These 6 minute period events are associated with the PDP's motion through the orbiter's plasma wake and the arrows mark the time when the PDP is in the center of the orbiter's wake. The features at 0134 and 0140 occur while the PDP is directly upstream (in the ram direction) from the orbiter. Correlations between the wave characteristics and the PDP's phase (or position) relative to the velocity vector are discussed briefly in the next section. The present section is devoted to discussion of more general characteristics of the waves.

The bottom panel in Figure 2-12 shows the variation in the quantity $V_{\parallel}/V_T$ for this time period. Recall that the quantities $V_{\parallel}$, $V_{\perp}$ and V_T are defined as the components of the orbiter's velocity vector (relative to the ionospheric plasma) parallel and perpendicular to the magnetic field and the orbiter's speed, respectively. Co-rotation of the ionospheric plasma is assumed: the plasma co-rotation speed is of order 0.5 kms^{-1}, compared to the shuttle's orbital speed of order 7.8 kms^{-1}. A strong correlation is visible in Figure 2-12 between the spectral density of the waves at any frequency below about 10 kHz and the ratio $V_{\parallel}/V_T$. When the quantity $V_{\parallel}/V_T$ is near its maximum around 0135 and 0215, in other words when the shuttle's velocity vector is most nearly parallel to the magnetic field, dramatically lower wave amplitudes are

observed and the waves have much smaller extents in frequency. On the other hand, when $V_{\parallel}/V_T$ is small and the shuttle moves almost perpendicular to the magnetic field, the wave amplitudes are always larger than those for large $V_{\parallel}/V_T$ and the waves extend to much higher frequencies. Note that two distinct periods of very low wave levels, separated by one half the shuttle's orbital period, occur near the peaks in $V_{\parallel}/V_T$.

Careful comparisons show that the centers of the wave nulls in Figure 2-12 do not coincide exactly with the peaks in $V_{\parallel}/V_T$. In particular, the centers of the null periods both occur between the two peaks in $V_{\parallel}/V_T$ and less than one half orbital period apart. Prior to the finding that wave nulls are observed at times of large | $V_{\parallel}/V_T$ | throughout the Spacelab-2 mission, this observation might have cast doubt on the simple correlation drawn above between the wave nulls and large values of | $V_{\parallel}/V_T$ |. However, interpreting the waves observed between 0217 and 0219 as being associated with the ionospheric density feature (perhaps related to the plasma wake) would explain the difference in length (2 minutes) of the two wave nulls and the failure of the second wave null to include the peak in $V_{\parallel}/V_T$ (in contrast to the first null period). Some support for this interpretation comes from observations of plasma waves associated with a similar ionospheric density depletion during the free-flight mission (not shown here). This interpretation therefore significantly strengthens the correlation drawn above between wave nulls and large values of | $V_{\parallel}/V_T$ | in Figure 2-12. Furthermore, Cairns and Gurnett [1991b] note that some relatively strong, transient wave features occur during the first wave null which are not directly associated with thruster firings. Thruster firing occur at 0134:1,2,3,44,45, 0136:7,15,16,59, 0137:0-4,48-50, 0138:17-18, 0140:42-45 and 0144:34. Accordingly, the waves preceding the 0136 firings and the waves during minute 0139 are not directly thruster-associated. These waves do not appear to be part of the usual orbiter associated spectrum and may be associated with particular roll phases of the orbiter and the attitude of the PDP spacecraft itself. Thus, these phase complications between the wave nulls and the peaks in $V_{\parallel}/V_T$ may also be due to waves that are weaker than the usual correlated wave spectrum becoming observable when | $V_{\parallel}/V_T$ | is large. The $V_{\parallel}/V_T$ effect

25

for the near zone shuttle waves is strongly analogous to the $V_\parallel/V_T$ effect, described in the previous sections, for some plasma waves (called mushroom spectral features) downstream from the orbiter during the free-flight mission.

Figure 2-13 shows another type of spectrogram for the XPOP roll (see Figure 2-14); in this case the color coding represents the average squared electric field in the frequency bandwidth of the channel at frequency f. It can be seen that each channel up to a frequency of 56 kHz has an rms electric field af least of order 0.1 mV/m. The maximum electric field in a channel is of order 3 mV/m. Two distinct peaks in the electric field are visible: one centered at about 178 Hz and one near the lower hybrid frequency $\sim$ 5.6 - 10 kHz. The low frequency peak is clearly not in the lowest frequency channel (center frequency 31 Hz), although fields of order 1 mV/m sometimes extend down to the lowest observed frequencies. Strong levels of waves are observed between the two peaks. The high frequency peak follows the time variations and magnitude of the theoretical lower hybrid frequency determined by changes in the local ionospheric magnetic field. This is strong evidence that the high frequency peak is associated with lower hybrid waves. Except for the sudden extensions of the high frequency waves to 178kHz, e.g. at 0141:40, 0147:00, and 0158:30, the high frequency waves only have significant spectral densities up to about 56 kHz.

The presence of two peaks in the wave spectrum is also visible in spectral density plots. Figure 2-15 shows the spectral density plot for the typical period 0145 - 0210. It clearly shows the fall-off at low frequencies, the presence of a low frequency peak near 178 Hz, a region with spectral densities decreasing approximately inversely with frequency between the low frequency peak and the lower hybrid frequency, a bulge around the lower hybrid frequency marking the second component, and a rapid fall-off at higher frequencies. Channels above 178 kHz (in the MFR receiver) show essentially background levels. The rapid fall-off at high frequencies is believed to be real. However, Cairns and Gurnett [1991b] note that this fall-off may also be due to the high frequency portion of the wave spectrum being undetectable due to the wavelengths being very short relative to the antenna length.

The frequency distribution of wave electric fields shown in Figure 2-13 is biased

by the effective frequency bandwidths of each Helios channel. Accurate distributions of wave electric fields with frequency are calculated by integrating the measured spectral densities over frequency intervals centered on, but spanning the entire frequency ranges between, Helios channels. Cairns and Gurnett [1991b] define the broadband electric field for the waves in the frequency range centered on the n'th channel, E_n, by

$$E_n^2 = \int_{\sqrt{(f_n f_{n-1})}}^{\sqrt{(f_{n+1} f_n)}} S(f) df$$

Here S(f) is the spectral density units of $V^2 m^{-2} Hz^{-1}$ and the frequency intervals chosen for the integration correspond to equally-spaced intervals in logarithmic frequency centered on the n'th channel. The total, broadband, frequency-integrated electric field over the entire Helios frequency, E_T is then defined by $E_T = \sum_n E_n$. Figure 2-16 shows the frequency distribution of the ratio R(f_n) = E_n/E_T of the electric field centered on the n'th channel to the total broadband electric field. The data plotted are for the period 0145-0210 shown also in Figure 2-15. The total average broadband electric field E_T for this time period was 51.1 mV/m. Two peaks are visible, superimposed on a uniform high level at frequencies below about 20 kHz. The first peak is at centered at low frequencies near 178 Hz, with a broad shoulder at significant amplitudes to the second peak which is situated between 5.6 kHz and 10 kHz. As described above, the lower hybrid frequency varies between 5 and 10 kHz during this time period, providing an excellent identification for the higher frequency peak. Above 56 kHz the measured electric fields are essentially negligible. We note now that the instability theory in the next chapters predicts, in some cases, maximum wave growth at wavelengths of order 0.8 meters, commeasurable with the antenna length (1.15 meters) for these observations. It is therefore likely that for such case the broadband wave electric field estimate above (51mV/m) is smaller than the actual field present in the plasma.

The interpretation of the data in Figures 2-12 to 2-16 in terms of components in the wave spectrum is not unique. However, the peaks in Figure 2-16 are only a factor

of 2 greater than the level between the peaks and at lower frequencies than the first peak. It therefore seems most appropriate to interpret the wave spectrum in terms of a fairly constant high level of waves (electric fields of order 2.5 mV/m per frequency interval) from 31 Hz to 10 kHz with two superposed peaks, one around 178 Hz and one near the lower hybrid frequency. These superposed peaks have electric fields a factor of two higher than the constant level of waves between 30 Hz and 10 kHz. These data require any high frequency waves above about 20 kHz to smoothly merge with the lower hybrid frequency waves; no evidence is found for any sharply peaked wave components in the frequency range of 10 to 40 kHz.

Comparison Between the Near Zone and Far Field Ion Trail Spectra

The solid line shown in Figure 2-18 gives the relative electric field spectrum measured over a one-minute interval (0304:45 to 0305:45 UT, Day 213, 1985) at the center of the "mushroom" during the free-flight mission. The dashed line corresponds to the relative electric field spectrum of near zone waves shown in Figure 2-16. The average absolute spectral density for both cases is shown in Figure 2-17. As can be seen, the waves observed in the near zone and the waves observed during the free-flight have similar spectra and are within the same intensity range. In the free flight case, the relative electric field spectrum also has a peak around the lower hybrid frequency and a similar uniform region, but the peak at the lower frequencies is of diminished intensity. The similarities strongly imply that the waves observed at the center of the "mushroom" are generated in the near zone region around the shuttle. The difference in the low frequency peaks between the two cases implies that the lower frequency waves may be heavily damped. Therefore, the lower frequency peak only appeared in the near zone but not in the free-flight spectrum. As discussed below, thruster firings may also enhance the lower frequency peak in the near zone case. Note that no thruster firings occur during the free-flight period chosen.

2.2.2 Variation of the Near Zone Waves with Roll Phase

The periodic patterns at the XPOP roll period in Figures 2-12 and 2-13 indicate that the plasma waves associated with the space shuttle show significant and often reproducible variations with position relative to the ram direction. Figure 2-14 shows the time variation of the phase angle ϕ between the ram direction and the PDP's position vector relative to the orbiter. Times when the PDP is directly in the orbiter's wake region ($\phi = 0^o$) are denoted by white arrows in Figure 2-12. It is clear that the high frequency null features occur when the PDP is in the orbiter's wake region [Murphy et al.,1983]. Tribble et al. [1989] find that the low frequency waves in the range 6-40 Hz also show a null region when the PDP is in the orbiter's wake. Cairns and Gurnett [1991b] argue that the characteristics of these null features have implications for the wavelengths of the waves, as follows. The important point to note is that the higher frequency waves always decrease in amplitude before the lower frequency waves when approaching the center of the shuttle plasma wake, with increases in amplitude occurring in a symmetric fashion while leaving the wake center. This behavior is consistent with the higher frequency waves having shorter wavelengths, thereby having greater difficulty propagating into the deep null observed in the plasma density [Murphy et al., 1983; Tribble et al.,1989] in the orbiter's wake.

In distinction to the usual plasma wave null when the PDP is in the orbiter's plasma wake, it is usual for the wave intensities to be largest when the PDP is located directly upstream from the orbiter ($\phi = -180^o$ or 180°). However, during the times of maximum $V_{\parallel}/V_T$, nulls in the plasma waves are seen when the PDP is in the ram direction (near 0134, 0140, and 0216) or in the wake. Low level waves are observed at other roll angles during these periods.

2.2.3 Observations of the Near Zone Waves During the Free-Flight Mission

We now discuss the wave data from 0230 to 0247 Day 213, 1985, during the PDP spacecraft's free-flight mission. A summary of the PDP's motion during this period is as follows. The PDP spacecraft is initially moving downstream from the upstream

region with small Y_P at a large and approximately constant distance along the magnetic field (Z_P coordinate) of order 215 m. The PDP has position $X_P = 0$ near 0239:15 (i.e., the PDP is magnetically connected to the orbiter's center of mass), and $Y_P = 0$ near 0241:10 when downstream from the shuttle (i.e., probing the center of the wake). In the plasma waves data observed in association with the upstream-downstream transition $X_P = 0$, a strong broadband burst of waves extending up to the lower hybrid frequency is observed as the PDP becomes magnetically connected to the space shuttle (i.e., $X_P = 0$). The maximum frequency of these broadband waves abruptly decreases from near the lower hybrid frequency to about 500 Hz at about 0241:00, and then tends to about 300 Hz with increasing distance downstream. At 0241:10 the PDP is magnetically connected to the center of the wake with $X_P \sim -50m$, $Y_P \sim -50m$, $Z_P \sim -50m$.

The important observation here is the onset of strong waves at frequencies up to and above the lower hybrid frequency when the PDP spacecraft becomes magnetically connected to the space shuttle. Inspection of the PDP survey slides indicate no obvious increases in electron or ion fluxes measures by the LEPEDEA, RPA, IMS or other particle instruments or changes in the DC electric field instruments. It does not appear correct, therefore, to interpret the observed plasma wave event in terms of waves generated locally (to the PDP spacecraft) due to particles originating at the space shuttle. Electrostatic waves with wavevectors (nearly) perpendicular to the magnetic field have wavefronts (almost) aligned along the magnetic field and the electric field of such a waves does not vary (rapidly) along the magnetic field, e.g., in an infinite homogeneous plasma. Cairns and Gurnett [1991b] therefore interpret the burst of waves observed between 0239:30 and 0241:00 in terms of the intense waves generated in the near vicinity of the space shuttle being observed along the magnetic field from the shuttle. This implies that the near zone waves, at least at frequencies below a few times the lower hybrid frequency, have wavevectors oriented perpendicular to the magnetic field. This interpretation places significant restrictions on theories attempting to explain the near zone waves. The evident decrease in amplitude for the free-flight waves compared with the near zone waves, and the restriction in the

frequency spectrum of the waves, may be qualitatively explained in terms of the inhomogeneous plasma environment of the shuttle and the smaller wavelengths for the higher frequency waves inferred from the high frequency nulls in the orbiter's wake (see last section). Next, additional evidence supporting Cairns and Gurnett's [1991b] interpretation of the wavevectors of the near zone waves is provided.

Figure 2-19 compares the spectral density of the burst of waves for the time period 0239:40-50 with the average spectral density of the near zone waves shown in Figure 2-15 (time period 0145 - 0210 Day 212). These spectral density profiles are surprisingly similar. The free-flight data shows two low frequency peaks, one near 178 Hz and one near the lower hybrid frequency of about 3 kHz, which compare well with the XPOP roll observations. Note that the lower hybrid frequency during this period of near zone data was above about 5 kHz, consistent with the frequency of the second peak. The high frequency fall-off above the lower hybrid frequency shows similar forms in both the free-flight and near zone data. These spectral density profiles coincide well if one multiplies the free-flight curve by a factor of 50, corresponding to electric fields a factor of 7 stronger. These spectral density profiles are therefore consistent with the interpretation that the observed free-flight signals are plasma waves generated in the Near Zone region with wavevectors perpendicular to the magnetic field (i.e., flute-like modes). In addition, in the next chapters we show that the linear theory predicts maximum growth at wavelengths of order 1 meter: the longer antenna length during free-flight (3.89 meters) compared with the XPOP roll (1.15 meters) then implies less efficient measurement of the waves electric fields. During the free-flight mission it is unusual to observe waves above about two times the lower hybrid frequency (except for thruster- and FPEG-associated waves and the interference spikes) except perhaps when well downstream in the wake region.

Evidence for spin modulation of the waves was sought to provide further support for the wavevector direction inferred above. However, except for a spacecraft-associated signal with one maximum-null pair per spacecraft rotation, the data showed no evidence of consistent spin modulation.

2.3 Waves Associated with Orbiter Water Releases

One of the scientific objectives of the PDP experiments on Spacelab 2 was to investigate the effects of shuttle orbiter water dumps on the orbiter environment. Two kinds of water dumps took place during Spacelab 2 flight [Pickett et al., 1989]: namely, supply and waste. The supply water is used to dispose the excess water produced by the fuel cells. In order to more effectively study the effects of water releases, certain times and PDP locations were set aside for this purpose [Pickett et al., 1989]. During times when the Spacelab 2 solar experiments were scheduled for prime viewing, the PDP was positioned on the remote manipulator system (RMS) at a designed location called "point solar". The term "point solar" refers to the stationary position of the PDP on the RMS with the PDP upright ~12 m from the port aside the orbiter. Point solar is an ideal position from which to obtain measurements during water dumps because the water exit ports are located on the port side of the orbiter just below the forward payload bay door and only ~12 m from the PDP.

Typical density fluctuation spectra for times before, during, and after the day 214 water dump are presented in Figure 2-20. The characteristic increase over ambient at all frequencies bellow $\sim f_{LH}$ is seen during the time water is being released. As Pickett et al. [1989] noted, the major increase in intensity corresponds to the low frequency peak component (see section above) of the near field spectrum (up to 50 dB at $f \sim 100$ Hz). The "after" spectrum was taken before the environment had fully recovered after the water valve was closed. As expected, this spectrum still shows an increase over ambient at frequencies bellow f_{LH}.

2.4 Waves Associated with Thruster Firings

The shuttle thrusters were fired frequently during the PDP free flight period. The thruster caused the yellow spikes at extremely low frequencies on the color-coded spectrum of Figure 2-2. The spectral characteristics of these low frequency enhancements are similar to those observed during water dump operations, described above.

The density of the neutral gas produced from the thruster firing can reach $10^7\,cm^{-3}$ locally, which is a thousand times higher than the ambient plasma density. A study by Gurnett et al. [1988] of the correlation between the amplitude of the electrostatic waves and thruster firings shows most of the lower hybrid waves are not directly related to thruster firings. However, many of the lower hybrid-type interference patterns were observed during times of high thruster activity [Feng et al., 1993]. Furthermore, in some cases thrusters firings were directly responsible for the observed lower hybrid waves. During these periods the PDP was approaching the magnetic conjunction with the shuttle [Feng et al., 1993]. Therefore, initially the background electric field levels were relative low. Right after each thruster firing, which typically has a duration of less than a second, the lower hybrid waves were enhanced for about 20 to 30 seconds. Since the neutral gas released from thruster firings has a much higher density than the ambient atmosphere around the shuttle, it is clear that thruster firings should enrich the shuttle water cloud for a considerable period of time, thereby enhancing the level of lower hybrid waves driven by pickup ions [Feng et al., 1993]. A summary of this chapter is presented in Section 7.1.

Table 2.1: Nominal XPOP Roll Parameters

Parameter	Value
n_e	$10^4 - 6 \times 10^5$ cm^3
T_e	2000 K
T_O	1000 K
f_{gO}	20-45 Hz
f_{LH}	4-8 kHz
f_{pO}/f_{gO}	100-200
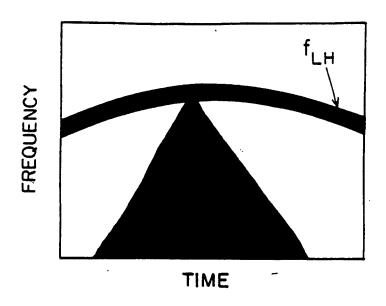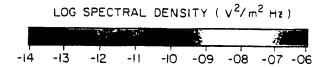
Figure 2-1: An idealized "mushroom" spectral feature (from *Cairns and Gurnett*, 1991a).
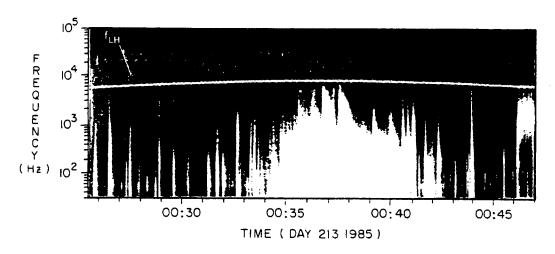
Figure 2-2: A frequency-time spectrogram with color-coded amplitude for the period 0025 - 0047, Day 213, 1985 during the PDP's free-flight mission (from *Cairns and Gurnett,* 1991a). The white curve shows the lower hybrid frequency. A "mushroom" spectral feature is seen between about 0031 and 0042. Wake transits occur near 0028, 0034 and 0041 with no accompanying changes in the wave spectrum.
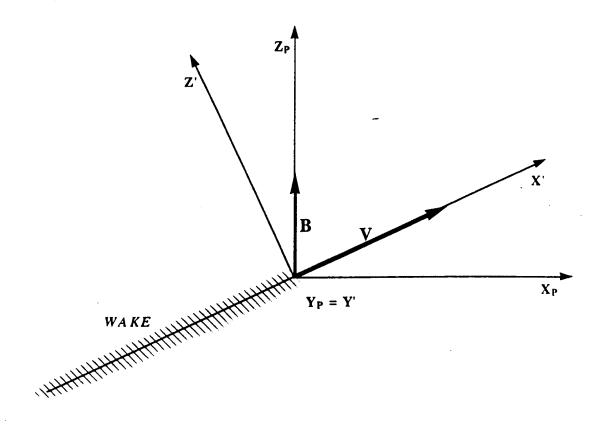
Figure 2-3: Coordinate systems used for the PDP wave data description. The Z_P-axis of the pickup coordinate system is aligned with the earth's magnetic field. The X'-axis of the primed coordinate system is aligned with the orbital velocity vector V. The Y_P and Y' axes are identical.
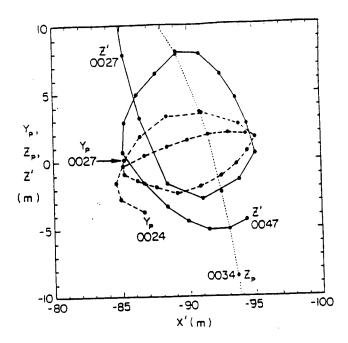
Figure 2-4: The time variations in the PDP's coordinates Z', Y_P and Z_P as a function of downstream position X_P for the period 0025 - 0047 using full, dashed and dotted lines, respectively (from *Cairns and Gurnett*, 1991a). The filled circles are separated in time by 1 minute. Noting the PDP's antenna length is approximately 4 m, the PDP remains almost stationary relative to the orbiter's plasma wake (coordinates X', Y_P and Z'). Wake transits occur near 0028, 0032 and 0041.
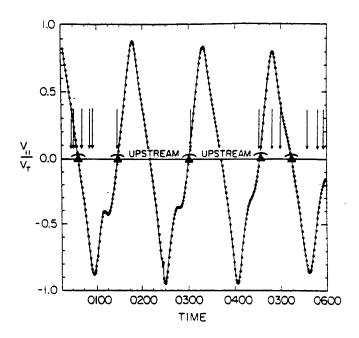
Figure 2-5: The variation of $V_{\parallel}/V_T$ during the PDP's free-flight mission (from *Cairns and Gurnett*, 1991a). Stylized mushrooms indicate where "mushroom" spectral features are observed and arrows indicate transits of the center of the orbiter's wake. Times when $V_{\parallel}/V_T = 0$ and the PDP is not downstream from the orbiter are specified. Mushroom features are observed whenever $V_{\parallel}/V_T = 0$ and the PDP is downstream from the shuttle.

FREQUENCY, kHz

20

10

0038:45   :50   :55

$X' = -87$ m $Y' = -5$ m $Z' = 1$ m

PDP,   DAY 213,   AUG. 1, 1985
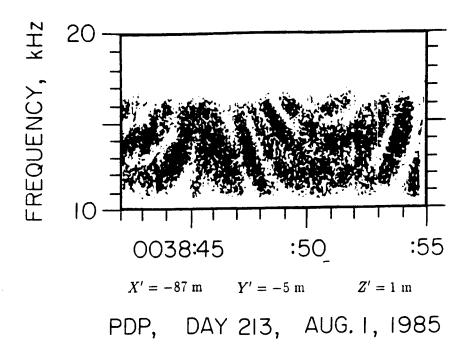
Figure 2-6: An example of an interference pattern observed in the 10 to 20 kHz electric field wideband spectrum (from *Feng et al.*, 1993). This frequency-time spectrum was obtained over a 13-second interval (0038:42 to 0038:55 UT) on August 1, 1985.

FREQUENCY, kHz

10

0

0200:15   :20   :25   :30   :35

$X' = -20$ m $Y' = -200$ m $Z' = 26$ m

PDP,   DAY 213,   AUG. 1, 1985
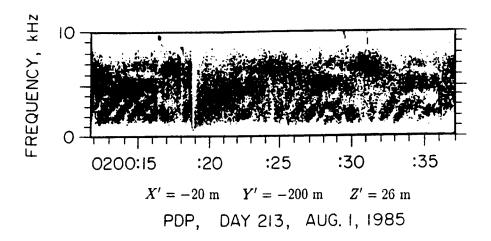
Figure 2-7: An example of an interference pattern observed in the 0 to 10 kHz electric field wideband spectrum. This spectrum was obtained over a 25-second interval (0200:12 to 0200:37 UT) on August 1, 1985 (from *Feng et al.*, 1993).

DISPERSION RELATION IN 2-D X'-Y' PLANE
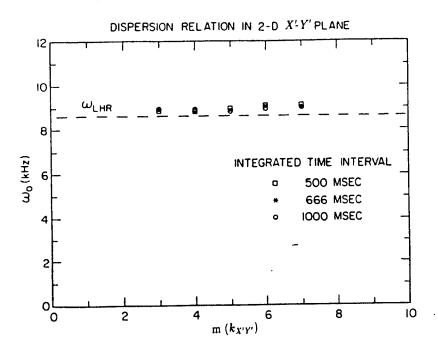
Figure 2-8: The dispersion relation of the lower hybrid waves in the 2-D X'-Y' plane for the 0038 UT event (from *Feng et al.*, 1993).

POWER SPECTRUM 0038:43 UT
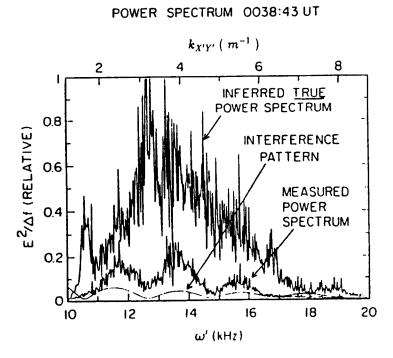
Figure 2-9: A power density spectra for the 0038 UT event (from *Feng et al.*, 1993).

PDP TRAJECTORY RELATIVE TO THE SHUTTLE
01:24 – 04:41 UT

Figure 2-10: The wavevector directions and magnetic field directions plotted as a function of the X', Y' position of the PDP during the period from 0124 to 0441 UT (from *Feng et al.*, 1993).
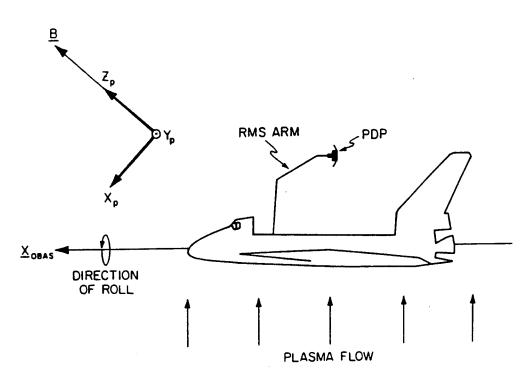
Figure 2-11: The geometry of the XPOP roll during the Spacelab-2 mission (from *Cairns and Gurnett*, 1991b). The shuttle rolls about the nose-tail or X_{OBAS} axis while its orbital velocity is perpendicular to the X_{OBAS} axis. The "pick-up" coordinate system $X_p - Y_p - Z_p$ is also defined.

42
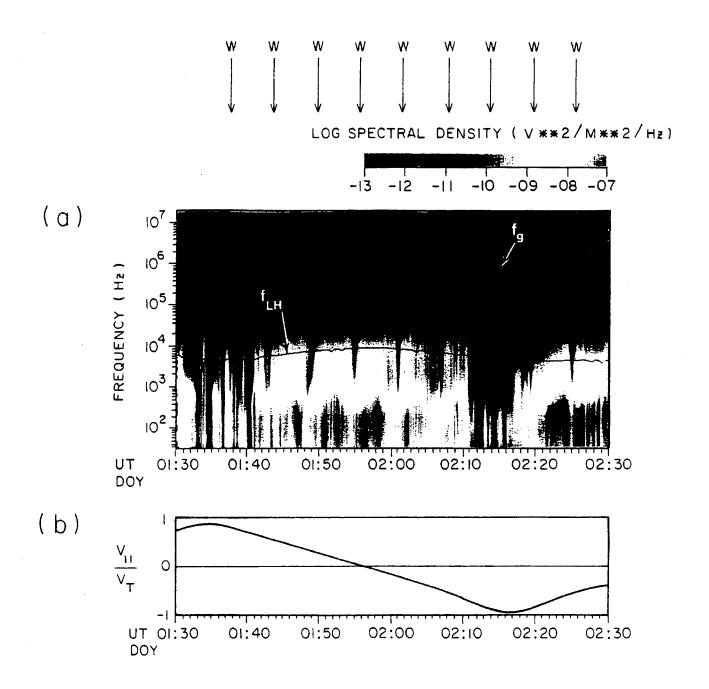
Figure 2-12: (a) A Helios-MFR color spectrogram for the period of the XPOP roll (from *Cairns and Gurnett*, 1991b). Spectral density is color-coded. Black lines show the variation in the electron gyrofrequency f_g and the lower hybrid frequency f_{LH}. (b) The variation in the quantity $V_\parallel/V_T$, measuring the ratio of the shuttle's orbital velocity parallel to the magnetic field and the orbital speed, during the XPOP roll. The nulls in the wave data are correlated with large values of $V_\parallel/V_T$.

LOG ELECTRIC FIELD SQUARED (V**2/M**2)
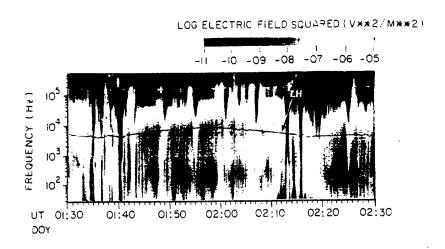
Figure 2-13: Spectrogram of Helios-MFR data showing the color-coded squared electric field measured in each channel bandwidth (from *Cairns and Gurnett*, 1991b). Two peaks are evident, one near 100 Hz and one at the lower hybrid frequency.
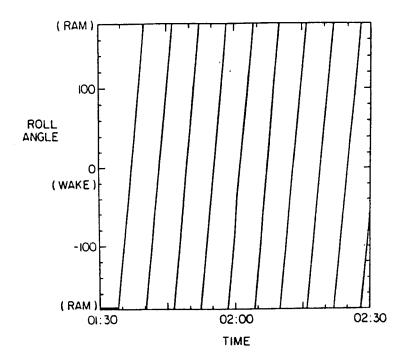
Figure 2-14: Roll angle versus time for the period 01:30 to 02:30 during the XPOP roll (from *Cairns and Gurnett*, 1991b). A phase angle of 0° corresponds to the PDP being in the center of the shuttle's wake.
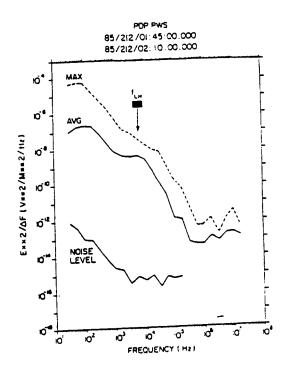
Figure 2-15: Spectral density as a function of channel frequency for the period 01:45-02:10 during the XPOP roll (from *Cairns and Gurnett*, 1991b). The solid curve shows the average spectral density, while the dashed curve shows the maximum observed spectral densities during this period. The other line shows the calibrated receiver noise level (before launch).

POP ROLL RELATIVE ELECTRIC FIELDS

Figure 2-16: Ratio R(f) of the average electric field in a frequency bandwidth divided by the total average broadband field as a function of frequency (from *Cairns and Gurnett*, 1991b). The wave fields are essentially constant from 30 Hz to 10 kHz and sharply lower at higher frequencies, reaching the background level by 100 kHz. Two peaks, by a factor of 2, are seen in the average wave fields: one at low frequencies near 178 Hz, and one at the lower hybrid frequency.
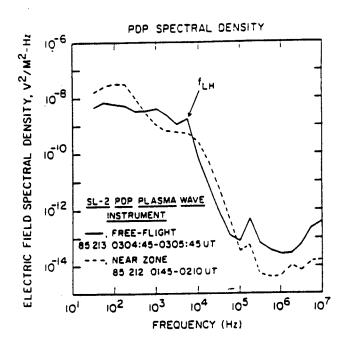
Figure 2-17: Comparison of average electric field spectral density as a function of frequency between the near zone and free flight waves (from *Feng et al.*, 1993). The dashed line shows the near zone spectra during the interval 0145 to 0210 UT on Day 212, 1985. The solid line is the free flight spectra measured at the center of the "mushroom" during the interval 0304:45 to 0305:45 UT on Day 213, 1985.

PDP RELATIVE ELECTRIC FIELDS
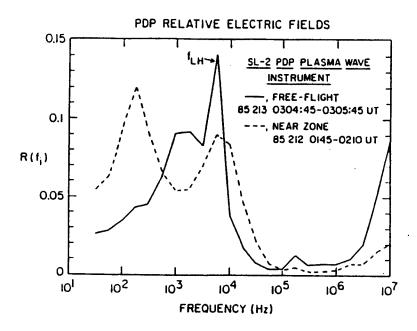
Figure 2-18: Comparison of the relative electric field spectra for the near zone and free flight waves (from *Feng et al.*, 1993). The dashed line is the average spectra for the near zone waves during the interval 0145 to 0210 UT on Day 212, 1985. The solid line is the free flight spectra measured at the center of the "mushroom" during the interval 0304:45 to 0305:45 UT on Day 213, 1985.

49
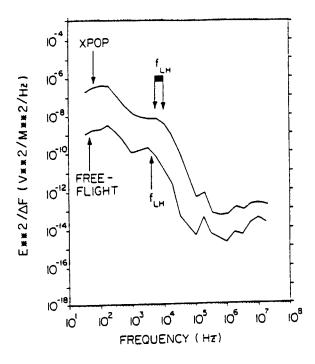
Figure 2-19: Comparisons of the spectral density profiles of the waves observed during the free-flight connection event (02:39::40-50, day 213) and during the XPOP roll (01:45 - 02:10, day 212) (from *Cairns and Gurnett*, 1991b). These curves are qualitatively similar with magnitudes differing by a factor of order 30 (the antenna lengths differ by a factor of order 3). These data support the interpretation that the connection event corresponds to observation of the near zone waves at a 200 meter distance along the magnetic field, implying that the near zone waves are flute-like modes.
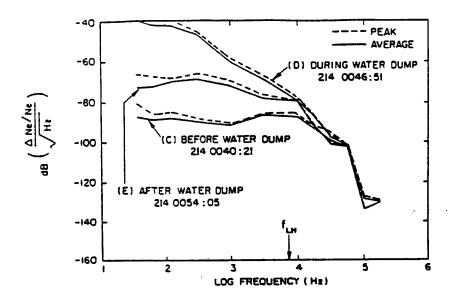
Figure 2-20: Density fluctuation spectra (35 Hz to 178 kHz) before (C), during (D), and after (E) the water dump (from *Pickett et al.*, 1989). Enhancement over ambient occurs only at frequencies below about the lower hybrid frequency. The "after" spectrum was taken before the environment had fully recovered and thus still shows enhancements over ambient (up to $\sim 20dB$ at $f \sim 100$ Hz).

Chapter 3

The Beam-Arc Velocity Distribution Function of Pick-Up Water Ions

The general scenario envisaged for the shuttle's interaction with the ionospheric plasma [e.g., *Shawhan et al.*, 1984; *Gurnett et al.*, 1988; *Hastings and Gatsonis.*, 1989; *Paterson and Frank*, 1989;] involves the outgassing of water vapor from the shuttle orbiter, the subsequent collisional charge exchange of these water neutral molecules with ionospheric oxygen ions (O^+) to form water ions, the generation of plasma waves by these water ions, and subsequent plasma heating. Evidence exists for a cloud of neutral water surrounding the shuttle [*Carignan and Miller*, 1983; *Narcisi et al.*, 1983] and water ions have indeed been observed, both by the shuttle's payload instruments [*Narcisi et al.*, 1983; *Hunton and Calo*, 1985] and the PDP instruments [*Grebowsky et al.*, 1987; *Paterson and Frank*, 1989]. During the PDP free-flight portion of the Spacelab 2 mission, *Paterson and Frank* [1989] observed "ringlike" distributions of ions with the basic characteristics expected of water ions produced by the charge exchange process. Paterson and Frank [1989] also found that water ions produced by charge exchange should be present in detectable amounts (in excess of 1% of the O^+ number density) throughout the shuttle missions. This suggest that the possible presence of ringlike distributions of water ions should be strongly considered in interpreting and modeling the data from the OSS 1, Spacelab 2, and other shuttle missions. A knowledge of the distribution functions and sources

of free energy is a prerequisite for constructing theories for the active and complex wave environment associated with the space shuttle.

In this chapter we develop a model of the distribution function of pick-up water ions for the region downstream of the space shuttle, that is, for the region of highest intensity waves (see Section 2.1.3). Cairns [1990] has modeled the water ion distribution for the region upstream of the orbiter. We show that in the shuttle frame water ions drift downstream and since most water ions are created in the near vicinity of the shuttle they form a long water ion trail downstream of the orbiter, of the order of 12 km, before they recombine. We develop a model of the water ion distribution in the ion trail and show that the characteristics of this distribution in some particular region of the trail are determined by the charge exchange rates local to and upstream of that particular region. We therefore find it necessary to also consider a model of the water ion distribution for the region upstream of the shuttle and for simplicity we adopt Cairns [1990] model, which we briefly discuss in the first two sections of this chapter. In our analysis of the water ion distribution of the ion trail we neglect wave effects but we determine analytically the effect of elastic collisions of water ions with the dominant neutral molecules of the region downstream of the shuttle. It should be pointed out that this analysis of the water ion distribution is also important since previous theoretical studies of the shuttle's plasma cloud [*Hastings and Gatsonis*, 1989; *Eccles et al.*, 1989; *Paterson and Frank*, 1989] ignored the particle distribution function in favor of a fluid description and did not consider the effects of the large water ion gyroradius ($\sim$ 40m). Hastings and Gatsonis [1989], Eccles et al. [1989], Paterson and Frank [1989], have assumed a (magnetized) fluid description for the plasma species in their simulations of water ion production and plasma electrodynamics in the vicinity of the shuttle; with the supposition, that ion-molecule collisions might randomize the water ions sufficiently rapidly to justify a fluid description. In this thesis we will show that this important supposition can be made valid only if wave-particle scattering effects are considered; we will show that the effect of elastic collisions on the water ion distribution is relatively small.

3.1 The Pick-Up Water Ion Distribution Function in the Region Upstream of the Shuttle

3.1.1 Model for the Charge Exchange Process in the Shuttle's Water Cloud

Let us consider a reference frame (X_p, Y_p, Z_p) moving with the space shuttle in which the ionospheric magnetic field $\mathbf{B}$ is along the Z_p axis. This reference frame is shown in Figure 3-6 and we shall call it the pickup reference (shuttle) frame. The origin of this reference frame is taken to coincide with the center of mass of the shuttle orbiter. Without loss of generality we assume that the velocity of the background plasma in this reference frame is of the form $(-V_\perp, 0, -V_\parallel)$; positive values of X_p then correspond to the region upstream of the shuttle. The motion of the background plasma across the magnetic field then implies the presence of a self-consistent motional electric field $\mathbf{E} = (0, -V_\perp B, 0)$ in this reference frame. Velocity is conserved during the charge exchange reaction. Now, however, the newly born water ion must respond to the crossed electric and magnetic fields, resulting in a cycloidal motion in the $X_p - Y_p$ plane. The equations of motion for the particle motion may be solved for the position and the velocity of the particle as a function of time given the position and velocity at some reference time. This motion may be summarized as follows: first, any particle speed along the magnetic field (the Z_p axis) remains constant: second, ignoring thermal motions for the moment, a newly born water ion starts out at zero velocity and is accelerated by the crossed electric and magnetic fields into motion with a gyrospeed $V_\perp$ centered on a velocity $(-V_\perp, 0, 0)$, and a gyroradius $V_\perp \tau_{cw}/(2\pi)$ where τ_{cw} is the water ion gyroperiod. This gyromotion maps out a ring in the $V_{X_p} - V_{Y_p}$ plane in velocity phase space. A "ring" distribution results if water ions are found at all gyrophases in this $V_{X_p} - V_{Y_p}$ plane, while a "beam" distribution results if the water ions are found in a well-defined range of gyrophases. Thermal motions produce a spread in gyrospeed and velocity along the magnetic field. Figure 3-1 is a schematic illustration of a partial ring distribution, which will be called a beam-arc distribution below. Beam arc distributions of water ions were predicted by Cairns [1990] to occur

near to and upstream from the space shuttle. In this section we review Cairns [1990] model of the water ion distribution for the near and upstream regions of the shuttle. A knowledge of Cairns [1990] model will be necessary in the next sections of this chapter, where we will develop a model for the water ion distribution of the near and downstream regions of the shuttle. The (X_p, Y_p, Z_p) reference frame is the natural one for the studies of water ion pickup around the shuttle.

Liouville's equation for the distribution function of charge-exchanged water ions, $f_w(\mathbf{r}, \mathbf{p}, t)$, is

$$\frac{d}{dt} f_w(\mathbf{r}, \mathbf{p}, t) = F_w(\mathbf{r}, \mathbf{p}, t) \tag{3.1}$$

where $F_w(\mathbf{r}, \mathbf{p}, t)$ is the source term. A formal solution exists [*White et al.*, 1983; Cairns, 1987]:

$$f_w(\mathbf{r}, \mathbf{p}, t) = \int_{-t}^{0} d\tau F_w(\mathbf{r}'(\mathbf{r}, \mathbf{p}, t; \tau), \mathbf{p}'(\mathbf{r}, \mathbf{p}, t; \tau), t + \tau) \tag{3.2}$$

where

$$\mathbf{r}'(\mathbf{r}, \mathbf{p}, t; 0) = \mathbf{r} \tag{3.3}$$

$$\mathbf{p}'(\mathbf{r}, \mathbf{p}, t; 0) = \mathbf{p} \tag{3.4}$$

and $-\tau$ is the travel time from $(\mathbf{r}', \mathbf{p}')$ to $(\mathbf{r}, \mathbf{p})$ along the particle path. The effects of the wave-particle scattering on the particle distribution function are ignored throughout this chapter.

An expression for the source term $F_w(\mathbf{r}, \mathbf{p}, t+\tau)$ for the collisional charge exchange follows from the binary nature of the collision and conservation of velocity for the particles:

$$F_w(\mathbf{r}, \mathbf{p}, t + \tau) = \gamma n_O(\mathbf{r}, t + \tau) f_{\bar{w}}(\mathbf{r}, \mathbf{p}, t + \tau) \tag{3.5}$$

55

where n_O is the number density of oxygen ions. This equation is consistent with the usual charge exchange equation involving number densities, allowing identification of the reaction rate γ as 2×10^{-9} $cm^3 s^{-1}$ [*Paterson and Frank*, 1989]. The remaining quantity $f_{\bar{w}}$ is the distribution function of the water neutral gas, which for time-steady outflow with thermal speed $v_{th\bar{w}}$ from the shuttle may be written

$$f_w(\mathbf{r}, \mathbf{p}, t + \tau) = \frac{n_{\bar{w}0}(r_0) r_0^2}{r^2} \frac{1}{(2\pi)^{3/2} v_{th\bar{w}}^3} e^{-v^2/2v_{th\bar{w}}^2} \tag{3.6}$$

Here $n_{\bar{w}0}(r_0)$ is the number density of water neutrals at a radial distance r_0 from the shuttle; note that $n_{\bar{w}0}$ obeys an inverse square law in time-steady outflow. The symbol v denotes the speed corresponding to momentum $\mathbf{p}$. For convenience it is assumed that the velocity and density of the background plasma, the magnetic field strength, and water gas thermal speed are constant over the time scales of interest. Normalizing all speeds by the water thermal speed $v_{th\bar{w}}(=(kT_{\bar{w}}/m_{\bar{w}})^{1/2})$ and distances by the characteristics distance $v_{th\bar{w}}\tau_{cw}$, these assumptions and equations 3.5 and 3.6 allow 3.2 to be rewritten as the product of constants times a "probability" integral for the charge exchange:

$$f_w(\mathbf{r}, \mathbf{p}, t) = \frac{\gamma n_O n_{\bar{w}0} r_0^2}{(2\pi)^{3/2}} \int_{-t}^{0} d\tau \frac{exp[-v'^2(\mathbf{r}, \mathbf{v}, t + \tau)/2]}{r'^2(\mathbf{r}, \mathbf{p}, t + \tau)} \tag{3.7}$$

with r' and v' implied by 3.3 and 3.4 and the equations of motion for the water ions. This "probability" integral is essentially an integral over travel time $-\tau$ of the probability of ions producing charge exchange at earlier times $t + \tau$ with eventual momentum $\mathbf{p}$ at the observation time t and position $\mathbf{r}$. The shape of the distribution function is specified by the probability integral alone.

Normalization of Velocities and Distances

Before proceeding, let us specify the normalization used in this chapter: all speeds are normalized by the water neutral thermal speed $v_{th\bar{w}}(=(kT_{\bar{w}}/m_{\bar{w}})^{1/2})$ and all distances are normalized by the characteristic distance $v_{th\bar{w}}\tau_{cw}$, where τ_{cw} is the water ion

cyclotron period. Therefore, assuming a constant water neutral gas temperature of 300 K, the normalized range of $V_\perp$ for the PDP free-flight mission is from about 7 to 21 clustered primarily near 20, and the value of 20 is used. During this time the shuttle's orbital speed V remained nearly constant with $V \sim 21$; smaller values of $V_\perp$ therefore correspond to times when the orbiter's velocity is more nearly parallel to the ionospheric magnetic field. Smaller values of $V_\perp$ tend first to increase the probability integral and so the total water ion number density for a given position and second to decrease the contrast in the distribution function over gyrophase for a given gyrospeed, making the distribution function more ringlike. The distance scale $v_{th\bar{w}}\tau_{cw}$ similarly varies from about 8 to 21 m with a characteristic value of the order of 15 m, which is used hereinafter (i.e. $X_p = 1$ corresponds to a distance of 15 m from the origin). In contrast, the water ions have Larmor radii (gyroradii) $r_{Lw} = V_\perp \tau_{cw}/(2\pi)$ ~ 40 m.

3.1.2 Results for the Water Ion Distribution Functions Directly Upstream from the Shuttle

The probability integral in Equation 3.7 has been solved by Cairns [1990] using standard techniques. Let us now discuss his results. Figure3-2 shows the water ion distribution functions resulting from charge exchange at various distances directly upstream from the shuttle ($Y_p = Z_p = 0$) and demonstrates the transition from a ring distribution to a beamlike distribution with decreasing distance from the shuttle. In this figure, this transition from the ring to beamlike distribution is investigated by using cuts along the line of constant gyrospeed $V_g = V_\perp$ normalized to the maximum value of the distribution function along the cut. The thickness of these distributions in gyrospeed is in all cases of order $v_{th\bar{w}}$. The distributions are displayed in gyrophase phase space formed by unfolding the ring feature in $X_p - Y_p$ velocity space (e.g., Figure 3-1) centered on the velocity ($-V_\perp, 0, 0$) for particles with zero speed along the magnetic field. (Calculating the distribution function with smaller steps in gyrophase smooths the sharp turnover in the cuts near a gyrophase of 10°.) The range of gyrophases $\Delta\phi$ in which the distribution function has over one half of its maximum value

57

decreases significantly as X_p decreases, and the ratio of this range in gyrophase to the total available (360°)also decreases significantly. It is important to note, however, that even at $X_p \sim 1$, corresponding to the approximate outer surface of the shuttle and so an inner limit for the theory's applicability, this width $\Delta\phi$ is of the order of 40° while for $X_p = 5$, $\Delta\phi \sim 90°$. The speeds in the X_p and Y_p directions are shown at the top of Figure 3-2 above the gyrophase axis and show that even at $X_p = 1$ the range of velocities in the $V_{X_p} - V_{Y_p}$ plane for which the distribution function is significant is relatively large. A conventional beam distribution is expected to be restricted to a narrow range of velocities centered on some velocity. It is therefore not appropriate to term these water ion distributions "beam" distributions in a absolute sense. Rather, Cairns [1990] suggested the term "beam arc" distributions, corresponding to a finite segment of a ring, to describe these distributions found close to the shuttle.

This transition from ring to beam arc distribution function with position upstream from the shuttle may be understood in terms of the spatial gradient in water neutral number density and the characteristics of the charge exchange process. Figure 3-3 illustrates the development of beam arc and ring distributions at $X_p = 1$ and $X_p = 15$, respectively, in the $X_p - Y_p$ plane for $V_\perp = 20$. The solid lines are contours of constant inverse distance squared $1/R_p^2$, and so constant charge exchange rate, spaced in powers of 10. The characteristics of the water ion distribution function at $X_p = 1$ and $X_p = 15$ follow on considering the primary source of particles with zero velocity (stars) and velocity ($-2V_\perp$, 0,0) (squares) at the observation points. Ignoring thermal motions (i.e., $v_{th\bar{w}} \ll V_\perp$), all picked-up water ions initially have zero velocity. Particles observed at zero velocity are therefore primarily produced (at the star symbols) very close to the observation point. Particles observed at velocity ($-2V_\perp$, 0, 0) have, however, followed their gyromotion along the dashed lines from their primary production points (squares) where they had zero velocity. At $X_p = 1$, therefore, the production rate of water ions observed at velocity ($-2V_\perp$, 0, 0) is less than one-hundredth that for ions observed near zero velocity, implying that the distribution function is a well-defined beam arc. In contrast, at $X_p = 15$ the production rates for ions with near-zero velocity and velocity ($-2V_\perp$, 0, 0) differ by only a factor $(15/25)^2 \sim 0.4$,

implying a ring distribution function with small contrast. Farther from the shuttle the ring distributions becomes more uniform. Beam arcs do not form exactly at zero gyrophase due to the thermal spread of the water neutrals.

Beam arc water distributions are also formed away from the X_p axis in the upstream region in regions where the charge-exchange rate is large. A general condition for formation of the beam arc distribution is that $R_p < 2$ with $X_p > 0$. In summary, the water ion should have a beam arc distribution function when upstream and within a radial distance of order 20-40 m ($R_p < 2$) from the shuttle in the upstream hemisphere. Pick-up ion data [*Paterson and Frank*, 1989] are not available to verify these predictions since the PDP spacecraft's orbit around the shuttle did not sample the required region where such beam-arcs occur.

Lastly, Cairns [1990] also claims that collisions between the water ions and water neutral gas molecules offer another means of establishing more beam-like water ion distribution functions: the beam arc distributions occur due to the water ions following their gyromotion; disruption of the regular ion gyromotion by collisions with low velocity water neutrals might then limit the water ions to a more limited range of gyrophases and so to a more beam-like distribution function. In contrast, we will show in the next sections that the effect of elastic collisions is negligible in determining the water ion distribution close to the shuttle.

3.2 The Pick-Up Water Ion Distribution Function in the Region Downstream of the Shuttle

3.2.1 The Water Ion Distribution in the Region of Highest Water Ion Density

In the remainder of this chapter we will develop a model of the water ion distribution for the region downstream of the shuttle. For this analysis we will use two key features of the charge exchange phenomenon in the region upstream of the shuttle i) in the region upstream of the shuttle the water ion densities are far larger within 10 m of the shuttle than farther upstream and ii) within 15 m upstream of the shuttle the

water ion distribution is the $X_p = 1$ beam-arc shown in Figure 3-2.

Feature (i) is consistent with the PDP data [e.g. *Paterson and Frank*, 1989] and is a result of the steady state spherical outflow of the water neutrals from the shuttle. For this situation, conservation of particles (i.e. the continuity equation) demands a $1/r^2$ radial variation of the water neutral density. The $1/r^2$ water neutral density profile has been used in various fluid models of the shuttle cloud [*Hastings and Gatsonis*, 1989; *Eccles et al.*, 1989; *Paterson and Frank*, 1989], and in a kinetic model which involves the numerical integration of Equation 3.7 to give the water ion number density as a function of position relative to the space shuttle [*Cairns*, 1990]. The results of these works are thus consistent with feature (i) and may be summarized as follows: (1) In the upstream region, the water ion density should decrease rapidly with the radial distance from the shuttle, r, and at distances larger than 150 m of the shuttle (i.e. $X_p \geq 10$) it should be down to less than 1% of the plasma density. (2) Within 10 m of the shuttle (i.e. $X_p < 1$) the water ion density should comprise at least 20% of the plasma density. (3) Pile-up of water ions due to a geometric effect of the circular ion trajectories should lead to an increase in plasma density close to the shuttle. This pile-up is not included in fluid predictions for the water ion density and can only be obtained by Cairns [1990] method (we shall discuss this effect later). We note that water ions and other pick-up ions sometimes comprise as much as 50% of the plasma density in the near vicinity of the space shuttle (e.g., Kurth and Gurnett, 1990).

Feature (ii) has been discussed in the previous sections and refers to Cairns [1990] prediction that a transition in the pickup water ion distribution from ring distribution to beam-arc distribution occurs with decreasing distance upstream from the orbiter (see Figure 3-2). We can therefore conclude that in the region upstream of the shuttle most of the water ions lie within 10 m upstream of the shuttle (i.e. $X_p < 1$) and have the $X_p = 1$ beam-arc distribution shown in Figure 3-2.

3.2.2 The Downstream Water Ion Trail

Let us recall that during the shuttle's orbital flight, water ions are constantly being created throughout the water neutral cloud which co-orbits with the shuttle. These ions are created at different rates (see Figure 3-3) and, since the highest rates occur in the near vicinity of the shuttle ($r \leq 10$ m), the region within 10 m of the shuttle is the region with the highest water ion densities. After being created, these high density water ions convect downstream of the shuttle with an $\mathbf{E} \times \mathbf{B}$ drift equal to $V_\perp$ since they get trapped in the earth's magnetic field. Because of their large drift the water ions leave rapidly the very near vicinity of the shuttle, which is the region of highest charge exchange rates, thus forming a long downstream water ion trail. The water ion densities in this trail are nearly equal to those of the near vicinity of the shuttle (assuming a steady state outgassing situation during which no thruster firings of water dumps occur) since further downstream of the shuttle charge exchange (source) and recombination (sink) rates are negligibly small. However, the long water ion trail extends only to downstream distances of the order of 12 km before it dissipates from recombination reactions.

It is useful to consider the motions of the water ions of the trail in the stationary earth's frame (in this section and the next one we shall only be concerned with the ion motions in the plane perpendicular to the magnetic field). In particular, in the earth's frame space the high density water ions are created, near the shuttle, with the shuttle velocity $V_\perp$ and subsequently stay trapped in the earth's magnetic field executing Larmor motion along circular orbits of radius $r_{Lw} = V_\perp/\omega_{cw}$ and at a frequency ω_{cw}. By the time the water ions complete their first orbit and thus return to their initial position (neglecting collisions) the shuttle will have traveled $2\pi r_{Lw}$ meters or a distance equal to π times the diameter of the water ion Larmor orbits. This situation is illustrated in Figure 3-5a which shows the earth's frame space at $t = t_0$, when the shuttle is at $X_{earth} = 0$. This figure only shows the orbits and positions of the high density water ions created in the near vicinity of the shuttle at times $t = t_0$, $t_0 - \tau_{cw}/3$, $t_0 - 2\tau_{cw}/3$, $t_0 - \tau_{cw}$, where $\tau_{cw} = 2\pi/\omega_{cw}$ is the ion cyclotron period.

3.2.3 The Water Ion Distribution in the Downstream Water Ion Trail

Figure 3-5b shows the shuttle frame velocity spaces at $t = t_0$ (when the shuttle is at $X_{earth} = 0$) of the high density water ions of various regions downstream of the shuttle. Specifically, it shows the shuttle frame velocity spaces at time $t = t_0$ of the downstream regions where the high density water ions created at times $t = t_0$, $t_0 - \tau_{cw}/3$, $t_0 - 2\tau_{cw}/3$, $t_0 - \tau_{cw}$ lie (see Figure 3-5a). For simplicity, in Figure 3-5b the water ion distributions are shown as beams. It is important to note that since the water ions drift downstream of the shuttle by gyrating along $\mathbf{E} \times \mathbf{B}$ cycloidal orbits, in the shuttle frame velocity space the gyrophase (angle) of their distributions increase with increasing distance downstream of the shuttle (we define a gyrophase increase clockwise, as shown in Figure 3-6b).

Now, let us note that the velocity distributions of the water ions in the ion trail are not simply beam distributions as shown in Figure 3-5b. In particular, the velocity distribution of the water ions near the shuttle, shown in the first velocity space from the right of Figure 3-5b, should be the $X_p = 1$ beam-arc distribution, as discussed in the previous sections. Furthermore, as the water ions near the shuttle drift downstream, this distribution should rotate clockwise in velocity space (at a constant angular rate ω_{cw}) and water ions should continuously be added to this distribution at the origin of the shuttle frame velocity space. This is because water ions are constantly being created, with zero velocity in the shuttle frame (neglecting thermal motions), throughout the downstream region where the ions drift, although at rates that decrease rapidly with increasing distance downstream of the shuttle.

In particular, neglecting wake effects and, again, assuming an uniform background ionosphere, because of the radial symmetry of the water neutral cloud, we can argue that in the region downstream of the shuttle the charge exchange rates will have the same spatial variation with radial distance from the shuttle as in the upstream region (Figure 3-3). Furthermore, by noting this upstream-downstream symmetry in charge exchange rates we can use the same arguments that explain the formation of the upstream beam-arc (i.e. the spatial variation of charge exchange rates along the

shuttle's orbital trajectory, see previous sections) to conclude that as the water ions will drift downstream of the shuttle their "rotating" distribution will evolve towards a final shape of a symmetric beam-arc, as shown in Figure 3-4. This evolution of the pickup water ion distribution function in the downstream water ion trail can be explained as follows. As the water ions near the shuttle will drift downstream of the shuttle, their $X_p = 1$ beam-arc velocity distribution will start to rotate and change its shape in velocity space since water ions will be added continuously to this distribution at the origin of velocity space. Because of the upstream-downstream symmetry in the charge exchange rates, the water ions picked up in the downstream region will be added to the rotating distribution at such rates that they will start mirroring the portion of the water ion distribution that corresponds to the ions picked up upstream of the shuttle (i.e the $X_p = 1$ beam-arc). The shape of the "rotating" distribution will evolve in this fashion, by the addition of the ions picked up downstream, until the drifting ions will reach the downstream region where the charge exchange rates are negligibly small compared to those near the shuttle. From Figure 3-3, we note that the ion trail region where the shape of the water ion distribution will stop evolving and thus reach its final form is at a distances of about πr_{Lw} downstream of the shuttle ($X_p \approx -9$), where the charge exchange rates are at least two orders of magnitude lower than those near the shuttle. Therefore, (neglecting wave effects and elastic collisions) because by the time the ions will have drifted to a distance of about πr_{Lw} downstream of the shuttle their distribution will only have rotated 180° (degrees), the final shape of their downstream "rotating" distribution will be the symmetric beam-arc shown in Figure 3-4. We shall call this symmetric beam-arc the $X_p = -\pi r_{Lw}$ beam-arc. Note that at distances smaller than πr_{Lw} downstream of the shuttle the water ion distribution will still be asymmetric whereas at downstream ion trail distances larger than πr_{Lw} the "rotating" distribution will be the $X_p = -\pi r_{Lw}$ symmetric beam-arc.

Let us now describe in more detail the $X_p = -\pi r_{Lw}$ symmetric beam-arc, shown in Figure 3-4. Because the downstream water ion distribution function rotates in velocity space (i.e. the gyrophase of the distribution increases with increasing downstream distance from the shuttle), it is convenient to describe its shape in terms of the

gyrophase (angle) relative to the gyrophase of the ions created at the shuttle. We shall define this angle as the relative gyrophase. Therefore, the symmetric $X_p = -\pi r_{Lw}$ beam-arc will be symmetric about the 0° relative gyrophase and have the same shape as the $X_p = 1$ beam arc in Figure 3-2 for relative gyrophases from 10° to 180° (see Figure 3-4). For relative gyrophases from -10° to -180° the $X_p = -\pi r_{Lw}$ beam-arc will have the same functional variation with relative gyrophase magnitude (but not sign) as the $X_p = 1$ beam-arc for gyrophases from 10° to 180°. Furthermore, because of the upstream-downstream symmetry in the charge exchange rates we expect that for relative gyrophases from -10° to 10° the $X_p = -\pi r_{Lw}$ beam-arc will have nearly the same largest value (thus 1 in normalized units) as the $X_p = 1$ beam-arc for gyrophase 10° (see Figure 3-4). Consequently, the effective arc $\Delta\Theta$ of the $X_p = -\pi r_{Lw}$ symmetric beam-arc will be of the order of 80° (twice the effective arc of the $X_p = 1$ beam-arc, see Figure 3-2), which is small (for simplicity, in various sections below we will treat this distribution analytically as a beam distribution).

It is therefore fairly accurate to think of the water ion distributions at various distances downstream from the shuttle as beams directed in different gyrophases, the gyrophases increasing with distance downstream from the shuttle, as shown in Figure 3-5b. Furthermore, it is important to note that these beam ions will always drift downstream with a drift speed equal to their Larmor speed. Figure 3-5c shows the earth frame velocity components of the beam distribution of water ions for the region downstream of the shuttle. It should be noted that because water ions drift downstream with a drift speed equal to their Larmor speed, they will have negative $V_{X_{earth}}$ components along almost 90 % of the downstream water ion trail. This particular type of $\mathbf{E} \times \mathbf{B}$ trajectories will also result in water ion density pile-ups near $X_p = 0$, $-2\pi r_{Lw}$, $-4\pi r_{Lw}$, ... and depletions near $X_p = -\pi r_{Lw}$, $-3\pi r_{Lw}$, ... as can be verified by comparing the relative distances between the bunches of the high density water ions in Figure 3-5a.

In the future, we will show that the water ion distributions to the sides of the high density water ions of the trail are more ringlike than those of the high density water ions. Finally, we should mention that, unfortunately, it is not yet possible to verify

64

the above predictions for the pick-up water ion distribution functions downstream of the shuttle since PDP data about these distributions has not yet been published.

3.2.4 Evolution of the Water Ion Distribution Due to Elastic Collisions

In the remainder of this chapter we will study how the water ion distribution is affected by collisions in the regions downstream of the shuttle. The dominant collisions of water ions in these regions are those with the ionospheric oxygen neutrals, except in the region near the shuttle where collisions with the water neutrals are also important (see Figure 3-7). Figure 3-6 shows the Maxwellian distributions of the oxygen neutrals and water neutrals in the shuttle frame velocity space. We will show analytically that collisions with the oxygen neutrals will tend to transform the water ion distribution into a shifted Maxwellian with the oxygen neutral temperature and drift, $-V_\perp$. Furthermore, collisions with the water neutrals will tend to transform the water ion distribution into a ring of radius $V_\perp$ and centered at $v_x = -V_\perp$. However, because water ions will drift downstream of the shuttle very rapidly they will not spend enough time inside the water neutral cloud (which co-orbits with the shuttle), colliding with the water neutrals, for their distribution to evolve into a ring distribution. Consequently, collisions with ionospheric oxygen neutrals at the frequency $\nu_{w\bar{O}}$ will eventually transform the water ion distribution into a shifted Maxwellian in a characteristic time $\nu_{w\bar{O}}^{-1}$ or, in the shuttle frame, at a downstream distance of $V_\perp \nu_{w\bar{O}}^{-1} \approx 10\text{km}$. Let us recall that at downstream distances of the order of the 12km the water ion trail will disappear due to the recombination of water ions. In conclusion, we will find that within 400 meters downstream of the shuttle, which was the largest distance reached by the PDP during the free-flight mission, the water ion distribution will essentially be unaffected by collisions with neutrals and will be approximately a beam with phase angle that increases with increasing downstream distance. In this analysis wave effects will be neglected.

In the following analytical derivations, we will examine separately the effects of collisions with water neutrals and oxygen neutrals on the water ion distribution. Al-

though these effects cannot be formally uncoupled in the water ion Boltzmann equation, when treated separately a procedure that yields exact solutions to the Boltzmann's equation can be followed. This procedure involves replacing the Boltzmann's collision integral by a simple relaxation model, and neglecting ions and neutrals density gradients. We will see that even with such assumptions the results will be very useful for gaining insight into the effects of collisions and the physics of the problem. Since we will only be interested in one ion species, for simplicity, we will use the subscripts w for the water ions and $\bar{w}$ and $\bar{O}$ for the water and oxygen neutrals, respectively.

3.2.5 The Collisionless Solution of the Water Ion Distribution

Before we discuss further the effect of collisions on the (water) ion velocity distribution function, it is instructive to consider the collisionless limit. When collisions and spatial gradients are neglected, the ion distribution function is governed by the following Boltzmann equation:

$$\frac{\partial f_w}{\partial t} + [\mathbf{\Gamma}_w + \mathbf{V}_w \times \omega_{cw}] \cdot \nabla_{\mathbf{V}_w} f_w = 0 \qquad (3.8)$$

where

$$\mathbf{\Gamma}_w = \frac{e_w}{m_w} \mathbf{E} \qquad (3.9)$$

$$\omega_{cw} = \frac{e_w \mathbf{B}}{m_w} \qquad (3.10)$$

and where $f_w(\mathbf{V}_w, t)$ is the ion distribution function, e_w the ion charge, m_w the ion mass, $\mathbf{V}_w$ the ion velocity, $\mathbf{E} = (0, -V_\perp B, 0)$ the motional electric field, $\mathbf{B} = (0, 0, B)$ the geomagnetic field, $\partial/\partial t$ the time derivative, and $\nabla_{\mathbf{V}_w}$ the velocity space gradient.

As shown in Figure 3-6, in this analysis we will use the right-handed cartesian pickup coordinate system in the shuttle frame with unit vectors pointing in the $-\mathbf{E} \times$

B, $-\mathbf{E}$ and **B** directions, respectively. For this coordinate system, Equation 3.8 becomes

$$\frac{df_w}{dt} = \frac{\partial f_w}{\partial t} + \omega_{cw} v_y \frac{\partial f_w}{\partial v_x} + \omega_{cw}(-V_\perp - v_x)\frac{\partial f_w}{\partial v_y} = 0 \qquad (3.11)$$

where $-V_\perp$ is the ion guiding center drift, $(v_x, v_y, v_\parallel)$ are the components of the ion velocity $\mathbf{V}_w$, and d/dt is the total time derivative taken along a particle path in velocity space. Equation 3.11 has the simple solution

$$f_w(v_x, v_y, v_\parallel, t) = f_w(v_x', v_y', v_\parallel', t'). \qquad (3.12)$$

Consequently, if the ion distribution function is known at some instant of time, t', it is known for all other times.

The relations connecting the velocity components at time t to those at time t' are

$$v_\parallel = v_\parallel' \qquad (3.13)$$

$$v_x = -V_\perp + (v_x' + V_\perp)\cos\omega_{cw}t + v_y' \sin\omega_{cw}t \qquad (3.14)$$

$$v_y = v_y' \cos\omega_{cw}t - (v_x' + V_\perp)\sin\omega_{cw}t \qquad (3.15)$$

which follow from the ion equations of motion. In this analysis it is convenient to take the time t' as the time when the (water) ions first acquire the shape of the $X_p = -\pi r_{Lw}$ symmetric beam-arc distribution. Thus, as the time when the drifting water ions arrive to $X_p = -\pi r_{Lw}$. Furthermore, since the effective arc of the $X_p = -\pi r_{Lw}$ beam-arc is small (see Figure 3-4) without loss of generality (as we shall see in the analysis that follows) we approximate the $X_p = -\pi r_{Lw}$ beam-arc by a Maxwellian distribution. Therefore, if the ion distribution function at time t' is Maxwellian with the temperature of the water neutral gas, $T_{\tilde{w}}$,

$$f_w(v_x', v_y', v_\parallel', t') = n_w \left(\frac{m_w}{2\pi k T_{\tilde{w}}}\right)^{3/2} \exp\left\{-\frac{m_w(v_\parallel'^2 + v_x'^2 + v_y'^2)}{2k T_{\tilde{w}}}\right\} \qquad (3.16)$$

67

then (using Equations 3.12 to 3.15) the distribution at time t becomes

$$f_w\Upsilon = n_w \left(\frac{m_w}{2\pi kT_{\tilde{w}}}\right)^{3/2}$$

(3.17)

$$\times \exp\left\{-\frac{m_w}{2kT_{\tilde{w}}}[v_\parallel^2 + (v_x + V_\perp)^2 + v_y^2 + V_\perp^2 - 2V_\perp((v_x + V_\perp)\cos\omega_{cw}t - v_y\sin\omega_{cw}t)]\right\}$$

where n_w is the ion density in the near vicinity of the shuttle and k is Boltzmann's constant. This is the collisionless velocity distribution, which we shall denote as $f_w\Upsilon$. Since collisions were neglected, the ions oscillate in phase at the ion gyrofrequency.

Let us now interpret the result in Equation 3.17 by considering the motion of a single ion. If at some initial time, $t' = 0$, an ion has velocity components (v_x', v_y', $v_\parallel'$) then, provided the ion does not suffer a collision, its velocity components at some later time t are given by Equations 3.13, 3.14 and 3.15.

Equation 3.13 indicates that the ion velocity component along the magnetic field is unaffected by either the electric or magnetic field and remains constant for $t > 0$. The perpendicular velocity components, however, are time dependent and oscillate at the ion gyrofrequency.

An equation describing the ion trajectory in the perpendicular plane in velocity space can be obtained by combining Equations 3.14 and 3.15. If we square each equation and add them, we obtain

$$(v_x + V_\perp)^2 + v_y^2 = r_v^2$$

(3.18)

where

$$r_v^2 = (v_x' + V_\perp)^2 + v_y'^2 \,.$$

(3.19)

The velocity-space trajectory of a single ion is therefore a circle centered on the $\mathbf{E} \times \mathbf{B}$-drift with a radius, r_v, which depends on the ion drift, $-V_\perp$, and the initial values of the perpendicular velocity components. This trajectory is illustrated schematically in Figure 3-6 It should be noted that, in general, the circular ion trajectory will not lie in the principal perpendicular plane ($v_\parallel' = 0$), but will be located above or below this plane depending on the initial value of the parallel velocity component.

The direction of rotation of the perpendicular velocity vector can be readily obtained by expressing the perpendicular velocity components in polar coordinates. If θ is the angle between the perpendicular velocity vector and the Hall-axis (see Figure 3-6), the ion velocity components become

$$v_y = -r_v \sin \theta \qquad (3.20)$$

$$(v_x + V_\perp) = r_v \cos \theta \qquad (3.21)$$

where from Equation 3.14 and 3.15 we have

$$\theta = \omega_{cw} t + \theta' \qquad (3.22)$$

$$\theta' = -tan^{-1} \left(\frac{v_y'}{v_x' + V_\perp} \right) \qquad (3.23)$$

Therefore, looking into the magnetic field the ion velocity vector rotates in a clockwise direction from some initial angle θ' at a rate governed by the ion cyclotron frequency.

If instead of a single ion we now have a distribution of ions, each ion in the distribution behaves in the manner described above, provided there are no collisions. The ion velocity-space trajectories are concentric circles centered on the Hall-axis at speed $-V_\perp$. There is a spread in radii due to the velocity spread of the initial ion distribution. Likewise, the circular ion trajectories are located in different perpendicular velocity planes due to this velocity spread. Since collisions are neglected, the ion distribution oscillates in time at the ion gyrofrequency. This confirms the results of our qualitative discussion of the previous section, shown in Figure 3-5.

3.2.6 Effect of Elastic Collisions with Water Neutrals

The effect of collisions with water neutrals on the (water) ion velocity distribution can be investigated by using a simple relaxation model, namely, a Krook collision operator [St-Maurice and Schunk, 1973]. For simplicity, we will assume that ion and

69

water neutral densities are spatially uniform (no density gradients), and later we will discuss the consequences of such assumption on the results. With this model Boltzmann's equation becomes

$$\frac{\partial f_w}{\partial t} + [\mathbf{\Gamma}_w + \mathbf{V}_w \times \omega_{cw}] \cdot \nabla_{\mathbf{V}_w} f_w = -\nu_{w\bar{w}}(f_w - f_{wm}) \tag{3.24}$$

or

$$\frac{df_w}{dt} = -\nu_{w\bar{w}}(f_w - f_{wm}) \tag{3.25}$$

where

$$f_{wm} = n_w \left(\frac{m_w}{2\pi k T_{\bar{w}}}\right)^{3/2} e^{-(m_w V_w^2 / 2k T_{\bar{w}})} \tag{3.26}$$

is a Maxwellian distribution at the temperature of the water neutral gas and $\nu_{w\bar{w}}$ is the velocity independent water ion collision frequency with water neutrals. The collision term in Equations 3.24 and 3.25 act to drive the ion distribution toward the Maxwellian distribution 3.26 at a rate governed by the relaxation time $\nu_{w\bar{w}}^{-1}$. In other words, what a Krook collision operator effectively models is a situation where ions that undergo "Krook" collisions leave the collision events with a velocity equal to that of their colliding partners, the stationary water neutrals (in the shuttle frame, see Figure 3-6). Therefore, after colliding the $\mathbf{E} \times \mathbf{B}$ drifting ions will appear at the origin of velocity space and will thus have changed their phases along their circular trajectories in the shuttle frame velocity space.

The integration of Equation 3.25 yields

$$f_w(v_x, v_y, v_\parallel, t) = f_w \Upsilon e^{-\nu_{w\bar{w}}t} + \nu_{w\bar{w}} n_w \left(\frac{m_w}{2\pi k T_{\bar{w}}}\right)^{3/2} \exp\left\{-\frac{m_w[v_\parallel^2 + (v_x + V_\perp)^2 + v_y^2 + V_\perp^2]}{2k T_{\bar{w}}}\right\}$$
$$\times \int_0^t dt' e^{-\nu_{w\bar{w}}t'} \exp\left\{-\frac{m_w V_\perp}{k T_{\bar{w}}}[(-V_\perp - v_x)\cos\omega_{cw}t' + v_y \sin\omega_{cw}t']\right\} \tag{3.27}$$

where we have assumed that at $t = 0$, $f_w = f_w \Upsilon$. A check on the solution can be obtained by substituting Equation 3.27 into Equation 3.24 and Equation 3.25.

Equation 3.27 indicates that the collisionless solution, $f_{w\Upsilon}$, or any initial distribution for that matter, is damped out with the characteristics time $t_d = \nu_{w\bar{w}}^{-1}$.

It should be pointed out that the solution, Equation 3.27, applies to any initial distribution $f_{w\Upsilon}$. In the case of the shuttle (water) ions it would be more accurate to take $f_{w\Upsilon}$ as the $X_p = -\pi r_{Lw}$ symmetric beam-arc distribution of the downstream region. Furthermore, for the largest $\nu_{w\bar{w}}$ values, which correspond to those of the near vicinity of the shuttle, Equation 3.27 indicates that the initial distribution $f_{w\Upsilon}$ would be damped out in a characteristic time of the order of $t_d = \nu_{w\bar{w}}^{-1} \approx 9$ sec or at a downstream distance of the order of $d_d = V_\perp \nu_{w\bar{w}}^{-1} \approx 60$ km. In fact, we would expect the values of t_d and d_d to be even larger since, if density gradients would be taken into account, the $\nu_{w\bar{w}}$ values would decrease rapidly with distance from the shuttle (see Figure 3-7). Therefore, since $d_d \approx 60$ km and in the real case the downstream water ion trail extends only to distances of the order of 12 km before most water ions recombine, we can conclude that water ion collisions with water neutrals will have a very small effect on the water ion distribution. In what follows we will examine the small effect of water neutral collisions on the water ion distribution by considering the steady state solution that our model predicts for $t \to \infty$. Although in the real case ions will never reach such state since they will recombine after ($\nu_{recom}^{-1} \approx$)1.5 sec, the steady state solution will give us a good idea of the configuration towards which water neutral collisions tend to drive the water ion distribution.

The steady state ion velocity distribution can be obtained from Equation 3.27 by letting $t \to \infty$,

$$f_w(v_x, v_y, v_\parallel) = \nu_{w\bar{w}} n_w \left(\frac{m_w}{2\pi k T_{\bar{w}}}\right)^{3/2} \exp\left\{-\frac{m_w[v_\parallel^2 + (v_x + V_\perp)^2 + v_y^2 + V_\perp^2]}{2kT_{\bar{w}}}\right\}$$
$$\times \int_0^\infty dt' e^{-\nu_{w\bar{w}}t'} \exp\left\{-\frac{m_w V_\perp}{kT_{\bar{w}}}[(-V_\perp - v_x)\cos\omega_{cw}t' + v_y \sin\omega_{cw}t']\right\} \quad (3.28)$$

Collisions act to destroy the coherent circular ion motion corresponding to the gyrating ion distribution in velocity space (the collisionless solution, $f_{w\Upsilon}$), and drive the ion distribution to a steady state distribution. In the steady state all information about the initial ion distribution is lost, and the ion velocity distribution depends only

in the magnetic and motional electric field strengths, the ion collision to cyclotron frequency ratio, and the water neutral temperature (see Equation 3.28).

In the strong collision frequency limit ($\nu_{w\tilde{w}}/\omega_{cw} \gg 1$), which does not correspond to the shuttle's plasma cloud but is interesting to consider, Equation 3.28 reduces to a Maxwellian distribution with the temperature of the neutral gas (Equation 3.26). This is to be expected since it is particle collisions that drive the distribution to its Maxwellian shape. This results can also be obtained directly from Boltzmann's equation by dividing both sides of Equation 3.24 by $\nu_{w\tilde{w}}$ and then letting $\nu_{w\tilde{w}}$ approach infinity.

In the weak collision frequency limit ($\nu_{w\tilde{w}}/\omega_{cw} \ll 1$), which corresponds to the shuttle's plasma cloud and ion trail, Equation 3.28 reduces to

$$f_w = n_w \left(\frac{m_w}{2\pi k T_{\tilde{w}}} \right)^{3/2} \exp\left\{ -\frac{m_w[v_\parallel^2 + (v_x + V_\perp)^2 + v_y^2 + V_\perp^2]}{2kT_{\tilde{w}}} \right\} \left\{ 1 + \sum_{r_v=1}^{\infty} \left[\left(\frac{\beta}{2} \right)^r \frac{1}{r!} \right]^2 \right\}$$

(3.29)

where

$$\beta = \frac{m_w V_\perp}{kT_{\tilde{w}}}[(-V_\perp - v_x)^2 + v_y^2]^{1/2}$$

(3.30)

For small values of $\nu_{w\tilde{w}}/\omega_{cw}$, the ions gyrate many times about the magnetic field before they suffer a collision, and the general behavior of a distribution of ions is similar to the collisionless behavior described in the previous section. Now, however, after colliding with the stationary water neutrals, the $\mathbf{E} \times \mathbf{B}$ drifting ions are displaced to the origin of the shuttle frame velocity space (since this is what "Krook" collisions model, see above) and thus change their gyrophases along their circular trajectories. Therefore, a steady state ion distribution is possible, and in the steady state there are an equal number of ions at any point along a given ion trajectory. In this case, the spread in radii and the location of the circular ion trajectories along the magnetic field are determined by the velocity spread of the water neutral distribution. This is in contrast to the collisionless case where they are determined by the velocity spread of the initial ion distribution.

The dependence of the steady state ion distribution on the parameters characterizing the water neutral velocity distribution can be shown by using simple physical arguments and the properties of the relaxation model. In the time interval between collisions, the equations describing the ion motion are given by Equations 3.13- 3.23. Now, however, the velocity components $(v'_x, v'_y, v'_\parallel)$ correspond to the ion velocity immediately after the collision. When the simple relaxation model is used to describe the ion-neutral collision process, the ion acquires the water neutral velocity after the collision. Since the water neutral gas is assumed to be stationary, we expect that on the average.

$$\langle v'_x \rangle = \langle v'_y \rangle = 0. \tag{3.31}$$

Furthermore, for the large motional electric field strengths in the shuttle frame, $V_\perp$ is, on the average, much greater than either $\mid v'_x \mid$ or $\mid v'_y \mid$ and, therefore, the average radius is approximately equal to the ion drift (see Equation 3.19),

$$\langle r_v \rangle \approx V_\perp. \tag{3.32}$$

The spread in radii about this average radius can be obtained from the expression

$$\langle [r_v - \langle r_v \rangle]^2 \rangle^{1/2} = [\langle r_v^2 \rangle - \langle r_v \rangle^2]^{1/2} \tag{3.33}$$

Using Equations 3.19, 3.31, and 3.32 this becomes

$$\langle [r_v - \langle r_v \rangle]^2 \rangle^{1/2} = \langle v'^2_x + v'^2_y \rangle^{1/2} = \left(\frac{2kT_{\bar{w}}}{m_w} \right)^{1/2}. \tag{3.34}$$

Equation 3.34 indicates that the spread in radii is equal to the neutral thermal speed, $v_{th\bar{w}} = (2kT_{\bar{w}}/m_w)^{1/2}$. This spread is a measure of the half-width of the ion distribution in the perpendicular velocity plane. The half-width of the ion distribution in the magnetic field direction is also equal to the neutral thermal speed, since the ion distribution along the magnetic field is a Maxwellian distribution with the temperature of the water neutral gas. The ion distribution therefore has the appearance of a ring in velocity space.

By using simple physical arguments and the properties of the relaxation model, we have been able to establish that ion-water neutral collisions tend to drive the ion velocity distribution to a steady state shape of a ring in the small collision frequency limit of the shuttle's plasma. We have also been able to establish that the ring lies in the perpendicular velocity plane with its center on the Hall-axis at speed $-V_\perp$, that the radius of the ring is approximately equal to $V_\perp$, and that the half-width of the ring is equal to the water neutral thermal speed. In the rest of this section, we will present a more detailed quantitative description of the ring ion velocity distribution.

The steady state ion velocity distribution, Equation 3.29, in the small collision frequency limit can be expressed in the form

$$f_w(v_\parallel, c_\perp) = n_w \left(\frac{m_w}{2\pi kT_{\bar{w}}}\right)^{3/2} \exp\left[-\frac{m_w}{2kT_{\bar{w}}}(v_\parallel^2 + V_\perp^2 + c_\perp^2)\right] I_0(\gamma c_\perp) \tag{3.35}$$

where

$$\gamma = \frac{m_w V_\perp}{kT_{\bar{w}}} \tag{3.36}$$

$$c_\perp = [(v_x + V_\perp)^2 + v_y^2]^{1/2} \tag{3.37}$$

and where I_0 is the modified Bessel function of order zero (Hildebrand, 1964). The quantity $c_\perp$ is the magnitude of the ion random velocity in the perpendicular velocity plane. Since the ion distribution (3.35) depends only on the magnitude of $c_\perp$, it is clear that the center of symmetry and thus the center of the ring occur at $c_\perp = 0$ ($v_x = -V_\perp$, $v_y = 0$). This agrees with the results we obtained earlier from simple physical arguments.

The location of the maximum of the ion distribution can be obtained from Equation 3.35 by setting the derivative of f_w to zero. This procedure yields an implicit equation for the position of the maximum ($c_\perp = R_v$),

$$\gamma c_\perp \frac{I_0(\gamma c_\perp)}{I_1(\gamma c_\perp)} = \frac{m_w V_\perp^2}{kT_{\bar{w}}} \tag{3.38}$$

74

where I_1 is a modified Bessel function of order one. The solution to Equation 3.38 is shown in Figure 3-8. The ring ion velocity distribution begins to appear when $V_\perp \approx v_{th\bar{w}}$. As the drift increases beyond this value, the radius of the ring first increases very rapidly and then asymptotically approaches the ion drift $V_\perp$. For motional electric field strengths such that $V_\perp \gtrsim 2v_{th\bar{w}}$, R_v is within 8 per cent of $V_\perp$.

Finally, since in the shuttle case $V_\perp$ is always much larger than $v_{th\bar{w}}$ and for large drifts $\gamma c_\perp \gg 1$, the steady state ion distribution 3.35 can be simplified by replacing the Bessel function I_0 with its asymptotic limit ($\gamma c_\perp \gg 1$). When this is done, Equation 3.35 becomes

$$f_w = n_w \left(\frac{m_w}{2\pi k T_{\bar{w}}}\right)^{3/2} (2\pi\gamma c_\perp)^{-1/2} \exp\{-[v_\parallel^2 + (c_\perp - V_\perp^2)^2]/v_{th\bar{w}}^2\} \qquad (3.39)$$

Because of the restriction on $\gamma c_\perp$, Equation 3.39 is not valid for a small region of velocity space near $c_\perp = 0$. Along the magnetic field $f_w \sim e^{-(u/v_{th\bar{w}})^2}$ while in the perpendicular velocity plane $f_w \sim (1/\sqrt{c_\perp})e^{-(c_\perp+V_\perp)^2/v_{th\bar{w}}^2}$, thus a ring of radius $V_\perp$.

3.2.7 Effect of Elastic Collisions with Ionospheric Oxygen Neutrals

The effect of collisions with ionospheric oxygen neutrals on the (water) ion velocity distribution can also be investigated by using the simple Krook relaxation model. For simplicity, we will assume that the ion and oxygen neutral densities are spatially uniform (no density gradients) and neglect ion-water neutral collisions. With this model Boltzmann's equation becomes

$$\frac{\partial f_w}{\partial t} + [\mathbf{\Gamma}_w + \mathbf{V}_w \times \omega_{cw}] \cdot \nabla_{\mathbf{V}_w} f_w = -\nu_{w\bar{O}}(f_w - f_{wsm}) \qquad (3.40)$$

or

$$\frac{df_w}{dt} = -\nu_{w\bar{O}}(f_w - f_{wsm}) \qquad (3.41)$$

where

75

$$f_{wsm} = n_w \left(\frac{m_w}{2\pi k T_{\bar{O}}} \right)^{3/2} \exp \left\{ -\frac{m_w[(v_\parallel + V_\parallel)^2 + (v_x + V_\perp)^2 + v_y^2]}{2k T_{\bar{O}}} \right\} \qquad (3.42)$$

is a shifted Maxwellian distribution at the temperature of the oxygen neutral gas and $\nu_{w\bar{O}}$ is the velocity independent (water) ion-oxygen neutral collision frequency. The collision term in Equations 3.40 and 3.41 act to drive the ion distribution toward the shifted Maxwellian distribution 3.42 at a rate governed by the relaxation time $\nu_{w\bar{O}}^{-1}$. In other words, we have a situation where ions that undergo ("Krook") collisions leave the collision events with a velocity equal to that of their colliding partners, the drifting oxygen neutrals. In the shuttle frame velocity space the oxygen neutrals drift with velocities $-V_\perp$ ($V_\perp$ is defined positive) along the hall-axis in the perpendicular plane (see Figure 3-6) and $-V_\parallel$ along the magnetic field, where $V_\parallel$ is the component of the shuttle velocity along the magnetic field.

The integration of Equation 3.41 yields

$$f_w(v_x, v_y, v_\parallel, t) = f_{w\Upsilon} e^{-\nu_{w\bar{O}} t} + (1 - e^{-\nu_{w\bar{O}} t}) f_{wsm} \qquad (3.43)$$

where we have assumed that at $t = 0$, $f_w = f_{w\Upsilon}$. A check on the solution can be obtained by substituting Equation 3.43 into Equations 3.40 and 3.41. Equation 3.43 indicates that the collisionless solution, $f_{w\Upsilon}$, or any initial distribution for that matter, is damped out with the characteristic time $t_d = \nu_{w\bar{O}}^{-1}$. Figure 3-9 shows the time variations of both terms in Equation 3.43 and the fact that for times larger than $t_d = \nu_{w\bar{O}}^{-1}$ the ion velocity distribution approaches asymptotically a steady state solution, which can be obtained from Equation 3.43 by letting $t \to \infty$,

$$f_w(v_x, v_y, v_\parallel) = f_{wsm} \qquad (3.44)$$

Therefore, collisions act to destroy the coherent circular ion motion corresponding to the initial gyrating ion distribution, $f_{w\Upsilon}$, in shuttle's velocity space and drive the ion distribution towards a shifted Maxwellian with the oxygen neutrals drift and temperature.

76

Finally, it should be pointed out that the solution, Equation 3.43, applies to any initial distribution $f_{w\Upsilon}$. In the case of the shuttle (water) ions it would be more accurate to take $f_{w\Upsilon}$ as the $X_p = -\pi r_{Lw}$ symmetric beam-arc distribution of the downstream region. Furthermore, for the average $\nu_{w\bar{w}}$ values of the shuttle plasma cloud and ion trail, Equation 3.43 indicates that the initial distribution $f_{w\Upsilon}$ will be damped out in a characteristics time of the order of $t_d = \nu_{w\bar{O}}^{-1} \approx 1.4$ sec or at a downstream distance of the order of $d_d = V_\perp \nu_{w\bar{O}}^{-1} \approx 10$ km. Therefore, since $d_d \approx 10$ km and in the real case the downstream water ion trail extends only to distances of the order of 12 km before most water ions recombine, we can conclude that only the ion distribution near the back of the ion trail will reach the steady state predicted by our model. Within 400 meters downstream of the shuttle, which was the largest distance reached by the PDP during the free-flight mission, the (water) ion distribution will essentially be unaffected by collisions with neutrals and will approximately be a symmetric beam-arc with phase angle that increases with increasing downstream distance. Wave effects on the ion distribution were so far neglected but will be analyzed in the next chapters.
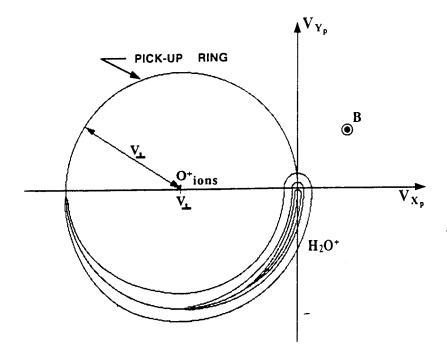
Figure 3-1: A beam arc distribution displayed in $V_{X_p} - V_{Y_p}$ space. Water ions are created near zero velocity and follow their gyromotion clockwise around the ring with gyrospeed $V_\perp$ centered on the oxygen flow speed $-V_\perp$. Zero gyrophase corresponds to zero velocity.
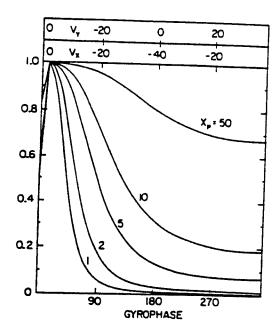
Figure 3-2: Normalized cuts of distribution functions along lines of constant gyrospeed $V_\perp$ and zero parallel velocity for positions along the positive X_p axis (from Cairns [1990]). Note the narrowing range of gyrophases and increasing contrast in the distribution functions with decreasing distance from the shuttle. The V_{X_p} and V_{Y_p} scales indicate the great extent in velocity space covered by the distribution even at $X_p = 1$.
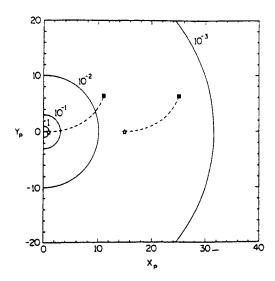
Figure 3-3: Explanation of the formation of beam arc and ring distributions of water ions close to and far from the space shuttle, respectively from Cairns [1990]. Solid lines show contours of constant charge exchange rate, spaced by factors of 10. The stars and squares show the positions (and so rates of charge exchange) at which ions observed near zero velocity and velocity $(-2V_\perp, 0, 0)$, respectively, at the observation positions are produced. Greatly differing rates of charge exchange imply a beam arc distribution at $X_p = 1$, while similar rates imply a ring distribution at $X_p = 15$.
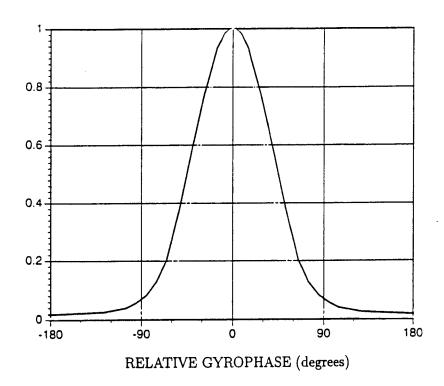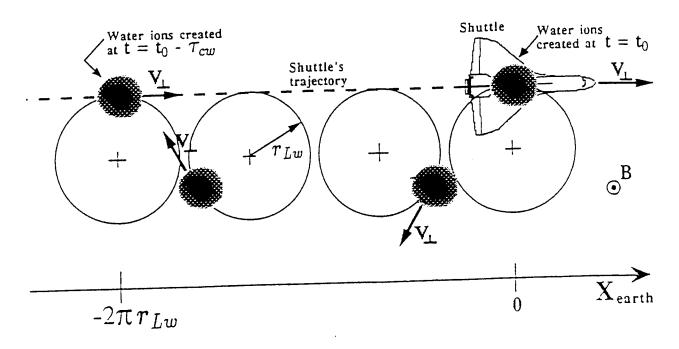
Figure 3-4: The $X_p = -\pi r_{Lw}$ symmetric beam-arc water ion distribution of the downstream region of the shuttle. Normalized cut of the velocity distribution function along a line of constant gyrospeed $V_\perp$ and zero parallel velocity.

(a)

(b)
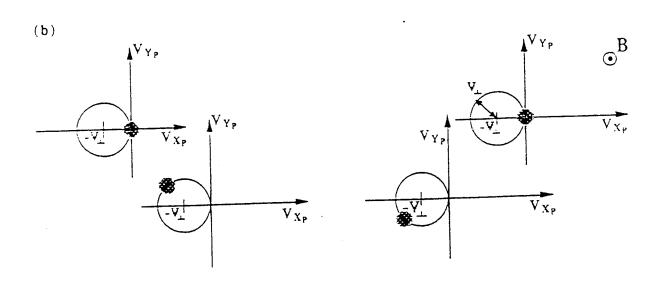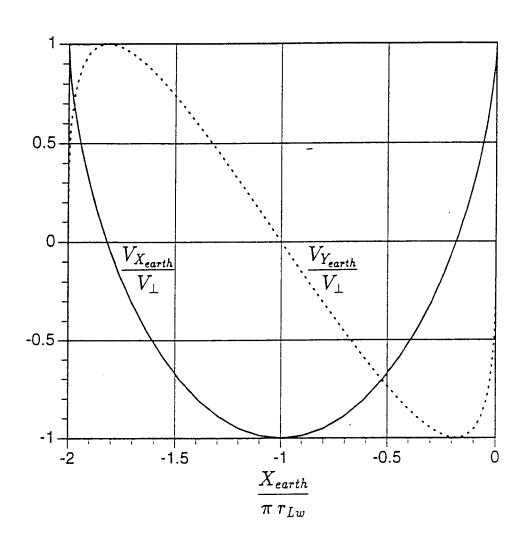
Figure 3-5: (a) Earth's frame space at $t = t_0$, when the shuttle is at $X_{earth} = 0$. Part (a) only shows the orbits and positions of the high density water ions created in the near vicinity of the shuttle at times $t = t_0$, $t_0 - \tau_{cw}/3$, $t_0 - 2\tau_{cw}/3$, $t_0 - \tau_{cw}$, where $\tau_{cw} = 2\pi/\omega_{cw}$ is the ion cyclotron period. (b) Shuttle frame velocity spaces at $t = t_0$ (when the shuttle is at $X_{earth} = 0$) of the water ions shown in (a), of the various regions downstream of the shuttle. (c) X_{earth} and Y_{earth} velocity components (in the earth's frame) of the high density water ions versus distance downstream from the shuttle. Note that along almost 90% of the downstream ion trail $V_{X_{earth}}$ is negative.

(c)

$\dfrac{X_{earth}}{\pi\, r_{Lw}}$
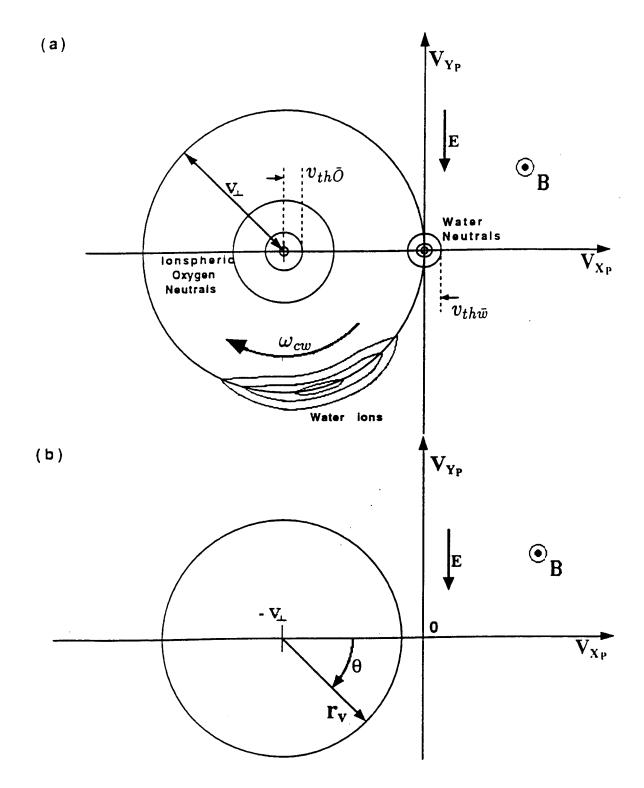
Figure 3-6: (a) Velocity space in the shuttle frame of the plasma in the region far downstream of the shuttle. The stationary Maxwellian distribution of water neutrals, the shifted Maxwellian distribution of ionospheric oxygen neutrals and the $X_p = -\pi r_{Lw}$ symmetric beam-arc distribution of water ions are shown. (b) Water ion velocity-space trajectory in the shuttle frame.

a)

b)
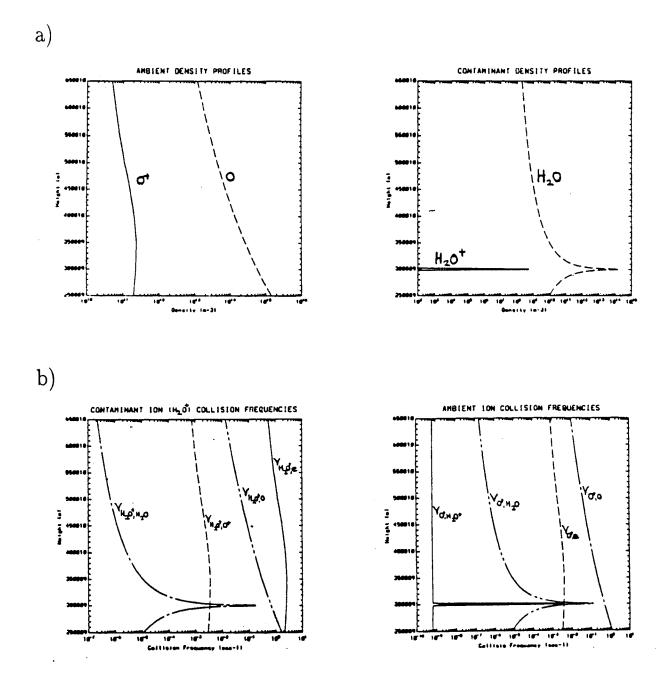
Figure 3-7: (a) Left: Ambient O and O^+ density profiles in the F_2 ionosphere. Right: Contaminant H_2O and H_2O^+ density profiles of the shuttle's cloud for an orbit near 300 km. (b) Ambient O^+ and contaminant H_2O^+ collision frequencies in the F_2 ionosphere for a shuttle orbit near 300 km (from Gatsonis and Hastings, 1991).
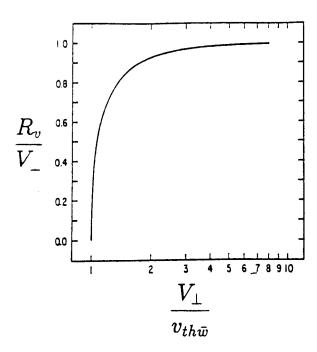
Figure 3-8: Radius of the ring as a function of $V_\perp/v_{th\bar{w}}$.
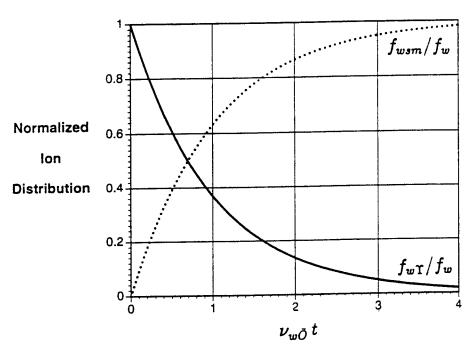
Figure 3-9: Time variation of the water ion distribution components due to collisions with ionospheric oxygen neutrals. The contribution of the collisionless distribution $f_{w\Upsilon}$ decays exponentially. At times greater than $\nu_{w\bar{O}}^{-1} \approx 1.4$ sec or distances downstream of the shuttle larger than $\nu_\perp \, \nu_{w\bar{O}}^{-1} \approx 10$ km the shifted Maxwellian feature of the ion distribution dominates.

Chapter 4

The Linear Theory of the Beam-Arc Plasma Instability

4.1 Introduction: A New Instability

In this chapter we develop the linear theory of a new instability that is capable of explaining various details of the PDP wave spectrum. This instability, which we shall call the beam-arc plasma instability, is excited by the free energy involving the interaction of the beam-arc distribution of water ions with the background ionospheric plasma. The instability analysis is thus motivated 1) (experimentally) by velocity phase space observations [*Paterson and Frank*, 1989] with the PDP that reveal " asymmetric-ringlike" distributions of ions with the basic characteristics expected of water ions produced by charge exchange process; and 2) (theoretically) by *Cairns* [1990] predictions (for the upstream region) and our predictions (for the downstream region, see Section 3.2) that show that the water ion distribution covers a significant region of velocity space corresponding to a finite section of a ring and is most correctly described as a "beam-arc" distribution (i.e., a slice of a ring distribution). A two-stream like instability occurs for $\mathbf{k} \perp \mathbf{B}$ when a small population of ions having a beam-arc velocity distribution function with effective arc $\Delta\Theta$ at speed V and arc thermal spread $v_{thw} < V$ interacts with a cool background plasma, $v_{thO} < V$ (see Figure 4-1). The (ion) beam-plasma instability ($\Delta\Theta = 0^o$) has been studied extensively by *Cordey and Houghton* [1973], *Berk et al.* [1975], *Gaffey* [1976] and *Seiler et al.* [1976] and the linear theory of the ring plasma instability ($\Delta\Theta = 360^o$)

has been studied numerically by *Tataronis and Crawford* [1970], *Mynick et al.* [1977] and *Lee and Birdsall* [1979]. In this chapter we develop the linear theory of the beam-arc plasma instability for all ranges of beam-arcs ($0^o \leq \Delta\Theta \leq 360^o$).

We examine the beam-arc plasma interaction through the linear (i.e. small amplitude) Vlasov theory for the electrostatic case. Because of the θ-dependence of the beam-arc distribution function the derivation of the dispersion relation requires a special treatment. In this analysis, we cannot use the conventional dispersion relation [*Drummond*, 1958; *Stix*, 1963; *Cap*, 1976], which in various equivalent forms has been applied throughout most of the fusion and space physics literature to analyze electrostatic instabilities in homogeneous magnetized Vlasov plasmas, since this dispersion relation cannot be used in problems where the equilibrium distribution functions depend on the phase angle θ in velocity space. Therefore, we find it convenient to deal with the θ-asymmetry of the beam-arc distribution by exploiting the linearity of the problem. We derive the dispersion relation by modeling the susceptibility of the beam-arc distribution as a summation of a large number of (shifted) Maxwellian susceptibilities for beamlets mapping the arc of the beam-arc distribution. The resulting electrostatic dispersion relation is solved numerically and the results are analyzed in detail.

In order to match the characteristics of the waves observed with the PDP (see Chapter 2) we look for electrostatic modes growing in time for real wavevectors (k) nearly perpendicular to the magnetic field. For the range of parameters near the PDP (see Table 2.1), we expect for small arcs, $\Delta\Theta \approx 0^o$, the beam-arc plasma instability to be similar to the nonresonant modified two-stream instability (MTS) [*Mikhailovskii and Tsypin*, 1966; *Krall and Liewer*, 1972; *McBride et al.*, 1972]. The MTS instability is driven by relative streaming of electrons and ions across the magnetic field B and has characteristic frequency and growth rate comparable to the lower Hybrid frequency. Moreover, in the modified two-stream instability the electrons behave as if they have an effective mass $\bar{m}_e = (k^2/k_\parallel^2)m_e$, which for large $k^2/k_\parallel^2$ is comparable to the ion mass, and play the role of the reactive medium that interacts with the beam ions in an unstable manner. In the case of the beam-arc plasma instability, however,

we expect the background plasma electrons and ions to play the role of the reactive medium and thus, in contrast to the case of the MTS instability, the beam-arc plasma instability should be excited even when $k_{\parallel} = 0$.

For large arcs, $\Delta\Theta \approx 360^o$, we expect the beam-arc plasma instability to be similar to the ring plasma instability [*Mynick et al.*, 1977; *Lee and Birdsall*, 1979]. For the range of density ratios considered in this paper, $n_w/n_e \geq 0.01$, the unstable modes should fall in *Lee and Birdsall*'s strong ring regime. Here, the most unstable mode is an ion acoustic-type mode which exists even when the magnetic field is turned off and is excited by the ring plasma combination even without the presence of electrons. In this case the role of the electron Debye shielding is carried by the hot and strong ring ion component.

Now, since in both limits of the beam-arc plasma instability, $\Delta\Theta \approx 0^o$ and $\Delta\Theta \approx 360^o$, we have unstable modes with growth rates much larger than the ion cyclotron frequencies, it is reasonable to expect comparable growth rates for beam-arcs with arcs $0^o < \Delta\Theta < 360^o$. Therefore, in the linear analysis of the beam-arc plasma instability we will assume that the ions are unmagnetized and justify this assumption later.

In Section 4.2, we develop the linear Vlasov model of the beam-arc plasma instability and solve the dispersion relation for all range of beam-arcs, $0^o \leq \Delta\Theta \leq 360^o$. Then, in Section 4.3, we discuss the numerical results by emphasizing the physical mechanisms that excite the unstable modes. In Section 4.3, 4.4 and 4.5, we also indicate the unique characteristics of the beam-arc plasma instability that are different from those of the beam-plasma and ring plasma instabilities. Finally, in Section 4.6, we show that the beam-arc plasma instability can explain various important features of the observed waves and details of the PDP wave spectrum.

4.2 Model of the Beam-Arc Plasma Instability

In this section we develop the linear model of the beam-arc plasma instability. This instability generates lower hybrid waves driven unstable by the free energy involving the interaction of the beam-arc distribution function of water ions with the back-

ground ionospheric plasma (see figure 4-1). Before we start modeling the instability, however, it should be pointed out that our calculations (and also *Cairns* [1990] calculation for the upstream region) of the beam-arc distribution function of water ions, in Chapter 3, assume a uniform background ionosphere and a water neutral cloud of time invariant geometry and density moving at the orbital speed. Therefore, the beam-arc distribution that was calculated is the steady state distribution that would be observed from the shuttle frame after the cloud has reached its steady state structure (this calculation neglects all wave effects). In contrast, note that this steady state situation in the shuttle frame would be an unsteady situation in the earth's frame. An observer in the earth's frame would see the distribution function to start out as a beam and evolve into a beam-arc as the neutral water cloud would pass by the earth's observation point.

In this chapter we shall develop the instability analysis by considering the steady state situation that is observed from the shuttle frame when wave effects on the equilibrium distribution function are neglected. Therefore, we will use a beam-arc distribution function of water ions as our starting point. For simplicity, however, we will derive the dispersion relation in earth's frame terms without affecting the validity of the analysis.

4.2.1 The Dispersion Relation

We now proceed to the development of the beam-arc plasma instability model. We start by first restricting our attention to the case where the orbiter moves exactly perpendicular to the earth's B-field. For simplicity, we model the beam-arc distribution function of the water ions as the summation of large numbers of Maxwellian beamlets, all having the same mean speed (8 Km/s) and lying in the plane perpendicular to the magnetic field but having different directions (see Figure 4-1). The beamlet directions span from the orbital velocity direction (0° in phase space) to $\Delta\Theta$, the phase angle where the water ion distribution function vanishes. This linear method for constructing the susceptibility or, equivalently, the distribution function (as the summation of large numbers of warm beamlets) is essentially the same as Dawson's

cold beamlet method [*Dawson, 1961*]. In this chapter, we examine the case where all the beamlets have the same density and are homogeneously distributed throughout the arc of the beam-arc distribution function. Therefore, we restrict our study to beam-arc distributions with shapes of slices of ring distributions; this will be more instructive for examining this new instability (the consequences of this assumption will be discussed in Section 4.6). We assume that the beam-arc is unmagnetized and treat the ionospheric oxygen ions as unmagnetized Maxwellians and the ionospheric electrons as magnetized Maxwellians (see Figure 4-1). The unmagnetized ions assumption will be justified later by showing that the growth rates of this instability are greater than the ion cyclotron frequencies. Therefore, in the reference frame of the stationary ionospheric plasma the electrostatic dispersion relation is:

$$1 + \chi_e(\mathbf{k}, \omega) + \chi_O(\mathbf{k}, \omega) + \chi_w(\mathbf{k}, \omega) = 0 \tag{4.1}$$

where $\chi_e(\mathbf{k}, \omega)$ and $\chi_O(\mathbf{k}, \omega)$, the electrostatic Maxwellian susceptibilities [*Chen, 1984*] of the background electrons and oxygen ions, and $\chi_w(\mathbf{k}, \omega)$, the susceptibility of the beam-arc ions, can be expressed as follows:

$$\chi_e(\mathbf{k}, \omega) = +\frac{k_{De}^2}{k_\parallel^2 + k_\perp^2} e^{-b_e} \sum_{n=-\infty}^{\infty} I_n(b_e) \left[1 + \zeta_{0e} Z(\zeta_{ne})\right]$$

$$\chi_O(\mathbf{k}, \omega) = -\frac{\frac{1}{2} k_{DO}^2}{k_\parallel^2 + k_\perp^2} Z'\left(\frac{\omega}{|k| v_{thO}}\right)$$

$$\chi_w(\mathbf{k}, \omega) = -\frac{\frac{1}{2} k_{Dw}^2}{k_\parallel^2 + k_\perp^2} \int_0^{\Delta\Theta} Z'\left(\frac{\omega - k_\perp V \cos(\theta - \theta_{k_\perp})}{|k| v_{thw}}\right) \frac{d\theta}{\Delta\Theta}$$

Here the subscripts e, O and w refer to the electrons, oxygen and water ions, respectively; I_n is the modified Bessel function of the first kind of order n with argument $b_s = \frac{1}{2} k_\perp^2 r_{Ls}^2$ for species s; $r_{Ls} = v_{ths}/\omega_{cs}$ is the Larmor radius, $v_{ths}^2 = 2KT_s/m_s$ is the thermal speed, $\omega_{cs} = |Z_s eB/m_s|$ is the cyclotron frequency, $k_{Ds}^2 = 2\omega_{ps}^2/v_{ths}^2 = \lambda_{Ds}^{-2}$ is the square of the Debye wavenumber, $\omega_{ps}^2 = n_s Z_s^2 e^2/\epsilon_0 m_s$ is the square of the plasma frequency and $\zeta_{ns} = (\omega + n\omega_{cs})/k_\parallel v_{ths}$ is the argument of the plasma dispersion function Z [*Fried and Conte, 1961*]. As shown in Figure 4-1, the coordinate system adopted is such that the orbital velocity $\mathbf{V}_{orb}$ has a phase angle of 0° in velocity space,

91

beamlets with mean velocity $\mathbf{V}$ have phase angles θ and $\mathbf{V}_{orb}$ and $\mathbf{V}$ always lie in the plane perpendicular to the B-field. The angle between the Shuttle velocity $\mathbf{V}_{orb}$ and the component of the propagation vector $\mathbf{k}$ perpendicular to the B-field, $k_\perp$, is denoted by $\theta_{k_\perp}$.

When solving this equation we use the nominal values of the PDP experiments [*Reasoner et al.*, 1986]. Normalized relative to the values for the oxygen ions, these are $T_e/T_O = 2$, $T_w/T_O = 0.25$ ($T_O = 1,160K$), $\omega_{pe}/\omega_{cO} = 139,000$ with an oxygen cyclotron frequency $\omega_{cO}/2\pi = 29$ Hz. The beamlet mean speed V is taken to be equal to the orbital speed 8 Km/s. All frequencies and growth rates calculated below are given in units of the oxygen cyclotron frequency. In these units the nominal lower hybrid frequency Ω_{LH} is 172 units.

Figure 4-2 shows numerical solutions of the beam-arc plasma dispersion relation for various beam-arcs. In all these cases the water ion to electron density ratio (n_w/n_e) is 15%, $\theta_{k_\perp} = 0°$ and the parallel propagation angle $\phi_{k_\parallel} \equiv \sin^{-1}(k_\parallel/k) = 0.385°$. These results predict strongly unstable waves with growth rates larger than the oxygen cyclotron frequency thus justifying the unmagnetized ions assumption.

In this chapter we shall be mainly concerned with the solutions of Equation 4.1 for electrostatic waves propagating quasi-perpendicular to the magnetic field. It is of no interest to examine the solutions of Equation 4.1 for electrostatic waves propagating quasi-parallel to the magnetic field since these are Landau damped. Furthermore, electrostatic waves propagating quasi-parallel to the magnetic field are not consistent with the available observational data [*Cairns and Gurnett*, 1991b].

It should also be pointed out that the perpendicular free energy of the beam-arc distribution can excite electromagnetic instabilities of the ion whistler types [*Davidson and Ogden*, 1975] which propagate quasi-parallel to the magnetic field. However, in the low-beta plasma environment of the shuttle we expect the growth rates of these electromagnetic instabilities to be a few orders of magnitude lower than those of the electrostatic instabilities described in Figure 4-2 Therefore, in this interpretation of the PDP wave data we shall not be concerned with the electromagnetic instabilities.

4.3 Analysis of the Beam-Arc Plasma Instability Dispersion Relation

It is interesting to note, by carefully examining the susceptibility of the beam-arc ions (last term of Equation 4.1) in the beam-arc plasma instability dispersion relation, that in this linear analysis only the characteristics of the equilibrium distribution for velocities along the propagation vector are important. We shall call this distribution for velocity components along $\mathbf{k}$ the reduced distribution function. Figure 4-3 shows schematically the reduced distribution function of the beam-arc ions for various arcs $\Delta\Theta$ for the case where $\mathbf{k}$ is in the direction of $\mathbf{V}_{orb}$ (i.e. $\theta_{k_\perp} = 0^o$, see Figure 4-1).

In this section we will show that there are two types of beam-arc plasma instabilities, the hydrodynamic and kinetic types, each having very different instability mechanisms. For small arcs, when the most unstable phase velocities are smaller than $V\cos\Delta\Theta$ (see Figure 4-3a), the beam-arc plasma instability is hydrodynamic (or fluidlike or reactive) and for large arcs the beam-arc plasma instability is kinetic (resonant) (see Figures 4-3c and 4-3d).

In order to gain physical insight into the beam-arc plasma instability mechanisms and understand the characteristics of the dispersion relation diagram, Figure 4-1, it is useful to analyze the "fluid limit" of the kinetic dispersion relation. We define the fluid limit of Equation 4.1 to be the limit where the Maxwellian distributions of the ionospheric electrons and ions and those of the beamlets that make up the beam-arc are reduced to delta functions. This limit can therefore be obtained by simplifying Equation 4.1 as follows: The electron terms are treated by retaining only the $n = 0, \pm 1$ terms in the electron magnetization, expanding the modified Bessel function in the limit $k_\perp^2 r_{Le}^2 \ll 1$, retaining only first order terms and assuming that $k_\parallel \ll k_\perp$. The unmagnetized oxygen ion term is treated by expanding the plasma dispersion function using the high phase speed expansion ($\omega/kv_{thO} \gg 1$). Finally, after expanding the water ion contribution using the high phase speed approximation and introducing the quantity $\delta \equiv k_\parallel^2 m_O/k^2 m_e$ one finds an equation of the form

$$1 - \frac{\omega_{pe}^2}{\omega^2 - \omega_{ce}^2} - \frac{\omega_{pO}^2(1+\delta)}{\omega^2} - \int_0^{\Delta\Theta} \frac{\omega_{pw}^2}{(\omega - k_\perp V \cos(\theta - \theta_{k_\perp}))^2} \frac{d\theta}{\Delta\Theta} = 0 \qquad (4.2)$$

The above equation can be rearranged with the definition of the lower Hybrid frequency $\Omega_{LHs}^2 \equiv \omega_{ps}^2/(1 + \omega_{pe}^2/\omega_{ce}^2)$ and the assumptions $\omega_{pe}^2/\omega_{ce}^2 \gg 1$, $\omega^2 \ll \omega_{ce}^2$, $n_e = n_O + n_w$, to give the dispersion equation

$$1 - \frac{\Omega_{LHO}^2(1+\delta)}{\omega^2} - \int_0^{\Delta\Theta} \frac{\Omega_{LHw}^2}{(\omega - k_\perp V \cos(\theta - \theta_{k_\perp}))^2} \frac{d\theta}{\Delta\Theta} = 0 \qquad (4.3)$$

where $\Omega_{LHO}^2 \approx \omega_{ce}\omega_{cO}(n_O/n_e)$ is the lower hybrid frequency of the oxygen ions and $\Omega_{LHw}^2 \approx \omega_{ce}\omega_{cw}(n_w/n_e)$ is the lower hybrid frequency of the water ions.

4.3.1 The Hydrodynamic Beam-Arc Plasma Instability

The Beamlet Plasma Instability

In order to analyze the characteristics of the fluid limit beam-arc plasma dispersion relation, Equation 4.3, for arcs in the hydrodynamic range; it is convenient to first consider the beamlet plasma dispersion relation. The waves described by the beamlet plasma dispersion relation are driven by a single beamlet of density n_b interacting with background ions of density n_i in a plasma system neutralized by magnetized electrons of density $n_e = n_i + n_b$ (only in this subsection we use these other subscripts for the beamlet and background ions to emphasize that here we are dealing with the beamlet plasma instability and not with the beam-arc plasma instability). Later we shall generalize the characteristics of the beamlet plasma waves to interpret qualitatively those of the hydrodynamic beam-arc plasma waves as being some type of "superposition" of beamlet plasma wave solutions for waves driven by beamlets in all directions θ ranging from 0° to $\Delta\Theta$. We start the beamlet plasma wave analysis by considering propagation perpendicular to the B-field ($\delta = 0$), and, without loss of generality, for convenience we set the propagation direction to $\theta_{k_\perp} = 0^o$. Then, it is easy to see from Equation 4.3 that the dispersion relation of the beamlet plasma system is:

$$1 - \frac{\Omega_{LHi}^2}{\omega^2} - \frac{\Omega_{LHb}^2}{(\omega - kV\cos\theta)^2} = 0 \qquad (4.4)$$

where $\Omega_{LHs}^2 = \omega_{ce}\omega_{cs}(n_s/n_e)$ is the lower hybrid frequency of species s. With this choice of $\theta_{k_\perp} (= 0^o)$, the beamlet phase angle θ is also equal to the angle between the propagation vector $\mathbf{k}$ and the beamlet velocity $\mathbf{V}$ (see Figure 4-1). In the analysis below we shall be interested only in the ω solutions of Equation 4.4 with positive real parts $\omega_r > 0$. Since these solutions can be shown to correspond to beamlets with $\cos\theta > 0$, the derivations in this section are restricted to $-90^o < \theta < 90^o$.

The beamlet plasma instability has the following physical explanation. The natural frequency of oscillations in the beamlet fluid is Ω_{LHb} and the natural frequency of oscillations in the background fluid is $\Omega_{LHi} \simeq \sqrt{n_i/n_b}\Omega_{LHb}$. Because of the Doppler shift of the Ω_{LHb} oscillations in the moving beamlet fluid, these two frequencies can coincide in the stationary frame if $kV\cos\theta$ has the proper value. We shall refer to this particular situation where the Doppler shifted natural frequency of beamlet fluid oscillations coincides with the natural frequency of background fluid oscillations as synchronism. Moreover, the beamlet ion oscillations can be shown to have negative energy. That is to say that the total kinetic energy of the beamlet ions is less when the oscillation is present than when it is absent. In the undisturbed beamlet, the kinetic energy per unit volume is $\frac{1}{2}mn_ov_o^2$. When there is an oscillation the kinetic energy is $\frac{1}{2}m(n_o + n_1)(v_o + v_1)^2$, where the subscript 1 denotes the perturbations. When this is averaged over space, it is less than $\frac{1}{2}mn_ov_o^2$ because of the phase relation between n_1 and v_1 required by the continuity equation. Consequently, the beamlet ion oscillations have negative energy, and the background ion oscillations have positive energy. Both waves can grow together while keeping the total energy of the system constant.

Another form of the dispersion relation Equation 4.4 which is more suggestive of this coupling between the plasma oscillations and the beamlet wave is

$$(\omega^2 - \Omega_{LHi}^2)(\omega - kV\cos\theta)^2 = \Omega_{LHb}^2\omega^2 \tag{4.5}$$

From this it is evident that for frequencies much higher than the background ion lower hybrid frequency, $|\omega| \gg \Omega_{LHi}$, we have essentially the unperturbed waves of

95

the beamlet fluid

$$(\omega - kV\cos\theta)^2 \approx \Omega_{LHb}^2 \tag{4.6}$$

On the other hand, near and below the background ion lower hybrid frequency the dispersion relation predicts instability. For

$$\eta \equiv \frac{\Omega_{LHb}^2}{\Omega_{LHi}^2} \simeq \frac{n_b}{n_i} \ll 1 \tag{4.7}$$

the strongest interaction and hence largest growth rate, may be expected where the plasma and beamlet terms are in synchronism,

$$|\omega| \approx \Omega_{LHi} \approx kV\cos\theta \tag{4.8}$$

there Equation 4.5 becomes approximately:

$$(\omega - \Omega_{LHi})(\omega - kV\cos\theta)^2 \approx \frac{1}{2}\Omega_{LHb}^2\Omega_{LHi} \tag{4.9}$$

Letting $\omega = \Omega_{LHi} + \varpi \approx kV\cos\theta + \varpi$, we find from Equation 4.9

$$\frac{\varpi}{\Omega_{LHi}} = \begin{cases} (\eta/2)^{1/3} \\ \left[-1/2 - i\sqrt{3}/2\right](\eta/2)^{1/3} \\ \left[-1/2 + i\sqrt{3}/2\right](\eta/2)^{1/3} \end{cases} \tag{4.10}$$

Clearly, the last one is the unstable root giving, for

$$k \approx \Omega_{LHi}/V\cos\theta \tag{4.11}$$

the following

$$\frac{\omega_r}{\Omega_{LHi}} \approx 1 - \frac{\eta^{1/3}}{2^{4/3}} \tag{4.12}$$

$$\frac{\gamma}{\Omega_{LHi}} \approx \frac{\sqrt{3}}{2^{4/3}}\eta^{1/3} \tag{4.13}$$

Note that even though we have assumed $\eta \ll 1$ (which makes $|\gamma/\omega_r| \ll 1$) this growth rate may be an appreciable fraction of the background ion lower hybrid frequency indicating a very strong, rapidly developing, instability.

Interpretation of the Hydrodynamic Beam-arc Plasma Waves as Being the Superpositions of many Beamlet Plasma Waves.

The characteristics of the hydrodynamic beam-arc plasma wave solution can be interpreted qualitatively by thinking of this solution as being the superposition of beamlet plasma wave solutions for waves driven by beamlets in all directions θ ranging from 0° to $\Delta\Theta$. This type of interpretation, however, is valid only qualitatively since the solution of the beam-arc plasma dispersion relation, Equation 4.3, cannot be obtained by the linear superposition of various solutions of the beamlet plasma dispersion relations, Equation 4.4 (i.e. ω and k appear as nonlinear parameters in the beamlet plasma dispersion relation). Nevertheless, in this section we will show that this concept of superposition is very useful in explaining the characteristics of the hydrodynamic beam-arc plasma waves and that these characteristics are essentially dictated by those of the single beamlet plasma waves derived above.

Figure 4-2a shows the dispersion relation diagram of the beam-arc plasma instability for arcs in the hydrodynamic range, $0^o \leq \Delta\Theta < 55^o$; obtained by solving Equation 4.1. Although this plot is for $\phi_{k_\parallel} \equiv \sin^{-1}(k_\parallel/k) = 0.385^o$, the results for $\phi_{k_\parallel} = 0^o$ are qualitatively the same. We shall therefore apply the theory developed in the previous section to interpret them. In Figure 4-2a, we note that for beam-arc distribution functions that are approximately beams ($\Delta\Theta \leq 1^o$) maximum growth occurs for wavenumbers around $k \approx \Omega_{LHO}/V$ which corresponds to the synchronism condition, Equation 4.11. This should be expected since in these cases all of the beamlets making up the beam-arcs have the same direction $\theta \approx 0$. In addition, we can see in Figure 4-2a. that for beam-arc distribution functions with arcs $1^o \ll \Delta\Theta \leq 55^o$, the range of wavenumbers for maximum growth is extended to higher wavenumbers. This is because in these cases the beamlets making up the beam-arcs have directions θ ranging from 0° to $\Delta\Theta$ and thus beamlets with larger θ achieve synchronism, which is the condition for maximum growth, at higher wavenumbers as predicted by Equation 4.11.

Figure 4-2a. also shows that the larger the arc $\Delta\Theta$ of the beam-arc the smaller the maximum growth rate value. This trend can be understood from the fact that

97

for a fixed beam-arc ion to electron density ratio (n_w/n_e) the beamlet density per angle θ is lower for larger arcs $\Delta\Theta$; therefore, since the maximum growth rate is proportional to the beamlet density at the phase angle θ of beamlets in synchronism (see Equation 4.13) larger arcs have smaller maximum growth rate values.

It is interesting to note that the real frequency curves in Figure 4-2a flatten around $\omega_r \approx \Omega_{LHO}$ in the wave number ranges for maximum growth. This is, of course, due to the fact that maximum growth rate is a situation where some beamlets are in synchronism and that occurs at the lower hybrid frequency of the background ions (see Equation 4.8). In addition, let us note that the flattening of the frequency curves in Figure 4-2a is analogous to that of the case of the ordinary two-stream instability [*Gary*, 1985]. It thus corresponds (in analogy to the ordinary two-stream instability) to the unstable wave changing its dispersion relation from beam-like dispersion with $\omega_r \sim kV$ at low wavenumbers to lower hybrid-like (or Langmuir-like) dispersion with $\omega_r \sim \Omega_{LH}$ (or ω_{pe}) at higher wavenumbers.

4.3.2 The Beam-Arc Plasma Instability for Arcs Between the Purely Hydrodynamic and Purely Kinetic Ranges

Density Threshold for a Purely Hydrodynamic Beam-Arc Plasma Instability

An approximate functional form of the reduced distribution function of beam-arc ions, that is, of the distribution for velocities v along the propagation vector $\mathbf{k}$ can be easily derived for the beam-arcs considered in our model (Figure 4-1) since these are roughly slices of symmetric ring distributions. For small arcs and $\theta_{k_\perp} = 0^o$ the reduced distribution of beam-arc ions is approximately $f_w(v) \sim n_w/\Delta\Theta\sqrt{V^2 - v^2}$ for $V\cos\Delta\Theta < v < V$ and decreases exponentially to near zero (since the beamlets that make up the beam-arc were assumed to have a Maxwellian thermal spread) at $v = V\cos\Delta\Theta$ and $v = V$ (see Figure 4-3a).

The positive (negative) slope of the reduced distribution function of beam-arc ions for $v \geq V\cos\Delta\Theta$ causes resonant damping (in the beam-arc ion frame) of hydrodynamic modes with phase velocities close to or greater than $V\cos\Delta\Theta$. Therefore, as

98

shown in Figure 4-3a., the condition necessary to avoid damping of hydrodynamic modes is that the phase velocity of the unstable modes be smaller than the speeds of the particles, that is,

$$\frac{\omega_r}{k} < V \cos \Delta\Theta \qquad (4.14)$$

Using Equations 4.11 and 4.12, this condition becomes

$$\left(1 - \left(\frac{n_w}{n_O}\right)^{1/3} \frac{1}{2^{4/3}}\right) < \cos \Delta\Theta \qquad (4.15)$$

or

$$\frac{n_w}{n_O} > 2^4 (1 - \cos \Delta\Theta)^3 \qquad (4.16)$$

which implies that for a particular arc $\Delta\Theta$ the beam-arc plasma instability will be of the hydrodynamic type if the density threshold given by Equation 4.16 is exceeded. This condition, however, applies only to arcs such that $V \cos \Delta\Theta > v_{thO}$ or $\Delta\Theta < \cos^{-1}(v_{thO}/V) \approx 80^o$ since for larger arcs the hydrodynamic modes would be Landau damped by the Maxwellian distribution of the stationary oxygen ions, see Figure 4-3a. Therefore, even for large n_w/n_O density ratios, hydrodynamic beam-arc plasma instabilities can only occur for arcs less than $\cos^{-1}(v_{thO}/V)$.

The Critical Arc of the Beam-Arc Plasma Instability

Figure 4-3b shows that for arcs slightly larger than the largest arc that satisfies the threshold for a purely hydrodynamic instability, Equation 4.15, the unstable modes with high phase velocities are kinetic while those with low phase velocities are hydrodynamic. We now define the critical arc, $\Delta\Theta_{crit}$, as being the arc where the maximum growth rate of the hydrodynamic modes is comparable to the maximum growth rate of the kinetic modes (i.e. $(\gamma_{max})_{hydro} \approx (\gamma_{max})_{kin}$). Therefore, $\Delta\Theta_{crit}$ is about the largest arc for which some of the unstable modes are hydrodynamic. This is because, in general, hydrodynamic two-stream instabilities are much stronger than kinetic two-stream instabilities for the same n_w/n_o density ratios. For arcs larger than $\Delta\Theta_{crit} + 5^o$ all of the unstable modes are kinetic. The definition of the critical arc will be very useful in later sections for the interpretation of the PDP wave data.

Now, let us note in Figure 4-2a that for $n_w/n_e = 0.15$ the critical arc is about 60°. The dip in the growth rate curve of the critical arc corresponds to (1) hydrodynamic modes with phase velocities $\omega_r/k \approx V \cos \Delta\Theta$ (see Figure 4-3b) that are affected by resonant damping (in the moving frame) from the large slope of the reduced distribution of the beam-arc ions at these velocities, and (2) kinetic modes with phase velocities greater than but close to $V \cos \Delta\Theta$ that are driven unstable by anti-Landau damping from the small positive slope in the plateau-like region of the reduced distribution of beam-arc ions at velocities greater than but close to $V \cos \Delta\Theta$ (see Figure 4-3b). The wavenumber at the dip of the growth rate curve is close to $k \approx \Omega_{LHO}/V \cos \Delta\Theta_{crit}$ since $\omega_r \approx \Omega_{LHO}$. Therefore, unstable modes with wavenumbers larger than this value are hydrodynamic while those with wavenumbers lower than this value are kinetic. This is because $\omega_r \approx \Omega_{LHO}$ for the most unstable hydrodynamic and kinetic modes and, as shown in Figure 4-3b, the unstable modes with low phase velocities ω_r/k are hydrodynamic and those with high phase velocities are kinetic.

Figure 4-4 shows the critical arcs for various water ion to electron density ratios. We note in this figure that larger critical arcs correspond to higher n_w/n_e density ratios. This is expected since $\Delta\Theta_{crit}$ is about the largest arc for which some of the unstable modes are hydrodynamic and for $\Delta\Theta \leq 80^o$ purely hydrodynamic beam-arc plasma instabilities can be excited only if the n_w/n_e density threshold of Equation 4.16 is exceeded.

Let us now go back to Figure 4-2 and note that as $\Delta\Theta$ is increased gradually from $\Delta\Theta_{crit} \approx 60^o$ to 65° the second bump in the growth rate curve, which corresponds to the unstable hydrodynamic modes and for $\Delta\Theta = 60^o$ peaks near $kV_{orb}/\omega_{cO} = 375$, gradually sinks into the negative γ-plane while shifting slightly to higher kV_{orb}/ω_{cO} values (not shown). In particular, for $\Delta\Theta = 64.5^o$ the hydrodynamic bump is almost entirely in the negative γ-plane with its peak down to $\gamma = 0^+$ and shifted to $kV_{orb}/\omega_{cO} = 480$ (not shown). This damping of the hydrodynamic modes is due to the fact that as $\Delta\Theta$ is increased above $\Delta\Theta_{crit}$ the reduced distribution function of beam-arc ions starts extending over all (not just some, as in Figure 4-3b) of the phase velocities of the unstable modes thus stabilizing the hydrodynamic ones by Landau

damping (in the beam-arc frame) from its positive (negative) slope. The instability for $\Delta\Theta = \Delta\Theta_{crit} + 5^o$ is therefore purely kinetic with the most unstable modes having phase velocities greater than $V\cos\Delta\Theta$.

4.3.3 The Kinetic Beam-Arc Plasma Instability

For arcs larger than $\Delta\Theta_{crit} + 5^o$ the only unstable modes that can be excited are kinetic and thus the beam-arc plasma instability is purely kinetic. The mechanism of the kinetic beam-arc plasma instability is anti-Landau damping. We can analyze the characteristics of this instability by also considering the case of propagation perpendicular to the B-field ($\delta = 0$) in the direction $\theta_{k_\perp} = 0^o$ (see Figure 4-1). Moreover, it is useful to make a change of variable $v = V\cos\theta$ in the integral of Equation 4.3 and rewrite this fluid limit dispersion relation as follows:

$$1 - \frac{\Omega_{LHO}^2}{\omega^2} - \frac{\Omega_{LHw}^2}{k^2}\int_{-\infty}^{\infty}\frac{\hat{f}_w(v)}{(v - \frac{\omega}{k})^2}dv = 0 \tag{4.17}$$

where Ω_{LHs}^2 is defined for species s as in Equation 4.4 and $\hat{f}_w(v)$ is the (normalized) reduced distribution function of the beam-arc water ions and has the following form

$$\hat{f}_w(v) = \begin{cases} \frac{1}{\Delta\Theta\sqrt{V^2 - v^2}} & \text{if } V\cos\Delta\Theta < v < V \\ 0 & \text{otherwise} \end{cases} \tag{4.18}$$

for $\Delta\Theta \leq 180^o$ and

$$\hat{f}_w(v) = \begin{cases} \frac{1}{\Delta\Theta\sqrt{V^2 - v^2}} & \text{if } V\cos\Delta\Theta < v < V \\ \frac{2}{\Delta\Theta\sqrt{V^2 - v^2}} & \text{if } -V < v < V\cos\Delta\Theta \\ 0 & \text{otherwise} \end{cases} \tag{4.19}$$

for $\Delta\Theta > 180^o$.

The integral of the dispersion relation Equation 4.17 has a singularity at $v = \omega/k$ which corresponds to the resonant particles, that is, the water ions with velocity components along the propagation direction equal to the phase velocity of the wave. This singularity is therefore consistent with the anti-Landau damping mechanism of the kinetic beam-arc plasma instability. The proper way to deal with this singularity is by evaluating the integral of Equation 4.17 using a Landau contour [*Krall and*

101

Trivelpiece, 1986] that would result in analytic continuation at $v = \omega/k$ in the complex v- plane. Before evaluating this integral, however, let us note in Equations 4.18 and 4.19 that the reduced distribution function $\hat{f}_w(v)$ is discontinuous at V and $V \cos \Delta\Theta$ (and also at $-V$ for $\Delta\Theta > 180^o$). These discontinuities are due to the fact that $\hat{f}_w(v)$ was derived from the fluid limit dispersion relation, Equation 4.3, which assumes that the distribution functions of the beamlets that make up the beam-arc are delta functions. Consequently, it is useful and more consistent with our numerical results (which assume that the beamlets have thermal spread) to smooth out these discontinuities, as shown in Figure 4-3, and define $\hat{f}_{wC}(v)$ as the smoothed out (or continuous or analytic) version of $\hat{f}_w(v)$. Furthermore, substituting $\hat{f}_w(v)$ by $\hat{f}_{wC}(v)$ (which is not given explicitly) in Equation 4.17, this dispersion relation can be integrated by parts using a Landau contour and becomes

$$1 - \frac{\Omega_{LHO}^2}{\omega^2} - \frac{\Omega_{LHw}^2}{k^2}\left[P \int_{-\infty}^{\infty} \frac{\hat{f}_{wC}'(v)}{v - \frac{\omega}{k}} dv + \frac{k}{|k|} i\pi \hat{f}_{wC}'(v = \frac{\omega}{k}) \right] = 0 \qquad (4.20)$$

where P refers to the principal value of the integral. Moreover, for $n_w/n_O \ll 1$ we obtain the following approximate solution of Equation 4.20

$$\omega_r \approx \Omega_{LHO} \qquad (4.21)$$

$$\gamma \approx \frac{\pi}{2}\Omega_{LHO}\frac{\Omega_{LHw}^2}{k^2}\hat{f}_{wC}'(v = \frac{\Omega_{LHO}}{k}) \qquad (4.22)$$

As shown in Figure 4-3, we note that for the kinetic beam-arc plasma instability $\hat{f}_{wC}'(v = \frac{\Omega_{LHO}}{k})$ is positive at the unstable phase velocities. This means that the resonant particles exchange energy with the wave with negative dissipation thus energizing the wave since now the whole system behaves like a positive energy wave. The wave grows oscillating near the natural frequency of the dominant ions, the lower Hybrid frequency of the background ions. It should be noted that the growth rate of the kinetic type instability is much smaller than the growth rate of the hydrodynamic type instability, Equation 4.13.

Figure 4-2b shows the dispersion diagram of the beam-arc plasma instability for arcs $\Delta\Theta \geq \Delta\Theta_{crit}$, obtained by solving Equation 4.1. Although this plot is for

$\phi_{k_\parallel} \equiv \sin^{-1}(k_\parallel/k) = 0.385^o$, the results for $\phi_{k_\parallel} = 0^o$ are qualitatively the same. We shall therefore apply the theory developed above to interpret them. Let us note, in Figure 4-2b, that for arcs in the range $\Delta\Theta_{crit} < \Delta\Theta < 270^o$ there is a decreasing trend of the growth rate values with increasing values of $\Delta\Theta$. This trend is due to the fact that the growth rates of the kinetic beam-arc plasma instability are proportional to the slope of the reduced distribution function $\hat{f}_{wC}(v)$ at the unstable phase velocities (see Equation 4.22) and $\hat{f}_{wC}(v)$ and thus $\hat{f}'_{wC}(v)$ are inversely proportional to $\Delta\Theta$ (see Equations 4.18 and 4.19). Consequently, larger arcs have smaller values of $\hat{f}'_{wC}(v)$ and thus smaller growth rates for kinetic modes with the same phase velocities.

It is interesting to note in Figure 4-2b that kinetic beam-arc plasma instabilities for arcs in the range $275^o < \Delta\Theta < 345^o$ have much smaller growth rates and ranges of unstable wavenumbers than those for other arcs in the kinetic range ($\Delta\Theta > \Delta\Theta_{crit} + 5^o$). This is due to the fact that near $v = V\cos\Delta\Theta$ the reduced distribution $\hat{f}_{wC}(v)$ decreases by a factor of 2 (see Equation 4.19) and thus the slope of $\hat{f}_{wC}(v)$ near $V\cos\Delta\Theta$ is negative (see Figure 4-3d). Therefore, kinetic beam-arc plasma waves with phase velocities near $v = V\cos\Delta\Theta$ are damped (see Equation 4.22). For arcs in the range $275^o < \Delta\Theta < 360^o$ the unstable modes have phase velocities much larger or smaller than $V\cos\Delta\Theta$ such that the slope of $\hat{f}_{wC}(v)$ at $v = \omega/k$ is positive.

Finally, it should be pointed out that in Figures 4-3c and 4-3d unstable modes with negative phase velocities should also be present (not shown). However, these modes that for $\theta_{k_\perp} = 0^o$ correspond to solutions of the dispersion equation (Equation 4.1) with $\omega_r < 0$ are exactly the same as those for $\theta_{k_\perp} = 180^o$ with $\omega_r > 0$. In fact, all of the unstable mode solutions of Equation 4.1 can be obtained by considering only those with $\omega_r > 0$ but for the entire range of $\theta_{k_\perp}$ (0° to 360°). Therefore, for simplicity we shall only consider the solutions with $\omega_r > 0$ and, later, extend our analysis to the entire range of $\theta_{k_\perp}$.

4.4 Propagation in Various Directions

4.4.1 The Effect of Finite $k_{\parallel}$

So far we have been restricting our analytical study of the hydrodynamic and kinetic beam-arc plasma instabilities to waves propagating exactly perpendicular to the B-field ($\delta = k_{\parallel}^2 m_i / k^2 m_e = 0$). Removing this restriction, however, we note from Equation 4.3 that for waves propagating with finite $k_{\parallel}$ the dispersion relations of the beamlet plasma instability, Equation 4.4, and kinetic beam-arc plasma instability, Equations 4.17 and 4.20, are each modified only by a factor of $(1 + \delta)$ in their second terms. Another equivalent way of taking this factor into account is by leaving the forms of Equations 4.4, 4.17 and 4.20 unchanged and increasing the value of Ω_{LHO} by a factor of $(1 + \delta)^{1/2}$. Since this can be thought of as an effective increase in the background ion density n_O by a factor of $(1 + \delta)$, we can see from Equation 4.13 that finite $k_{\parallel}$ will increase the maximum growth rate value of the hydrodynamic type instability by a factor of $(1 + \delta)^{1/6}$ and thus make the instability stronger. Similarly, we note from Equation 4.22 that finite $k_{\parallel}$ will increase the growth rate of the kinetic type instability by a factor of $(1 + \delta)^{1/2}$. However, for larger $k_{\parallel}$ electron thermal effects become important. Therefore, the condition necessary to avoid electron Landau resonance, $k_{\parallel} v_{the} < |\omega|$, becomes a condition on the angle of wave propagation. For the hydrodynamic type, using Equation 4.8 this gives roughly $k_{\parallel} v_{the} < kV \cos \Delta\Theta$ or

$$\frac{k_{\parallel}}{k} \leq \frac{V \cos \Delta\Theta}{v_{the}} \tag{4.23}$$

and for the kinetic type, using Equation 4.21 the condition $k_{\parallel} v_{the} < |\omega|$ becomes

$$k_{\parallel} < \frac{\Omega_{LHO}}{v_{the}} \tag{4.24}$$

Figure 4-5 shows that the strongest beam-arc plasma instabilities occur for propagation vectors nearly perpendicular to the magnetic field. It is interesting to note that for arcs in the kinetic range, $\Delta\Theta_{crit} < \Delta\Theta \leq 360°$, maximum growth occurs at almost the same parallel propagation angle, around $\phi_{k_{\parallel}} \equiv \sin^{-1}(k_{\parallel}/k) \approx 0.385°$. This agrees with the condition of Equation 4.24. Furthermore, Figure 4-5 also shows that,

as expected from the condition in Equation 4.23, for arcs in the hydrodynamic range $\Delta\Theta < \Delta\Theta_{crit}$ the optimum parallel propagation angle is larger for the smaller arcs.

4.4.2 Propagation at Various Angles $\theta_{k_\perp}$ in the Plane Perpendicular to the Magnetic Field

Let us now consider cases of propagation at various angles $\theta_{k_\perp}$ in the plane perpendicular to the magnetic field. For any beam-arc with effective arc $\Delta\Theta$ the range of propagation angles $\theta_{k_\perp}$ for the most unstable modes is $0^o \leq \theta_{k_\perp} \leq \Delta\Theta$ (see Figure 4-1). This is because for propagation directions outside of this range the difference between the perpendicular speeds of the reduced distribution functions of beam-arc ions and background plasma (i.e. the free energy that drives the instability) is smaller. It is convenient to examine the dispersion relation characteristics of the beam-arc plasma instability for propagation directions in the range $0^o \leq \theta_{k_\perp} \leq \Delta\Theta$ by noting some symmetries in the dispersion relation formulations Equations 4.1, 4.2 and 4.3. In particular, we can argue that the dispersion diagram for any arc $\Delta\Theta$ is identical for $\theta_{k_\perp} = 0^o$ and $\theta_{k_\perp} = \Delta\Theta$ and the most it can vary is for $\theta_{k_\perp} = \Delta\Theta/2$ where it is the same as that of an "equivalent" arc $(\Delta\Theta)_{eq} = \Delta\Theta/2$ with $(\theta_{k_\perp})_{eq} = 0^o$ or $\Delta\Theta/2$. This also implies that for any arc $\Delta\Theta$ the propagation direction for the most unstable modes is $\theta_{k_\perp} = \Delta\Theta/2$. Similarly, it should be pointed out that the critical arc $\Delta\Theta_{crit}$ is also a function of $\theta_{k_\perp}$, the smallest $\Delta\Theta_{crit}$ corresponds to $\theta_{k_\perp} = 0$ and $\theta_{k_\perp} = \Delta\Theta = \Delta\Theta_{crit}$, and the largest corresponds to $\theta_{k_\perp} = \Delta\Theta/2$ where $\Delta\Theta_{crit}$ is twice the value of that for $\theta_{k_\perp} = 0$ with the same density ratio n_w/n_e. However, in this chapter we shall be concerned only with the critical arc for $\theta_{k_\perp} = 0^o$ and thus refer to it simply as the critical arc.

Let us finish this section by giving a specific example: the beam-arc plasma instability dispersion diagram for the arc $\Delta\Theta = 60^o$ is identical for the propagation directions $\theta_{k_\perp} = 0^o$ (Figure 4-2) and $\theta_{k_\perp} = 60^o$. Moreover, for $\Delta\Theta = 60^o$ the propagation direction for the most unstable case (i.e. largest growth rate) is $\theta_{k_\perp} = 30^o$. For this case the dispersion diagram is identical to that for $\Delta\Theta = 30^o$ with $\theta_{k_\perp} = 0^o$.

4.5 Effects of Varying Parameters

4.5.1 Effect of Beam-Arc Ion Density

Figures 4-6a and 4-6b show the beam-arc plasma instability maximum growth rate (γ_{max}) and corresponding wavenumber $(k)_{\gamma_{max}} \equiv k^*$ and frequency $(\omega_r)_{\gamma_{max}} \equiv \omega_r^*$ for various density ratios n_w/n_e (with $n_e = (n_O + n_w)$ held constant) for two cases, $\Delta\Theta = 45^o$ and $\Delta\Theta = 180^o$ (obtained by solving Equation 4.1). We should point out that for the entire range of n_w/n_e ratios considered in this figure the modes for $\Delta\Theta = 180^o$ are kinetic and, according to Equation 4.16, for $n_w/n_e > 0.07$ the modes for $\Delta\Theta = 45^o$ are hydrodynamic. As expected from Equation 4.13 and 4.22, Figure 4-6a shows that the maximum growth rate γ_{max} increases as $n_w/n_e = n_w/(n_O + n_w)$ increases. This can be explained from the fact that the free energy of the beam-arc distribution function increases as the density n_w of beam-arc ions increases. Furthermore, it is interesting to note in Figure 4-6a, specially for $\Delta\Theta = 45^o$, that increases in the n_w/n_e ratio produce larger increases in γ_{max} at small density ratios $(n_w/n_e < 0.5)$ than at large n_w/n_e values. This is because we are considering the case where $n_e = n_O + n_w =$ constant and this implies that increases in the ratio $n_w/n_e = n_w/(n_O + n_w)$ increase n_w and thus the beam-arc free energy but decrease n_O the reactive medium density. Therefore, increases in the beam-arc free energy are to some extent counterbalanced by decreases in the energy density of the background ion positive energy wave. We should also note that, as expected, for the entire range of n_w/n_e values considered in Figure 4-6b, the maximum growth rate of the hydrodynamic $(\Delta\Theta = 45^o)$ and kinetic $(\Delta\Theta = 180^o)$ modes occurs near the natural frequency of oscillations of the dominant ion species, that is, the lower Hybrid frequency of the background oxygen ions $(\Omega_{LHO}^2 = \omega_{ce}\omega_{cO}(n_O/n_e))$.

Figure 4-7 shows the dispersion diagram for $\Delta\Theta = 45^o$ for various n_w/n_e density ratios. This figure clearly illustrates the fact, discussed in Section 4.3, that for arcs smaller than $\cos^{-1}(v_{thO}/V)$ and n_w/n_e ratios that exceed the the threshold of Equation 4.16 the beam-arc plasma modes are purely hydrodynamic. Moreover, in

agreement with Figure 4-4, we note in Figure 4-7 that $\Delta\Theta = 45^o$ is close to the critical arc for $n_w/n_e = 0.01$. Therefore, for n_w/n_e ratios lower than 0.01 the beam-arc plasma modes for $\Delta\Theta = 45^o$ are purely kinetic.

4.5.2 Effect of Beam-Arc Ion Thermal Spread

Figures 4-8a and 4-8b show the beam-arc plasma instability maximum growth rate (γ_{max}) and corresponding wavenumber k^* and frequency ω_r^* for various v_{thw}/v_{thO} ratios (with v_{thO} held constant) for two cases, $\Delta\Theta = 45^o$ and $\Delta\Theta = 180^o$ (obtained by solving Equation 4.1). We note in Figure 4-8a that the maximum growth rate γ_{max} of the beam-arc plasma modes decreases as v_{thw} increases. The stabilizing effect of increasing the beam-arc thermal spread is due to reducing effectively the difference between beam-arc and plasma perpendicular speeds decreasing the free energy available to drive the instability. We should also note that for the entire range of v_{thw}/v_{thO} ratios considered in Figure 4-8b, the maximum growth rate of the beam-arc plasma instability occurs near the natural frequency of oscillations of the dominant ion species, that is, the lower Hybrid frequency of the background oxygen ions.

Figure 4-9 shows the dispersion diagram of the beam-arc plasma instability for $\Delta\Theta = 45^o$ for various v_{thw}/v_{thO} ratios (with v_{thO} held constant). Now, it should be mentioned that the threshold condition for purely hydrodynamic instabilities (see Section 4.3) applies only to cases of relatively cool beam-arc ions with $v_{thw}/v_{thO} \leq 1$. Such cases are those considered in all the previous subsections (where $v_{thw}/v_{thO} = 0.5$ corresponding to the case of the shuttle plasma cloud) and it is also the case for $v_{thw}/v_{thO} = 0.5$ in Figure 4-9. On the other hand, for large enough v_{thw}/v_{thO} ratios, such as the cases for $v_{thw}/v_{thO} = 2$ and 4 in Figure 4-9, the beam-arc plasma instability is kinetic even for small arcs $\Delta\Theta$ and large n_w/n_O density ratios. This is because for larger v_{thw}/v_{thO} ratios the large slope of the reduced distribution function near $v = V\cos\Delta\Theta$ (see Figures 4-3a and 4-3b) is significantly flattened such that the reduced distribution function of the beam-arc ions spreads over the range of phase velocities of the unstable modes.

4.5.3 Effect of Plasma Thermal Spread

It can be shown that increasing the plasma thermal spread (v_{thO}) (with v_{thw} held constant) decreases the maximum growth rate γ_{max} of the beam-arc plasma instability. The stabilizing effect of increasing v_{thO} is also due to reducing effectively the difference between the beam-arc and plasma perpendicular speeds thus decreasing the free energy available to drive the instability.

4.6 Interpretation of the PDP Wave Data in Terms of the Linear Instability Theory

4.6.1 The Doppler-Shifted Beam-Arc Plasma Instability

In this section we use the detailed analysis of beam-arc plasma waves performed above to interpret the PDP wave spectrum. For purposes of comparing the theoretical characteristics of the beam-arc plasma waves with the PDP wave spectrum data, it is convenient to express these characteristics in plots of growth rates versus wave frequency in the reference frame of the shuttle. This is because the PDP instruments made all their measurements while moving with the shuttle. The wave frequency in the moving frame, which we shall call the observable wave frequency ω_o, is the Doppler-shifted frequency

$$\omega_o = \omega - k_\perp V_{orb} \cos\theta_{k_\perp} \tag{4.25}$$

where ω is the wave frequency in the stationary ionospheric frame and $\theta_{k_\perp}$ is the angle between the orbital velocity $\mathbf{V}_{orb}$ and the component of the propagation vector $\mathbf{k}$ in the plane perpendicular to the magnetic field. We shall refer to the plots of growth rates versus observable frequency as the growth rate spectra of the beam-arc plasma waves.

Figure 4-10 shows plots of growth rates versus observable wave frequency for the various beam-arc plasma waves of Figure 4-2; recall that for these cases $\theta_{k_\perp} = 0^o$ and $\phi_{k_\parallel} = \sin^{-1}(k_\parallel/k) = 0.385^o$. The plots of Figure 4-10a show that the growth

rate spectra for the smallest arcs $\Delta\Theta \approx 1^0$ have the largest growth rates $(50\omega_{cO})$ and relatively narrow bandwidths with center frequencies around $55\omega_{cO}$. Larger arcs, $\Delta\Theta \approx 20^o - 55^o$, have growth rate spectra with larger bandwidths and ranges of frequencies for maximum growth extending to higher frequencies. Moreover, the growth rate spectra for arcs in the range $56^o \leq \Delta\Theta \leq \Delta\Theta_{crit}$ have two peaks, one at $50\omega_{cO}$ and the other around Ω_{LH}, the latter shifting to slightly higher frequencies for the larger arcs in this range. Let us also note that as $\Delta\Theta$ is increased gradually from $\Delta\Theta_{crit} \approx 60^o$ to 65° the second bump in the growth rate spectrum, which corresponds to the peak near Ω_{LH}, gradually sinks into the negative γ-plane while shifting slightly to higher frequencies (not shown). In particular, for $\Delta\Theta = 64.5^o$ the second bump is almost entirely in the negative γ-plane with its peak down to $\gamma = 0^+$ and shifted to $1.4\Omega_{LH}$ (not shown). Therefore, as shown in Figure 4-10b, the growth rate spectra of arcs larger than $\Delta\Theta = \Delta\Theta_{crit} + 5^o$ have no high frequency peak and only the low frequency peak. However, the bandwidths for growth for arcs in the ranges $\Delta\Theta_{crit} < \Delta\Theta \leq 270^o$ and $345^o \leq \Delta\Theta \leq 360^o$ are still quite large extending approximately from 0 to Ω_{LH}.

Let us now consider more general cases of beam-arc plasma instabilities, in particular, cases where the propagation direction differs from the orbital velocity direction ($\theta_{k_\perp} \neq 0^o$). Figures 4-11a and 4-11b show the growth rate spectra of beam-arc plasma waves for various propagation angles $\theta_{k_\perp}$, obtained by solving Equation 4.1. Two different beam-arcs are considered in these figures, one with an arc $\Delta\Theta = 60^o \leq \Delta\Theta_{crit}$ (Figure 4-11a) and the other with an arc $\Delta\Theta = 270^o$ much larger than $\Delta\Theta_{crit}$ (Figure 4-11b). It should be noted that the major effect of changing the propagation angle $\theta_{k_\perp}$ is to shift the peaks of the spectrum. This shifting is mostly due to the Doppler shift effect, Equation 4.25, since the beam-arc plasma instability dispersion relation in the stationary frame changes just slightly with the choice of $\theta_{k_\perp}$ (for $0^o \leq \theta_{k_\perp} \leq \Delta\Theta$, the most unstable cases). In particular, some symmetries can be noted from the dispersion relation formulation, Equation 4.1: the dispersion relation in the stationary frame of an arc $\Delta\Theta$ should be identical for $\theta_{k_\perp} = 0^o$ and $\theta_{k_\perp} = \Delta\Theta$ and the most it can vary is for $\theta_{k_\perp} = \Delta\Theta/2$ where it is the same as that of an "equivalent" arc

$(\Delta\Theta)_{eq} = \Delta\Theta/2$ with $(\theta_{k_\perp})_{eq} = 0^o$ or $\Delta\Theta/2$. Along the same lines, it should be pointed out that the critical arc $\Delta\Theta_{crit}$ is also a function of $\theta_{k_\perp}$, the smallest $\Delta\Theta_{crit}$ corresponds to $\theta_{k_\perp} = 0$ and $\theta_{k_\perp} = \Delta\Theta = \Delta\Theta_{crit}$, and the largest corresponds to $\theta_{k_\perp} = \Delta\Theta/2$ where $\Delta\Theta_{crit}$ is twice the value of that for $\theta_{k_\perp} = 0$ with the same density ratio n_w/n_e. However, in this chapter we shall be concerned only with the critical arc for $\theta_{k_\perp} = 0^o$ and thus refer to it simply as the critical arc.

Therefore, going back to Figure 4-11a we note that for the arc $\Delta\Theta = 60^o$ the differences between the spectrum curves for $\theta_{k_\perp} = 0^o$ and 60° are only due to the Doppler shift effect, Equation 4.25. On the other hand, in addition to being Doppler shifted the spectrum curve for $\theta_{k_\perp} = 30^o$ has a much larger growth rate than those for the other propagation angles. This is due to the fact that in the stationary frame the dispersion relation corresponding to this curve is the same as that of a smaller equivalent arc $(\Delta\Theta)_{eq} = 30^o$ with $(\theta_{k_\perp})_{eq} = 0^o$ (see Figure 4-2a).

It is interesting to note in the growth rate spectra of the arc $\Delta\Theta = 270^o$, Figure 4-11b, that for waves propagating at $\theta_{k_\perp} = 180^o$ the peak of the spectrum is shifted all the way to $2.5\Omega_{LH}$. This peak near $2.5\Omega_{LH}$ is typical for the growth rate spectra of arcs $\Delta\Theta \geq 180^o$ with $\theta_{k_\perp} = 180^o$. It can be explained from Equation 4.25 by noting in Equations 4.21 and 4.22 that for maximum growth rate $\omega \approx \Omega_{LHO}$ and $k \geq \Omega_{LHO}/V$.

4.6.2   Comparison of the Beam-Arc Plasma Wave Characteristics With the PDP Wave Data of the Near Field Region

Let us now compare our theoretical results with the experimental data of the near field region of the shuttle, described in Section 2.2. In Figure 4-12, we compare the relative contribution of the electric fields $R(f_i)$ with the growth rate spectra of the beam-arc plasma instability for an arc $\Delta\Theta = 60^o$ for two propagation directions (1) $\theta_{k_\perp} = 0^o$ and (2) $\theta_{k_\perp} = 35^o$. Although, this is a comparison of nonlinear (experimental) with linear quantities, it is reasonable to use it for a qualitative discussion, since our simulation results of the next chapters will show that significant mode coupling does not take place in the nonlinear regime of the instability. We note that the characteristics of the

beam-arc plasma instability, for (effective) arcs $\Delta\Theta$ that the water ion distribution function is expected to have in the near field region (i.e. the $X_p = 1$ beam arc, see Section 3.1), fit well the details of the PDP wave spectrum data taken within 10 meters of the shuttle. Specifically, Figures 4-10 and 4-12 show that the beam-arc plasma waves corresponding to arcs close to but not greater than $\Delta\Theta_{crit} = 60^o$, propagating parallel to the orbital velocity direction $\theta_{k_\perp} = 0^o$, can explain the high frequency portion of the uniform first component of the spectrum (the component that extends from 31 Hz ($1\omega_{cO}$) to 10 kHz ($345\omega_{cO}$)) and the third component of the spectrum which is the peak at the lower hybrid frequency ($172\omega_{cO}$). In this case, the linear theory would also explain why the Ω_{LH} peak in the PDP spectrum data follows the orbital variations in the magnetic field. This is because the peak near Ω_{LH} in the growth rate spectra for arcs $\Delta\Theta \leq \Delta\Theta_{crit}$ (Figure 4-10a) corresponds to the strongly unstable high wavenumber (hydrodynamic) modes of Figure 4-2a that are the result of some beamlets being in synchronism, Equation 4.8, at the stationary frame wave frequency $\omega \approx \Omega_{LH}$ which is proportional to the magnitude of the B-field. Consequently, the Doppler-shifted (moving frame) frequency of this peak (Figure 4-10a) is also proportional to the magnitude of the B-field. In the next section, however, it will be argued that the linear theory is unlikely to explain the peak near Ω_{LH} in the PDP wave spectrum because in the nonlinear regime the beam-arc increases in thermal spread and in turn changes the instability to a purely kinetic version.

The second component, the peak at low frequencies, and the low frequency portion of the uniform first component of the PDP wave spectrum can be explained by the beam-arc plasma waves of arcs close to $\Delta\Theta_{crit}$ propagating at angles $\Delta\Theta_{crit}/2 \leq \theta_{k_\perp} \ll \Delta\Theta_{crit}$ to the orbital velocity direction (see Figure 4-12). This is clearly shown in Figure 4-11a which shows that the maximum growth rates for arcs $\Delta\Theta \approx \Delta\Theta_{crit}$ occurs for waves propagating at $\theta_{k_\perp} \approx \Delta\Theta/2$ and that these waves have low frequencies ($0 - \frac{1}{4}\Omega_{LH}$) in the moving frame, that match those of the second component of the PDP wave spectrum. Furthermore, propagation at various angles $\theta_{k_\perp}$ perpendicular to the magnetic field should be expected because the phase velocity of the beam-arc plasma waves is highly dependent on the density ratio n_w/n_e (see

Equation 4.12) and since, in general, this ratio decreases with increasing distance from the orbiter the waves should undergo refraction. This also agrees with the experimental fact that the PDP free-flight data shows no spin modulation, that is, the direction of $k_\perp$ is arbitrary (see Section 2.1).

It is interesting to note that the enhancements in the low frequency or second component waves observed in the PDP wave spectrum during water dump operations (see Section 2.3) can be explained in terms of the "refracted" beam-arc plasma waves propagating at $\theta_{k_\perp} \approx \Delta\Theta/2$ (see Figure 4-11a) having the maximum growth rates for arcs with $\Delta\Theta \leq \Delta\Theta_{crit}$. This is because the n_w/n_e ratio changes greatly in the water dump region and thus waves should be refracted accordingly.

There are other important characteristics of the beam-arc plasma instability that are consistent with those of the near field PDP electrostatic wave data. In particular, we note the following three characteristics: (1) as shown in Figure 4-5, the beam-arc plasma instability propagates preferentially in directions nearly perpendicular to the magnetic field; this agrees with the wave observations of the PDP free-flight data, (2) in Figure 4-2 we note that the wavelengths of the unstable modes range from 0.6 to 3.5 meters which is also consistent with the range of wavelengths that could be detected with the PDP antenna and (3) the beam-arc plasma wave dispersion relation, in the stationary frame (see Figure 4-2), is such that higher frequencies correspond to higher wavenumbers; therefore, since this is also true in the reference frame of the shuttle (i.e. the observable frequency, that is, the vertical distance between the $\omega_r = kV_{orb}$ line and the ω_r curves in Figure 4-2, see Equation 4.25, increases with wavenumber) this agrees with the experimental fact that high frequency waves disappear as the PDP enters in the wake.

4.6.3 Discussion on the Linear Theory

Effect of Beam-Arc Thermal Spread

In Chapter 5, we shall see that simulations of the reactive beam-arc plasma instability show that after an early stage of strong turbulence in which the beam arc particles are strongly heated, the instability settles down into a milder stage of the type of

112

a kinetic (warm) beam arc plasma instability. Therefore, significant heating of the beam-arc ions occurs in the nonlinear regime of the hydrodynamic beam-arc plasma instability.

Figure 4-13 shows the growth rate spectra of the critical arc corresponding to $n_w/n_e = 0.15$ ($\Delta\Theta_{crit} \approx 60°$, see Figure 4-4) for various values of the beam-arc temperature. In this figure, we note that as the beam-arc thermal spread is increased the peak near Ω_{LH} in the growth rate spectra flattens out. Therefore, for large values of $T_w(\geq T_O)$ the hydrodynamic modes corresponding to this peak (see Section 4.3) are damped and the instability is purely kinetic at the critical arc. Although this seems to contradict our original definition of the critical arc as being the arc for which there is a balance in the growth rates of the hydrodynamic and kinetic modes (see Section 4.3), we found (by inspecting a series of plots analogous to those of Figure 4-10, for various $\Delta\Theta$, but for larger values of T_w) that even for large values of $T_w(\sim 2T_O)$ the critical arcs, which are defined for $T_w/T_O = 0.25$ (see Figure 4-10), retain the following unique property: they are the arcs for which the growth rate spectra have the widest range of unstable frequencies (in the shuttle frame) even though for large T_w values the spectra do not have a peak near the lower hybrid frequency. Consequently, even for large beam-arc thermal spread the linear theory of beam-arc plasma waves for arcs near $\Delta\Theta_{crit}$ can still explain the high frequency portion of the uniform component of the near field wave spectrum. This can be seen in Figure 4-12 by noting that the growth rate spectra for large T_w should be similar to the curve with triangle symbols but with its two peaks smoothed out (see Figure 4-13).

At this point in our analysis, it appears that the peak near Ω_{LH} in the PDP wave spectrum is a result of nonlinear effects since the heating of beam-arc ions by the hydrodynamic instability changes the instability to a purely kinetic version which, according to linear theory, does not involve significant growth near Ω_{LH}. However, the PDP wave spectrum interpretation by using this linear analysis where the identification of the hydrodynamic and kinetic regimes was made by assuming a time invariant unperturbed distribution function should be relevant because although the beam-arc distribution should be heated by the instability, the heating should be par-

113

tially offset by the continuous creation of cold beam-arc ions from charge exchange reactions. In particular, in the region near the shuttle, which is the region of highest water neutral density and charge exchange rates, the beam-arc distribution should partially regenerate itself due to the charge exchange reactions that produce cold (i.e. at the low temperatures of the water neutrals) beam-arc ions. The regeneration of the beam distribution should be analogous to the case of the persistence of the unstable bump-on-tail electron velocity distribution in the Earth's foreshock [*Klimas and Fitzenreiter*, 1988]. The effects of charge exchange reactions will be discussed further in the following chapters.

Finally, we should mention that in the nonlinear regime the ionospheric ions and electrons are also expected to be heated. We have analyzed the effects of increasing the background species temperatures T_O and T_e by factors of 4. We found that increasing the background ion temperature does not affect the results and that increasing T_e does not change the results significantly except for a slight decrease in the angle $\phi_{k_\parallel}$ for maximum growth rate (see Figure 4-5), as can be expected from Equations 4.23 and 4.24.

Effect of a Smoother θ Dependence of the Beam-Arc Distribution

In Chapter 3, we have found that the beam-arc distribution functions formed in the shuttle plasma cloud are not simply "slices of ring distributions", as those studied in this chapter, but decrease more continuously with θ at phase angles near $\Delta\Theta$ (e.g. see Figure 3-2). The beam-arc plasma instability dispersion relation for these "smoother" beam-arc distribution functions can easily be obtained by introducing a weighing factor, a function of θ, in the integral of the beam-arc ion susceptibility χ_w in the dispersion relation Equation 4.1. However, since the θ dependence enters only as a weighting factor in this integral, the results for the "slices of ring distributions" that we have analyzed in the previous sections are very representatives of those that should be expected from the smoother models of beam-arc distributions.

In particular, we have examined the linear instability theory for the beam-arcs predicted for the near upstream region of the shuttle. For this analysis, the θ-dependence

of the weighing factor was thus taken from the plot of the normalized cuts of the distribution functions along lines of constant gyrospeed $V_\perp$ and zero parallel velocity shown in Figure 3-2. The numerical results of this computation turned out to be very similar to those for arcs $\Delta\Theta \geq 65^o$ of Figures 4-2b and 4-10b. Therefore, the Figure 3-2 beam-arcs have effective arcs larger than the critical arc thus corresponding to the kinetic regime of the beam-arc plasma instability (this should be expected since the reduced distributions corresponding to the Figure 3-2 beam-arcs are smoother near $V\cos\Delta\Theta$ and not as sharp as in Figure 4-3b). This implies that the Figure 3-2 beam-arcs have effective arcs slightly larger than those that can explain the Ω_{LH} peak in the PDP wave spectrum with the linear theory of the beam-arc plasma instability. Consequently, assuming that the Figure 3-2 predictions are reasonable, nonlinear effects appear to be important in the characterization of the saturated fields of the beam-arc plasma instability. Nevertheless, the basic analysis of the various unique properties of the linear beam-arc plasma instability and their correlations with the characteristics of the PDP wave observations that we have done in this chapter is fundamental for the simulation studies to be discussed in Chapter 5.

Effect of the Species Inhomogeneity

Let us now discuss the effects of the density gradients of the various species. The charged particle density gradients in the shuttle's plasma environment can be expected to be a source of free energy that could modify the wave spectrum by coupling to the beam-arc plasma instability or by exciting new drift instabilities. However, the results of a preliminary analysis on the inhomogeneity effects indicate that there is no coupling. They show that density gradients do not alter significantly the shape of the growth rate curves of the beam-arc plasma instability, Figures 4-10 and 4-11. The major effect is a slight increase or decrease in the magnitude of the growth rate, depending on the orientation of the density gradient with respect to both the propagation and magnetic field directions. We have also found in this analysis that water and oxygen ion density gradients can excite an unstable drift mode in the (moving frame) frequency range from 0 to Ω_{LH}. The growth rate of the drift mode, in this

frequency range, is almost uniform and slightly peaks at low frequencies ($0.25\Omega_{LH}$). The magnitude of the drift mode growth rate, however, is of the order of $5\omega_{cO}$ and thus much smaller than those of the beam-arc plasma instability, Figures 4-10 and 4-11. Therefore, it is likely that the major source of electrostatic waves in the shuttle induced environment is the excitation of the beam-arc plasma instability.

Figure 4-14 shows the growth rate spectra of beam-arc plasma instabilities for various density ratios n_w/n_e in the range of interest for the shuttle environment (1-20%). These plots are for the critical arcs corresponding to the various n_w/n_e density ratios (see Figure 4-4). It should be noted that, for the range of density ratios of interest, the critical arc growth rate spectra have, in all cases, relatively the same characteristics: they extend from 0 to about Ω_{LH} and peak near Ω_{LH}. Therefore, the characteristics of the PDP wave spectrum in the shuttle near field environment should be relatively insensitive to the local values of the water ion density. On the other hand, they should be sensitive to the spatial distributions of the water neutral and oxygen ion densities since, as discussed in Chapter 3, these determine the arcs of the distributions.

Waves Observed Above Several Times the Lower Hybrid Frequency

As noted in Section 2.1 and 2.2, the PDP wave spectrum above the lower hybrid frequency shows only a smooth decrease without apparent structure (see Figure 4-12). The wave data indicate that broadband near zone waves extend up to frequencies of order 50 kHz, corresponding to 5 - 10 times the lower hybrid frequency. Now, let us recall that, as shown in Figure 4-11b, the peak in the growth rate spectra of beam-arc plasma instabilities for large arcs $\Delta\Theta \geq 180^o$, such as those expected in the far upstream region (i.e. Figure 3-2), is upshifted to $2.5\Omega_{LH}$ for waves propagating at $\theta_{k_\perp} = 180^o$ (anti-parallel to the orbital velocity). This peak can be upshifted further, all the way to $4\Omega_{LH}$, if the beamlet water ion to oxygen ion temperature ratio, which determines the thickness of the beam-arc in velocity space, is reduced from its nominal value of $T_w/T_O = 0.25$ to less than 0.01. Therefore, beam-arc plasma waves convecting with $\theta_{k_\perp} = 180^o$ from the far upstream region of the shuttle, where

116

arcs are $\Delta\Theta > 180°$, could explain the extensions of the PDP wave spectrum to several times the lower hybrid frequency. Further work is required on correlating this theoretical result with the shuttle's temperature data. Moreover, it should be pointed out that the linear theory is incapable of explaining the weak observed waves above about $4\Omega_{LH}$. An analysis on the effects of nonlinear processes and spatial inhomogeneity must be carried out in an effort to explain the source of these high frequency waves.

4.7 Summary

We have developed the linear theory of the beam-arc plasma instability, which is driven by the free energy involving the interaction of the beam-arc distribution function of the pickup water ions with the background ionospheric plasma. The beam-arc distribution function was modeled as a summation of large numbers of Maxwellian beamlets having directions mapping the arc of the distribution and the same mean speed. This study was first restricted to beam-arc distributions of the form of slices of ring distributions since the beamlets making up the beam-arc were homogeneously distributed throughout the arc. It was assumed that the beam-arc water ions have zero drift parallel to the magnetic field. We have analyzed, numerically and analytically, the dispersion relation for all ranges of beam-arcs, from beams to rings. We have classified this instability into three different beam-arc regimes according to the instability mechanisms: (1) hydrodynamic for small arcs, (2) hydrodynamic and kinetic for effective arcs close to the critical arc ($\Delta\Theta_{crit} \approx 60°$) and (3) kinetic for large arcs. It was found that the beam-arc plasma instability shows new characteristics that are different from those of the beam-plasma [*Gaffey*, 1976] and ring-plasma [*Tataronis and Crawford*, 1970; *Lee and Birdsall*, 1979] instabilities. In particular, for arcs close to but not greater than the critical arc (in the second regime) the Doppler-shifted growth rate spectrum of the instability is much broader and peaks near the lower hybrid frequency. The critical arc was found to increase with the water ion to electron density ratio.

The results of the linear analysis show that the beam-arc plasma instability has

unique characteristics that can explain most details (i.e. the three components) of the wave spectrum detected with the PDP within 10 meters of the shuttle. However, an analysis on the effects of varying beam-arc parameters such as the angular dependence and thermal spread shows that the spectrum peak near the lower hybrid frequency (Ω_{LH}) appears to be a result of nonlinear effects. This is because the heating of beam-arc ions expected in the nonlinear regime should lead to a resonant type instability which according to the linear theory does not involve significant growth near Ω_{LH}. The other results of the comparison of the linear beam arc plasma instability theory with the PDP data can be summarized as follows:

- The wave propagation directions and wavelengths predicted with the linear theory are consistent with those observed with the PDP.

- The linear theory can explain the enhancements of the low frequency component of the spectrum, observed during water dumps, in terms of waves being refracted in the highly inhomogeneous region of the water dump.

- The linear theory predicts that the major free energy source that drives the shuttle environment waves is the beam-arc (i.e. non-Maxwellian) shape of the water ion distribution rather than the plasma density gradients.

- The instability frequency spectrum is highly dependent on the shape of the beam arc water ion distribution but relatively independent of the water ion to plasma density ratio (n_w/n_e).

- The effective arc of the $X_p = 1$ beam arc distribution of the near upstream region is close to but greater than the critical arc and thus corresponds to the third regime of the instability.

- The linear theory can explain waves with frequencies above the lower hybrid frequency in terms of waves propagating anti-parallel to the orbital velocity direction.

This linear theory analysis is a fundamental requirement for the simulation studies of the beam-arc plasma instability. Most of the results of this chapter have been

118

published in *Rivas and Hastings* [1992]. In the next chapters, the above data interpretations will be confirmed and extended further by using the results from PIC code simulations of the beam-arc plasma instability.
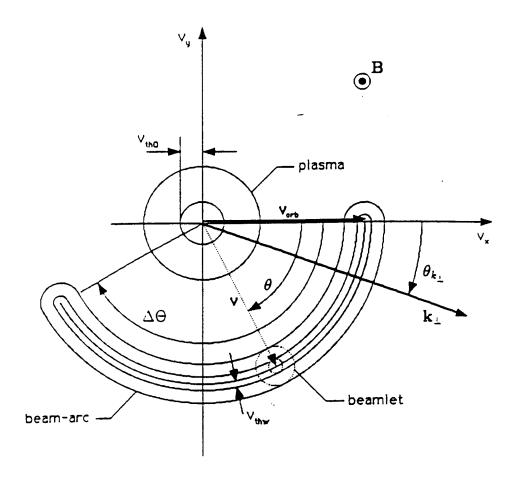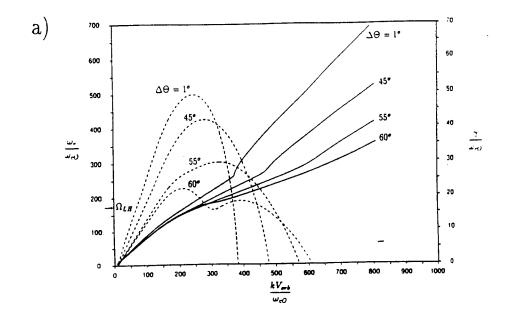
Figure 4-1: Illustration of the beam-arc distribution function of water ions and Maxwellian distribution function of ionospheric oxygen ions in the velocity space of the stationary ionospheric frame. The Maxwellian distribution function of one of the beamlets that makes up the beam-arc is shown in dotted lines. Superimposed on this figure are also shown the geometries of the vectors $k_\perp$, V_{orb}, and V. For simplicity, angles are defined positive clockwise.
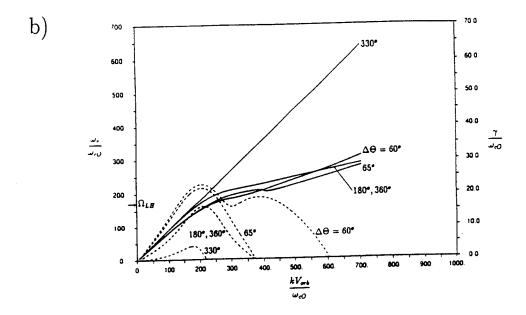
Figure 4-2: Dispersion diagram (in the ionospheric plasma frame) of beam-arc plasma waves for various arcs $\Delta\Theta$ of the water ion distribution function. In all these cases, $n_w/n_e = 0.15$ and the propagation direction is $\theta_{k_\perp} = 0°$ and $\phi_{k_\parallel} = 0.385°$. The real-frequency and growth rate curves are shown in solid and dashed lines, respectively.
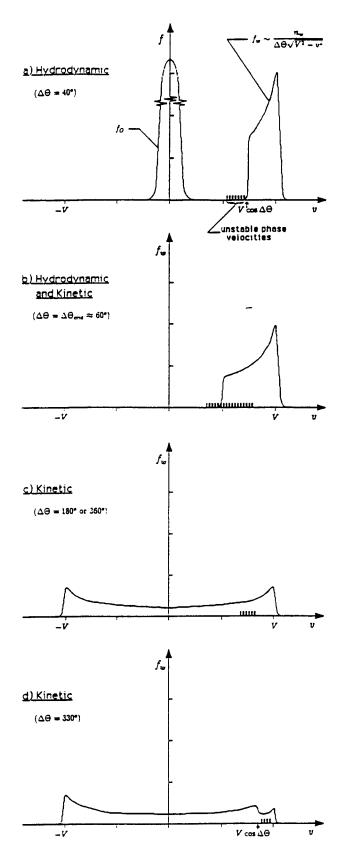
Figure 4-3: Illustration of the reduced distribution function of beam-arc water ions for various arcs for the case where **k** is in the direction of $\mathbf{V}_{orb}$ (i.e. $\theta_{k_{\perp}} = 0°$). In (a) the reduced distribution function of oxygen ions is also shown. The phase velocities of the unstable modes are indicated on the v axes.

122
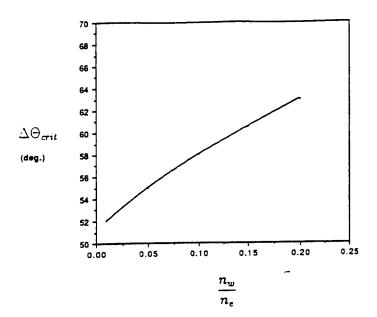
Figure 4-4: Critical arc of the water ion distribution function for various water ion to electron density ratios. These results are for beam-arc plasma waves propagating at $\theta_{k_\perp} = 0°$ and $\phi_{k_\parallel} = 0.385°$.
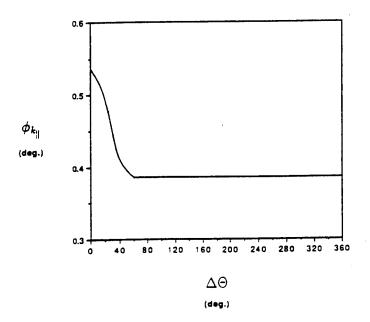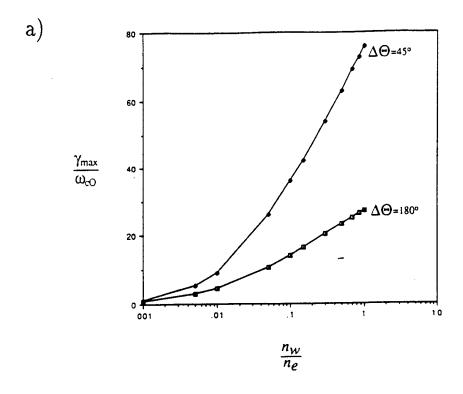
Figure 4-5: Parallel propagation angle for maximum growth versus arc of the water ion distribution function. These results apply to waves propagating at $\theta_{k_\perp} = 0°$.

a)

b)
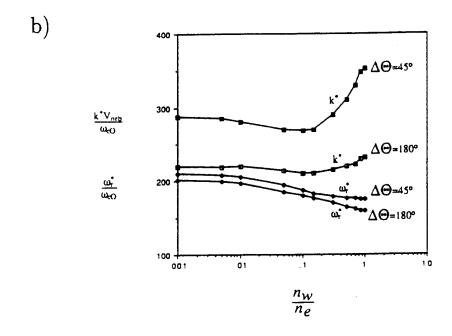
Figure 4-6: (a) The beam-arc plasma instability maximum growth rate for various n_w/n_e density ratios (with $n_e = n_O + n_w$ fixed) for two cases, $\Delta\Theta = 45°$ and $\Delta\Theta = 180°$. In all these cases $v_{thw}/v_{thO} = 0.5$ and the propagation direction is $\theta_{k_\perp} = 0°$ and $\phi_{k_\parallel} = 0.385°$. (b) The wavenumbers and frequencies corresponding to the beam-arc plasma instability maximum growth rate cases of (a).

124
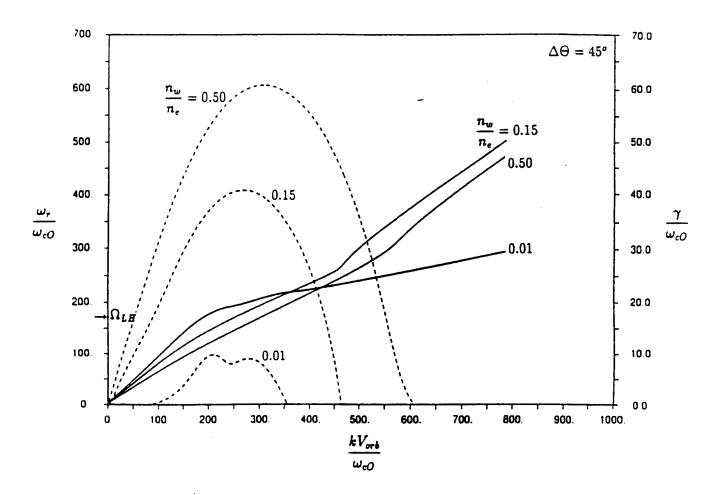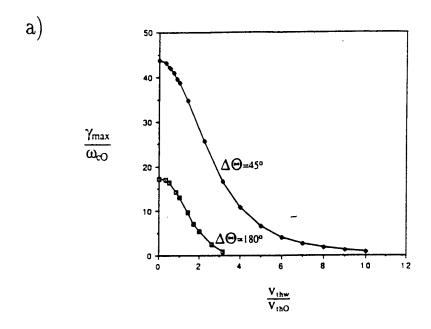
Figure 4-7: Dispersion diagram of beam-arc plasma waves for $\Delta\Theta = 45°$ for various n_w/n_e density ratios. In all these cases $v_{thw}/v_{thO} = 0.5$ and the propagation direction is $\theta_{k_\perp} = 0°$ and $\phi_{k_\parallel} = 0.385°$. The real frequency and growth rate curves are shown in solid and dashed lines, respectively.

a)

b)
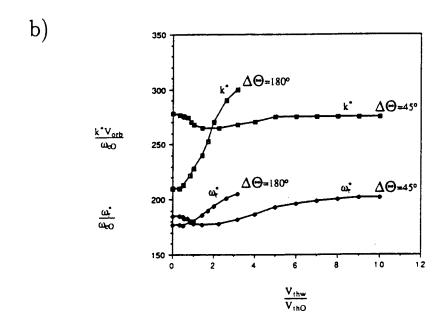
Figure 4-8: (a) The beam-arc plasma instability maximum growth rate for various v_{thw}/v_{thO} thermal velocity ratios (with v_{thO} fixed) for two cases, $\Delta\Theta = 45°$ and $\Delta\Theta = 180°$. In all these cases $n_w/n_e = 0.15$ and the propagation direction is $\theta_{k_\perp} = 0°$ and $\phi_{k_\parallel} = 0.385°$. (b) The wavenumbers and frequencies corresponding to the beam-arc plasma instability maximum growth rate cases of (a).
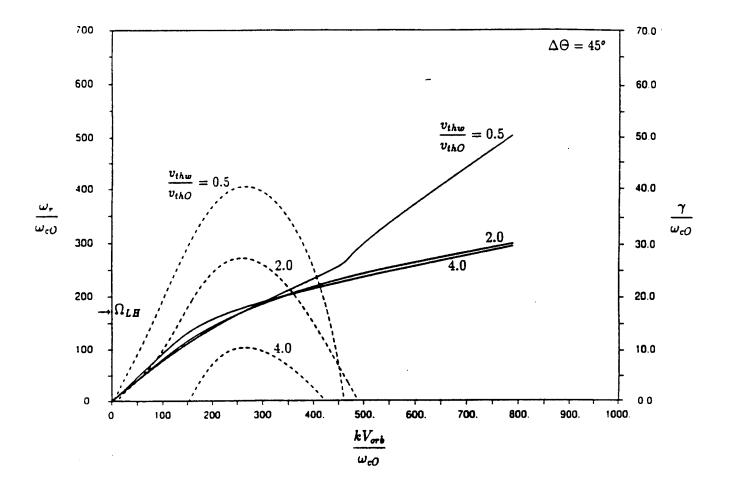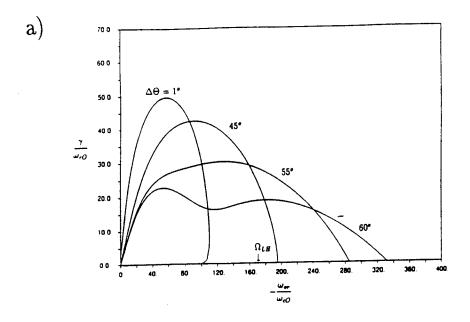
Figure 4-9: Dispersion diagram of beam-arc plasma waves for $\Delta\Theta = 45°$ for various v_{thw}/v_{thO} thermal velocity ratios. In all these cases $n_w/n_e = 0.15$ and the propagation direction is $\theta_{k_\perp} = 0°$ and $\phi_{k_\parallel} = 0.385°$. The real frequency and growth rate curves are shown in solid and dashed lines, respectively.
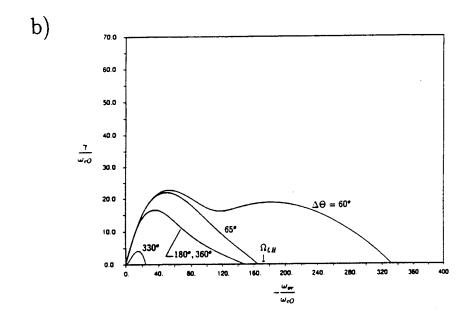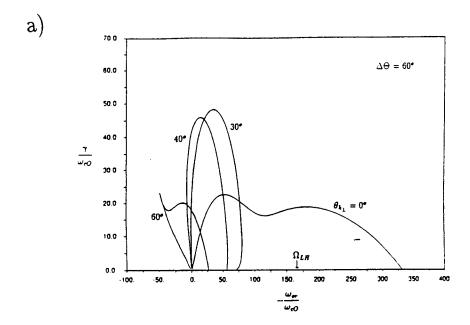
Figure 4-10: (a) Growth rates versus (observable) wave frequency for the various beam-arc plasma waves of Figure 4-2a. (b) Growth rates versus (observable) wave frequency for the various beam-arc plasma waves of Figure 4-2b.
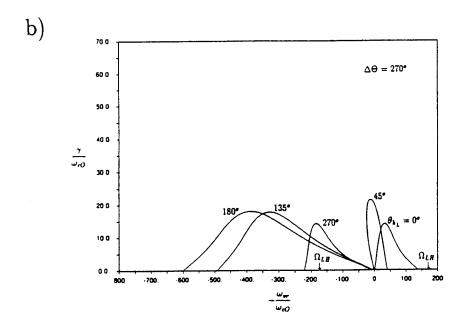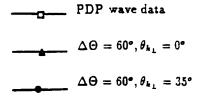
Figure 4-11: Growth rates versus (observable) wave frequency of beam-arc plasma waves propagating at various angles $\theta_{k_\perp}$ (with $\phi_{k_\parallel} = 0.385°$) for $n_w/n_e = 0.15$. The arc of the water ion distribution function is in all these cases (a) $\Delta\Theta = 60°$, (b) $\Delta\Theta = 270°$.
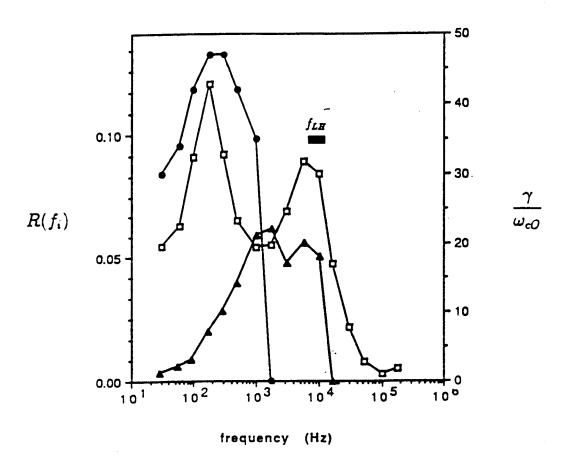
Figure 4-12: Ratio $R(f)$ of the average electric field in a frequency bandwidth divided by the total average broadband field ($E_T = 51.1$ mV/m) as a function of frequency (see text for a detailed definition). Superimposed on this PDP wave data plot are the theoretical growth rate spectra curves of the beam-arc plasma instability for an arc $\Delta\Theta = 60°$ for two propagation directions (1) $\theta_{k_\perp} = 0°$ and (2) $\theta_{k_\perp} = 35°$ ($\phi_{k_\parallel} = 0.385°$ in both cases).

130
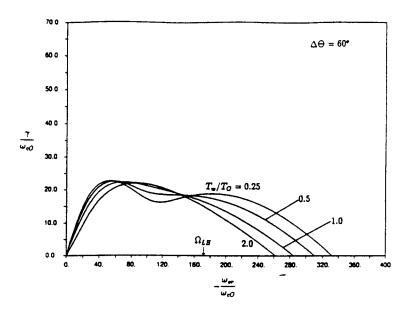
Figure 4-13: Growth rates versus (observable) wave frequency for various beam-arc temperatures T_w with $\Delta\Theta = 60°$, $n_w/n_e = 0.15$, $\theta_{k_\perp} = 0°$, $\phi_{k_\parallel} = 0.385°$, and T_O held constant.
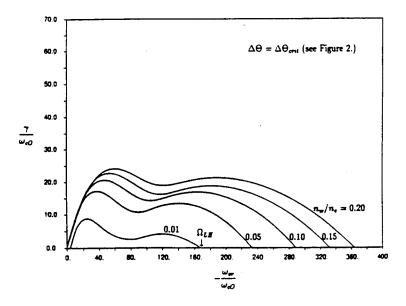
Figure 4-14: Growth rates versus (observable) wave frequency for the critical arcs corresponding to various water ion to electron density ratios (see Figure 4-4).

Chapter 5

Simulation of the Beam-arc Plasma Instability

5.1 Introduction to the Nonlinear Regime

5.1.1 Analogy of the Beam-Arc Plasma Instability to the Bump-on-tail Instability

It is important to note that the linear behavior of the beam-arc plasma instability is analogous to that of the ordinary (i.e. unmagnetized) bump-on-tail instability (driving Langmuir waves). The forms of the linear dispersion relations of the hydrodynamic and kinetic beam-arc plasma instabilities (Equation 4.4 and Equation 4.17, respectively) are the same as those of the reactive and gentle bump-on-tail instabilities [Gary, 1985], respectively, except for the fact that the magnetic field makes the natural frequency of oscillations in the beam-arc plasma system the lower hybrid frequency (Ω_{LH}) instead of the plasma frequency (ω_{pe}). In this chapter we will show analytically and through PIC-code simulations that, to some extent, this analogy between the beam-arc plasma instability and the ordinary two-stream instability persists in the nonlinear regime. This will be evident when we shall see that for the time scales of interest, in the nonlinear regime, the beam-arc and background ions will behave as unmagnetized. More importantly, we will show that the electrons will also behave as unmagnetized but with an effective mass comparable to those of the ions.

5.1.2 The State-of-the-art of the Nonlinear Analysis of the Bump-on-tail Instability

Despite a venerable history, the role of nonlinear processes in the evolution of electron plasma waves driven by an electron beam, or bump-on-tail instability, is still not resolved. Nonlinear processes are often believed important in the saturation of the beam instability, the generation of electromagnetic radiation at multiples of the plasma frequency and strong turbulence processes. For instance, nonlinear processes relevant to saturation of the linear instability include saturation of a reactive instability by trapping [e.g. *Kainer et al.*, 1972; *Cairns and Nishikawa*, 1989; *Dum*, 1990b], or removal of waves from the growth region in wavenumber space by the Langmuir wave decay $L \rightarrow L' + S$ (e.g., see *Goldman* [1984]). This Langmuir wave decay involves a forward propagating Langmuir wave(L) decaying into a backward propagating Langmuir wave (L') and a forward propagating ion acoustic wave (S). Theoretical models for generating electromagnetic radiation at multiples of the plasma frequency, as observed in solar radio bursts [*McLean and Labrum*, 1985] and the Earth's harmonic radiation [*Dunckel*, 1974; *Hoang et al.*, 1981; *Cairns*, 1986], also usually involve nonlinear processes such as scattering off thermal ions [*Ginzburg and Zheleznyakov*, 1959; *Dum*, 1990a, b, d; *Mushietti and Dum*, 1991] or the Langmuir wave decay [e.g., *Cairns and Melrose*, 1985; *Cairns*, 1988]. Strong turbulence processes (e.g., review by *Goldman* [1984]) are essentially nonlinear due to inclusion of the ponderomotive force and formation of cavitons.

Practically all of the analytical studies of turbulent theories of the bump-on-tail instability, ranging from quasi-linear theory to strong turbulence, have been developed from a model in which the beam does not affect the nature of the wave mode but merely destabilizes the plasma eigenmode. Therefore, these theoretical studies could only identify general trends because, for instance, the dispersion relation and the quasi-linear transfer rates were evaluated for Maxwellian or Lorentzian distribution functions of beam and bulk plasma. PIC code simulation experiments, on the other hand, have the potential of nearly unlimited diagnostics and various authors [e.g. Dum, 1990; Nishikawa and Cairns, 1991] were able to follow the dynamics of

the evolution in the distribution and the spectrum, which were shown to be closely coupled. Simulations thus offer an adequate means to study the nonlinear regime of beam plasma type instabilities. In the remainder of this section we shall therefore review the most accurate simulations of the electrostatic bump-on-tail instability. The results of such simulations should give us some idea of what to expect in the nonlinear regime of the (reactive and kinetic) beam-arc plasma instability. This is, of course, due to the similarities between the beam-arc plasma instability and bump-on-tail instability, discussed in the previous section.

To date, the most successful simulation of a gentle (i.e. kinetic) bump-on-tail electron instability was performed by Dum [1990a] while considering the generation of Langmuir waves in the earth's foreshock. It was shown that with appropriately designed simulation experiments, quasi-linear theory could be quantitatively verified for parameters corresponding to the electron foreshock. In these simulations, the distribution function developed a plateau by resonant diffusion, and changes outside this velocity range were negligible, except for the contribution of nonresonant diffusion to acceleration of the bulk electrons. The dispersion relation was solved for the evolving distribution function and exhibited the dynamics of wave growth and changes in real frequency. The integral of the quasi-linear equations was also used to relate the evolution of distribution function and wave spectrum and gave agreement with the simulations. Even in extremely long simulation runs there was practically no evolution in wave energy or the distribution function, once a plateau had been formed. The saturated field levels were much lower than the estimates that are generally used to assess the importance of additional weak or strong turbulence effects. These effects could not prevent plateau formation and were only noticeable if ions were also included in the model. They then lead to a redistribution of the spectrum toward low wave number modes which propagated mainly opposite to the beam. This occurred long after plateau formation and played no significant role in the overall system dynamics or energy balance. Dum [1990a] thus concluded that quasi-linear theory is a key ingredient for a global model of the gentle bump-on-tail instability in connection with the foreshock wave phenomena.

134

For the reactive bump-on-tail instability (i.e. for stronger, narrower beams) which could give rise to frequencies substantially different from the plasma frequency, only two, contradictory, models exist. It has been suggested [Shapiro, 1963] that in the first stage of the evolution of a cold beam-plasma system the beam would be heated, transforming it into a gentle bump-on-tail of the electron distribution. In the second stage the gentle bump would then be flattened by quasi-linear diffusion thus saturating the instability, just as if one had started with this regime. More frequently, however, an entirely different picture is assumed, in which the instability evolves into a single coherent wave mode [Drummond et al., 1970]. The progressive narrowing of the wave spectrum is generally assumed to arise from e-folding of a strongly peaked growth rate. Other authors [e.g. Cairns and Nishikawa, 1989] claim that the phase bunching mechanism is particularly sensitive to the interaction with other waves. The wave of largest linear growth rate is thus supposed to nonlinearly suppress the growth of neighboring modes [Melrose, 1986].

The single-wave models seem to be largely inspired by computer simulations in which the excitation of many wave modes is precluded a priori by the small system size. Computational restrictions were naturally most severe in early simulation studies, but even in recent studies, modes are often spaced far apart, especially if one attempts two-dimensional studies. The wave particle interaction in such cases is perhaps adequately described by the ubiquitous trapping model. More recently, however, a more elaborate simulation of the reactive bump-on-tail instability, by Dum [1990b], shows that after an early stage of strong turbulence in which the beam particles are strongly heated, the instability settles down into a milder kinetic stage. The subsequent evolution is essentially the same as in runs which already started with a broad beam (i.e. gentle bump), except that the wave levels are higher. With higher wave levels, mode coupling effects are more prominent, but still are unable to prevent plateau formation. Furthermore, Dum's [1990b] runs show that the feedback effect by the wave-particle interaction on wave growth is important, even in the extreme case of reactive instability. Many wave modes are excited in such runs, even when the spectrum temporarily narrows during the late reactive phase. There is no evi-

dence for any special nonlinear effect that would cause dominance of a single mode. Furthermore, after saturation the transition from reactive to kinetic instability takes place. Although trapping effects are seen during the transition period itself, these are followed by complete randomization in phase space. It is noted that quasi-linear theory may not be valid during the transition phase itself, but is expected to hold for the early reactive phase and the late kinetic phase.

5.1.3 Remarks on the Simulation of the Beam-Arc Plasma Instability

In the following analysis of the beam-arc plasma instability for the interpretation the PDP wave data, we will be interested in designing a simulation that is aimed primarily to the determination of the wave electric field spectrum of the instability. Designing such simulation will prove to be a delicate task since we will find that the total electrostatic field energy of the waves is very small compared to the thermal and drift energies of the particles. The field energy will be of the order of 1% of the total energy in the simulation system. In contrast, in the case of the (unmagnetized) bump-on-tail instabilities, discussed above, the field energy is comparable to the final thermal energy of the particles, that is, about 12% of the total energy. Therefore, in the case of the beam-arc plasma instability the spectral field energy of the modes will be a much more sensitive quantity. This implies that in order to obtain reasonable results, our simulation will have to include the effects of resonant and non-resonant diffusion and the quasi-linearlike feedback of wave-particle interaction, which were found to be important in the recent simulations of the analogous case of the bump-on-tail instabilities, discussed above. In particular, the transition to kinetic instability and subsequent quasi-linear evolution will require closely spaced wave modes (i.e. very long simulation systems) to lead to a proper evolution of the spectrum towards a quasi-steady state. In the Section 5.3 we shall design the simulation.

136

5.2 Nonlinear Theory

5.2.1 Mass Ratio Scaling of the Full Nonlinear Equations

As is usually done in simulations using explicit PIC codes, for computational efficiency, the simulation of the beam-arc plasma instability will be performed by using a reduced ion to electron mass ratio (i.e. $m_O/m_e = 512$). Therefore, before designing this simulation it is useful to look briefly at the nonlinear equations governing this instability and show that these equations can be expressed in a normalized form which is independent of the mass ratio. This is an important point in a numerical sense, since it implies a mass ratio scaling for the nonlinear system, that is, simulations performed with a reduced mass ratio can be used to determine the solution at realistic mass ratios.

In order to simplify our nonlinear analysis, we shall assume that the time scale on which the instability operates is much shorter than the ion Larmor period but much longer than the electron Larmor period. Our solutions to the linear dispersion relation have already shown that these conditions are satisfied in the regions of interest in parameter space see Chapter 4. Thus, the ions can be treated as unmagnetized, and the electron motion across the magnetic field may be treated in the drift approximation since the electron Larmor radius is also much smaller than the wavelengths of interest. The full nonlinear system is then described by the Vlasov-Poisson system

$$\frac{\partial f_j}{\partial t} + \mathbf{v} \cdot \frac{\partial f_j}{\partial \mathbf{x}} + \frac{q_j}{m_j} (\mathbf{E} + \mathbf{v} \times \mathbf{B}) \cdot \frac{\partial f_j}{\partial \mathbf{v}} = 0 \tag{5.1}$$

$$\nabla^2 \phi = -\frac{1}{\epsilon_0} \sum_j q_j \int f_j d\mathbf{v} \tag{5.2}$$

Using the above assumption of unmagnetized ambient oxygen ions and beam-arc water ions, we have

$$\frac{\partial f_O}{\partial t} + \mathbf{v} \cdot \nabla f_O - \frac{q_O}{m_O} \nabla \phi \cdot \frac{\partial f_O}{\partial \mathbf{v}} = 0 \tag{5.3}$$

and

137

$$\frac{\partial f_w}{\partial t} + \mathbf{v} \cdot \nabla f_w - \frac{q_w}{m_w} \nabla \phi \cdot \frac{\partial f_w}{\partial \mathbf{v}} = 0 \qquad (5.4)$$

The electrons are treated in the drift approximation giving

$$\frac{\partial f_e}{\partial t} + v_z \frac{\partial f_e}{\partial z} - \frac{q_e}{m_e} \frac{\partial \phi}{\partial z} \frac{\partial f_e}{\partial v_z} + \nabla \cdot (\mathbf{v}_d f_e) = 0 \qquad (5.5)$$

where $\mathbf{v}_d$ is the electron drift velocity given by

$$\mathbf{v}_d = \frac{\mathbf{E} \times \mathbf{B}}{B^2} - \frac{m_e}{eB^2} \left\{ \frac{\partial \mathbf{E}_\perp}{\partial t} + \mathbf{v}_d \cdot \nabla \mathbf{E}_\perp + v_z \frac{\partial \mathbf{E}_\perp}{\partial z} \right\} \qquad (5.6)$$

Under the further assumption that variations are permitted only in the x-z plane and that the variations in the electric field are much greater across the magnetic field (the direction denoted by x) than along the magnetic field (the direction denoted by z), the above equations may be written as

$$\frac{\partial \hat{f}_O}{\partial \hat{t}} + \hat{v}_x \frac{\partial \hat{f}_O}{\partial \hat{x}} - \frac{\hat{q}_O}{\hat{m}_O} \frac{\partial \hat{\phi}}{\partial \hat{x}} \frac{\partial \hat{f}_O}{\partial \hat{v}_x} = 0 \qquad (5.7)$$

$$\frac{\partial \hat{f}_w}{\partial \hat{t}} + \hat{v}_x \frac{\partial \hat{f}_w}{\partial \hat{x}} - \frac{\hat{q}_w}{\hat{m}_w} \frac{\partial \hat{\phi}}{\partial \hat{x}} \frac{\partial \hat{f}_w}{\partial \hat{v}_x} = 0 \qquad (5.8)$$

and

$$\frac{\partial \hat{f}_e}{\partial \hat{t}} + \hat{v}_z \frac{\partial \hat{f}_e}{\partial \hat{z}} - \frac{\hat{q}_e}{\hat{m}_e} \frac{\partial \hat{\phi}}{\partial \hat{z}} \frac{\partial \hat{f}_e}{\partial \hat{v}_z} + \frac{\partial (\hat{v}_p \hat{f}_e)}{\partial \hat{x}} = 0 \qquad (5.9)$$

where $\hat{t} = \omega_{pO} t$, $\hat{x} = x \omega_{pO}/V$, $\hat{m} = m/m_O$, $\hat{\phi} = e\phi/m_O V^2$, $\hat{v} = v/V$, $\hat{q} = q/e$, $f(t, \mathbf{x}, \mathbf{v}) = \hat{f}(\hat{t}, \hat{\mathbf{x}}, \hat{\mathbf{v}})$ and V is the radius of the beam-arc in velocity space. Only the polarization drift, v_p, is retained in the electron drift velocity, v_d (i.e. the $\mathbf{E} \times \mathbf{B}$ drift drops out of the equation under the current assumptions):

$$\hat{v}_p = \frac{v_p}{V} = \frac{n_O \omega_{pe}^2}{n_e \omega_{ce}^2} \left\{ \frac{\partial}{\partial \hat{t}} + \hat{v}_p \frac{\partial}{\partial \hat{x}} + \hat{v}_z \frac{\partial}{\partial \hat{z}} \right\} \frac{\partial \hat{\phi}}{\partial \hat{x}} \qquad (5.10)$$

Although the assumptions leading to the neglect of the $\mathbf{E} \times \mathbf{B}$ drift may not be quite applicable to the real situation, they are applicable to one- and two- dimensional simulations (in the x-B plane) which are of interest to us. It should be emphasized

138

that the purpose here is to investigate the physics of the beam-arc plasma instability. In non-dimensionalized form, the Poisson Equation is also written as

$$\frac{\partial^2 \hat{\phi}}{\partial \hat{x}^2} = -\sum_j \hat{q}_j \hat{n}_j \int \hat{f}_j \, d\mathbf{v} \qquad (5.11)$$

Let us now note that system of Equations 5.7 to 5.11 imply a mass ratio scaling: the mass ratio $\hat{m}_e = m_e/m_O$ may be removed from the problem by rescaling in the z-direction as follows

$$z^* = \hat{z}\sqrt{\frac{m_e}{m_O}}$$

$$v_z^* = \hat{v}_z\sqrt{\frac{m_e}{m_O}} \qquad (5.12)$$

The existence of the mass ratio scaling in the full non-linear equations (within the assumption of no $\mathbf{E} \times \mathbf{B}$ drift) is very important. This will allow one- and two-dimensional simulations (in the x-B plane) to be performed with unrealistic mass ratios. Mc Bride et al. [1972] and Biasca [1992] have found similar mass ratio scalings for the modified two stream and beam-plasma instabilities, respectively.

5.2.2   Quasilinear Theory

Applying the standard quasilinear procedure [Davidson, 1972] to the nonlinear set of equations 5.2 to 5.6, we obtain quasilinear diffusion equations for the spatially averaged distribution functions $\bar{f}_O$, $\bar{f}_w$ and $\bar{f}_e$ and for the average electron kinetic energy in cross-field drifts which we denote $K_{\perp e}$,

$$\frac{\partial \bar{f}_O}{\partial t} = \frac{\partial}{\partial \mathbf{v}} \cdot \mathbf{D}_O \cdot \frac{\partial \bar{f}_O}{\partial \mathbf{v}} \ ,$$

$$\mathbf{D}_O = \frac{q_O^2}{m_O^2} \sum_{\mathbf{k}} \frac{\mathbf{k}\mathbf{k}|\phi(\mathbf{k})|^2 \gamma_{\mathbf{k}}}{(\omega_{r\mathbf{k}} - \mathbf{k} \cdot \mathbf{v})^2 + \gamma_{\mathbf{k}}^2} \ , \qquad (5.13)$$

$$\frac{\partial \bar{f}_w}{\partial t} = \frac{\partial}{\partial \mathbf{v}} \cdot \mathbf{D}_w \cdot \frac{\partial \bar{f}_w}{\partial \mathbf{v}} \ ,$$

$$\mathbf{D}_w = \frac{q_w^2}{m_w^2} \sum_{\mathbf{k}} \frac{\mathbf{k}\mathbf{k}|\phi(\mathbf{k})|^2 \gamma_{\mathbf{k}}}{(\omega_{r\mathbf{k}} - \mathbf{k} \cdot \mathbf{v})^2 + \gamma_{\mathbf{k}}^2} \ , \qquad (5.14)$$

139

$$\frac{\partial \bar{f}_e}{\partial t} = \frac{\partial}{\partial v_z} D_e \frac{\partial \bar{f}_e}{\partial v_z} \,,$$

$$D_e = \frac{q_e^2}{m_e^2} \sum_{\mathbf{k}} \frac{k_z^2 |\phi(\mathbf{k})|^2 \gamma_{\mathbf{k}}}{(\omega_{r\mathbf{k}} - k_z v_z)^2 + \gamma_{\mathbf{k}}^2} \,, \tag{5.15}$$

$$\frac{dK_{\perp e}}{dt} = \frac{\omega_{pe}^2}{\omega_{ce}^2} \frac{d}{dt} \sum_{\mathbf{k}} |\mathbf{E_k}|^2 / 8\pi \,, \tag{5.16}$$

where the solution of the dispersion relation is denoted $\omega_{\mathbf{k}} = \omega_{r\mathbf{k}} + i\gamma_{\mathbf{k}}$. Since our solutions to the linear dispersion relation, imply that waves are primarily perpendicular to $\mathbf{B}$ with the maximum growth rates for $|\mathbf{k}_\perp| \sim (m_O/m_e)^{1/2} k_z$ (see Figure 4-5), we may, therefore, approximate $\mathbf{kk}$ in Equations 5.13 and 5.14 by $\mathbf{k}_\perp \mathbf{k}_\perp$. It is thus clear from Equations 5.13 and 5.14 that the ion heating is primarily perpendicular to $\mathbf{B}$, while Equation 5.15 implies electron heating along $\mathbf{B}$. The energy change represented in Equation 5.16 must be thought of as a type of "reversible" heating since it merely represents the kinetic energy in $\mathbf{E} \times \mathbf{B}$ drifts associated with the wave motion. Although ion gyromotion is on a time scale much longer than the linear wave growth rate, for long times ($t \succeq 2\pi\omega_{cO}^{-1} \approx 2\pi\omega_{cw}^{-1}$), the first Equations of 5.13 and 5.14 must be replaced, respectively, by

$$\frac{\partial \bar{f}_O}{\partial t} + \omega_{cO}(\mathbf{v} \times \vec{z}) \cdot \frac{\partial \bar{f}_O}{\partial \mathbf{v}} = \frac{\partial}{\partial \mathbf{v}} \cdot \mathbf{D}_O \cdot \frac{\partial \bar{f}_O}{\partial \mathbf{v}} \,. \tag{5.17}$$

and

$$\frac{\partial \bar{f}_w}{\partial t} + \omega_{cw}(\mathbf{v} \times \vec{z}) \cdot \frac{\partial \bar{f}_w}{\partial \mathbf{v}} = \frac{\partial}{\partial \mathbf{v}} \cdot \mathbf{D}_w \cdot \frac{\partial \bar{f}_w}{\partial \mathbf{v}} \,. \tag{5.18}$$

In both equations, the effect of the ion gyroterm in conjunction with the diffusion operator $\mathbf{D}$ is to isotropize $\bar{f}_O$ and $\bar{f}_w$ in the plane perpendicular to $\mathbf{B}$ in a few ion gyrotimes. In our simulations we consider times $t < 2\pi\omega_{cO}^{-1} \approx 2\pi\omega_{cw}^{-1}$.

Quasilinear Energy Transfer Rates in the Hydrodynamic Limit

It is of interest to investigate the quasilinear equations in the hydrodynamic limit for a beam-arc with small arc. We have already developed the linear theory for this case in Section 4.3.1. As was done in this section, the beam-arc is now treated as a

cold beam with drift $\mathbf{V} = (\int \bar{f}_w v \, d\mathbf{v})/(\int \bar{f}_w d\mathbf{v})$, thus $\mathbf{v}$ in Equation 5.14 is replaced by $\mathbf{V}$ and for the (cold) stationary background ions and electrons $\mathbf{v}$ in Equation 5.13 and v_z in Equation 5.15 are taken as zero. Furthermore, for a density ratio $n_w/n_e = 0.15$, which will be used in the simulations, and a small parallel propagation angle $k_z/k \approx (m_e/m_O)^{1/2}$, which corresponds to the direction for maximum growth rate, we find, from Section 4.3.1, the maximum growth rate is $\gamma_k \approx (0.386)\Omega_{LHO}$ and occurs at $\omega_{rk} \approx (0.777)\Omega_{LHO}$ and $k_x \approx \Omega_{LHO}/V$ [where $\Omega_{LHO} \equiv \omega_{pO}/\xi$ and $\xi \equiv (1 + \omega_{pe}^2/\omega_{ce}^2)^{1/2}$]. Putting this in Equations 5.13, 5.14 and 5.15 (with $k_y = 0$, $\mathbf{V} \equiv V\vec{\mathbf{x}}$) and taking moments we obtain

$$\frac{dK_{xO}}{dt} = (1.02)\, \xi^2 \frac{d\mathcal{E}}{dt} \, , \tag{5.19}$$

$$\frac{dK_{xw}}{dt} = (3.89)\, \xi^2 \frac{d\mathcal{E}}{dt} \, , \tag{5.20}$$

$$\frac{dK_{ze}}{dt} = (1.02)\, \xi^2 \frac{d\mathcal{E}}{dt} \, , \tag{5.21}$$

$$\frac{dK_{\perp e}}{dt} = \frac{\omega_{pe}^2}{\omega_{ce}^2} \frac{d\mathcal{E}}{dt} \tag{5.22}$$

and from energy conservation

$$\frac{d}{dt}\left(\frac{1}{2}\, m_w \, n_w \, V^2\right) = -(6.93)\, \xi^2 \frac{d\mathcal{E}}{dt} \, , \tag{5.23}$$

where $\mathcal{E}(t)$ is the total electric field energy, $\mathcal{E}(t) = \sum_k |E_k|^2/8\pi$, and K_{ze}, K_{xO} and K_{xw} are the parallel electron and perpendicular ion kinetic energies in the rest frame of that species. These equations, 5.19 to 5.23, will be compared with simulation results later. Note that in the hydrodynamic limit the ion and electron heating, Equations 5.19, 5.20 and 5.21, is purely nonresonant heating (i.e., reversible).

Solution to the Quasilinear Equations for a Beam-Arc with Small Arc

Let us continue considering the quasilinear theory of the beam-arc plasma instability for a beam-arc with small arc, specifically, for the case where the beam-

arc is treated as a beam with drift V. We now, however, remove the hydrodynamic limit restriction and consider the general case. This will be of interest to interpret our 1-dimensional simulations. Furthermore, in the case of a small arc (i.e. a beam) a standard solution to the quasilinear equations by Formisiano et al. [1982] and Galeev [1967] can be adopted as follows. For unmagnetized ions, the non-dimensionalization of the quasilinear equations is carried out by defining $\tilde{t} = \Omega_{LHO} t$, $\tilde{k} = kV/\Omega_{LHO}$, $\tilde{\phi} = e\phi/m_O V^2$, $\tilde{n} = n/n_e$, $\tilde{v} = v/V$ and $\tilde{\omega} = \omega/\Omega_{LHO}$. Dropping the tildes for notational convenience, the quasilinear equation for the development of the space-averaged beam ion distribution function, $\bar{f}_w(t, \mathbf{v})$, is similar to that found in the previous sections:

$$\frac{\partial \bar{f}_w}{\partial t} = \sum_{\mathbf{k}} \mathbf{k} \cdot \frac{\partial}{\partial \mathbf{v}} |\phi_{\mathbf{k}}|^2 \frac{\gamma_{\mathbf{k}}}{(\omega_{r\mathbf{k}} - \mathbf{k} \cdot \mathbf{v})^2 + \gamma_{\mathbf{k}}^2} \mathbf{k} \cdot \frac{\partial \bar{f}_w}{\partial \mathbf{v}} \tag{5.24}$$

where $k^2|\phi_{\mathbf{k}}|^2/8\pi$ is the electric field energy of mode $\mathbf{k}$, and $\omega_{r\mathbf{k}}$ and $\gamma_{\mathbf{k}}$ are the real and imaginary parts of the solution to the dispersion relation. Here, an equivalent form of Equation 4.3 is used for the normalized dispersion relation:

$$1 - \frac{1}{\omega^2} - \frac{m_O}{m_e} \frac{n_e}{n_O} \sin^2(\phi_{k\parallel}) \frac{1}{\omega^2} + \frac{m_O}{m_w} \frac{1}{n_O} \frac{1}{k^2} \int_{-\infty}^{\infty} dv \frac{\mathbf{k} \cdot \partial \bar{f}_w/\partial \mathbf{v}}{\omega - \mathbf{k} \cdot \mathbf{v}} = 0 \tag{5.25}$$

By further assuming that initially the beam ions have a delta function distribution, and the relaxed distribution function is one-dimensional, i.e.

$$\bar{f}_w(t = 0, \mathbf{v}) = \delta(v_x - 1)\,\delta(v_z)\,\delta(v_y) \tag{5.26}$$

and

$$\bar{f}_w(t, \mathbf{v}) = \bar{f}_w(t, v_x)\,\delta(v_z)\,\delta(v_y) \tag{5.27}$$

the distribution function may be seen to satisfy the diffusion equation

$$\frac{\partial \bar{f}_w(t, v_x)}{\partial t} = \frac{\partial}{\partial v_x} D_w \frac{\partial}{\partial v_x} \bar{f}_w(t, v_x) \tag{5.28}$$

where

$$D_w = \pi \sum_{\mathbf{k}} k^2 |\phi_k|^2 \delta(\omega_{\mathbf{k}} - k_x \cdot v_x) \tag{5.29}$$

The solution to Equation 5.28 [Formisiano, 1982] for the relaxed distribution function is a one-dimensional plateau:

$$\bar{f}_w(v_x) = \begin{cases} 1/V & \text{for } 0 \leq v_x \leq V \\ 0 & \text{for } v_x < 0 \text{ and } v_x > V \end{cases} \tag{5.30}$$

Furthermore, by integrating over the relaxed distribution function, the amount of ion beam energy transferred to the background plasma and to the excited waves through the existed waves may be obtained,

$$\eta = 1 - \int_{-\infty}^{\infty} v_x^2 \bar{f}_w(v_x) dv_x = \frac{2}{3} \tag{5.31}$$

Before we give a physical interpretation of the above results let us note that an interesting fact can be deduced from Equations 5.13 through 5.15 relating the electron response. As indicated by the results of the linear theory, the fastest growing waves of the beam-arc plasma instability have $k_z/k \sim \sqrt{m_e/m_O}$. Thus, taking also $v_z/v_x \sim \sqrt{m_O/m_e}$, the electron response may be rewritten as

$$\frac{\partial \bar{f}_e}{\partial t} \sim \frac{\partial}{\partial v_x} \left[D'_e \frac{\partial \bar{f}_e}{\partial v_x} \right] \tag{5.32}$$

where

$$D'_e \sim \frac{q_e^2}{m_O^2} \sum_{\mathbf{k}} \frac{k_x^2 |\phi_{\mathbf{k}}|^2 \gamma_{\mathbf{k}}}{(\omega_{r\mathbf{k}} - k_x v_x)^2 + \gamma_{\mathbf{k}}^2} \tag{5.33}$$

Equations 5.32 and 5.33 indicate that the electrons respond to the waves not as a low mass species that is highly magnetized, but as an unmagnetized species with an effective mass near m_O. This occurs because the electrons are closely tied to the magnetic field lines which are nearly perpendicular to the wave vector.

With the viewpoint that the electrons act as if they were unmagnetized and have a high effective mass, comparable to that of the ions, it becomes apparent that the quasilinear development of the beam-arc plasma instability should be similar to that of the (ordinary) gentle bump-on-tail instabilities. As we have described in Section 5.1.2, these bump-on-tail instabilities saturate through a process of plateau formation, which

is in fact what Equation 5.30 implies as the saturation mode for the case of the beam-arc plasma instability. Therefore, in this case of an ion beam propagating across a magnetized ambient plasma, initially, we expect waves with phase velocities in the range of the positive gradient of the beam ion distribution function to grow by anti-Landau damping. Then we expect the beam distribution to start to fill in the unstable region between the bulk and the beam distribution, by quasilinear diffusion. As the plateau forms the background ambient ions and electrons should simultaneously begin to heat in bulk as they interact in a nonresonant manner with the waves. Furthermore, as the plateau forms, the unstable region of the wave spectrum should broaden. Eventually, because of the growing plateau region the ambient ions and electrons should also become resonant with the unstable waves. The final state, should be one in which the entire unstable region has been filled in by the total (i.e. beam + background) ion distribution function. This interpretation should hold as long as the quasilinear theory assumptions are not violated. In our simulations we will find a somewhat different picture since, in reality, for the parameters of the shuttle environment instability it is not possible to satisfy all the assumptions of the quasilinear theory.

5.3   Design of the Simulation

5.3.1   Rescaling of the Dispersion Relation for the Simulation

It is mandatory that we design the simulation of the beam-arc plasma instability such that the computational (CPU) time of the runs falls within reasonable ranges (e.g. four days in a DEC 5000 machine). We shall accomplished this task, without significantly sacrificing accuracy, by decreasing the mass ratio from the real value of $\frac{m_\Omega}{m_e} = 29337$ to 512 and by decreasing the $\frac{\omega_{pe}}{\omega_{ce}}$ ratio from the nominal PDP experiment value of 4.78 to 1. In Section 5.2.1, we have already shown that, for this instability, the results for realistic mass ratios can be deduced from simulations using reduced mass ratios. We now show that the mass ratio scaling law is, of course, also valid in the linear theory and, more importantly, we show another linear property: the solutions

of the linear dispersion relation of the beam-arc plasma instability, normalized by the natural frequency of oscillations (the lower hybrid frequency, see Section 4.3), are independent of the $\frac{m_\Omega}{m_e}$ and $\frac{\omega_{pe}}{\omega_{ce}}$ ratios.

The invariance property of the linear dispersion relation with respect to the $\frac{m_\Omega}{m_e}$ and $\frac{\omega_{pe}}{\omega_{ce}}$ ratios is very important. This is because the topology of the dispersion relation may critically affect the kind of nonlinear interaction that can take place. For instance, in the case of the ordinary bump-on-tail instability the strength of nonlinear interaction (mode coupling) depends directly on the dispersion in frequency. This is true for weak turbulence as well as strong turbulence effects which represent the competition between wave dispersion and nonlinear frequency shifts [Goldman, 1984]. In the case of weak turbulence, quasi-linear theory predicts that the wave growth is determined by the linear dispersion relation evaluated for the evolving ensemble-averaged (in practice space- or time-averaged) distribution function. Furthermore, the (quasi-) linear dispersion relation determines the width of the wave spectrum in wave number and frequency, and for the validity of quasi-linear theory and the other weak turbulence theories this width should be large enough to guarantee an autocorrelation time small compared to all other time scales (such as trapping time).

Dispertion Relation:

Let us now show the scaling properities of the linear dispersion relation mentioned above and start the design of the simulation. For this, it is useful to rewrite explicitly the dispersion relation of the beam-arc plasma instability (Equation 4.1) as follows:

$$1 + \frac{2\omega_{pe}^2}{k^2 v_{the}^2} e^{-b_e} \sum_{n=-\infty}^{\infty} I_n(b_e) \left[1 + \zeta_{0e} Z(\zeta_{ne})\right] \tag{5.34}$$

$$- \frac{\omega_{pO}^2}{k^2 v_{thO}^2} Z'(\zeta_O) - \frac{\omega_{pw}^2}{k^2 v_{thw}^2} \int_0^{2\pi} Z'(\zeta_w) f_{arc}(\theta) \frac{d\theta}{2\pi} = 0$$

where

$$\zeta_{ne} = \frac{\omega + n\,\omega_{ce}}{k_\parallel\, v_{the}}$$

$$\zeta_O = \frac{\omega}{k\, v_{thO}} \tag{5.35}$$

145

$$\zeta_w = \frac{\omega - k_\perp V \cos(\theta - \theta_{k_\perp})}{k\, v_{thw}}$$

In the susceptibility of the water ions (fourth term of Equation 5.34), which here is constructed from a superposition of Maxwellian beamlets, we have introduced a weighing function $f_{arc}(\theta)$ to take into account the θ dependence of the beam-arc distribution, where $f_{arc}(\theta)$ has been normalized such that $\int_0^{2\pi} f_{arc}(\theta)\frac{d\theta}{2\pi} = 1$. Therefore, the function $f_{arc}(\theta)$ can be extracted directly from Figures 3-2 and 3-4 for the various beam-arcs, as we have discussed in Section 4.6.3.

We continue our analysis by expanding $I_0(b_e)e^{-b_e}$ for $b_e \ll 1$, which is in the regime of interest, as follows:

$$I_0(b_e)e^{-b_e} = (1 - b_e - \dots)(1 + \frac{b_e^2}{4} + \cdots) \approx 1 \tag{5.36}$$

Furthermore, using this expansion and retaining only the $n = 0$ term in the summation of the electron term, the dispersion relation reduces to

$$1 + \frac{2\omega_{pe}^2}{k^2 v_{the}^2}\left[1 + I_0(b_e)e^{-b_e}\zeta_{0e}Z(\zeta_{0e})\right] \tag{5.37}$$

$$- \frac{\omega_{pO}^2}{k^2 v_{thO}^2}Z'(\zeta_O) - \frac{\omega_{pw}^2}{k^2 v_{thw}^2}\int_0^{2\pi} Z'(\zeta_w)f_{arc}(\theta)\frac{d\theta}{2\pi} = 0$$

Equation 5.37 can be rewritten in terms of nondimensional groupings:

$$1 + \frac{1}{\kappa^2}\frac{\omega_{pe}^2}{\omega_{ce}^2}\left[1 + I_0(b_e)e^{-b_e}\zeta_{0e}Z(\zeta_{0e})\right] \tag{5.38}$$

$$- \frac{1}{2\kappa^2}\frac{\omega_{pe}^2}{\omega_{ce}^2}\frac{T_e}{T_O}\frac{n_O}{n_e}Z'(\zeta_O) - \frac{1}{2\kappa^2}\frac{\omega_{pe}^2}{\omega_{ce}^2}\frac{T_e}{T_w}\frac{n_w}{n_e}\int_0^{2\pi} Z'(\zeta_w)f_{arc}(\theta)\frac{d\theta}{2\pi} = 0$$

with the parameters expressed as

$$\sin\phi_{k_\parallel} = k_\parallel / k$$

$$\kappa = \frac{k\, v_{the}}{\sqrt{2}\,\omega_{ce}}$$

$$b_e = \kappa^2 \cos^2(\phi_{k_\parallel})$$

$$\zeta_{0e} = \frac{1}{\sqrt{2}}\frac{\omega}{\omega_{pO}}\frac{\omega_{pe}}{\omega_{ce}}\frac{1}{\kappa\sin(\phi_{k_\parallel})}\sqrt{\frac{m_e n_O}{m_O n_e}} \tag{5.39}$$

$$\zeta_O = \frac{1}{\sqrt{2}}\frac{\omega}{\omega_{pO}}\frac{\omega_{pe}}{\omega_{ce}}\frac{1}{\kappa}\sqrt{\frac{T_e n_O}{T_O n_e}}$$

$$\zeta_w = \frac{1}{\sqrt{2}}\frac{\omega}{\omega_{pO}}\frac{\omega_{pe}}{\omega_{ce}}\frac{1}{\kappa}\sqrt{\frac{T_e n_O m_w}{T_w n_e m_O}} - \frac{V \cos(\theta - \theta_{k_\perp})\cos(\phi_{k_\parallel})}{v_{thw}}$$

Therefore, the solution of the dispersion relation ($\omega(\kappa)$) is seen to depend on the 9 nondimensional groupings $\phi_{k_\parallel}$, ω_{pe}/ω_{ce}, m_e/m_O, n_O/n_e, T_e/T_O, m_w/m_O, V/v_{thw}, T_w/T_e, and n_w/n_e. In what follows we provide an analysis of the dispersion relation in terms of these parameters.

Let us now note the first important scaling relating the mass ratio: the variable $\phi_{k_\parallel}$ appears to lowest order only in the grouping $\phi_{k_\parallel}\sqrt{m_O/m_e}$. Hence, for small values of $\phi_{k_\parallel}$ (the parameter range of interest since waves at large values of $\phi_{k_\parallel}$ are heavily damped by electron Landau damping) the results of the dispersion relation are the same for constant $\phi_{k_\parallel}\sqrt{m_O/m_e}$. The second very important scaling that applies is for $\kappa \ll 1$ and $\phi_{k_\parallel} \ll 1$, i.e. for wavelengths long compared to the electron Larmor radius, which is the regime of interest. In this case the electron susceptibility may be simplified as follows:

$$\frac{1}{\kappa^2}\frac{\omega_{pe}^2}{\omega_{ce}^2}\left[1 + I_0(b_e)e^{-b_e}\zeta_{0e}Z(\zeta_{0e})\right] = \frac{1}{\kappa^2}\frac{\omega_{pe}^2}{\omega_{ce}^2}\left[1 - I_0(b_e)e^{-b_e}\left(1 + \frac{1}{2}Z'(\zeta_{0e})\right)\right] \quad (5.40)$$

Furthermore, expanding $I_0(b_e)e^{-b_e}$ for $b_e \ll 1$,

$$I_0(b_e)e^{-b_e} = (1 - b_e - \dots)(1 + \frac{b_e^2}{4} + \cdots) \approx 1 - b_e \quad (5.41)$$

and substituting $b_e = \kappa^2$ gives

$$\frac{1}{\kappa^2}\frac{\omega_{pe}^2}{\omega_{ce}^2}\left[1 - I_0(b_e)e^{-b_e}\left(1 + \frac{1}{2}Z'(\zeta_{0e})\right)\right] \approx \frac{\omega_{pe}^2}{\omega_{ce}^2} - \frac{1}{2\kappa^2}Z'(\zeta_{0e}) \quad (5.42)$$

By using this expression and defining new variables

$$\bar{\phi}_{k_\parallel} = \phi_{k_\parallel}\sqrt{m_O/m_e} \quad (5.43)$$

$$\bar{\kappa} = \kappa\frac{\omega_{ce}}{\omega_{pe}}\sqrt{1 + (\omega_{pe}/\omega_{ce})^2}$$

$$\bar{\omega} = \frac{\omega}{\omega_{pO}}\sqrt{1 + (\omega_{pe}/\omega_{ce})^2}$$

Equation 5.38 may be rewritten as

147

$$1 - \frac{1}{2\bar{\kappa}^2} Z'(\zeta_{0e}) - \frac{1}{2\bar{\kappa}^2}\frac{T_e}{T_O}\frac{n_O}{n_e} Z'(\zeta_O) - \frac{1}{2\bar{\kappa}^2}\frac{T_e}{T_w}\frac{n_w}{n_e} \int_0^{2\pi} Z'(\zeta_w) f_{arc}(\theta)\frac{d\theta}{2\pi} = 0 \quad (5.44)$$

with the parameters expressed as

$$
\begin{aligned}
\zeta_{0e} &= \frac{1}{\sqrt{2}}\frac{\bar{\omega}}{\bar{\kappa}\bar{\phi}_{k_\parallel}}\sqrt{\frac{n_O}{n_e}} \\
\zeta_O &= \frac{1}{\sqrt{2}}\frac{\bar{\omega}}{\bar{\kappa}}\sqrt{\frac{T_e n_O}{T_O n_e}} \\
\zeta_w &= \frac{1}{\sqrt{2}}\frac{\bar{\omega}}{\bar{\kappa}}\sqrt{\frac{T_e n_O m_w}{T_w n_e m_O}} - \frac{V\cos(\theta - \theta_{k_\perp})}{v_{thw}}
\end{aligned}
\quad (5.45)
$$

Therefore, we can see that the space of nine parameters for the dispersion relation has been reduced to seven. The parameters may be further reduced by assuming overall neutrality of the system, i.e. $(n_O + n_w)/n_e = 1$, which may be used to remove n_w from Equation 5.44 and reduce the number of parameters to six.

In summary, we have found that given the values of the six non-dimensional parameters $\bar{\phi}_{k_\parallel}$, n_O/n_e, T_e/T_O, m_w/m_O, V/v_{thw}, and T_w/T_e the corresponding solution $\bar{\omega}(\bar{\kappa})$ of the dispersion relation is independent of the values of m_O/m_e and ω_{pe}/ω_{ce}. Now, since T_e/T_O and T_w/T_e are part of the set of non-dimensional parameters the parameter V/v_{thw} can be replaced by V/v_{thO}. Therefore, given the values of the six non-dimensional parameters $\bar{\phi}_{k_\parallel}$, n_O/n_e, T_e/T_O, m_w/m_O, V/v_{thO}, and T_w/T_e the dispersion $\bar{\omega}(\bar{\kappa})$ is independent of the values of m_O/m_e and ω_{pe}/ω_{ce}. Furthermore, for our purposes it is convenient to express the dispersion relation $\bar{\omega}(\bar{\kappa})$ in terms of the lower hybrid frequency

$$\Omega_{LH} \equiv \frac{\omega_{pO}}{\sqrt{1 + \left(\frac{\omega_{pe}}{\omega_{ce}}\right)^2}} \quad (5.46)$$

for which case, given the values of the six non-dimensional parameters, the dispersion relation $\bar{\omega} = \frac{\omega}{\Omega_{LH}}$ versus $\frac{kV}{\Omega_{LH}}$ is independent of the values of m_O/m_e and ω_{pe}/ω_{ce}. Figure 5-1 shows the dispersion relation for the instability corresponding to the $X_p = 5$ beam-arc for two propagation directions $\theta_{k_\perp} = 45^o$ and $\theta_{k_\perp} = 135^o$. Two cases are considered for each propagation direction: (1) $m_O/m_e = 29,377.77$ and $\omega_{pe}/\omega_{ce} = $

4.78 (dashed lines) corresponding to the real values for the ionospheric plasma near the shuttle and (2) $m_O/m_e = 512$ and $\omega_{pe}/\omega_{ce} = 1$ which will be the values used in the simulations. In both cases the values of the six non-dimensional parameters are: $\bar{\phi}_{k_\parallel} = 1$, $n_O/n_e = 0.85$, $T_e/T_O = 2$, $m_w/m_O = 1.125$, $V/v_{thw} = 7.316$, and $T_w/T_e = 0.001$. As predicted by the scalings, the results in Figure 5-1 appear identical for both cases (even though these results were obtained by using the full dispersion relation (Equation 4.2) and not the reduced form, Equation 5.37 which was used to show the scalings). These values for the six non-dimensional parameters are the real values for the plasma near the shuttle and will be the values used in the simulations (the T_w/T_e value is lower than in the real case but has negligible effects in the results). Furthermore, in the simulations we will use $\bar{\phi}_{k_\parallel} = 1$, which corresponds to $\phi_{k_\parallel} = \sqrt{\frac{m_e}{m_O}} \approx 0.3343^o$ (degrees) for the real ionospheric mass ratio, since this is close to the value for largest growth rates (for beam-arcs of large arcs) as shown in Figure 4-5.

In what follows we shall denote the simulation run of the instability with the $X_p = 5$ beam-arc and for the propagation direction $\theta_{k_\perp} = 45^o$, with the simulation parameters specified above, as the X5a45 run. Clearly, the (initial) linear dispersion relation for this run is that shown in Figure 5-1a. Similarly, we shall denote the simulation run corresponding to the dispersion relation shown in Figure 5-1b, with the simulation parameters specified above, as the X5a135 run. For other runs corresponding to other beam-arcs and propagation directions we shall also use this system of notation (e.g. X5a90 run, X1a20 run, etc.). The time units in the runs will be normalized by the lower hybrid period $\tau_{LH} \equiv \frac{2\pi}{\Omega_{LH}}$.

5.3.2 The PIC Code

The PIC code used in the simulation of the beam-arc plasma instability is the well known code ES1 [Birdsall and Langdon, 1985]. This is an explicit PIC code, 1 dimensional in space and 3 dimensional in velocity, which uses a Poisson solver to determine the fields. It is therefore useful for modeling electrostatic plasma processes under the influence of a constant magnetic field. ES1 has periodic boundary conditions and

149

can only be loaded with (shifted) Maxwellian and cold distribution functions. We have thus modified this PIC-code so as to make it possible to load beam-arc distribution functions with a quiet start algorithm (see Chapter 16 of Birdsall and Langdon, 1985). Furthermore, we have increased significantly the diagnostics capabilities of the PIC code, especially in connection with a 2 dimensional (i.e. space and time) Fourier analyzer of the electric field, as we shall discuss later.

5.3.3 System Length

In Section 5.1.2, we have made a critical examination of bump-on-tail instability simulations which has shown that even up to this day, simulation parameters are mostly inappropriately chosen for the purpose of testing quasi-linear theory. Rather intense beams are used in order to escape the enhanced noise level due to the small number of macroparticles and in order to shorten computation times. The system L is generally much too small. The number of unstable modes is then restricted, often to unity, by a trivial geometric effect,

$$k = \frac{2\pi m}{L} \qquad m = 0, 1, 2, \ldots \qquad (5.47)$$

in the case of periodic boundary conditions. The assumptions of quasi-linear theory are certainly not satisfied in this case, and it remains an open question if there are additional nonlinear effects that lead to a nearly coherent behavior with a single dominant mode and particle trapping.

In Sections 5.1.2 and 5.2.2 we have also shown that in the nonlinear regime of the beam-arc plasma instability, resonant diffusion and other quasilinear effects are expected to be important. Furthermore, we have concluded that in order to include all these effects in the simulation we would have to consider extremely long systems, in which the effect due to the discretization of the modes, Equation 5.47, can be shown to be negligible. In what follows we design the system length of the simulation.

The system length is determined by the requirement that the effects of artificial discretization (Equation 5.47) by periodic boundary conditions be minimized. The system length should be large enough to allow for many modes in the initially unstable

wave number range and for a shift of this range by the evolution of the system. The spacing in phase velocity between neighboring modes should be smaller than the resonance width given by either the growth rate or turbulent and collisional resonance broadening [Dum, 1990a]. Using $\omega \approx \Omega_{LH}$ and Equation 5.47 this condition is

$$\frac{\Delta v_{res}}{\Delta v_{ph}} \approx \frac{\gamma}{\Omega_{LH}} \frac{kL}{2\pi} \gg 1 \qquad (5.48)$$

for the ratio between linear resonance width γ/k and the spacing in phase velocity. Thus this ratio must be greater than 1. For each of our simulation runs the minimum system length was determined on this basis. For instance, for the X5a45 run the solution of the linear dispersion relation shown in Figure 5-1a, indicates that 55 modes between mode numbers $m = 5$-60 should be unstable initially (i.e. L is approximately 1114 debye lengths). The linear resonance width γ/k for the maximally growing mode $m = 40$, is 0.1236 (in units of the drift velocity V), and the next modes are spaced $0.014V$ apart in resonance velocity. Although this situation is far better than in the somewhat analogous bump-on-tail instability studies using shorter systems, it may still seem marginal for a continuous diffusion process. However, since the resonance shape is, in general, a slowly decreasing Lorentzian [Dum, 1990a], there is actually a considerable overlap of wave-particle resonances, even without additional turbulent or collisional resonance broadening. Actually, reducing the system length L to one half, which halves the number of modes and doubles their spacing in phase velocity, leads to no noticeable differences in the evolution of the system.

5.3.4 Time Step and Grid Cell Size

In PIC codes the electric fields are determined on a grid [Birdsall and Langdon, 1985] and accuracy requires that grid spacing be small compared to the shortest wavelengths of interest, $k\Delta x \ll 1$. Moreover, modes generated by grid aliasing should be damped, which leads to the usual condition $\Delta x \leq 1$ to $2\,\lambda_{De}$. For the computational parameters specified in Section 5.3.3 and the minimum system length determined in the previous subsection the latter condition leads to a design of the runs with 2048 grid points (a power of 2 is required for the fast Fourier transforms). Increasing the number of grid

151

points by itself leads only to an insignificant increase in computation time, but smaller grid spacing should also be accompanied by a smaller time step. This is because the Courant condition for the beam-arc $V\Delta t < \Delta x$, which for particle simulations is only an accuracy condition, also has to be satisfied. However, in our case the most stringent condition for choosing the time step is that it should be small compared to the electron gyroperiod (of course, even more stringent than the condition that the time step should be small compared to the wave period $\Omega_{LH}\Delta t \ll 1$). For all our simulation runs, it leads to our choice of $\omega_{pe}\Delta t = 0.2$.

5.3.5 Number of Macroparticles

The number of simulated macroparticles should be as large as possible in order to reduce computational noise and have a good statistical representation of the particle distributions in the important velocity regions. For this, the Maxwellian distributions of the background ionospheric ions and electrons and the beam-arc distributions of the water ions are loaded using inverse distribution functions, giving ordered velocities ("quiet start"). The quiet start algorithms that we use for loading the particles are described in Chapter 16 of Birdsall and Langdon, 1985. We use 131072 particles (64/cell) to represent the background ions and an equal number of particles (64/cell) to represent the electrons. We should note that initially in the simulation of the Maxwellian distributions, with our particle loading procedure, velocities in excess of say 5 thermal velocities have a poor statistical representation; however, with negligible effects on the results. In comparison to the n_w/n_e density ratio, we represent the beam-arc by a much larger number of particles. We use 262144 particles (128/cell) to represent the beam-arc ions. These particle numbers are chosen such that we can have exponential growth in wave energy over 1-2 orders of magnitude (note that there is always a rapid initial change of electric field energy while self-consistent correlations between particles are established.) Similar to real experiments, particle distribution functions in the simulation are determined by collecting particles in bins. We use 66 equally spaced bins, which are adjusted instantaneously to cover the entire particle velocity range of each species. Statistical fluctuations are reduced by (linear)

interpolation when assigning particles to velocity bins. It is interesting to note here that some restrictions of quasi-linear theory are actually eased in a modified theory which allows for averaging by limited velocity resolution in observations or simulation experiments [Klimas and Fitzenreiter, 1988]. This is because quasi-linear theory predicts that the wave growth is determined by the linear dispersion relation evaluated for the ensemble-averaged (in practice space- or time-averaged) distribution function.

5.3.6 Verification of the Simulation Accuracy

The independence of simulation results from computational parameters within a reasonable range must be verified. We have done a complete analysis for this purpose and some of the results of the verification runs are shown in Appendix B. For the particle simulations, momentum conservation follows from symmetries in the chosen algorithm [Birdsall and Langdon, 1985], but energy conservation needs to be monitored. With our conservative design, errors connected with energy conservation turn out to be truly negligible, however (typically at most 0.02% of the total energy or about 1% of the electric field energy). As pointed out by Dum [1990a], the accurate design of the beam-plasma type simulations is surprisingly difficult, and many compromises have to be made. The present models are adequate for the PDP data interpretation intended in this thesis. They can be improved, a posteriori, for the investigation of special effects, but this usually requires larger computational resources.

5.4 Results of the Simulation

Figure 5-2 shows a schematic diagram of the beam-arc water ion and background oxygen ion distributions in velocity space (the electron distribution is not shown). Superimposed in this figure are wavevectors in the propagation directions considered in this thesis ($\theta_{k_\perp} = 0^o, 20^o, 45^o, 60^o, 90^o, 135^o$). These propagation directions were chosen for our study since they are representative of the various instability processes that take place in the azimuthal directions nearly perpendicular to the magnetic field (i.e. $\bar{\phi}_{k_\parallel} = 1$). Note that the results for $180^o \leq \theta_{k_\perp} \leq 360^o$ will not be shown since they are exactly the same as those for the opposite (i.e. $\theta_{k_\perp} - 180^o$) propagation

directions except that the former results show phase velocities of the opposite sign and thus actually correspond to the same waves as the latter results.

Figures 5-3 and 5-5 show the initial beam-arc and background ion distributions (solid lines) of the $X_p = 1$ and $X_p = 5$ beam-arc plasma instabilities, respectively, for various propagation directions $\theta_{k_\perp}$ in the plane nearly perpendicular to the magnetic field (in all these cases the parallel propagation angle $\bar{\phi}_{k_\parallel} = 1$, as mentioned above, which corresponds to the fastest growing modes for all $\theta_{k_\perp}$'s). These are the initial ion distributions used in the 1-dimensional simulations and thus represent the reduced ion distributions, that is, the ion distributions of velocity components along the propagation directions [Rivas and Hastings, 1992]. Also shown in these figures are the beam-arc distributions for the late stages of the instabilities or quasi-steady states (dashed lines). We do not show the electron distributions or "final" background ion distributions; the latter are similar to the initial ones shown in the figures. Furthermore, we have included, in Figures 5-3 and 5-5 plots for the beam-plasma and ring-plasma instabilities which for the density ratio considered here can be though of special cases of the beam-arc plasma instability.

We have found that because the beam-arc plasma instability is strong (with large growth rates) the beam-arc distributions get broadened or heated very quickly by the waves (the heating process will be discussed in detail in the next subsections). As a result of the heating, shortly after the start of the runs and significantly before the saturation stages the broadened (or heated) beam-arc distributions in the runs for the various propagation directions start resembling each other (except with those of the X1a90 and X1a135 runs which correspond to very weak instabilities and thus are of secondary importance). Furthermore, we have found that because of this resemblance in the early stage distributions, the results of the various runs for the different propagation directions are qualitatively the same. The differences therefore lie mostly in the magnitudes of the various effects of physical processes that occur in the nonlinear regime, as is evident from Figures 5-4 and 5-6 which show the field energy time histories. These quantitative differences will be very important in Chapter 6 for the interpretation of the PDP wave data; however, since the results of the different runs

154

are qualitatively the same, in the remainder of this section we shall only study in detail one of the most representative runs, namely, the X5a45 run. We have chosen this run because it illustrates clearly various important nonlinear effects that need to be considered in our study. As can be noted from Figure 5-4b, the X5a45 run corresponds to a strong beam-arc plasma instability. Later, in Appendix A, we shall consider the X5a135 run which corresponds to a weak beam-arc plasma instability, as shown in Figure 5-6b. We shall see that the X5a45 and X5a135 runs are indeed qualitatively the same. In the rest of this section, we shall thus restrict our attention to the X5a45 run.

5.4.1 Initial Reactive Phase of the Instability

Figure 5-8a shows the time history of the electric field energy for the X5a45 run. It is seen that the electric field energy has an exponential growth phase over about 2 orders of magnitude. The average growth rate inferred from this figure is 0.21 (in units of Ω_{LH}), comparable with the peak growth rate 0.22 in Figure 5-1a which shows the dispersion relation that initially corresponds to this run. Initially, the X5a45 run instability is nonresonant: the phase velocities of the linearly most unstable modes are below the beam speed, where the values of the beam-arc distribution function are low. This situation is shown schematically in Figure 4-3. Therefore, the wave modes should be destabilized by the reactive instability (i.e. from the bunching of the different species). As the wave amplitudes grow the space-averaged distribution is broadened by the sloshing motion and starts to fill in the region of the unstable phase velocities. This is seen in the beam-arc distribution for $\bar{t} = 5.5$ in Figure 5-9a (we define $\bar{t} \equiv t\Omega_{LH}$ hereafter). However, at these early times the instability is still reactive, dominated by the bunching mechanism. In Figure 5-10, we can see that at $\bar{t} = 5.5$ bunching by the fastest growing modes in the simulation (modes near 40) is apparent in the velocity-position diagrams. Actually, strong bunching of the beam-arc distribution function are apparent by time $\bar{t} = 3$ (not shown). In contrast to previous simulations (e.g. simulations of bump-on-tail instabilities), for our long system, these structures are only seen when a section of the system is magnified.

In Figure 5-10, only 1/8 of the total system length is shown, comprising about 5 wavelengths (only 1% of the total number of macroparticles are shown, they were randomly selected). The closely periodic appearance of the velocity-position plots in Figure 5-10b indicate that the primary modes in the simulation system are the modes near 40, as expected from Figure 5-1a. The deviation from periodicity in Figure 5-10b indicate that various modes do growth to significant amplitudes.

Figure 5-10b also shows the velocity-position plots of the background ions at early times. Strong modulation of the background ions by the wave fields is apparent (e.g.,perturbations in their density of the order of 25%); some background ions are accelerated to high velocities by the large wave fields. In comparing the phase space plot of the beam-arc ions with that of the background ions in Figures 5-10b it is clear that both the beam-arc and background ions are bunched by the growing waves. The beam-arc ions are bunched in regions were the wave potential is negative, being bounded by the points were the wave potential is zero and the wave fields have their maximum amplitudes. In contrast the background ions are bunched out of phase with the beam-arc ions in the regions of positive potential with accompanying maxima in the total (beam-arc + background) ion density. No significant density perturbations of the background electron distribution functions are seen in the simulations. The increase in the velocity perturbations of the background ions with time as the wave electric fields increase, together with the positions of (1) the positive and negative perturbations in the background ions' velocity and the positions (2) the density enhancements and depressions and (3) potential maxima and minima, are consistent with these perturbations in the background ions being the forced motions of the background plasma which set up and maintain the electric fields of the waves.

5.4.2 Saturation by Trapping

Going back to Figure 5-8a, for the X5a45 run it is seen that the electric field energy has an exponential growth phase of about 2 orders of magnitude which is terminated with one (small) oscillation in the electric field energy. This oscillation suggests that the instability saturates by the trapping mechanism, and as we show in this section this is

156

indeed the case. For the X5a45 run, the time span of $\bar{t} = 4\text{-}22$, which corresponds to very large beam-arc density modulations, can be considered as the strongly nonlinear transition period between reactive and kinetic instability in which quasi-linear theory and other perturbation theories are likely to be inapplicable. The instability is well into the strong turbulence regime by time $\bar{t} = 5.8$, i.e., $\mathcal{E} / n k T_e \sim 0.06 > (k \lambda_{DE})^2 \sim 0.05$. The density perturbation in the beam-arc at this stage is of the order of the unperturbed beam-arc density. Snapshots of the x-v phase space, Figure 5-10b, show that from $\bar{t} = 6$ on there are the usual vortices indicating beam trapping, and clearly the breakdown of the usual perturbation expansions. We should note, again, that in contrast to simulations of other instabilities, for our long system, these structures are only seen when a section of the system is magnified. In Figure 5-10, only 1/8 of the total system is shown, comprising about 5 wavelengths. In our simulations, the electric field still consists of many wave modes. It is perhaps more useful to describe the electric field, or its potential, as a carrier wave with strong (and random) amplitude modulation, somewhat similar to a television signal.

Therefore, the simulation results clearly indicate that saturation of the instability is due to particle trapping in the potential troughs of the waves. In order to understand how trapping stops the growth of the wave amplitudes let us first reconsider the physical explanation of the reactive beam-plasma instability (see Section 4.3.1) as follows. The natural frequency of oscillations in the beam fluid is Ω_{LHw} and the natural frequency of oscillations in the background fluid is $\Omega_{LHO} \simeq \sqrt{n_O/n_w}\Omega_{LHw}$. Because of the Doppler shift of the Ω_{LHw} oscillations in the moving beam fluid, these two frequencies can coincide in the stationary frame if kV has the proper value. We have referred to this particular situation where the Doppler-shifted natural frequency of beam fluid oscillations coincides with the natural frequency of background fluid oscillations as synchronism. Moreover, the beam ion oscillations can be shown to have negative energy. That is to say that the total kinetic energy of the beam ions is less when the oscillation is present than when it is absent. In the undisturbed beam, the kinetic energy per unit volume is $\frac{1}{2}mn_ov_o^2$. When there is an oscillation the kinetic energy is $\frac{1}{2}m(n_o + n_1)(v_o + v_1)^2$. When this is averaged over space, it is less than

$\frac{1}{2}mn_ov_o^2$ because of the phase relation between n_1 and v_1 required by the continuity equation. Consequently, the beam ion oscillations have negative energy, and the background ion oscillations have positive energy. For modes in synchronism both waves can grow together while keeping the total energy of the system constant. However, when the amplitudes of the growing waves reach the level where the beam particles get trapped in the potential troughs of the waves, the "average" speed (of the bulk) of the beam particles changes drastically from V to ω/k (to the phase velocity of the fastest growing modes). Correspondingly, the Doppler shift of beam oscillations changes and disrupts synchronism, the coupling between the positive and negative energy waves that produces wave growth. Thus growth of the fastest growing modes stops at this point in time which corresponds to the saturation of the instability.

Let us now estimate the effects of trapping on the beam-arc plasma instability. Trapping theory is well known in plasma physics and is described in detail in Drummont et al. [1970]. Here we shall omit the details of this theory and simply use the theoretical results given in Drummont et al. [1970] to interpret the simulations. In the stationary (earth's) frame of reference, the wave potential energy required to begin trapping the beam-arc and background ions is, respectively,

$$e\phi_w = \frac{1}{4}m_w\left[V - (\omega/k)\right]^2 , \tag{5.49}$$

$$e\phi_O = \frac{1}{4}m_O\left[(\omega/k)\right]^2 , \tag{5.50}$$

where $V - \omega/k$ and ω/k define the trapping widths for beam-arc and background ions at saturation, respectively. Since the electrons are tied to the magnetic field lines and thus can move freely only along **B**, the wave potential energy necessary to begin trapping them is given in terms of their phase velocity parallel to **B** : $e\phi_e = \frac{1}{4}m_e(\omega/k_z)^2 = \frac{1}{4}\bar{m}_e(\omega/k)^2$ where the effective electron mass $\bar{m}_e \sim m_O$, as we have noted in Section 5.2.2. Which species begins to trap first depends on

$$\frac{\phi_w}{\phi_e} = \frac{m_w}{\bar{m}_e}\frac{(V - \omega/k)^2}{(\omega/k)^2} \tag{5.51}$$

$$\frac{\phi_O}{\phi_e} = \frac{m_O}{\bar{m}_e}\frac{(\omega/k)^2}{(\omega/k)^2} \tag{5.52}$$

158

If $\phi_w/\phi_e > 1$ and $\phi_O/\phi_e > 1$, the electrons begin to trap first while if $\phi_w/\phi_e < 1$ and $\phi_O/\phi_e \geq 1$, the beam-arc ions begin to trap first. Similarly, for $\phi_w/\phi_e \geq 1$ and $\phi_O/\phi_e < 1$, the background ions begin to trap first. Numerical solutions of the linear dispersion relation show that $\phi_w/\phi_e < 1$ and $\phi_O/\phi_e \approx 1$, for the values of $m_O/\bar{m}_e$ of most interest [e.g., for the parameters of Figure 5-1 and the parallel propagation angle which corresponds to the fastest growing wave]. Thus, based on Equations 5.51 and 5.52 beam-arc ions will always be trapped first, and we expect them to transfer a substantial amount of their energy to the waves as shown in the simulations (Figure 5-8b).

An estimate of the ratio of electrostatic wave energy to plasma thermal energy at saturation can easily be obtained from Equation 5.49. The result is

$$\frac{\mathcal{E}}{n K T_e} = \frac{k^2 \lambda_{De}^2}{16} \frac{(V - \omega/k)^4}{(K T_e/m_w)^2} , \qquad (5.53)$$

where $\mathcal{E}$ is the electrostatic energy density, T_e is the electron temperature, and ω and k correspond to the fastest growing mode. In particular, using the results from the linear theory for the fastest growing mode, which occurs near $\bar{\phi}_{k_{\parallel}} = 1$, we can replace k and ω/k in Equation 5.53 with $k = \sqrt{3}\omega_{pi}/(1 + \omega_{pe}^2/\Omega_e^2)^{1/2} V$ and $0.7V$, respectively, corresponding to the fastest growing mode at $\bar{\phi}_{k_{\parallel}} = 1$, we obtain

$$\mathcal{E} / n K T_e \sim 0.1(1 + \omega_{pe}^2 / \Omega_e^2)^{-1} . \qquad (5.54)$$

This agrees quite well with the computer simulation results as shown in Figure 5-8a.

We reiterate that the numerical solutions to the linear dispersion relation, Figure 4-5, indicate that the most important waves (i.e. fastest growing) have $\bar{\phi}_{k_{\parallel}} \sim 1$. We should point out that as predicted by the energy transfer rates Equations 5.21 and 5.22, which apply under the quasilinear theory assumptions, we have observed in the simulations that the cross-field electron heating is much smaller than the parallel electron heating. Further comparison with the quasilinear rate equations, Equations 5.19 to 5.23, shows that the initial nonlinear development of the instability can be described by quasilinear theory with the energy being partitioned to the particles and field at about the rate indicated by these equations. During the time interval

$\bar{t} = 1.7$ to 4 the observed change in parallel electron thermal energy and perpendicular background ion thermal energy relative to the change in electrostatic field energy was 2.0 and 2.3 (see Figure 5-8), respectively, compared with the theoretical values 2.04 and 2.04, respectively, predicted by Equations 5.21 and 5.19. However, for later times the parallel electron and perpendicular background ion thermal energies increase much faster than the nonlinear quasilinear equations indicate, leading to final thermal energies over an order of magnitude larger than the final electric field energy (see Figure 5-8). The inapplicability of the nonresonant quasilinear arguments to the final heating phase is expected due to the presence of strongly nonlinear processes which lead to irreversible heating, e.g., particle trapping. Lastly, let us also note that the total wave energy partition in the case of the beam-arc plasma instability is very different from that in the case of the bump-on-tail instability. In the case of the latter, the Langmuir wave energy is partitioned equally between the electric field energy and the kinetic energy in forced motions of the background plasma which supports the wave [e.g., Melrose, 1985, or any standard plasma physics text]. In contrast, in the case of the beam-arc plasma instability the change of the electric field energy, relative to the change in the electron thermal energy, is very small as can be seen in Figure 5-8. The effect of the magnetic field should obviously play a major role in accounting for this difference.

5.4.3   Transition from Reactive to Kinetic Instability

Further evidence for the identification of the reactive instability as a bunching instability comes from the time history of the wave energy (dominated by the modes near 40) in Figure 5-8a; the exponential growth phase of the electric field energy is terminated with one oscillation in the electric field energy, the beam-arc kinetic energy, and the drift and thermal energies (Figure 5-8). Similar oscillations in wave energy (usually several more oscillations before they are damped out) have been observed for other bunching instabilities [e.g., Sprangle and Smith, 1980; Winglee, 1985]. The increases and decreases in wave amplitude may be understood as follows: the wave amplitude increases when the dominant wave modes (near mode 40) collect a bunch

of beam-arc ions in v and drive the bunch toward lower v as seen at time $\bar{t} = 7.3$ in Figure 5-10c, thereby converting beam kinetic energy into wave energy. Decreases in wave amplitude occur when the wave fields drive the beam-arc ions toward higher v. Multiple oscillations in field energy (not observed in the current run but readily seen in runs using shorter systems or in simulations of other instabilities, e.g., Cairns and Nishikawa, 1989) would then correspond to the beam-arc ion vortices undergoing multiple rotations toward low v and then high v. These rotation(s) cause smearing out of the vortices and associated bunches (in both space and v) with accompanying reductions in the amplitude of, and eventually the presence of, the oscillations in the wave energy. The period of the oscillation in the current run (see Figure 5-8) is consistent with the trapping or "bounce" time τ_B [Mc Bride et al. 1972]. For the beam-arc ions, the trapping time is

$$\tau_{B_w} = (m_w/ek^2\phi_w)^{1/2} \sim 3\tau_{LH}, \tag{5.55}$$

As discussed above the bouncing of the beam-arc ions causes stabilization of the exponential wave growth. Eventually, after a time of the order of τ_{B_w}, all species acquire their (almost) final temperatures. At late times the thermal energies change at a constant linear rate, rather than exponential (see Figure 5-8d).

An important observation to make is that some time after saturation, approximately after several bounce times at ($\bar{t} \sim 20$), a transition from reactive to kinetic instability occurs. This transition results from (1) the broadening of the space-averaged beam-arc distribution function (Figure 5-9a) by the sloshing motion of the particles in the vortices and (2) the randomization of the vortices, which increase significantly the number of beam-arc ions in the resonant region. Thus with a large number of resonant ions the instability becomes kinetic, dominated by wave-beam interaction. Further evidence of the transition from reactive to kinetic instability comes from the fact that the oscillations in the wave field energy are damped out (with an appearance somewhat analogous to a damped oscillator), as discussed above. The damping of the oscillations is caused by the (resonant) diffusion of and mixing in the bunches of beam-arc ions that support these oscillations. Therefore, the vortex structures

161

are randomized (depending, of course, on how closely one looks) by the end of the nonlinear phase of strong density modulations (see Figure 5-10d). This also explains why, unlike in the current run where we see only one oscillation, several such bounces were observed in simulations using shorter systems [i.e. using a smaller number of (resonant) modes]. The fact that we have many more wave modes than in the latter simulations (and in most previous simulations of other instabilities, e.g. Cairns and Nishikawa, 1989) certainly plays the decisive role in this randomization. We reach a stage in which quasi-linear theory and other turbulence theories can again be expected to apply, especially when it is noted that these theories strictly apply not to a single run but to an ensemble average over many realizations. This averaging procedure removes many nonlinear terms.

5.4.4 The Wave Modes Spectra and Time Histories

Competition Between Modes in the Large k-scale

As we have noted in the previous section the very initial growth stage of the instability (i.e. at low amplitudes) can be described by quasi-linear theory. For this stage quasilinear theory predicts that the dispersion relation of the modes should very roughly be the initial dispersion relation shown in Figure 5-1a. Figure 5-12a shows the mode number spectrum for a time period immediately after this stage. In this figure, we see that the wave energy is concentrated near the range of linearly fastest growing modes; however, in contrast to the quasilinear predictions we observe very low energy levels for modes outside this range (especially at low mode numbers, $m < 31$). It thus seems that, because of their greater bunching ability, the linearly fastest growing modes absorb some of the free energy that was initially available for the excitation of the other (i.e. linearly slower growing) modes. We shall call this effect competition between modes in the large k scale.

This effect in which the linearly fastest growing modes absorb most of the free energy of the instability and inhibit the low wavenumber modes from growing is partly due to the e-folding of the growth of wave mode amplitudes. Initially wave mode amplitudes should grow exponentially and thus small differences in the modes growth

162

rates should lead to large differences in the energy levels that modes eventually reach in a time of the order of the saturation time. However, it should also be noted in the time history plots of the low wavenumber modes, Figure 5-11a, that the absorption of the free energy by the linearly fastest growing modes is so dominant that the low wavenumber modes do not even have a chance to start growing at their growth rates predicted by the linear theory. The low wavenumber modes do not start to grow almost until the time the linearly fastest growing modes saturate. Only then the low wavenumber modes start to grow, with growth rates larger than those predicted by the linear theory, but saturate at much lower energy levels than those reached by the linearly fastest growing modes (see figure 5-11a). Therefore, since the low wavenumber modes start to grow when the linearly fastest growing modes are already in the strong turbulence regime, the faster growth rates (faster than that those predicted by the linear theory) of the low wavenumber modes should be attributed to nonlinear effects.

The Stochastic Nature of Turbulence

The spectrum plots for the current run, Figure 5-12, show that the mode number spectrum has a rather erratic fine structure (i.e. discontinuous with respect to mode number and time). Similar erratic spectrum structures had already been noticed in dealing with other instabilities in particle simulations [Biskamp and Welter, 1972; Adam et al., 1980] and by Theilhaber et.al. [1987], using a Vlasov code. One is drastically reminded of the stochastic nature of turbulence theories when many wave modes are present; in our simulation the system length is 40 times the wavelength of the linearly fastest growing mode as opposed to 3 or 4 times as in most other instability simulations where stochastic, erratic, mode spectra were not observed. The spectral estimate obtained as usual from a Fourier transform of a sample of the electric field is itself a stochastic variable. The energy in individual wave modes undergoes fluctuations at the 100% level. Individual wave modes show then a rather erratic time dependence, unless there is some averaging. With many closely spaced wave modes present, we can afford to use spectral windowing over a few neighboring modes. The process would closely correspond to measurements if we had electronic

filters of finite bandwidth in wave number rather than frequency. For instance, we could use a triangular window function over typically 4 modes in order to reduce stochastic fluctuations, which in the case of computer simulations depend on the initial loading of particles in phase space. In this case, it would then be necessary to make sure that the results do not depend in any significant way on our "instrument function".

With a large system one can also make use of another method designed to reduce the variance of spectral estimates. Specifically, if the electric field is considered a stochastic process [O'Neil, 1974], then it should actually not be too surprising that the estimate of the spectrum from the Fourier transform of a finite length sample is itself a stochastic variable. Increasing the length of the sample does not decrease its variance from the 100% level, but instead spreads the information to a more closely spaced set of wave numbers. However, if the system length is much longer than any wavelength of interest, as in our simulations, then we can divide the sample into independent segments. Averaging the spectral estimates from M such segments reduces the variance by $1/M$ or the standard deviation by $1/(M)^{1/2}$. A larger reduction can be achieved if segments are overlapped by one half of their length and a spatial window function is applied to the data before the Fourier transform [Welch, 1967]. The number of segments is doubled, but they are not statistically independent. The variance is reduced by approximately $11/9M$, but with M doubled. Dum [1990b] has used this method to obtain the spectra of the ordinary bump-on-tail instability with a triangular window function applied to eight overlapping segments of the sampled potential. This was not sufficient for complete smoothing, but reduced strongly fluctuating peaks which occurred in just a few wave modes.

It is important to mention that increasing the number of modes in the simulation does not eliminate the erratic fine structure of the spectrum, it is always there and in real space plasmas something of this nature should occur. In simulations the rather erratic time dependence of individual modes and the resultant fine structure of the spectrum are directly dependent on microscopic initial conditions such as the loading of particles in phase space or the initial wave phases. With a large computing

budget one can therefore also obtain smooth spectra by averaging over an ensemble of simulation runs, each run with different microscopic initial conditions [Adam et al., 1980]. All turbulence theories, after all, explicitly assume such ensemble averaging.

Lastly, it should be pointed out that the magnitudes of the spectral field energy of the Fourier modes, shown in Figure 5-12, are related to the magnitudes of the electric field energy in real space through the discrete form of the Parseval's theorem [Elliot and Rao, 1982]

$$\sum_{k=0}^{N-1} |e_k|^2 = \frac{1}{N} \sum_{n=0}^{N-1} |E_n|^2 \tag{5.56}$$

where e_k is the spectral field magnitude of mode k in fourier space, E_n is the electric field magnitude at the grid point n in real space and N is the number of grid points in the system.

Competition Between Modes in the Small k-scale

The physical mechanism that produces the erratic fine structure of the mode number spectrum is related to the competition between modes in the small k scale (i.e. between adjacent modes). Figure 5-11c shows the time history of the field energies of modes 45, 46 and 47. For modes 45 and 47 the agreement of growth rates with the linear theory is surprisingly good, considering that both the determination of the distribution functions and the determination of the wave spectrum are subject to statistical fluctuations. However, we see that mode 46 starts to grow only after the adjacent modes (45 and 47) are in the nonlinear regime. The delay in the onset of growth of this mode and its subsequently much larger growth rate (than that linearly predicted) are due to the fact that, in the early stage of the instability evolution, particles get distributed in space stochastically to produce the bunches that form the wave modes. Therefore, statistically speaking some modes initially bunch a larger number of particles than others and tend to absorb the energy of those adjacent modes which initially bunch a smaller number of particles (e.g. mode 46). The latter modes do not start to grow until the nonlinear development of the wave fields spreads the wave energy between adjacent modes.

As shown in Figure 5-1b, for the modes 38, 39 and 40 the end of the linear growth

regime near time $\bar{t} = 2.3$ is implied by the deviation of the log (spectral field energy) versus time curves. Significant competition between the growing modes and tendency toward monochromaticlike growth (locally in k space) are apparent in Figure 5-11b after the end of the purely linear growth regime: From time $\bar{t} = 2.5$ until saturation of the instability by trapping around time $\bar{t} = 3$, modes 38 and 40 show rapid and sudden decreases, and sometimes subsequent increases, in amplitude or remain at a small fairly constant level. This is again consistent with mode 39 taking energy from, or preventing further growth of, the other adjacent modes due to its greater bunching ability as a result of the stochastic nature of the initial conditions of the simulation design.

As we have discussed in section 5.4.3, some time after saturation of the modes growth (i.e. at $\bar{t} \sim 20$), a transition in the instability mechanism occurs in which the wave modes start to be driven exclusively by a nonlinear version of a kinetic instability. However, even before this transition kinetic growth is partly responsible for producing the erratic time dependence of the mode energies. As shown in Figure 5-11, after saturation the mode energies oscillate in a non-periodic fashion within one order of magnitude below the saturation level, with periods of growth and decay of different durations and rates but as a whole decaying slowly. The kinetic growth occurring after saturation of the reactive instability is presumably due to the spatially localized gradients in velocity space visible in Figure 5-10c; wave growth would then tend to eliminate these gradients and homogenize the system, consistent with the simulation results at long times. The particle density gradients that exist locally in x-v space (Figure 5-10c) are obviously invisible in the plots of the space-averaged distribution functions (Figure 5-9).

The Saturation Spectrum

Figure 5-12a shows the mode number spectrum during the saturation of the instability. It should be noted that in our run many wave modes are excited before and during saturation. There is no evidence for any special nonlinear effect that would cause dominance of the linearly most unstable mode. Most previous simulations (of other

166

instabilities) use systems which are too short to allow the excitation of more than just a few discrete modes at best. The ubiquitous trapping model in the linearly most unstable mode may be quite adequate to describe some of these simulations, but turbulence theories cannot be expected to apply. Moreover, as we will show in sections below, after saturation the bandwidth of the wave spectrum actually increases considerably as the beam-arc evolves by diffusion. These findings invalidate frequent arguments that eventually the mode of largest linear growth rate will dominate.

It should be pointed out that in the analogous case of the ordinary bump-on-tail instability, Shapiro [1963] assumed that the energy at the end of the reactive phase is negligible, compared to the electric field energy that is eventually reached in the kinetic quasi-linear regime that follows. He also assumed that during the reactive phase the spectrum is concentrated in a small range at the lower wave number edge of the final wave spectrum. We find that this is not the case. In the present run the transition to kinetic instability occurs after saturation and the electric field level at the time of the transition is close to the level reached at the time of saturation.

The Frequency Spectrum

Figure 5-13 shows the frequency versus mode number evolution of the electric field for the X5a45 run. Again, we can see that the spectral estimate is subject to statistical fluctuations. It is obtained here by fast Fourier transform (in frequency and mode number) of the electric field in the entire system, without zero padding. The intrinsic width in frequency of these spectral estimates hence is $\Delta\omega = 2\pi/T$, where T is the time span chosen for the analysis. With 256 sampled points and $\Delta t = 3.2/\omega_{pe}$, $\Delta\omega = 0.00767\omega_{pe}$. The time span T should be small compared to the characteristic time for macroscopic changes. Therefore, this imposed a limit on the maximum time spans that could be chosen to reduce the intrinsic width or improve the statistics.

Figure 5-14 shows the solutions of the linear dispersion relation for snapshots in time of the evolving distributions. The solutions are composed of the fast lower hybrid (fLH), fast beam (fB), slow beam (sB) and unstable beam (uB) branches, as indicated in this figure (i.e. fast and slow refer to the magnitudes of the phase velocities relative

to V). Only the growth rate corresponding to the unstable beam branch is shown in this figure; the other branches are neutrally stable. It is interesting to compare these linearly predicted frequencies with the frequency analysis of the simulation wave modes (Figure 5-13). For the choice of numerical parameters in the present run, dispersion in real frequency is as expected from linear (or quasi-linear) theory only for the early stage of the reactive phase. We see that in the early reactive phase (Figure 5-13a) we have indeed a relatively broad frequency spectrum with frequencies below the lower hybrid frequency, corresponding to the unstable beam mode. At later times, however, we see a narrow frequency spectrum, near the lower hybrid frequency. This finding is in disagreement with the dispersion relations in Figure 5-14 which predicts that at late times the frequency spectrum should still correspond to the beam mode and thus remain relatively broad. This disagreement is likely to be a result of the large wave amplitudes of the modes, at these late times, that violate the linear or quasilinear theory assumptions.

It should be pointed out that in the snapshots of the linear dispersion relation evolution (Figure 5-14) we do not see a detachment of the fast (and slow) lower hybrid branches from the fast (and slow) beam branches to take place nor a subsequent reconnection of the fast with the slow lower hybrid branches (actually the dispersion relation does not even have a slow lower hybrid branch solution). This type of linear dispersion relation evolution would be expected since it was observed by Dum [1990b] to take place in the analogous case of the reactive bump-on-tail instability. We have found, however, that for this evolution to occur the ratio of the beam-arc ion to the background electron density would have to be at least an order of magnitude smaller (i.e. $n_w/n_e \sim .015$). Nevertheless, we have not performed simulations for these lower density ratios since they are not relevant for the interpretation of the PDP data taken near the Shuttle and also because of computational constraints; such simulations would require running times an order of magnitude larger than the current ones.

Destabilization of Large Wavenumber Modes by the Beam-Arc Wave Interaction

After saturation and before the transition to a "purely" kinetic instability the beam-arc relaxes in a somewhat quasi-linear manner, due to a wave spectrum that was created in essence during the reactive growth phase. Diffusion at this stage is mostly resonant, i.e., restricted to the phase velocity range of the wave spectrum. This is particularly evident as the range of phase velocities of the modes with high energy levels (which can be deduced from the red signals in the color coded dispersion relation, Figure 5-13) coincides with the range of velocities of the bulk of the broadened beam-arc distribution (i.e. $0.56V \leq \omega/k \leq V$, see Figure 5-9a at $\bar{t} = 7.3$).

Let us consider again Figure 5-9a, which shows snapshots of the evolving beam-arc distribution. Particularly prominent is the development of a steep front, followed by a plateau, which moves toward smaller velocities (at the left edge of the plateau). Furthermore, it is important to note that waves with larger and larger wave numbers (smaller phase velocities) are destabilized by anti-Landau damping as the beam-arc distribution develops this steep front which moves toward smaller velocities. Evidence for this important beam arc-wave interaction also comes from Figure 5-11d where we see that, initially, the linearly unstable large wavenumber modes (e.g. mode 54) grow at their linear growth rates, whereas modes with wave numbers larger than 60 (i.e. the largest linearly unstable mode) start their growth phases later, with larger growth rates (from the steepness of the beam-arc front) and then reach comparable levels. Landau damping by the background ions will ultimately arrest this process. However, since beam-arc peak and bulk of background ions are well separated in velocity initially, then for a long time, beam-arc dynamics alone determines wave growth.

5.4.5 Quasi-Steady State

The evolution of the wave spectrum, shown in Figure 5-12, also indicates that the wave-beam arc interaction plays a decisive role by broadening of the spectrum in the kinetic phase. The development of the steep beam-arc distribution front that

advances to lower and lower velocities, followed by a plateau which moves toward smaller velocities, causes the growth of larger and larger wave number modes (i.e. with smaller phase velocities) in the early kinetic stage (e.g. compare Figure 5-12a with Figure 5-12b). However, the energy contained in these modes remains small (compared to that of the linearly most unstable modes), and the rate of this process decreases until it terminates by flattening of the bump in the total (beam-arc + background) ion distribution. At this point, wave growth at larger and larger wave numbers is arrested by Landau damping from background ions. Figure 5-7 shows that the advance of the beam-arc front to lower velocities and the formation of a high-energy tail in the background ion distribution combine to produce a plateau in the total (i.e. beam-arc + background) ion distribution at $\bar{t} \sim 22$. Once this plateau is formed, changes in the total ion distribution remain very small. A quasi-steady state is therefore reached by $\bar{t} \sim 22$ which is also evident from the time history of energies shown in Figures 5-8 and 5-11. In the quasi-steady state only the field energy, which constitutes a small fraction ($\sim \%1$) of the total energy in the simulation system, continues to evolve slowly. The field energy which at these times is mostly concentrated near modes 30-40 continues to decay slowly.

It should be pointed out that because ions are treated as unmagnetized in the simulation, the runs are only valid for times shorter than about 25 lower hybrid periods. For longer times, magnetic field effects on ions should be included; nevertheless, since the simulation results show that a quasi-steady state is already reached before a time of the order of $22\tau_{LH}$, our unmagnetized ions assumption is quite appropriate. Moreover, in the case of the shuttle environment instability the beam-arc distribution function of pickup water ions should partially regenerate itself [Rivas and Hastings, 1992] due to the continuous source of cold beam-arc ions from the charge exchange reactions (which are not included in the simulation). Therefore, the simulation times of interest for the interpretation of the PDP wave data should be those from near saturation up to the quasi-steady state.

Broadening of the Distribution Functions by Resonant and Nonresonant Diffusion

Let us note, in Figure 5-7, that the monotonic connection (i.e. without undershoot) of the plateau of the total (beam-arc+background) ion distribution to the bulk of the background ion distribution is in part due to nonresonant diffusion, by the large wave fields. As shown in Figure 5-9b nonresonant and resonant diffusion combine to draw a substantial tail in the background ion distribution which ultimately extends as far as the phase velocity range of the excited wave spectrum (the resonance region). This acceleration process also draws a substantial amount of the wave energy liberated by the beam-arc.

Similarly, in Figure 5-9c we note that nonresonant diffusion (before and after saturation) and resonant diffusion (after saturation) combine to draw a relatively strong tail in the electron distribution of velocities along the magnetic field. This tail extends as far as the resonance region; for the current run the upper velocity is $v_z \sim 6$ (in PIC code units, see Figure 5-9c). The heating of the electrons along the magnetic field draws a substantial fraction of the wave energy and is partly responsible for the decreases in the field energy after saturation as can be seen in the field energy history plot (Figure 5-8a).

Furthermore, in the electric field energy after saturation and during the kinetic phase, we find that the energy actually decreases from a maximum of about 0.07 to 0.01 at the start of the quasi-steady state ($\bar{t} \sim 22$). Such damping in the wave field energy is due mostly to Landau damping by the background ions . This is because since the background ion distribution is significantly broadened during the reactive phase of the instability, by nonresonant diffusion, and as a result of which it acquires a more negative slope in the range of phase velocities of the most energetic modes. The change in slope is noticeable in the background ion distribution plots shown in Figure 5-9b. Electron Landau damping parallel to the magnetic field also absorbs some of the wave field energy as the high energy tail in the parallel electron distribution grows (see Figure 5-9c).

Finally, Figure 5-9a shows that at very late times, the plateau develops a slightly

negative net slope. Discrete particle effects, i.e., spontaneous wave emission and a corresponding drag force, which in the simulations are much bigger than in reality, are the most likely explanation. Discreteness effects are not entirely negligible in simulation with macroparticles [Birdsall and Langdon, 1985]. Furthermore, the continued nonresonant diffusion of the background ion tail and beam-arc particles may also contribute to the slightly negative slope in the plateau region. It should be mentioned that nonresonant diffusion also leads to some smoothing of the edges in the plateau. In addition, in Figure 5-9a we note that, while the plateau is formed mostly by resonant diffusion, the region of the beam-arc distribution accelerated above V must evolve by nonresonant diffusion.
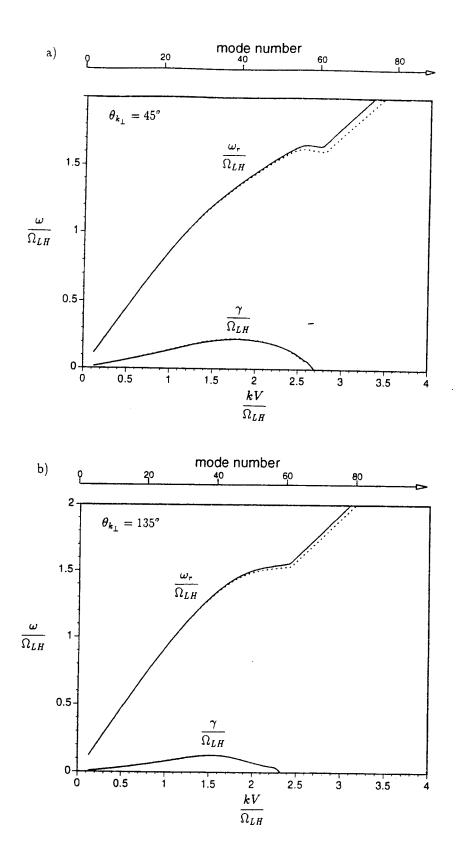
Figure 5-1: Linear dispersion relation of the $X_p = 5$ beam-arc plasma instability for two propagation directions (a) $\theta_{k_\perp} = 45°$ and (b) $\theta_{k_\perp} = 135°$. The results for two cases are shown in (a) and (b): (1) $m_O/m_e = 29,377$ and $\omega_{pe}/\omega_{ce} = 4.78$ (dashed lines) corresponding to the real values for the ionospheric plasma near the shuttle and (2) $m_O/m_e = 512$ and $\omega_{pe}/\omega_{ce} = 1$ (solid lines) which are the values used in the simulations.
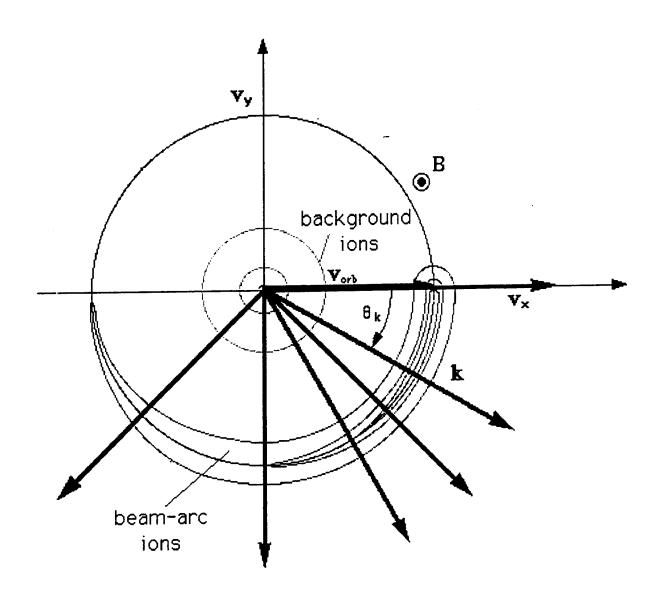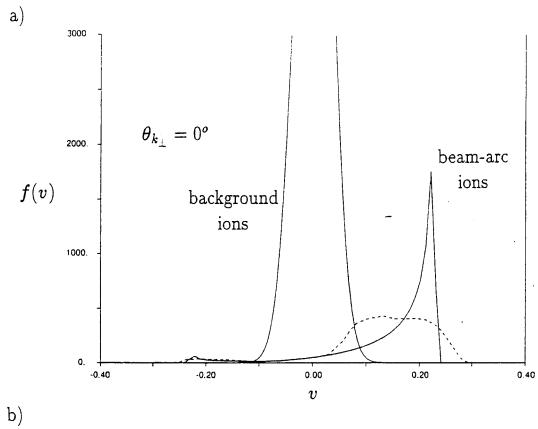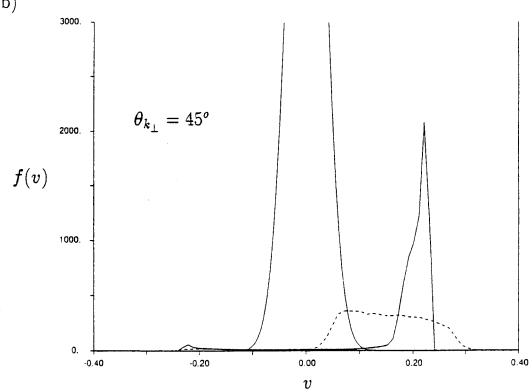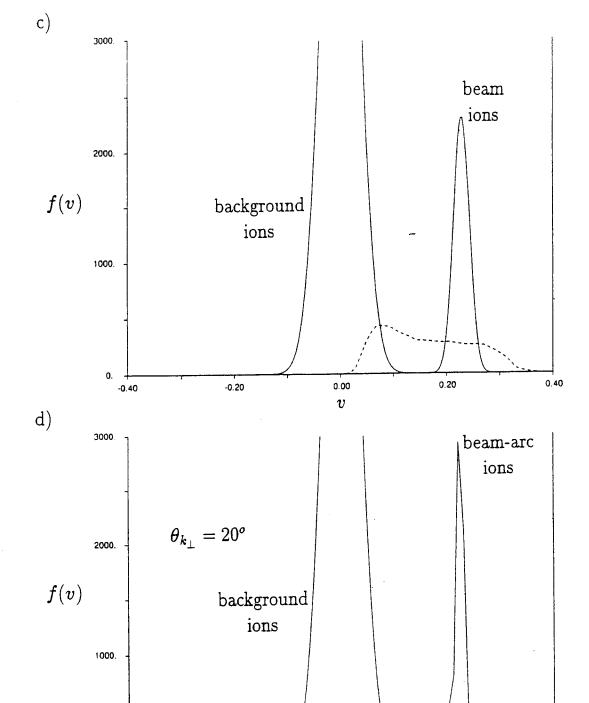
Figure 5-2: Schematic diagram of the beam-arc water ion and background oxygen ion distributions in velocity space (the distribution of the electrons is not shown). Superimposed in this figure are the wavenumber vectors for the propagation directions $\theta_{k_\perp} = 0°$, $20°$, $45°$, $60°$, $90°$, and $135°$.
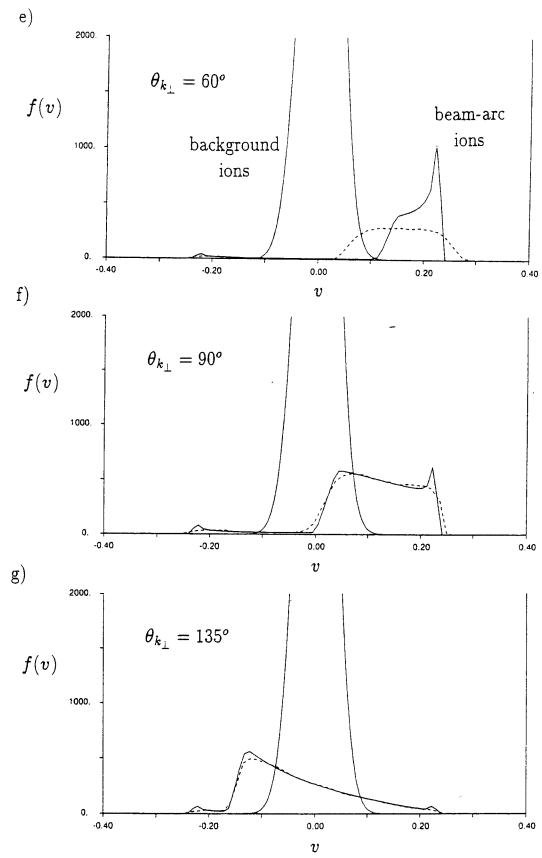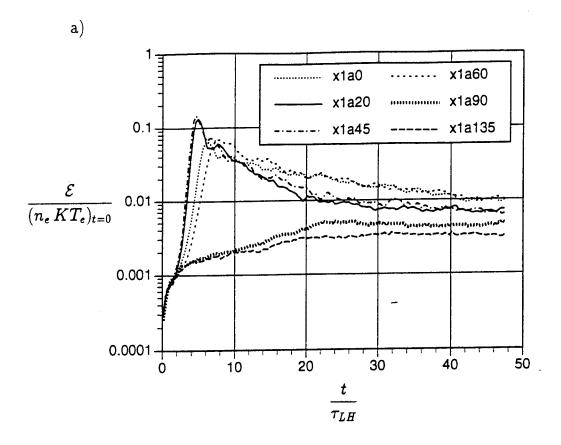
a)

b)

c)

d)

e)

f)

g)

Figure 5-3: Initial beam-arc and background (reduced) ion distributions (solid lines) of the $X_p = 1$ beam-arc plasma instability for various propagation directions, (a) $\theta_{k_\perp} = 0^o$ (b) $\theta_{k_\perp} = 45^o$ (d) $\theta_{k_\perp} = 20^o$ (e) $\theta_{k_\perp} = 60^o$ (f) $\theta_{k_\perp} = 90^o$ (g) $\theta_{k_\perp} = 135^o$, nearly perpendicular to the magnetic field ($\bar{\phi}_{k_\parallel} = 1$ in all cases). The beam-arc distributions of the quasi-steady state are also shown (dashed lines). The ion distributions for the case of the beam plasma instability are shown in (c).
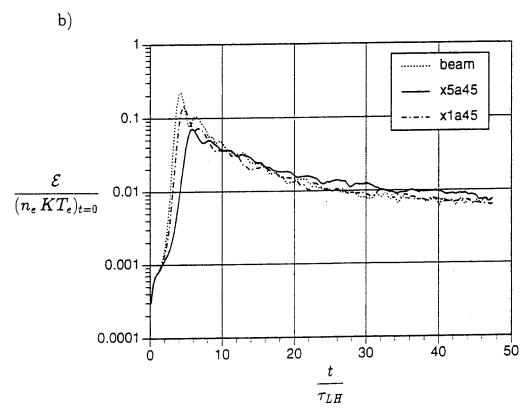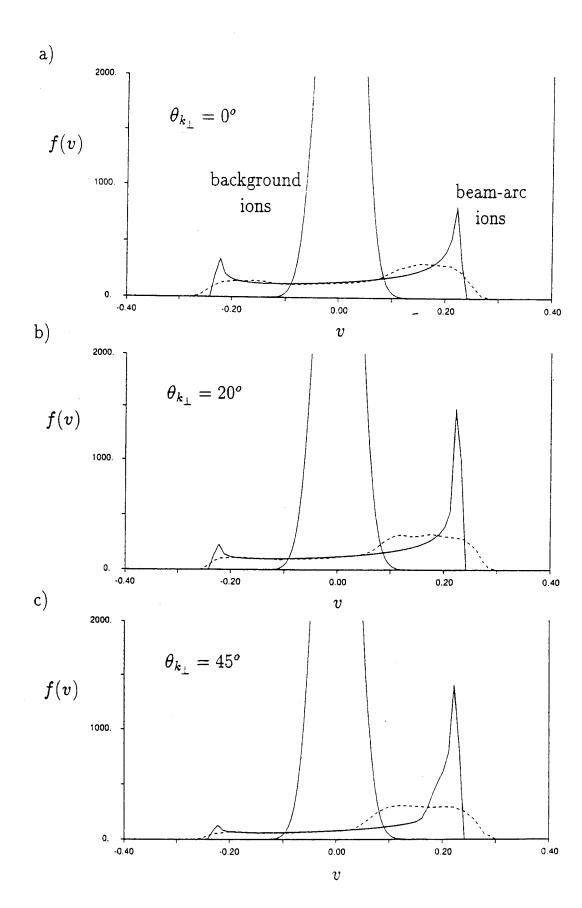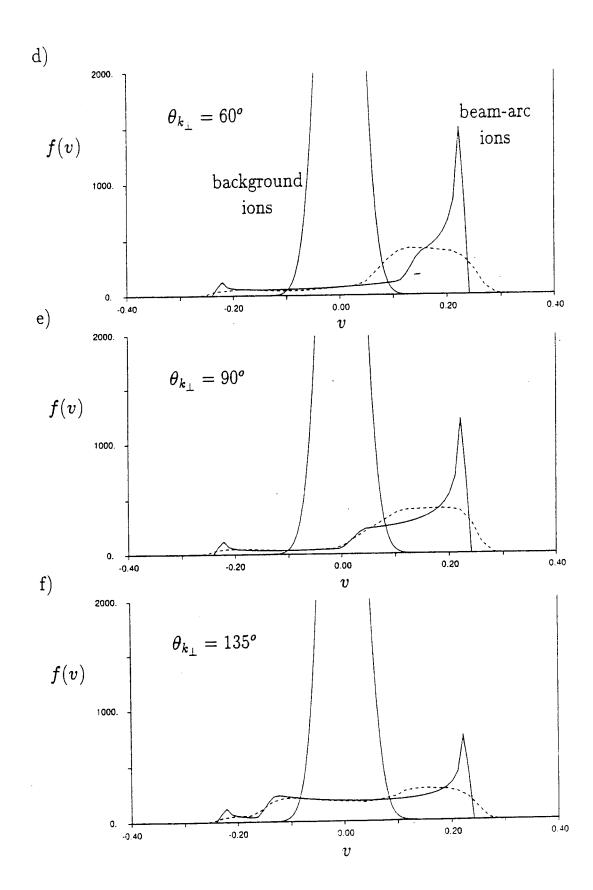
a)

b)

Figure 5-4: Field energy time histories. (a) The $X_p = 1$ beam-arc plasma instability in various propagation directions nearly perpendicular to the magnetic field. (b) Comparison between strong beam-arc plasma instabilities and the beam plasma instability.
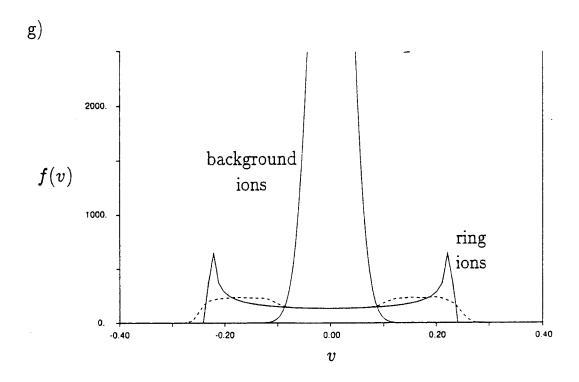
178

a)

$\theta_{k_\perp} = 0^o$

background
ions

beam-arc
ions

$f(v)$

v

b)

$\theta_{k_\perp} = 20^o$

$f(v)$

v

c)

$\theta_{k_\perp} = 45^o$

$f(v)$

v

d)

$f(v)$

$\theta_{k_\perp} = 60^o$

background
ions

beam-arc
ions

e)

$f(v)$

$\theta_{k_\perp} = 90^o$

f)

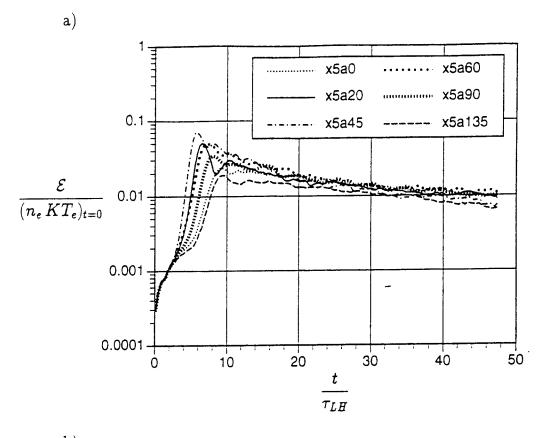$f(v)$

$\theta_{k_\perp} = 135^o$

180

g)

Figure 5-5: Initial beam-arc and background (reduced) ion distributions (solid lines) of the $X_p = 5$ beam-arc plasma instability for various propagation directions, (a) $\theta_{k_\perp} = 0°$ (b) $\theta_{k_\perp} = 20°$ (c) $\theta_{k_\perp} = 45°$ (d) $\theta_{k_\perp} = 60°$ (e) $\theta_{k_\perp} = 90°$ (f) $\theta_{k_\perp} = 135°$, nearly perpendicular to the magnetic field ($\bar{\phi}_{k_\parallel} = 1$ in all cases). The beam-arc distributions of the quasi-steady state ($\bar{t} \geq 22$) are also shown (dashed lines). The ion distributions for the case of the ring plasma instability are shown in (g).
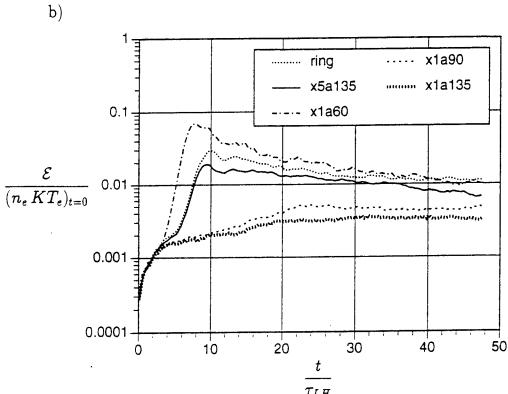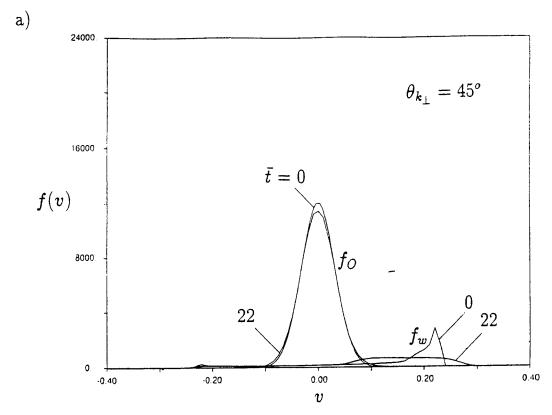
a)

b)

Figure 5-6: Field energy time histories. (a) The $X_p = 5$ beam-arc plasma instability in various propagation directions nearly perpendicular to the magnetic field. (b) Comparison between weak beam-arc plasma instabilities and the ring plasma instability.

a)

b)
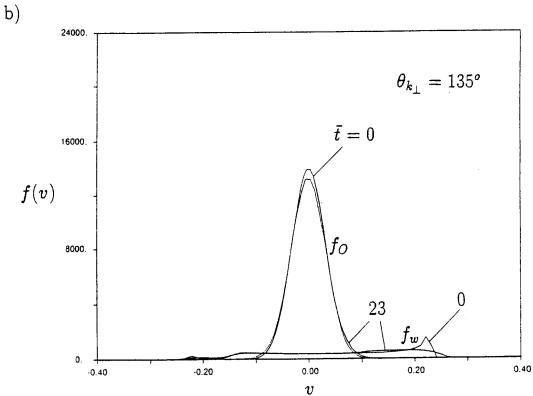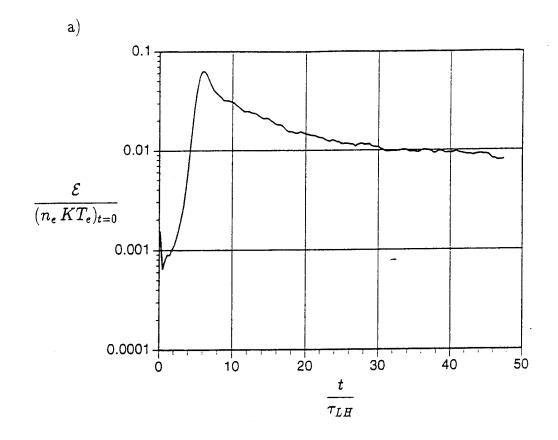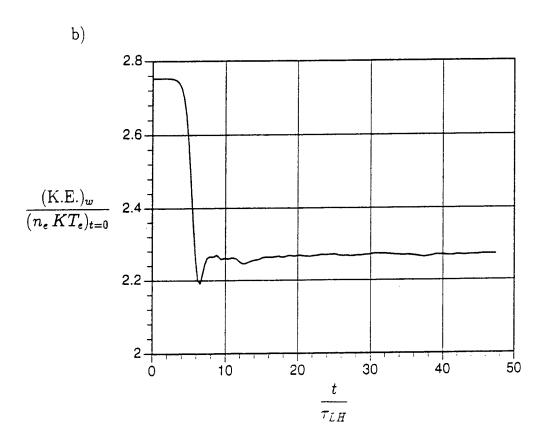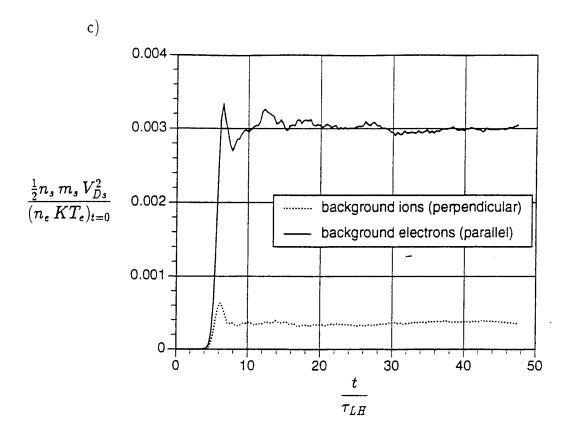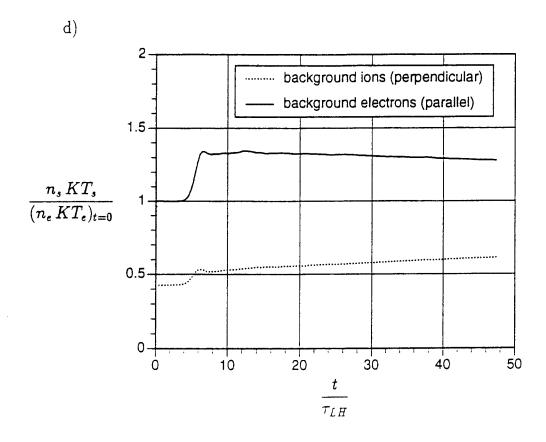
Figure 5-7: Initial and quasi-steady state (reduced) distribution functions of the beam-arc water ions and background oxygen ions for the $X_p = 5$ beam-arc plasma instability in two propagation directions: (a) $\theta_{k_\perp} = 45^o$ and (b) $\theta_{k_\perp} = 135^o$.

a)

$$\frac{\mathcal{E}}{(n_e\,KT_e)_{t=0}}$$

$$\frac{t}{\tau_{LH}}$$

b)

$$\frac{(K.E.)_w}{(n_e\,KT_e)_{t=0}}$$

$$\frac{t}{\tau_{LH}}$$

184

c)

$$\frac{\frac{1}{2}n_s\,m_s\,V_{Ds}^2}{(n_e\,KT_e)_{t=0}}$$

.... background ions (perpendicular)

———— background electrons (parallel)

$$\frac{t}{\tau_{LH}}$$

d)

$$\frac{n_s\,KT_s}{(n_e\,KT_e)_{t=0}}$$

.... background ions (perpendicular)

———— background electrons (parallel)

$$\frac{t}{\tau_{LH}}$$

185

e)
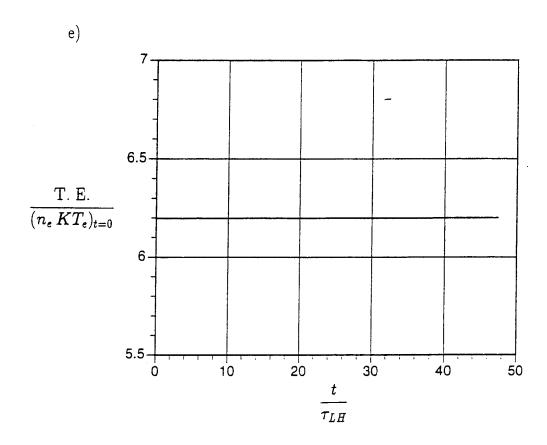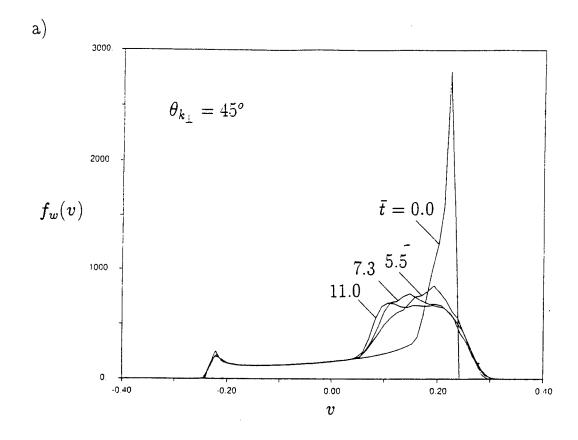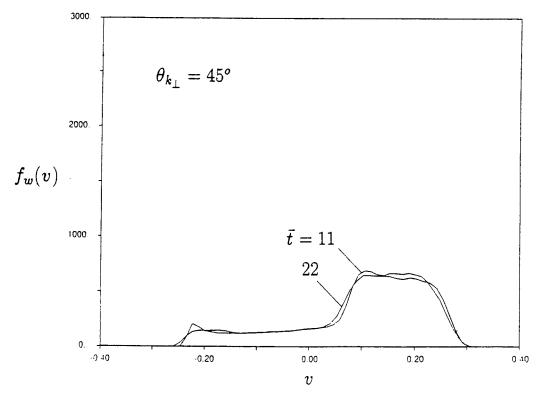
Figure 5-8: Time history of energies for the X5a45 run. (a) Electric field energy. (b) Total (drift+thermal) energy of beam-arc water ions. (c) Drift energies of background ions and electrons. (d) Thermal energies of background ions and electrons. (e) Total (field+drift+thermal) energy in the simulation system.

186

a)

$f_w(v)$

$\theta_{k_\perp} = 45^o$

$\bar{t} = 0.0$

7.3 5.5

11.0

v

$f_w(v)$

$\theta_{k_\perp} = 45^o$

$\bar{t} = 11$

22

v

b)

c)
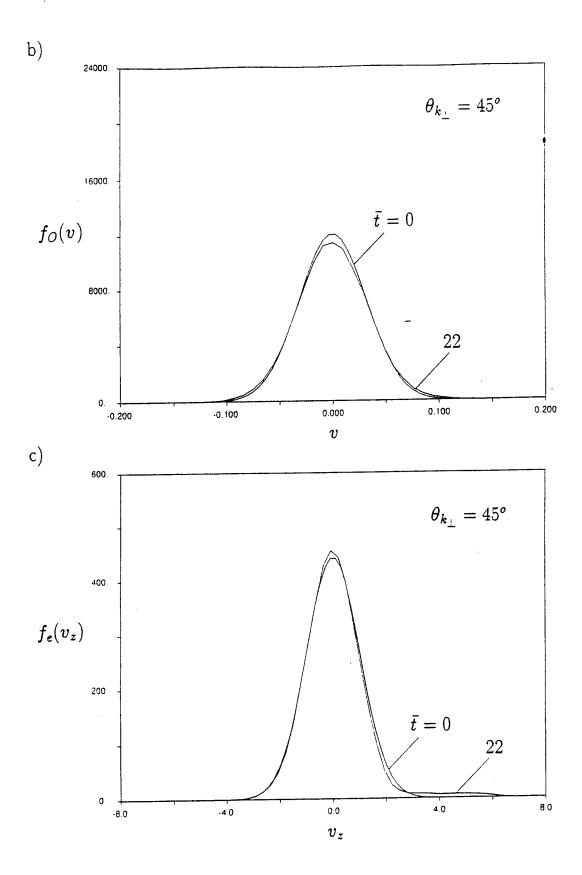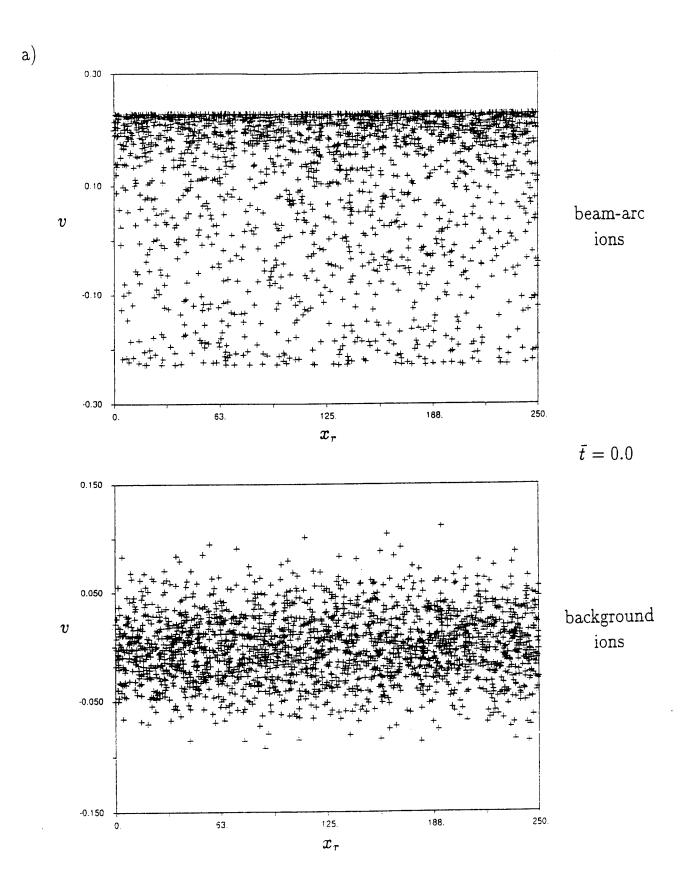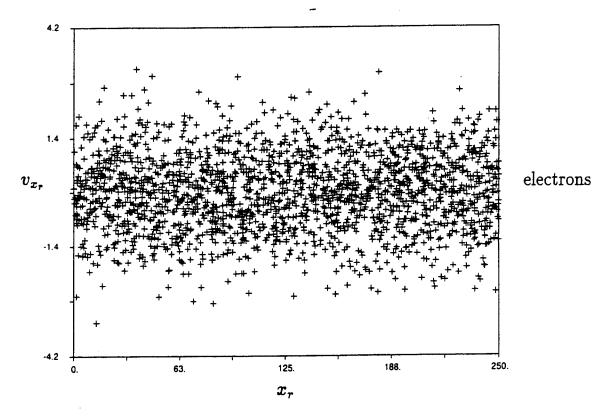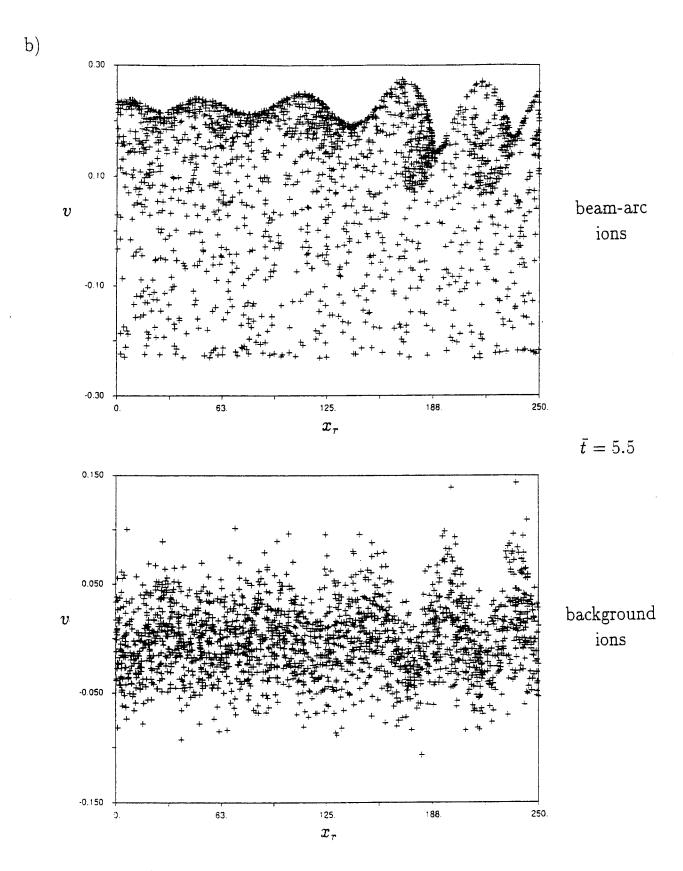
Figure 5-9: Reduced distribution plots for the X5a45 run. (a) Evolution of the beam-arc ion distribution; the advance of the beam-arc front to lower velocities and the plateau formation are seen. (b) and (c) show the initial and quasi-steady state distributions of the background ions and electrons, respectively.

a)

beam-arc
ions

$\bar{t} = 0.0$

background
ions

189

$\bar{t} = 0.0$

electrons

b)

beam-arc
ions

$\bar{t} = 5.5$

background
ions

191

$\bar{t} = 5.5$

electrons

c)

beam-arc
ions

$\bar{t} = 7.3$

background
ions

193

$\bar{t} = 7.3$

electrons

d)

beam-arc
ions

$\bar{t} = 22.0$

background
ions

$\bar{t} = 22.0$

electrons
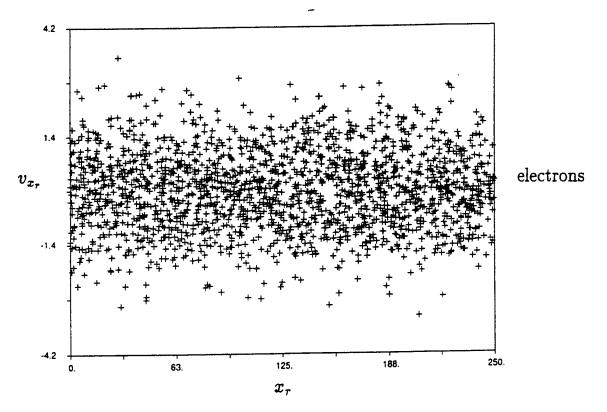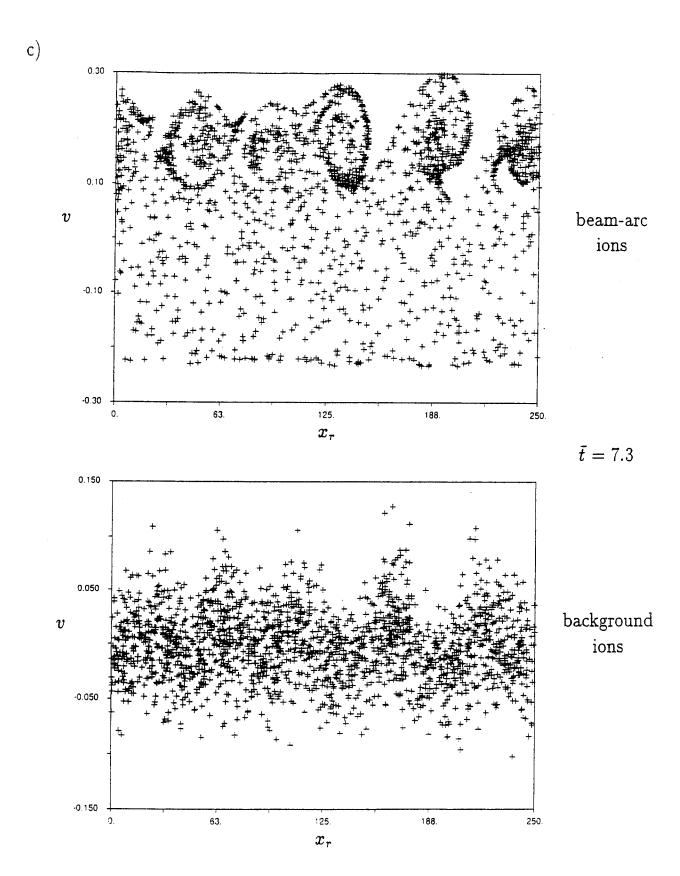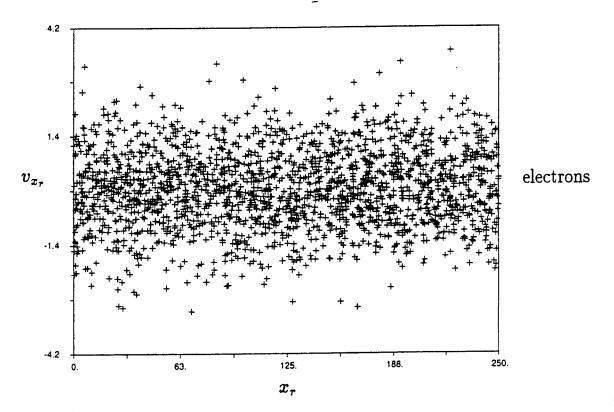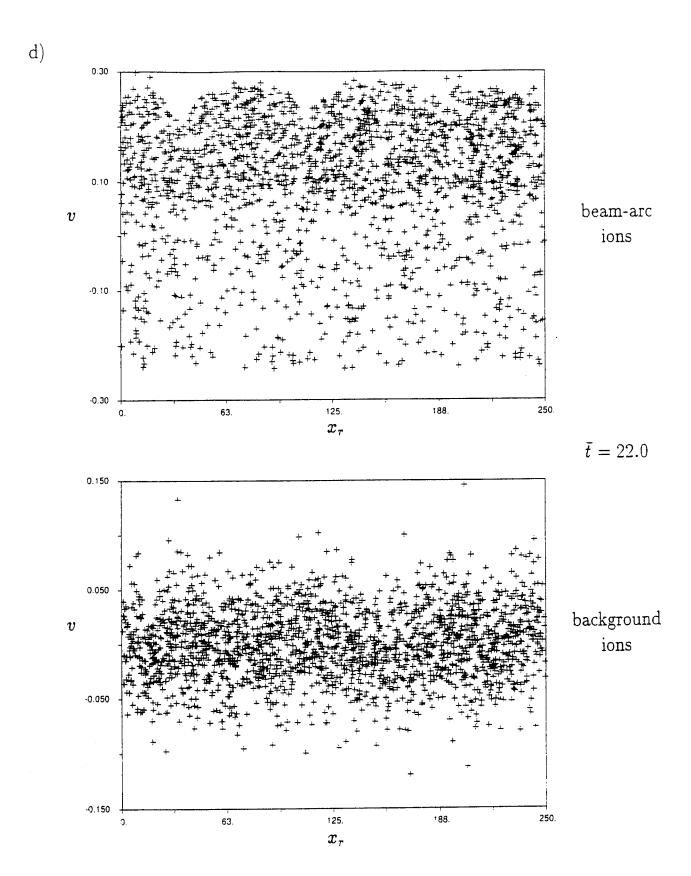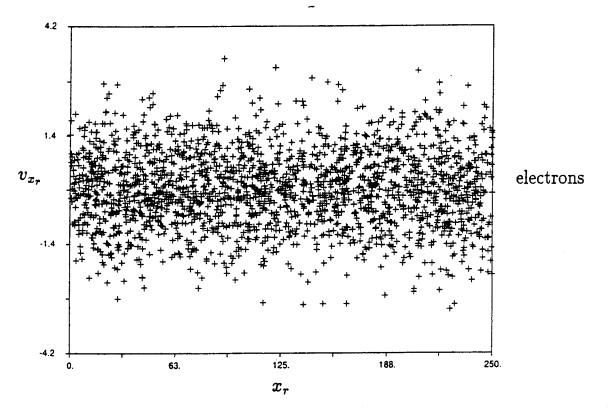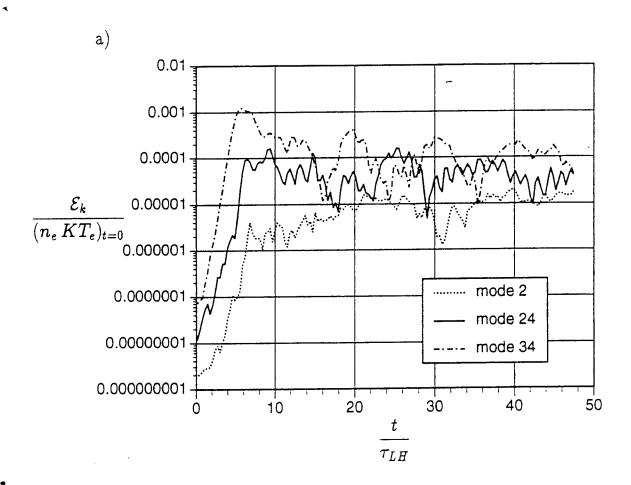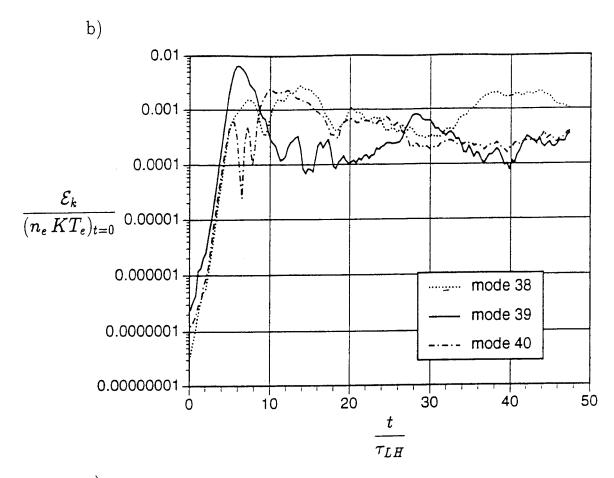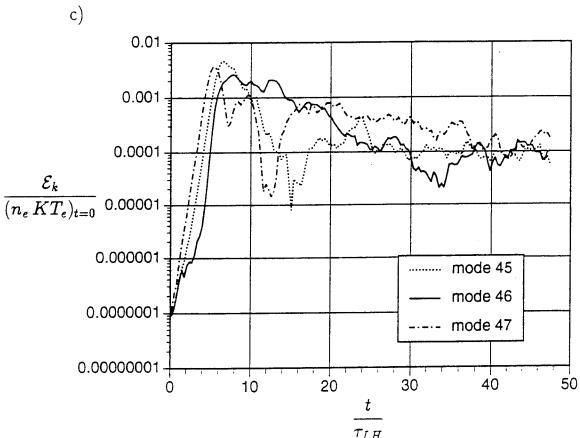
Figure 5-10: Evolution of ions and electrons in phase space for the X5a45 run (only 1/8 of the system length and about 1% of the ions are shown). (a) At $\bar{t} = 0$. (b) Strong bunching by the fastest growing modes before saturation. (c) Vortices indicating beam-arc ion trapping near saturation. (d) In the quasi-steady state, vortices are smeared out by the randomization of the particles by the many modes.

a)

b)

c)

198

d)
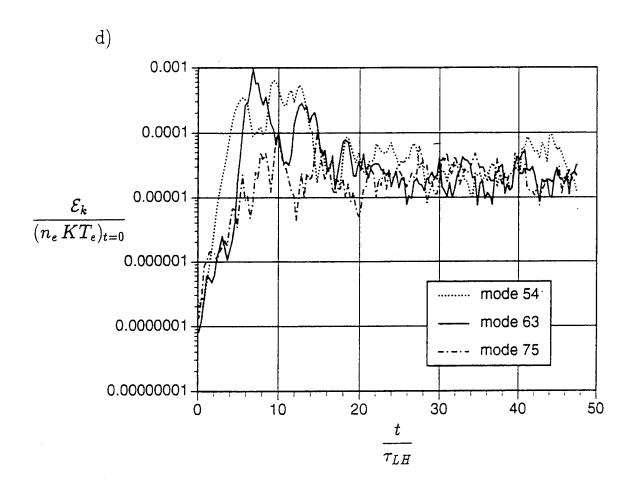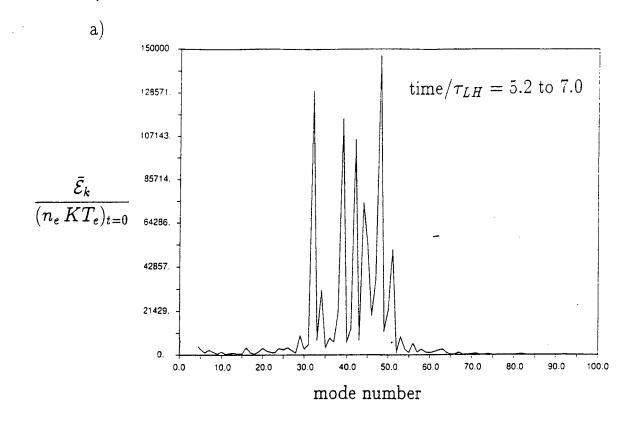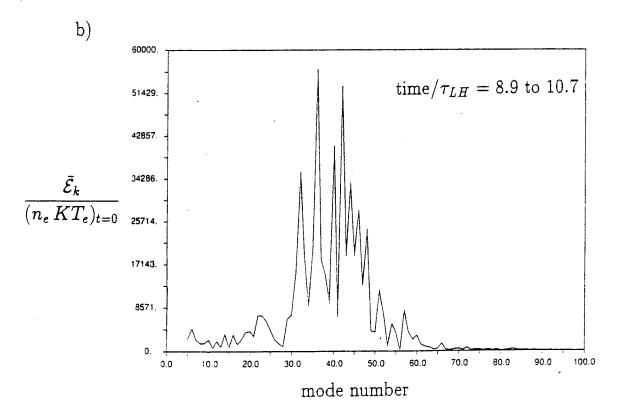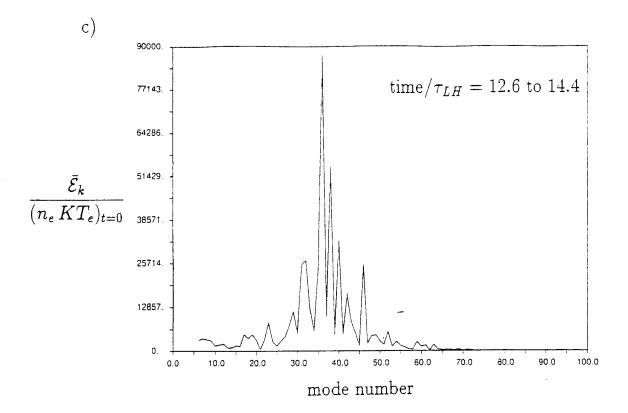
Figure 5-11: Time history of mode energies for the X5a45 run. (a) Competition between modes (in the large k scale). The greater bunching ability of the most linearly unstable modes prevents the low wavenumber modes from growing. (b) and (c) Competition between modes (in the small k scale). Before saturation, modes with greater bunching ability prevent adjacent modes from growing. When many modes are present the stochastic nature of turbulence is evident: individual wave modes show a rather erratic time dependence, unless there is some averaging. (d) Destabilization of large wavenumber modes. Linearly stable, large wavenumber modes are destabilized due to the advance of a beam-arc front to lower velocities.

a)

$$\frac{\bar{\mathcal{E}}_k}{(n_e\,KT_e)_{t=0}}$$

time/τ_{LH} = 5.2 to 7.0

mode number

b)

$$\frac{\bar{\mathcal{E}}_k}{(n_e\,KT_e)_{t=0}}$$

time/τ_{LH} = 8.9 to 10.7

mode number

c)

d)
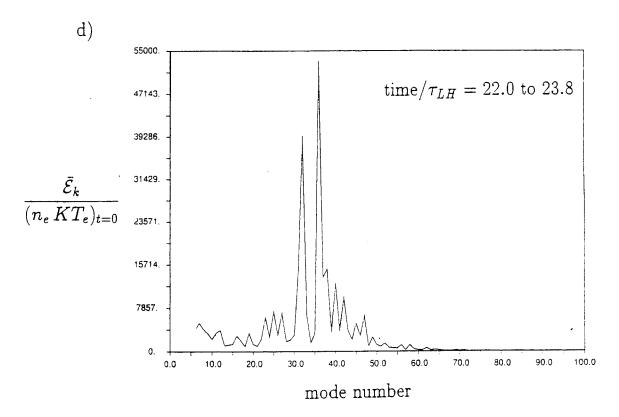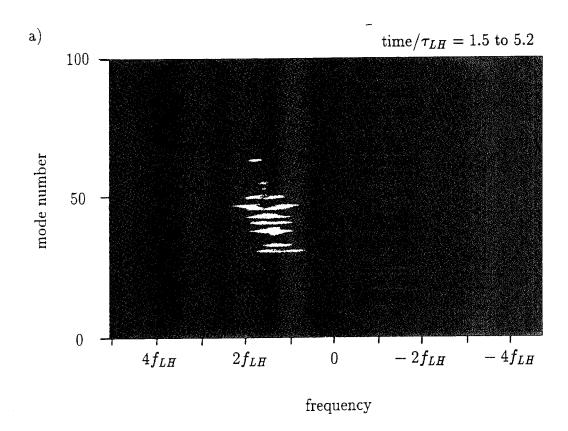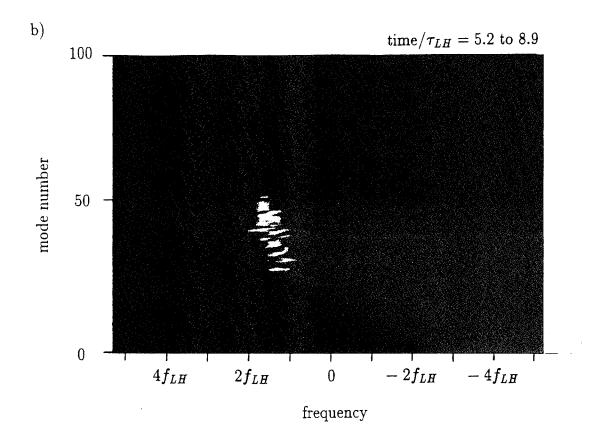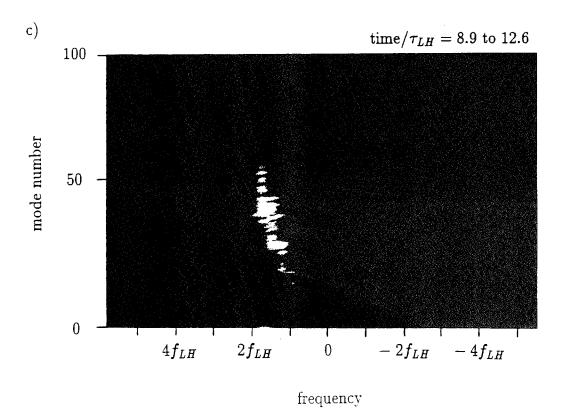
Figure 5-12: Average mode number spectral field energies for various time periods of the X5a45 run. (a) During saturation, the spectrum is broad but restricted to the range of most linearly unstable modes. (b) After saturation, large wavenumber modes are destabilized due to the advance of the beam-arc front to lower velocities. (c) Before the quasi-steady state, background ions and electrons Landau damp some of the most linearly unstable large wavenumber modes. (d) The quasi-steady state spectrum.

201

time/τ_{LH} = 1.5 to 5.2

b)

time/τ_{LH} = 5.2 to 8.9

c)

time/τ_{LH} = 8.9 to 12.6

d)

time/τ_{LH} = 20.1 to 23.8
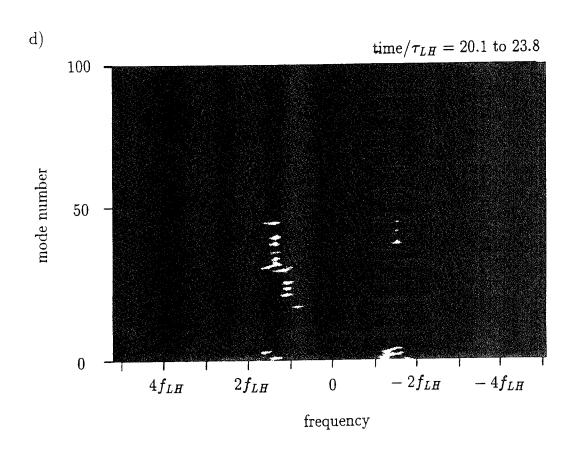
Figure 5-13: Electric field energy density spectrum (frequency versus mode number) for various time periods of the X5a45 run. The color coded intensities decrease by about one order of magnitude in each color in the following order: red, yellow, green, light blue and dark blue. (a) Broad frequency spectrum in the reactive phase before saturation. (b) During saturation the frequency spectrum narrows. (c) After saturation and (d) in the quasi-steady state, the frequency spectrum remains narrow with $f \sim f_{LH}$ and concentrated near the linearly fastest growing modes.
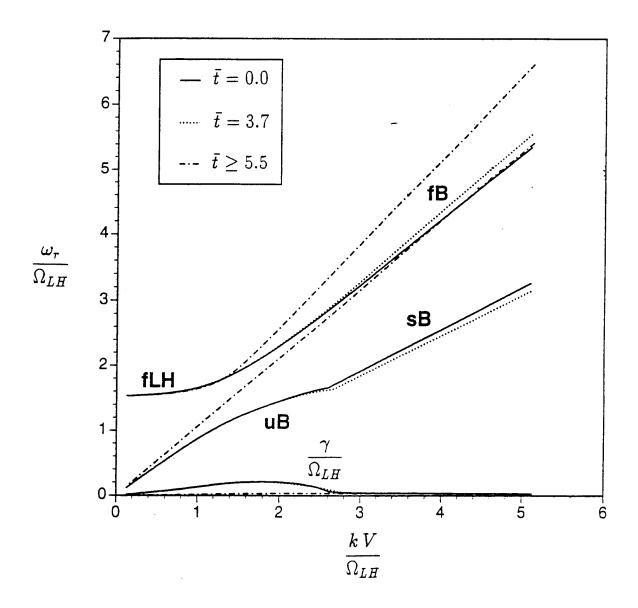
Figure 5-14: Solutions of the linear dispersion relation for snapshots in time of the evolving distributions of the X5a45 run. The solutions are composed of the fast lower hybrid (fLH), fast beam (fB), slow beam (sB) and unstable beam (uB) branches (i.e. fast and slow refer to the magnitudes of the phase velocities relative to V). Only the growth rate curve of the unstable beam branch is shown; the other branches are neutrally stable. At late times, these linear solutions do not match those of the simulation Fourier analyses, therefore, when nonlinear effects are dominant.

Chapter 6

Interpretation of the PDP Wave Data

In this chapter, we put all of the theoretical pieces developed in the previous chapters together to give a fairly complete interpretation of the extensive PDP wave data. We use the study of the pickup water ion distribution of the shuttle environment (Chapter 3) and the linear and nonlinear analyses of the beam-arc plasma instability (Chapters 4 and 5, respectively) to interpret the wide variety of properties of the shuttle environment waves that have been extracted from the PDP wave data (Chapter 2). All the sections (expect Section 6.1.1) of this chapter contain new results which in most cases represent significant progress in the understanding of the nature of the shuttle environment waves.

The Doppler Shifted Frequencies Observed in the Moving Frame

We start the interpretation of the PDP wave data by making three important remarks. The first remark has to do with the earth frame frequencies ($\omega \sim \omega_{LH}$) of the waves, the second with the wavevector magnitudes and directions of the waves and the third with the shuttle frame (Doppler shifted) frequencies of the waves.

First, let us recall some of the results of the beam-arc plasma instability simulation. Figures 5-4a and 5-6a show that the beam-arc plasma instability excites waves in various propagation directions nearly perpendicular to the magnetic field. The am-

plitudes of the waves are different for the various propagation directions and depend on the shape of the beam-arc. In the stationary ionospheric (or earth's) frame, the frequencies of the largest amplitude wave modes, in each direction, are near $1.5\Omega_{LH}$ (see Figures 5-13). Therefore, what the beam-arc plasma instability effectively does is to excite the lower hybrid modes of the ionospheric plasma in various directions. For simplicity, in the discussion that follows we shall simply use the term "waves" to refer to these lower hybrid waves of the earth's frame since these will be the only waves of interest to us. We should also recall that our simulation results are expressed in terms of the lower hybrid frequency of the background oxygen ions Ω_{LH}, defined by Equation 5.46, whereas the PDP wave data is given in terms of the ionospheric lower hybrid frequency $\omega_{LH} \approx \sqrt{\omega_{cO}\,\omega_{ce}}$. These frequencies are related through the density ratio as follows, $\Omega_{LH} = \sqrt{n_O/n_e}\,\omega_{LH}$. For the density ratio used in the simulations, $n_O/n_e = 0.85$ (or $n_w/n_e = 0.15$), this relation is $\Omega_{LH} = (0.922)\,\omega_{LH}$.

Second, as shown in Section 4.4, the beam-arc plasma instability propagates preferentially in the directions nearly perpendicular to the magnetic field. This agrees with the wave observations during the PDP free-flight mission (see Section 2.2.3). Furthermore, the simulation results in Figure 5-12 show that the wavelengths of the most energetic modes range from 0.6 to 3.5 meters which is also consistent with the range of wavelengths that could be detected with the PDP antenna. In Section 6.3.4, we shall make a more rigorous comparison of the simulation dispersion relations and propagation directions with those inferred from the interference patterns of the wideband data.

Third, the simulation analysis of the beam-arc plasma instability (Chapter 5) was done by using the stationary ionospheric frame of reference. Therefore, in order to use the simulation results for the interpretation of the PDP wave data, it is necessary to express these results in the moving reference frame, that is, in the shuttle frame. This is because the PDP instruments made all their measurements while moving with the shuttle (i.e. the PDP velocity relative to the shuttle is negligible compared to the orbital velocity). The wave frequencies in the moving frame (ω') can be obtained from the wave frequencies in the stationary ionospheric frame ω by taking into account the

Doppler shifts

$$\omega' \approx \omega - k_\perp V_\perp \cos\theta_{k_\perp} \qquad (6.1)$$

where $\theta_{k_\perp}$ is the angle between the components of the orbital velocity vector $\mathbf{V}$ and the propagation vector $\mathbf{k}$ in the plane perpendicular to the magnetic field (see Figure 5-2) [*Cairns and Gurnett*, 1991a]. The contribution of the parallel components is negligible since, as discussed above, $k_\parallel \ll k_\perp$ for the waves of interest. We shall see that since $\omega \sim \omega_{LH}$ and $k_\perp V_\perp \sim \omega_{LH}$ for the most energetic waves (see Section 4.3.1), the effect of the direction of propagation $\theta_{k_\perp}$ will be crucial in interpreting the PDP wave spectra.

6.1 Interpretation of the PDP Wave Spectrum Observed in the Near Vicinity of the Shuttle

6.1.1 Cairns and Gurnett's Observational Characterization of the PDP Wave Spectrum of the Near Vicinity of the Shuttle.

Let us start this section by summarizing some of the characteristics of the spectrum of waves observed within 10 meters of the space shuttle during the XPOP roll period of the PDP Spacelab-2 mission. Figure 2-16 shows *Cairns and Gurnett's* [1991b] plot of the relative contribution of the electric fields centered on the i'th channel to the total average broadband, frequency-integrated electric field E_T versus the frequency of the i'th channel (see Section 2.2.1). The detailed definition of this quantity is $R(f_i) = E_i / \sum_i E_i$ with $E_i^2 = \int S(f) df$ with upper and lower limits of integration $f_u = \sqrt{f_i f_{i+1}}$ and $f_L = \sqrt{f_i f_{i-1}}$, respectively. Here $S(f)$ is the spectral density, and the frequency intervals for integration are equally spaced in logarithmic frequency. The data plotted are for the period 0145-0210 UT of the XPOP roll when the total average broadband electric field E_T was 51.1 mV/m. *Cairns and Gurnett* [1991b] have made a detailed observational characterization of this spectrum and it is useful to recall it here for our interpretation. They have noted that the near field wave data reveals high wave levels from 31 Hz to 10 kHz (near the lower hybrid frequency

on a log scale); above 10kHz the wave levels decrease with frequency, reaching the background level near 56 kHz. *Cairns and Gurnett* have interpreted the frequency distribution of the wave electric field in terms of three components. The primary component is a fairly uniform, high level of waves covering the frequency range from 31 Hz to 10 kHz. The two other components are superimposed in this frequency range and have electric fields of order twice the uniform level. The second component is a low frequency peak in the range 100-178 Hz. The third component is a peak near 7 kHz (near the lower hybrid frequency) that follows the trend of the lower hybrid frequency. *Cairns and Gurnett* have found no evidence for a high frequency component localized above about 10 kHz.

6.1.2 The Uniform First Component

Let us now interpret the wave spectrum described above which was obtained when the PDP was on the RMS arm of the shuttle, at a distance of about 10 m. from the shuttle's fuselage. Throughout this interpretation we should bear in mind that in the near vicinity of the shuttle, within 10 m., the water ion distribution is expected to be the $X_p = 1$ beam-arc, as was discussed in Section 3.1.2 (see Figure 3-2).

The central portion of the uniform first component of the spectrum, which lies between the two other components, can be explained by beam-arc plasma waves propagating in the range $-15^o < \theta_{k_\perp} < 15^o$ and near $\theta_{k_\perp} \approx 50^o$ (see Figure 5-2). These waves are Doppler shifted in the shuttle frame to the frequency range between the second and third components. In Figure 6-1, we see that waves propagating in the orbital velocity direction ($\theta_{k_\perp} = 0^o$) have frequencies that fall near the center of the first component of the spectrum. Recall that this was also the interpretation of the first component of the spectrum deduced from the linear theory by considering the peaks of the Doppler shifted growth rate spectra of the waves (see Figure 4-12). This confirmation of the interpretation should be expected since, as shown by the simulations of the beam-arc plasma instability (Chapter 5), the linearly fastest growing modes in any particular propagation direction are the modes that reach the highest energy levels in the nonlinear regime (i.e. there is no significant mode-mode

coupling). In Figure 6-1, the error bars for the waves propagating in the $\theta_{k_\perp} = 0^o$ and $\theta_{k_\perp} = 60^o$ directions denote, roughly, the ranges of wave amplitude fluctuation right before the saturation stages of the X1a0 and X1a60 runs (see Figure 5-4), respectively. We use the wave amplitudes corresponding to the near saturation stages because, as we will show in Section 6.2.1, the group velocity of these (lower hybrid) waves should be very large ($v_g \gg V$) and almost parallel to the magnetic field. In particular, the energy of the excited waves should radiate away from the wave source region very rapidly along the magnetic field (at the group velocity $v_{g\parallel} \sim 1000$ Km/sec) and thus the time that the wave energy should take to convect a distance of the order of the water cloud radius (~ 100 m.) should be $\sim 3\tau_{LH}$, which is comparable to the time that the fastest growing waves (i.e. X1a20 and X1a45) would take to saturate (see Figure 5-4). Therefore, for this interpretation of the Near Zone wave spectrum the simulation results of interest should be those of the early stages, near the saturation period of the fastest growing waves.

Lastly, it should be pointed out that although the beam-arc distribution should be heated by the instability as shown in the simulation, the heating should be partially offset by the continuous creation of cold beam-arc ions from charge exchange reactions. In particular, in the region near the shuttle, which is the region of highest water neutral density and charge exchange rates, the beam-arc distribution should partially regenerate itself due to the charge exchange reactions that produce cold (i.e. at the low temperatures of the water neutrals) beam-arc ions. If the regeneration of the beam-arc distribution in the near shuttle environment would be significant, it would be analogous to the case of the persistence of the unstable bump-on-tail electron velocity distribution in the Earth's foreshock [*Klimas and Fitzenreiter*, 1988]. However, since the characteristic time for saturation of the beam-arc plasma instability is only about $3\tau_{LH}$ (see Figure 5-4) whereas the characteristic time for charge exchange collisions (near the shuttle) is of the order of $200\tau_{LH}$ [Hastings and Gatsonis, 1989], we do not expect the regeneration effect of charge exchange reactions to be important in the interpretation of the PDP wave data using the simulation results for the saturation stages of the instability. Our simulation models do not include this effect of charge

exchange reactions.

6.1.3 The Second Component: The Peak at Low Frequencies

As we have mentioned above, within 10 m. from the Shuttle the beam-arc distribution of water ions is expected to be the $X_p = 1$ beam-arc (Figure 3-2). Figure 5-4a shows the field energy time histories of the $X_p = 1$ beam-arc plasma instability for waves propagating in various directions . It can be seen that waves that propagate near $\theta_{k_\perp} = 45^o$ have the largest field energies in the initial growth stages and near saturation. This is because the initial cold $X_p = 1$ beam-arc reduced distribution for this direction has a larger free energy than those for the other directions, as can be seen in Figure 5-3.

Furthermore, in the shuttle frame, the $X_p = 1$ beam-arc plasma waves propagating near $\theta_{k_\perp} = 45^o$ have Doppler shifted frequencies around 200 Hz which is precisely the frequency of the second component of the spectrum, the low frequency peak. Recall that this was also noted in the interpretation using the linear theory by considering the growth rate spectra curves shown in Figure 4-11. Figure 6-1 shows a comparison of the amplitudes of the waves propagating near $\theta_{k_\perp} = 20^o$ and $\theta_{k_\perp} = 45^o$, inferred from the X1a20 and X1a45 runs of the simulations (Figure 5-4), with the PDP data. The error bars denote the range of the electric field amplitude fluctuations near saturation. The agreement with the experimental data is good.

6.1.4 The Third Component: The Peak Near the Lower Hybrid Frequency

Let us try to interpret the peak near the lower hybrid frequency of the near zone PDP spectrum in terms of the beam-arc plasma waves propagating in the range $90^o \leq \theta_{k_\perp} \leq 270^o$. The Doppler shifted frequency of these waves is indeed near the lower hybrid frequency (in log scale plots of the PDP spectrum). However, the $X_p = 1$ beam-arc of the near shuttle region excites only low amplitude waves for $90^o \leq \theta_{k_\perp} \leq 270^o$ (i.e. low compared to the amplitudes of the forward propagating waves, as can

be seen from the results of the X1a90 and X1a135 runs shown in Figure 5-4) which could not explain the spectrum peak near the lower hybrid frequency. On the other hand, in Chapter 3 we have shown that the water ion distribution function changes from a beamlike beam-arc to a more ringlike beam-arc with increasing upstream distance from the shuttle (see Figure 3-2). The waves excited in the propagation directions $90^o \leq \theta_{k_\perp} \leq 270^o$ in the upstream region of the shuttle by the more ringlike beam-arcs have larger amplitudes than those excited in these directions by the local near region beam-arc distribution. Therefore, it could be that, because of the plasma density inhomogeneities and warm plasma effects, some downstream convection of these (lower hybrid) waves generated upstream might actually occur that would correlate with the lower hybrid frequency peak of the near zone spectrum. In the remainder of this section we discuss this possibility further.

In particular, at a distance of about 75 meters upstream from the shuttle the beam-arc distribution is expected to be the $X_p = 5$ beam-arc. In Figure 5-6, the results of the simulation of the $X_p = 5$ beam-arc plasma instability show that after $30\tau_{LH}$ of the waves being excited, in the quasi-steady state, the amplitudes of the waves which propagate downstream $90^o \leq \theta_{k_\perp} \leq 270^o$ are comparable to the amplitudes of the most linearly unstable waves (i.e. which propagate in the $\theta_{k_\perp} = 45^o$ direction). Furthermore, since lower hybrid waves have small group velocity components (in the earth's frame, small compared to the orbital velocity) perpendicular to the magnetic field (see Section 6.2.1), if downstream convection of waves would occur, we would expect that (in the shuttle frame) most waves would convect downstream along with the background ionospheric plasma. This would imply that the time that the waves excited by the $X_p = 5$ beam-arc 75 meters upstream of the shuttle would take to convect to the near vicinity of the shuttle (within 10 m.) would be larger than $30\tau_{LH}$. Therefore, by the time the upstream generated waves would reach the near shuttle region they would have larger amplitudes than those of waves generated in the near vicinity of the shuttle with $90^o \leq \theta_{k_\perp} \leq 270^o$. This can be confirmed by the simulation results shown in Figures 5-4 and 5-6 by comparing the quasi-steady state wave amplitudes of the X5a90 and X5a135 runs with the amplitudes before saturation

of the X1a90 and X1a135 runs, respectively.

Similarly, waves generated in other regions directly upstream of the shuttle, propagating with $90^o \leq \theta_{k_\perp} \leq 270^o$, would convect downstream to the near vicinity of the shuttle and would have relatively large amplitudes by the time they would reach the near shuttle region. Therefore, they would also contribute to the lower hybrid frequency peak of the near field spectrum. In Figure 6-1, the error bars near the lower hybrid frequency peak denote the ranges of wave amplitude fluctuation near the quasi-steady state of the X5a90 and X5a135 runs. It should be noted that, even assuming that downstream convection of waves would occur, the amplitudes of the convected waves would not be large enough to explain the spectrum peak near the lower hybrid frequency. Further research is thus required to explain this peak of the near zone PDP spectrum.

In this attempt to interpret the lower hybrid frequency peak of the spectrum by assuming that downstream convection of waves would occur, we have not taken into account the fact that the water ion density decreases with increasing upstream distance from the shuttle. Figure 6-4 shows the field energy time histories of the X5a45 instability for the density ratio near the shuttle $n_w/n_e = 0.15$, which is the density ratio used in the simulations discussed above, and for lower density ratios, namely, $n_w/n_e = 0.05$ and 0.01 corresponding to those found at distances of 50 m. and 100 m. upstream of the shuttle, respectively. It is important to note that for the various density ratios in the range of interest, the quasi-steady state wave field energies have almost the same levels. Therefore, since the effect of water ion density decreases upstream from the shuttle on the quasi-steady state wave field energies is relatively minor, this effect should not change significantly the results of the above attempt to interpret the lower hybrid frequency peak of the spectrum by assuming downstream convection of waves. Finally, we should mention that the quasi-steady state dispersion relations for the density ratios of interest for the upstream shuttle region are almost the same. Specifically, the dispersion relations corresponding to these density ratios have their highest mode energies with earth's frame frequencies close to but slightly above the lower hybrid frequency and correspond to the most

linearly unstable wave mode numbers (i.e. wavelengths in the range of 2-4 meters). Furthermore, the instability evolutions for these cases are qualitatively the same as that with the higher density ratio ($n_w/n_e = 0.15$), which we have studied in detail in Chapter 5, although for the smaller ratios the instabilities show earlier transitions to kinetic instability and tend to saturate mostly by quasilinear plateau formation rather than by particle trapping.

We shall discuss further the nature of the lower hybrid frequency peak in Section 6.2.2 where we will interpret the far field ion trail wave spectrum, which also has a peak near ω_{LH}.

6.2 Interpretation of the Mushroom Features of the Far Downstream Ion Trail Spectrum

The PDP wave data of the far downstream region of the shuttle shows that the wave spectrum in these regions is characterized by "mushroom" type spectral features (see Figures 2-1 and 2-2). In Chapter 2, we have seen that the mushroom features are dependent on the magnitude of the orbital velocity component parallel to the magnetic field (i.e. the $V_\parallel/V_T$ effect). Besides this dependence, at that point in our analysis we were unable to interpret the other major features of the spectrum. Figure 2-18 shows the wave spectrum of the region 250 m. directly downstream of the shuttle for a time corresponding to the center of the mushroom. The wave spectrum of the near field region (within 10 m. from the shuttle) is also shown in dashed lines. Both spectra are seen to have similar characteristics and be within the same intensities. As the near field wave spectrum, the downstream wave spectrum is also characterized by the peak near the lower hybrid frequency and the uniform component at frequencies below the lower hybrid frequency peak. The far downstream spectrum, however, does not have a peak at low frequencies (near 200 Hz); in contrast, it has low intensities at these frequencies, lower than those of the uniform component. It is important to note, by considering Figure 2-2 that the top cap component of the mushroom (i.e. the lower hybrid frequency peak) persists as the major component of the far downstream wave spectrum even at large values of $V_\parallel/V_T$ whereas the uniform component of the

214

spectrum decreases in intensity as $V_\parallel/V_T$ increases.

6.2.1   The Source of the Downstream Water Ion Trail Waves

In Chapters 4 and 5, we have shown that the net effect of the beam-arc plasma instability in the space shuttle environment is the excitation of the lower hybrid modes of the ambient ionosphere; specifically, lower hybrid waves in various propagation directions nearly perpendicular to the magnetic field. The (earth frame) plasma dispersion relation of these waves, in the infinite plasma fluid limit, can thus be given approximately by

$$\omega^2 \approx \omega_{LH}^2 \sin^2\phi + \omega_{ce}^2 \cos^2\phi \qquad (6.2)$$

where ϕ is the angle between the propagation vector and the magnetic field (i.e. $\phi = 90^o - \phi_{k_\parallel}$) [Bittencourt 1986, or any standard plasma physics textbook]. Now, the important waves have frequencies $\omega \sim \omega_{LH}$ and propagate nearly perpendicular to the magnetic field with $\cos\phi \sim \omega_{LH}/\omega_{ce} \ll 1$ and $\sin\phi \sim 1$ (i.e. the fastest growing waves propagate with $\phi_{k_\parallel} \sim \sqrt{m_e/m_O}$, see Chapters 4 and 5), such that $\omega_{LH} \sin\phi \sim \omega_{ce} \cos\phi$, or equivalently,

$$\omega \sim \omega_{LH} \sin\phi \sim \omega_{ce} \cos\phi \qquad (6.3)$$

In addition, $\omega \sim \omega_{ce} \cos\phi = \omega_{ce} k_\parallel/k \sim \omega_{ce} k_\parallel/k_\perp$, which implies that the group velocity parallel to the magnetic field is approximately

$$\frac{\partial\omega}{\partial k_\parallel} \sim \frac{\omega_{ce}}{k_\perp} \qquad (6.4)$$

Using our simulation results or the PDP data, which show that the (perpendicular) wavenumbers scale as $k_\perp \approx \omega/V \approx \omega_{LH}/V$ (where we have dropped the subscript T in the orbital velocity), we can express the group velocity parallel to the magnetic field as follows

$$v_{g\parallel} = \frac{\partial\omega}{\partial k_\parallel} \sim V\frac{\omega_{ce}}{\omega_{LH}} = V\sqrt{m_O/m_e} \gg V \qquad (6.5)$$

[Martinez-Sanchez, 1993]. Furthermore, the PDP data and the simulation results show that in any plane nearly perpendicular to the magnetic field the dispersion

215

relation is fairly flat with $\omega \sim \omega_{LH}$, which implies that the group velocity in the plane perpendicular to the magnetic field is almost zero and thus lower than the orbital velocity V

$$v_{g\perp} \sim 0 \qquad\qquad (6.6)$$

Therefore, since the group velocities of the lower hybrid waves excited in the ionosphere by the beam-arc plasma interaction should be very large and nearly parallel to the magnetic field, the energy of the excited waves should radiate away from the wave source regions very rapidly along the magnetic field lines (that is, in the direction almost perpendicular to the orbital plane). This means that in the shuttle frame waves should not have enough time to convect downstream along with the ionospheric plasma before their energy radiates along the magnetic field lines to far away regions above and below the orbital plane [Martinez-Sanchez, 1993]. Consequently, the source of waves observed in the downstream ion trail should be the local ion trail; the waves observed by the PDP (when it flew mostly in the orbital plane during the free-flight mission) should have been generated near the PDP.

It should be pointed out that since the energy of the excited waves should radiate away from the wave source region along the magnetic field at the group velocity $v_{g\parallel} \sim$ 1000 Km/sec, the time that the wave energy should take to convect a distance of the order of the water cloud radius (~ 100 m.) should be $\sim 3\tau_{LH}$, which is comparable to the time that the growing amplitudes of the excited waves would take to saturate (see Figure 5-4). Therefore, in the interpretation of the downstream ion trail waves that follows the simulation results of interest will be those for the early stages near saturation. We should note that although the field energy amplitudes in the various runs (for the different propagation directions) change rapidly in the early stages near saturation (see Figure 5-4), the relative differences between the amplitudes of the various runs stay approximately the same or at least preserve the same relative order within about $2\tau_{LH}$ from saturation. This will thus gives us some flexibility in our comparisons of the simulation amplitudes with those of the PDP spectra which will be represented by error bars in the plots where these comparisons will be shown.

It is not unlikely that the source of the downstream ion trail waves is the local ion trail since the beam-arc water ion densities in the ion trail are high. Recall that the beam-arc water ion densities in the downstream ion trail regions are comparable to the high densities near the shuttle (e.g., $n_w/n_e = 0.15$) because water ions stay downstream of the shuttle trapped in the earth's magnetic field [Paterson and Frank, 1987]. Furthermore, various characteristics of the PDP data also suggest that the source of downstream waves is the local ion trail. The fact that the wave electric fields are stronger, exceeding 1 mV, downstream from the shuttle and along the magnetic field lines connected to the shuttle is consistent with the proposed wave source regions and with our prediction that the energy of the waves should radiate away rapidly from the wave source regions along the magnetic field. The PDP data also shows that the noise is weakest upstream of the shuttle and that the mushroom spectral features were observed only downstream of the shuttle and not in the upstream region (see Figure 2-5). The weaker wave intensities in the upstream region are consistent with the simulation results shown in Figure 6-4 which indicate that the (saturation) fields of waves generated in regions of lower water ion densities should be smaller.

In contrast to our suggestions discussed above, Feng et al. [1993] have proposed that the source of the waves observed in the downstream ion trail should be the downstream convection of the waves generated in the near vicinity of the shuttle. This proposition was based partly on the PDP data of Figure 2-18 which shows that the wave spectra of the near region and downstream region of the shuttle both have a uniform component and a peak near the lower hybrid frequency and are within the same intensity ranges. Moreover, they have argued that since, in the plane perpendicular to the magnetic field, the group speeds of lower hybrid waves are small compared to the shuttle speed (see Figure 5-13), in the shuttle frame the waves should mostly convect downstream along with the ambient ionospheric plasma. However, Feng et al. [1993] have completely ignored the fact that the group velocity component of lower hybrid waves parallel to the magnetic field is very large. Therefore, we expect that our prediction that the source of downstream waves is the local ion trail should be more accurate than their (almost opposite) prediction.

6.2.2 Interpretation of the Top Cap Component of the Mushroom

In the previous section, we have noted that the source of the downstream ion trail waves should be the local ion trail. Let us recall that the water ion distribution in the downstream trail of the shuttle is a "rotating" symmetric $X_p = -\pi r_{Lw}$ beam-arc (see Figures 3-4 and 3-6), as discussed in Chapter 3. Since the $X_p = -\pi r_{Lw}$ beam-arc is symmetric and has a small effective arc length, it should behave approximately as a beam distribution. In Figure 3-5b, we show that the gyrophase angle of the beam-like distribution increases with increasing distance downstream from the shuttle, as discussed in Chapter 3. Furthermore, since the strongest waves that these beamlike distributions should excite through the $X_p = -\pi r_{Lw}$ beam-arc plasma instability should have propagation directions in the local beam velocity direction, we expect most waves generated in the downstream region of the shuttle to have propagation directions in the range $90^o \leq \theta_{k_\perp} \leq 270^o$. This is because the instability time scale (τ_{LH}) is much smaller than the cyclotron period of the water ions ($\tau_{cw} \sim 172\tau_{LH}$) and the $\mathbf{E} \times \mathbf{B}$ cycloidal trajectories of the water ions (in the shuttle frame) have corresponding beam distribution velocities (in the earth's frame) with negative $V_{X_{earth}}$ components along almost 90% of the downstream water ion trail, as shown in Figure 3-5c. Consequently, most of the waves generated throughout the downstream water ion trail should have propagation directions in the range $90^o \leq \theta_{k_\perp} \leq 270^o$. Now, the Doppler shifted frequency of these strong waves, which is obtained by using Equation 6.1, is near the lower hybrid frequency (in a log scale plot) as shown in Figure 6-2 and thus can explain the lower hybrid frequency peak of the far field ion trail wave spectrum (i.e. the top cap of the mushroom spectral feature). In Figure 6-2, the error bar near the lower hybrid frequency denotes the wave field amplitude variation for the time period near saturation of the X1a45 run. Note that we have used the results of the X1a45 run to represent the fields of the $X_p = -\pi r_{Lw}$ beam-arc plasma instability for the propagation direction of the strongest modes, that is, for the direction of the beam (corresponding to the gyrophase angle of the plane of symmetry of the $X_p = -\pi r_{Lw}$ beam-arc). This is because for both of these cases the reduced

218

distributions, which are used in 1d PIC code simulations, should be approximately the same.

6.2.3 Waves Observed Above Several Times the Lower Hybrid Frequency

As *Cairns and Gurnett* [1991a,b] noted, the PDP wave spectrum above the lower hybrid frequency shows only a smooth decrease without apparent structure. The wave data indicate that the broadband waves, observed near the shuttle and far in the downstream ion trail, extend up to frequencies of the order of 50 kHz, corresponding to 5 - 10 times the lower hybrid frequency (see Figures 2-16 and 2-18). Now, in our linear analysis of the beam-arc plasma instability, we have found that waves propagating backwards ($\theta_{k_\perp} = 180^o$) could explain waves up to about $2.5\Omega_{LH}$ (see Figure 4-11b). This was found by using Equation 6.1 with $\theta_{k_\perp} = 180^o$ and noting that for the linearly fastest growing modes ($k_{\gamma\mathrm{max}}$) in this propagation direction $\omega \approx 1.3\Omega_{LH}$ and $k \approx 1.3\Omega_{LH}/V$. For this interpretation using the linear theory we have assumed that the linearly most unstable modes ($k_{\gamma\mathrm{max}}$) are the modes that eventually reach the largest field energies in the nonlinear regime. Although our simulation results showed that this assumption was relatively accurate, they also show that in the nonlinear regime large wavenumber modes, with wavenumbers up to about $2k_{\gamma\mathrm{max}}$, are destabilized due to evolution of the beam-arc distribution. In particular, in Section 5.4.4 we have seen that the destabilization of large wavenumber modes is due to the advance of the beam-arc front to lower velocities (see Figure 5-9a). Therefore, since these are large wavenumber modes ($k_{\gamma\mathrm{max}} < k < 2k_{\gamma\mathrm{max}}$) their contribution to the Doppler shifted spectrum is to frequencies around 5 times the lower hybrid frequencies and thus they can explain waves observed above several times the lower hybrid frequency.

It should be pointed out that since in the earth's frame the bunches of high density water ions created very close to the shuttle, shown in Figure 3-5a, have circular trajectories of large radius, they effectively see less perturbed ionospheric regions as they move along their trajectories. This should make the process of destabilization of

the large wavenumber modes more efficient since, as we have discussed in Section 5.4.4, this process (which is due to the advance of the beam-arc front to lower velocities) is arrested by Landau damping from the ionospheric ion distribution as this distribution merges with the advancing beam-arc front. Therefore, since this merging would be delayed if the background ion distribution would not be broadened by the waves, the constant motion of the bunches of high density water ions to regions of less perturbed ionosphere should favor the process of destabilization of large wavenumber modes. We should also note that the partial regeneration of the beam-arc distribution due to charge exchange reactions should also delay the merging (or the plateau formation, see Section 5.4.5) and thus favor the destabilization of large wavenumber modes.

6.2.4   Interpretation of the Uniform First Component of the Far Downstream Ion Trail Spectrum

As we have discussed above, the source of waves observed in the downstream ion trail should be the local ion trail. In Section 6.2.2, we have interpreted the lower hybrid frequency peak of the spectrum of the downstream regions by noting that in these regions the water ion distribution is the $X_p = -\pi r_{Lw}$ "rotating" symmetric beam-arc having beam velocities (i.e. the velocities in the direction of the center of the arc or center of symmetry) with negative $V_{X_{earth}}$ components along almost 90 % of the downstream water ion trail (see figure 3-5c). Now, we can argue that since the $X_p = -\pi r_{Lw}$ beam-arc distribution is not a beam but has a finite arc, waves should not only be excited in the beam direction (which is the propagation direction of the most linearly unstable modes) but also in the other directions within the range of gyrophase angles of the arc. As discussed in Section 6.2.2, the field energies of the waves driven in the beam direction should be given by the results of the X1a45 run (Figure 5-4) since this run should be equivalent to a $-X\pi r_{Lw}$a0 run (at least in 1-d simulations where the reduced distributions for both of these cases is almost the same). Similarly, the field energies of the waves driven in directions other than the beam direction, within the range of gyrophase angles of the arc, should be given by the results of the X1a0 and X1a60 runs. We note from the results of the X1a0 and X1a60 runs,

shown in Figure 5-4a, that the contribution of the relatively large amplitudes of these waves to the downstream wave spectrum should be important. Furthermore, because the beam velocity of the beam arc distribution has a direction within the range $-90^o \leq \theta_{k_\perp} \leq 270^o$ along almost 90% of the downstream water ion trail (see Figure 3-5) and the effective arc of this $(X_p = -\pi r_{Lw})$ beam-arc is about 84° (see Figure 3-4), there should be various regions in the downstream ion trail where the waves driven in directions within the effective arc but other than the beam direction should have propagation directions within the ranges $-90^o \leq \theta_{k_\perp} \leq -50^o$ or $50^o \leq \theta_{k_\perp} \leq 90^o$. Therefore, in general, the waves generated downstream with propagation directions in the ranges $-90^o \leq \theta_{k_\perp} \leq -50^o$ or $50^o \leq \theta_{k_\perp} \leq 90^o$ should have relatively large amplitudes and could explain the spectrum amplitudes in the frequency range of the uniform component since this is the range where these waves Doppler shifted frequencies fall. In Figure 6-2, the error bars in the range of the Doppler shifted frequencies corresponding to the uniform spectrum component represent the ranges of wave amplitude fluctuations near saturation of the X1a0 and X1a60 runs, inferred from Figure 5-4a.

Further evidence of the contribution of these waves to the uniform component will be shown in our analysis of the interference pattern data in Section 6.3.

6.2.5 The Lack of the Low Frequency Peak in the Far Field Ion Trail Spectrum

Figure 2-18 shows a comparison of the wave spectrum of the region far downstream of the shuttle (solid line), for a time period corresponding to the center of the mushroom spectral feature, with the wave spectrum obtained within 10 m. from the shuttle (dashed line). As we have already noted, in contrast to the near field wave spectrum, the spectrum of the downstream region does not have a peak at low frequencies (near 200 Hz). In the downstream spectrum the wave intensities at these low frequencies are lower than those of the uniform first and the lower hybrid frequency peak components, which both spectra have. The reduced intensities at low frequencies in the downstream spectrum can be explained by extending the arguments used in the previ-

ous section. In particular, we have shown that because the beam velocity of the downstream beam-arc distribution has a direction within the range $-90^o \leq \theta_{k_\perp} \leq 270^o$ along almost 90% of the downstream ion trail, the strongest waves in the downstream region should be generated with propagation directions within this range. We have also noted that because the downstream beam-arc distribution is not simply a beam but has a finite effective arc, strong waves should also be excited with propagation directions within the ranges $-90^o \leq \theta_{k_\perp} \leq -50^o$ and $50^o \leq \theta_{k_\perp} \leq 90^o$. Now, we can extend these arguments to predict that in the downstream ion trail the waves generated with propagation directions in the range $-50^o \leq \theta_{k_\perp} \leq 50^o$ should have relatively low amplitudes. This is because these waves would be generated in the directions opposite to the beam-arc (that is, in directions almost always opposite to the beam velocity of the downstream beam-arc distribution). The amplitudes of these waves should therefore be equivalent to those of the X1a135 and X1a90 runs shown in Figure 5-4. Furthermore, downstream waves propagating within the range $-50^o \leq \theta_{k_\perp} \leq 50^o$ have low ($\sim$ 200 Hz) Doppler shifted frequencies and thus can explain the lack of the low frequency peak in the far downstream ion trail spectrum. In Figure 6-2, the error bars a and b denote the ranges of wave amplitude fluctuations before but near saturation of the X1a135 and X1a90 runs, respectively.

Lastly, let us recall from Chapter 2 that the lower hybrid type interference patterns observed in the wideband data correspond to the uniform and lower hybrid frequency peak components of the downstream region spectrum. Since the 0-10kHz wideband channel had a lower cutoff at 400 Hz, no information is available on the low frequency peak (near 200 Hz). No interference patterns can be identified in the 400-1000Hz channel, but this channel may be too narrow for interference patterns to be clearly identified.

6.2.6 The $|V_\parallel/V_T|$ Effect and the Low Frequency Triangular Spectral Features of the Free-Flight Mission Spectrograms

The wave spectrum of the far downstream ion trail region detected during the PDP free-flight mission shows significant wave activity mostly from the low frequency range (~ 10 Hz) up to the lower hybrid frequency (see Figure 2-2). As we have discussed in Section 2.1, *Cairns and Gurnett* [1991a] have analyzed this spectrum and have shown that in the far downstream ion trail the wave amplitudes are affected by the magnitude of the orbital velocity component parallel to the magnetic field ($V_\parallel$). Specifically, they have found that when the flow is approximately perpendicular to the magnetic field ($V_\parallel/V_\perp \sim 0$) large wave amplitudes and characteristic "mushroom" wave structures are observed, whereas more nearly parallel flows $|V_\parallel| \sim V_\perp$ are characterized by low wave levels.

As discussed in Section 2.1.2, *Cairns and Gurnett's* [1991a] have argued that the mushroom spectral features arising from variations in the spectrum wave amplitude that are inversely proportional to $|V_\parallel/V_T|$ can be explained in terms of the $V_\parallel/V_T$ effect as follows: (1) larger values of $|V_\parallel/V_T|$ imply smaller $V_\perp$ which in turn result in beam-arc distribution functions with arcs of smaller radius, and thus lower free energy, which would correlate directly with lower wave amplitudes in the spectrum and (2) if the source of the far downstream ion trail waves is the convection of waves from the near field, the different motions (parallel to the magnetic field) of the water ions driving the waves and the ionospheric plasma convecting the waves would imply that the waves will have a minimum (maximum) path length available for growth when $|V_\parallel/V_T|$ is large (small), thereby explaining the differences in intensity.

Now, let us extend this theory about the $V_\parallel/V_T$ effect by making the following observations in light of our simulation results. Figure 6-3 shows results of simulation runs that we have made in order to examine the effect of changing the values of $|V_\parallel/V_T|$ on the wave field energies. In this figure, we show the results of X5a45 runs (i.e. $X_p = 5$ beam-arc plasma instability with $\theta_{k_\perp} = 45^o$ and $\bar\phi_{k_\parallel} = 1$) for three values of $|V_\parallel/V_T|$. For these three cases the values of the arc radii (in velocity space) were

223

given by $V_\perp = \sqrt{V_T^2 - V_\parallel^2}$, correspondingly. We note that changes in the values of $|V_\parallel/V_T|$ have a significant effect on the amplitudes of the wave field energies. The field energy decreases by about one order of magnitude as $|V_\parallel/V_T|$ increases from 0.0, which is the lowest value in orbit, to 0.8, which is the maximum value in orbit. Therefore, the correlation of the wave field decreases, in the lower frequency ($\omega < \omega_{LH}$) portion of the mushroom spectral features, with the increases of $|V_\parallel/V_T|$ observed in the PDP experiments (see Figures 2-5 and 2-12) can indeed be explained (1). That is, larger values of $|V_\parallel/V_T|$ imply smaller $V_\perp$ values which in turn result in beam-arc distribution functions with arcs of smaller radius, and thus lower free energy, which then drive weaker waves.

Let us now discuss (2) by recalling that in contrast to Feng et al. [1993] prediction that the source of far downstream ion trail waves is the convection of waves from the near vicinity of the shuttle, in Section 6.2.1 we have shown, by using fluid theory for an infinite homogeneous plasma, that the source of the ion trail waves should be the local ion trail. Therefore, the mechanism (2) is unlikely to occur or contribute to the $|V_\parallel/V_T|$ effect. However, it could be that because of the density inhomogeneities and warm plasma effects some convection of waves would occur in the plane perpendicular to the magnetic field. If this was the case we could argue that the wave amplitude variations, in the lower frequency ($\omega < \omega_{LH}$) portion of the mushroom spectral features, could also be partly due to variations in the paths lengths available for the convective growth of the waves. In particular, note that the water ions driving the waves are confined to the downstream ion trail which extends parallel to the orbital velocity direction, has a finite cross section (with a diameter of the order of the neutral water cloud diameter) and drifts relative to the background ionospheric plasma at a velocity $V_\parallel$ (parallel to the magnetic field). Consequently, waves would grow in the background ionospheric plasma, to significant levels, only if they would spend enough time in the ion trail (i.e. only if the path lengths available for their growth would be sufficiently large). Now, let us recall that waves in the frequency range below ω_{LH} can be explained in terms of Doppler shifted waves propagating with $-90^o \leq \theta_{k_\perp} \leq 90^o$. Specifically, Doppler shifted waves propagating with $-50^o \leq \theta_{k_\perp} \leq 50^o$ can explain the lower frequency

waves of this range and those propagating sidewise, with $-90^o \leq \theta_{k_\perp} \leq -50^o$ or $50^o \leq \theta_{k_\perp} \leq 90^o$, can explain the higher frequency waves of this range. It would thus seem that the reason why the higher frequency waves of the frequency range below ω_{LH} dissapear first as $|V_\parallel/V_T|$ increases (Figures 2-1 and 2-2) would be that the path lengths available for convective growth of the waves would be reduced mostly in directions perpendicular to the ion trail (i.e. to the right and to the left of the ion trail, and not as much in the direction parallel to the ion trail) as $|V_\parallel/V_T|$ increases. Actually, this reduction in the path lengths available for growth in the direction perpendicular to the ion trail would be expected because of two following factors that would become more important as $|V_\parallel/V_T|$ increases and the instability becomes weaker (i) the finite cross section of the ion trail and (ii) the drift of the ion trail, in the direction parallel to the magnetic field, relative to the background ionospheric plasma. Therefore, at large $|V_\parallel/V_T|$ only forward propagating waves (which can explain the foot of the mushroom) and backwards propagating waves (which can explain the top cap of the mushroom) would have long enough path lengths for growth, and this would be in agreement with PDP wave data (see Figures 2-2, 2-5 and 2-12).

6.2.7 Enhancements of Low Frequency Waves During Thruster Firings or Water Releases

In Sections 2.3 and 2.4, we have discussed the fact that water releases (e.g., thruster firings, water dumps and flash evaporator releases) produce enhancements of the wave amplitudes at low frequencies ($\omega < \omega_{LH}/6$) as shown, for instance, in Figure 2-20 for the case of water dumps. Roughly speaking, the water neutral density of the neutral cloud that surrounds the shuttle increases rapidly as a result of the releases. For the case of thruster firings, Hoffman and Hetreck [1982] have estimated that the neutral water density should be 3 orders of magnitude higher than the ambient plasma density at distances of the order of 100 m. from the thruster during the firing. Now, the water neutral molecules of higher density resulting from the releases should undergo charge exchange reactions and produce water ions. Near the shuttle (within 20 m.) these water ions should have a beamlike beam-arc distribution similar to

the $X_p = 1$ distribution and the water ion to electron density ratio should be larger than the nominal 15%. The water ion distribution should then drive waves by the $X_p = 1$ beam-arc plasma instability and, as shown by the simulation results of this instability (see Figure 5-4a), the waves driven near the $\theta_{k_\perp} = 45^o$ propagation direction should reach the largest field amplitudes. Furthermore, as shown in Figure 6-1, waves propagating in the $\theta_{k_\perp} = 45^o$ direction have low (Doppler shifted) frequencies ($\omega < \omega_{LH}/6$), in the shuttle frame, which are in the frequency range of the enhanced low frequency waves observed during water releases. Therefore, since the water ion to electron density ratio increases during the water releases and the simulation results in Figure 6-4 show that the wave field amplitudes increase as the n_w/n_e ratio increases, the waves propagating near $\theta_{k_\perp} = 45^o$ can explain the low frequency field enhancements observed during the water releases, when the PDP was placed on the RMS arm of the shuttle (within 10 m. from the shuttle). It should be pointed out that since the water neutral density around the shuttle increases significantly during, and right after, the water releases, the resulting larger charge exchange rates should lead to a larger regeneration of the water ion beam-arc distribution. Consequently, as discussed in Section 6.1.3, the simulation times of interest to take into account this effect should be those near saturation of the instability (e.g., $t = 5\tau_{LH}$ for the X1a45 run) since the beam-arc distribution at these times should be equivalent to the partially regenerated beam-arc distribution. The regeneration mechanism should also explain why the enhancements of low frequency waves last as much as 10 to 20 sec even though the thruster firings only last a fraction of a second. This is because the higher density neutrals from the water releases should continue to co-orbit with the shuttle and undergo charge exchange reactions even after the water release operation stops.

The wave data obtained when the PDP was far downstream from the shuttle, during the free-flight mission, also shows that thruster firings cause mostly enhancements of low frequency waves (e.g., Figure 12 of Feng et al. 1993). Now, the fact that thruster firings produce mostly enhancements of low frequency waves not only in the near vicinity of the shuttle but also far downstream of the shuttle may im-

ply that the downstream rotating beam-arc distribution scenario may not apply in some thruster firing cases. This is because thruster firings may produce water neutral density increases over large non-spherical volumes and not only mostly around the shuttle as in the case of the steady state shuttle water cloud. Further work on this issue is required.

Lastly, there is another possible explanation for the low frequency waves observed during water releases. This explanation does not involve the excitation of the beam-arc plasma instability but the following process. Shuttle surface potentials of at least 20 volts could generate currents to and from these surfaces due to the ionization of the extra water vapor around during water releases, as in the case of a plasma contactor. In the shuttle case these currents would act as sources of plasma waves with near zero frequencies in the shuttle frame. Further research is necessary on this issue.

6.3 Interpretation of the Lower Hybrid Interference Patterns of the PDP Spectrograms

As discussed in Section 2.1.3, lower hybrid interference patterns in the wideband data were observed frequently during the time period from 01:24UT to 04:41UT of the free flight mission (see Figure 2-10). Let us recall that interference patterns indicate the times when the PDP was in regions where waves with different wavelength propagated in only one direction. It is important to note that the regions where interference patterns were observed were the regions with the strongest waves. As discussed in Section 2.1.3, the observed lower hybrid interference patterns can be divided in two groups. Group 1 interference patterns are those that were observed in the shuttle wake region when the PDP was about 100 m and 250 m directly downstream of the shuttle. Most interference patterns were in this group, upwardly and downwardly shifted. Feng et al. [1993] have argued that this group of waves corresponds to near zone waves that propagate downstream mostly in the orbital (X'-Y') plane (since they are symmetric interference patterns). Group 2 also consists of upwardly and downwardly shifted interference patterns. These were observed when the PDP was approaching the regions directly downstream of the magnetic field lines

227

passing through the shuttle. The group 2 includes the "tilted" interference patterns which are relatively rare. According to Feng et al. [1993], this second group of waves are not generated in the near vicinity of the shuttle and are not likely to be generated along the magnetic field lines connected to the shuttle.

6.3.1 Source of Group 1 Interference Pattern Waves

Feng et al. [1993] have argued that the source of waves that form the group 1 interference patterns, which were observed in almost directly downstream of the shuttle, is the convection of waves from the near vicinity of the shuttle (within 20 m. from the shuttle). In contrast, we have argued that the source of the downstream waves, including the group 1 waves, should be the local ion trail. We now show evidence that the waves that form the group 1 interference patterns should be the generated near the downstream location of the PDP. For this analysis of interference patterns it is useful to remember that the water ion density in the water ion trail directly downstream of the shuttle is fairly constant (and near its maximum value) and that the water ion distribution function in the ion trail is the rotating $X_p = -\pi r_{Lw}$ symmetric beam-arc (see Figure 3-5).

There are various experimental facts that suggest that the source of waves that form the group 1 interference patterns is the region near the downstream location of the PDP. First, all of the group 1 interference pattern events were observed in the region directly downstream of the shuttle which is the region where the wave fields are the largest, exceeding 1 mV. The noise is the weakest upstream of the shuttle. This is consistent with our simulation results that show that weaker waves should be excited by smaller water ion to electron density ratios (see Figure 6-4). Second, during the observations of interference patterns the wave activity was clearly enhanced near the lower hybrid frequency, which provides further evidence that the interference pattern waves are generated in the region downstream of the shuttle. This is because the interference pattern waves are in the frequency ranges of the uniform and lower hybrid peak components of the far downstream wave spectrum and, as we have shown in Sections 6.2.2 and 6.2.4, such components are most likely to be composed of waves

generated in the downstream ion trail by the local "rotating" $X_p = -\pi r_{Lw}$ symmetric beam-arc distribution.

In particular, major evidence that the group 1 interference patterns waves are generated near the regions where they are detected, in the downstream ion trail, comes from the agreement of the wave propagation directions inferred from the interference pattern data with those predicted from the characteristics of the rotating beam distribution of the downstream water ion trail. In what follows we show this evidence. Figure 2-10 shows, in the X'-Y' plane, the propagation directions, of the interference pattern waves along the PDP trajectory for the period from 01:24 UT to 04:41UT. In the trajectory near $X' = -120$ m. most interference pattern waves propagate antiparallel to the orbital velocity direction and in the trajectory near $X' = -250$ m. most waves propagate parallel to the orbital velocity direction. Now, let us note that these experimental results are in agreement with those predicted assuming that these waves are generated near the PDP and thus propagate in the direction of the beam velocity of the local rotating beam distribution. This is because in Figure 3-5 we see that at $X' = -\pi r_{Lw} \approx -120$ m. the beam velocity of the water ion distribution is antiparallel to the orbital velocity direction and that at $X' = -2\pi r_{Lw} \approx -240$ m. the beam velocity is parallel to the orbital velocity. Furthermore, let us also note that, as shown in Figure 2-10, the interference pattern waves observed near ($X' = -150$ m, $Y' = -50$ m) and ($X' = -240$ m, $Y' = 100$ m) have propagation directions with positive Y' components, which agrees with our suggestion that the interference pattern waves should be generated by the local water ion distribution near the PDP propagating in the beam velocity direction. This is because the beam velocity of the water ion distribution has a positive Y' component for $-2\pi r_{Lw} < X' < -\pi r_{Lw}$ as shown in Figure 3-5c.

6.3.2 Source of Interference Pattern Waves Observed Near the Magnetic Field Lines Passing Through the Shuttle

Feng et al. [1993] analysis of the PDP wave data shows that the regions of highest wave intensities are the regions directly downstream of the shuttle and along the mag-

netic field lines passing through the shuttle. Furthermore, they show that interference patterns (group 2) were observed when the PDP was near the magnetic field lines passing through the shuttle. Cairns and Gurnett [1991a] concluded that these waves near the PDP-shuttle magnetic conjunctions correspond primarily to waves generated near the shuttle being observed along the magnetic field lines. They argue that this is because lower hybrid waves have wavevectors nearly perpendicular to the magnetic field and thus their electric fields should vary slowly with distance along the magnetic field.

Now, we can interpret more accurately the group 2 interference pattern waves observed along the PDP-shuttle magnetic conjunctions by noting that they should be a result of the large flow of wave energy along the magnetic field lines, of the waves generated near the shuttle (i.e. due to the very large lower hybrid wave group velocity parallel to the magnetic field, see Section 6.2.1). In particular, as we have discussed in the previous sections, the waves generated near the shuttle should be excited by the $X_p = 1$ beam-arc plasma instability preferentially in the $\theta_{k_\perp} = 45^o$ propagation direction (see Figure 5-4a). Therefore, since these waves have propagation vectors in mostly one direction ($\theta_{k_\perp} = 45^o$) and their energy flows rapidly along the magnetic field, they can explain the formation of group 2 tilted interference patterns. In Figure 2-10, we see that the group 2 tilted interference pattern waves of the 0310 UT and 0200 UT events may have propagation directions close to $\theta_{k_\perp} = 45^o$. It is difficult to verify this suggestion since the X'-Y' plane is not the plane perpendicular to the magnetic field. However, there seems to be at least some agreement with our suggestion that the waves of the 0310 UT and 0200 UT events propagate in the $\theta_{k_\perp} = 45^o$ direction because in the X'-Y' plane (Figure 2-10) these waves are seen propagating forward.

We can also argue that although in the region directly downstream of the shuttle, along the water ion trail, the water ion densities should be fairly high and constant [Paterson and Frank, 1993] and the water ion distribution should be a rotating beam-arc (see Figure 3-5), the strongest waves should be generated mostly near the shuttle. This is because, as shown by our simulation results, the beam-arc ion distribution

evolves rapidly, with characteristic time scales of the order of several lower hybrid periods τ_{LH} (see Figure 5-9a). Therefore, by the time the water ions should convect to the regions far downstream of the shuttle (i.e. at speeds comparable to the orbital speed, in the shuttle frame) they should have already released substantial amounts of their free energy through the strong waves generated in the near field. The water ion distribution should then excite mostly weaker waves in the downstream ion trail. Correspondingly, the wave energy released along the magnetic field in the local downstream ion trail should then be of lower intensities along the magnetic field, in agreement with the experimental data.

6.3.3   Source of Tilted Interference Patterns

As noted by Feng et al. [1993], lower hybrid tilted interference patterns are formed in regions where lower hybrid waves of different wave numbers propagate in different directions in the plane nearly perpendicular to the magnetic field. For tilted interference to be formed, however, the range of propagation directions still has to be relatively small, less than 15°. Feng et al. [1993] data analysis shows that tilted interference patterns were observed when the PDP coordinates had large Y' values and not when the PDP was directly downstream of the shuttle. For instance, the 0200 UT and 0310 UT events shown in Figure 2-10 correspond to the tilted interference patterns. In both of these cases the PDP was approaching, from the downstream direction, the magnetic lines that passed through the shuttle. Furthermore, in the series of interference patterns observed, from 0250 UT to 0310 UT, when the PDP was traveling in the trajectory near $X' = -250$ m. from negative to positive Y' coordinates (see Figure 2-10) only the last one was a tilted interference pattern, namely, the 0310 UT event. This tilted interference pattern was observed just after the PDP had crossed the wake boundary well downstream of the shuttle. After UT 0310, when the PDP was further away from the wake boundary, no interference patterns were observed. Now, we can argue that all this seems to imply that (1) inside the wake, in the region of the ion trail, waves propagate mostly in one direction thus forming symmetric interference patterns, (2) near the edge of the wake, which should also be the region

231

near the edge of the ion trail, waves propagate in a small range of directions (e.g., less than 15°) near the plane perpendicular to the magnetic field thus forming tilted interference patterns and (3) outside the water ion trail, far from the wake's edge, waves should propagate in various directions perpendicular to the magnetic field and thus cannot form interference patterns.

In particular, (1), (2) and (3) are consistent with our prediction that the source of the downstream ion trail waves should be the local ion trail. We have already discussed (1) in Section 6.3.1. Let us discuss (2) and (3) by noting that the local distribution of water ions near the edge of the water ion trail should not be a rotating beam distribution which tends to excite waves in only one direction (in the direction of the beam) as in the case of the region directly downstream of the shuttle (see Figure 3-5). Near the edge of the water ion trail, the distribution function of water ions should be more ringlike since the water ion density variations upstream, along the regions parallel to the orbital path, are smaller for the regions near the edge of the water ion trail than for those closer to the center of the water ion trail, directly downstream of the shuttle (i.e. recall from Figures 3-2 and 3-3 that the larger the water ion density variations upstream, along the regions parallel to the orbital path, the smaller the effective arc of the beam-arc distributions near the shuttle and downstream). Therefore, the more ringlike distributions of the regions near the edges of the water ion trail should tend to excite waves in various directions in the plane perpendicular to the magnetic field (as in the case of the $X_p = 5$ beam-arc plasma instability, see Figure 5-6a) and thus produce tilted interference patterns or no interference patterns. Furthermore, at the edge of the wake we expect the density gradients to be large and waves in these regions should be refracted accordingly. This effect should also tend to make waves propagate in different directions and thus contribute to the formation of tilted interference patterns.

Finally, it should be pointed out that our interpretation of tilted interference patterns is slightly different from Feng et al. [1993] interpretation. Feng et al. [1993] have argued that the source of waves that formed the 0310 UT event tilted interference patterns was the convection of waves from a region not too far upstream of the PDP

(about 30 m. upstream). They find that this should be the case because the group speed of lower hybrid waves, perpendicular to the magnetic field, is small (compared to the shuttle speed) and thus the waves should not propagate very far. Especially, since the regions where tilted interference patterns were observed had a large Y' coordinate and were not directly downstream of the shuttle. They also claim that since the group speed of lower hybrid waves depends on wavenumber, waves of different wavelength are likely to come from different source regions. Therefore, they argue that although lower hybrid waves always propagate near the plane perpendicular to the magnetic field, at some observation points waves originating from different regions of 3d space are likely to propagate in different directions in the plane perpendicular to the magnetic field.

6.3.4 Comparison of the PDP Data Dispersion Relation with the PIC Code Dispersion Relation

Figure 6-5 shows the earth's frame dispersion relation for the waves near 0038 UT (i.e. Figure 2-8) determined experimentally, from the analysis of the interference pattern data, by Feng et al. [1993]. The dispersion relation predicted by the simulation results of the X5a45 run, which is practically the same as that for the X1a45 waves that were proposed to explain the 0038 UT waves (see Section 6.3.1), is also shown with error bars. The error bars denote the frequency ranges where most of the wave energy is concentrated right after saturation of the X5a45 instability (see also Figure 5-13). We can see that the wavenumbers predicted by the simulation are in good agreement with the PDP data. The frequencies determined by the simulation are also in agreement with the experimental data, although they are slightly higher on the average. By noting the form of the dispersion relation Equation 6.2, we can argue that the slightly higher frequencies predicted in the simulation are probably due to the fact that the angle between the propagation vector and the magnetic field used in the simulation is slightly smaller than that of the waves observed by the PDP. Nevertheless, we can conclude that the net effect of the beam-arc plasma instability on the shuttle environment is a perturbation which involves the excitation of the

natural frequency modes of the ionospheric plasma, the lower hybrid modes.
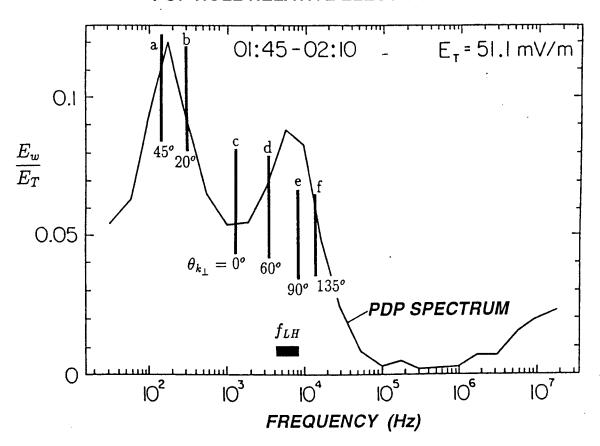
POP ROLL RELATIVE ELECTRIC FIELDS

Figure 6-1: Comparison of the PDP wave spectrum of the near vicinity (within 10 m.) of the shuttle with the simulation results. The solid curve shows the PDP wave spectrum for the period 01:45-02:10 during the XPOP roll. The error bars show the wave field amplitude fluctuations of (a and b) the X1a45 and X1a20 instabilities near saturation, (c and d) the X1a0 and X1a60 instabilities right before saturation and (e and f) the X5a90 and X5a135 instabilities near the quasi-steady state. Only (e) and (f) represent waves generated upstream of the shuttle and not near the shuttle, as in the other cases. The error bars are placed at the Doppler shifted frequencies of the corresponding waves (see text for details of the interpretation).

235

PDP RELATIVE ELECTRIC FIELDS

Figure 6-2: Comparison of the far downstream PDP wave spectrum with the simulation results. The solid curve shows the wave spectrum of the region 250 m. directly downstream of the shuttle for a time corresponding to the center of the mushroom. The error bars represent the wave field amplitude fluctuations near the saturation stages of the (a) X1a135, (b) X1a90, (c) X1a0, (d) X1a60 and (e) X1a45 instabilities. The error bars are placed at the Doppler shifted frequencies of the corresponding waves (see text for details of the interpretation). (e) corresponds to the strongest waves generated downstream of the shuttle, which should propagate mostly in the range $90^{\circ} \leq \theta_{k_{\perp}} \leq 270^{\circ}$.
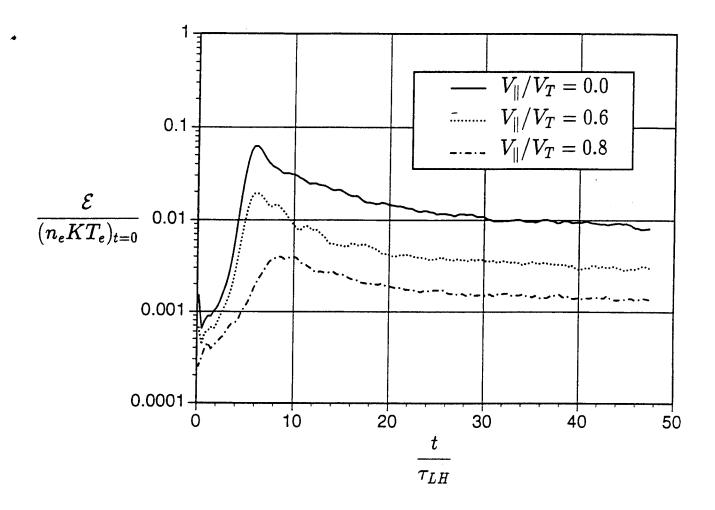
Figure 6-3: Field energy time history of the X5a45 beam-arc plasma instability (i.e. $X_p = 5$ beam-arc plasma instability with $\theta_{k_\perp} = 45°$ and $\bar{\phi}_{k_\parallel} = 1$) for three values of $V_\parallel/V_T$. It should be noted that smaller angles between the shuttle velocity and the earth's magnetic field, which correspond to beam-arc distributions of smaller arc radii in velocity space, result in lower wave amplitudes during the entire instability evolution.

237
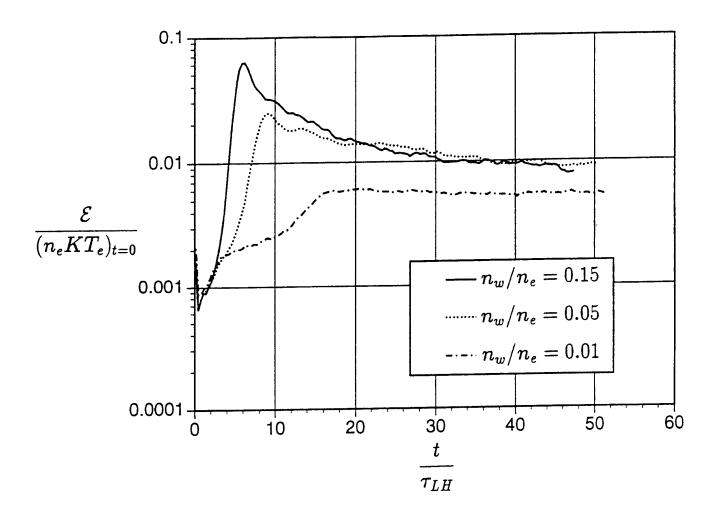
Figure 6-4: Field energy time history of the X5a45 beam-arc plasma instability (i.e. $X_p = 5$ beam-arc plasma instability with $\theta_{k_\perp} = 45°$ and $\bar{\phi}_{k_\parallel} = 1$) for three n_w/n_e density ratios. For the smaller n_w/n_e density ratios the instability shows an earlier transition to kinetic instability and tends to saturate mostly by quasilinear plateau formation rather than by particle trapping.

Figure 6-5: Comparison of the X5a45 run dispersion relation with the earth's frame dispersion relation inferred from the interference pattern waves observed in the 0038 UT event. It should be noted that the wavenumbers and frequencies predicted by the simulations are in good agreement with the PDP wave data.

Chapter 7

Summary of Results and Conclusions

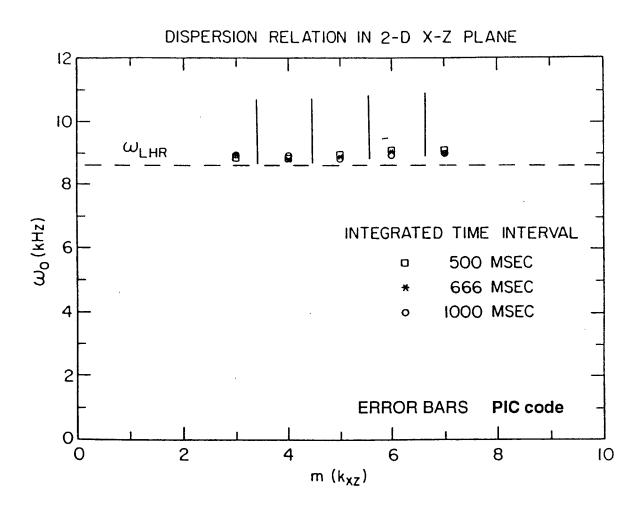One of the important observations of the Plasma Diagnostic Package (PDP) experiments that were designed to probe the environment around the shuttle was the high degree of electrostatic turbulence in the ambient plasma compared to what has been observed from similar instruments flown on unmanned spacecraft. In this thesis, we have shown that the turbulence is caused by a process which involves the outgassing of water vapor from the shuttle orbiter, the subsequent collisional charge exchange of these water neutral molecules with ionospheric oxygen ions to form "pick-up" water ions, and the excitation of the beam-arc plasma instability. This is a new instability which is driven by the interaction of the beam-arc (i.e. asymmetric ring) velocity distribution function of the contaminating water ions with the background ionospheric plasma. In what follows we give a summary of the results of this thesis and the conclusions.

7.1 The Plasma Diagnostic Package (PDP) Wave Data: Description and Qualitative Interpretation

In Chapter 2, we have put together a description and a qualitative interpretation of the plasma diagnostic package (PDP) wave data. We have discussed first the observations of waves during the free flight mission. During the 6-hour free flight mission, the PDP

completed 2 fly-arounds of the shuttle at distances up to 400 meters. In addition to the fly-arounds, a series of wake transits were performed to survey the wake region directly downstream from the shuttle. Cairns and Gurnett [1991a] analysis of the PDP data of the free flight mission showed that the far downstream wave spectrum was characterized by mushroom spectral features which occur in conjunction with the variations of the angle between the orbital velocity vector and earth's magnetic field vector, the so called $| V_\parallel / V_T |$ effect. In this analysis, the mushroom spectral features were found not to be associated with specific structures in the orbiter's plasma wake. Cairns and Gurnett [1991a] have proposed two simple models for the source region of the plasma waves forming the mushroom spectral features: the waves are (1) generated throughout the region containing water ions produced from the orbiter's water cloud (this region was referred to as the shuttle's water ion trail), or (2) generated within the near zone region of the orbiter and convected downstream. It was noted that these models are not mutually incompatible and both are plausibly consistent with the $| V_\parallel / V_T |$ effect.

Further analysis of the PDP wave data by Feng et al. [1993] showed that the highest intensity waves are observed directly downstream of the shuttle and along the magnetic field lines passing through the shuttle. Feng et al. [1993] have analyzed the interference (fingerprint) patterns in the PDP wideband data, which correspond to regions where waves propagate in mostly one direction. They have divided them into two groups. Group 1 interference patterns are those that were observed in the shuttle wake region when the PDP was directly downstream of the shuttle. Group 2 interference patterns, which include the tilted interference patterns, are those that were observed when the PDP was approaching the region directly downstream of the magnetic field lines passing through the shuttle. Their analysis of interference pattern data allowed them in some cases to determine various properties of the waves (i.e. the wavelength, the plasma rest frame frequency, the direction of propagation, the power spectrum, and the location of the source). For most waves the rest frame wave frequencies were found to be very close to but slightly above the lower hybrid frequency and the range of the wavelengths was about 1 to 4 meters, with the intensity

peaking near 2 meters.

We have also described the observations of the near zone waves made during the XPOP roll, when the PDP probed the orbiter's environment while attached to the shuttle's RMS arm (at distances less than about 10 meters). We have reviewed Cairns and Gurnett's [1991b] characterization of the near zone wave spectrum. This characterization involves three components: a peak near the lower hybrid frequency another peak near 200 Hz and a uniform component between the two peaks, the wave amplitudes of both peaks being only about twice as large as that of the uniform component. We have noted that Feng et al. [1993] have shown that the spectrum in the downstream ion trail also shows the lower hybrid frequency peak and the uniform component but the low frequency peak is damped and has lower amplitudes than the other two components. Furthermore, the most important results of Cairns and Gurnett's [1991b] analysis of the near zone PDP wave data were also reviewed: (1) the $| V_{\parallel}/V_T |$ effect in the spectrograms, (2) the variations of the near zone waves with the roll phase involving plasma wave nulls when the PDP is in the orbiter's wake and (3) the observations of strong near zone waves when the PDP spacecraft becomes magnetically connected to the shuttle, during the free flight mission, due to the fact that waves propagate perpendicular to the magnetic field and thus their electric fields vary slowly along the magnetic field. Finally, we have described Pickett et al. [1989] analysis of waves associated with orbiter water releases and truster firings. This analysis shows wave amplitude increases at all frequencies below the lower hybrid frequency during the time water is released. The largest increases correspond to the low frequency peak component of the near zone spectrum (up to 50 dB at $f = 100$ Hz).

In Chapter 6, we have interpreted the PDP data summarized above, including other major aspects of the data, by using the results of our theoretical and simulation studies of the beam-arc distribution and beam-arc plasma instability of the shuttle's environment. Next, we summarize the results of these studies.

7.2 The Beam-Arc Velocity Distribution Function of Pick-Up Water Ions

In Chapter 3, we have developed a theoretical analysis of the pick-up water ion distribution function by considering the general scenario envisaged for the shuttle's interaction with the ambient ionospheric plasma. This general scenario involves the outgassing of water vapor from the shuttle orbiter, the subsequent collisional charge exchange of these water neutral molecules with ionospheric oxygen ions to form "pick-up" water ions, the generation of plasma waves by these ions, and the subsequent plasma heating. An analysis of the pick-up distribution function was therefore a prerequisite for constructing our theory for the active and complex wave environment associated with the space shuttle. We started this analysis by discussing Cairns [1990] theory for the water ion distribution produced near the space shuttle. His theory shows that the water ion beam-arc distribution undergoes a transition from ring distribution to beamlike distribution with decreasing distance upstream from the orbiter. It also predicts that the water ion to oxygen ion density ratio has typical values in excess of 2% within 50 m. of the shuttle and maximum values of the order of 20 % near the shuttle.

One of the important results of our analysis was the determination of the water ion distribution function for the region downstream of the shuttle. We have noted that since most water ions are created in the near vicinity of the shuttle and then drift downstream in the shuttle frame, they form a long water ion trail downstream of the orbiter, of the order of 12 km before they recombine. We have shown that the water ion velocity distribution in the downstream water ion trail is a symmetric beam-arc since the water ion creation rates have a spherically symmetric spatial distribution about the orbiters position. Furthermore, because of the gyromotion of the water ions, the gyrophase angle of the distribution increases with increasing downstream distance from the shuttle. Correspondingly, the cycloidal $E \times B$ drift motion of the water ions (in the shuttle frame) with a drift speed equal to the Larmor speed results in the beam-arc ions having negative X_{earth} velocity components $V_{X_{earth}}$ (in the earth's

frame) along almost 90% of the ion trail.

We have calculated the effect of water ion-neutral collisions on the water ion beam-arc distribution. Our results show that water ion-water neutral collisions tend to drive the beam-arc distribution to a steady state shape of a ring in the small collision frequency limit of the shuttle's plasma. Furthermore, elastic collisions with the ionospheric oxygen neutrals act to destroy the coherent circular motion of the water ions and drive their distribution towards a shifted Maxwellian with the oxygen neutrals drift and temperature (in the shuttle frame). However, we have concluded that since the downstream water ion trail extends only to distances of the order of 12 km, only near the back of the ion trail the distribution may reach the steady state predicted by our model. Within 400 m downstream of the shuttle, which was the largest distance reached by the PDP during the free flight mission, the water ion distribution should be a gyrating symmetric beam-arc essentially unaffected by collisions with neutrals. Wave scattering effects on the water ion distribution were neglected in this theoretical analysis but were found to be important later in the PIC-code simulations.

7.3 The Linear Theory of the Beam-Arc Plasma Instability

In Chapter 4, we have developed the linear theory of the beam-arc plasma instability. This is a new instability which is driven by the free energy involving the interaction of the beam-arc distribution function of the pickup water ions with the background ionospheric plasma. For the derivation of the linear dispersion relation, the beam-arc distribution function was modeled as a summation of large numbers of Maxwellian beamlets having directions mapping the arc of the distribution and the same mean speed. This study was first restricted to beam-arc distributions of the form of slices of ring distributions since the beamlets making up the beam-arc were homogeneously distributed throughout the arc. It was assumed that the beam-arc water ions have zero drift parallel to the magnetic field. We have analyzed, numerically and analytically, the dispersion relation for all ranges of beam-arcs, from beams to rings. The

244

instability was classified in three different beam-arc regimes according to the instability mechanisms: (1) hydrodynamic for small arcs, (2) hydrodynamic and kinetic for effective arcs close to the critical arc ($\Delta\Theta_{crit} \approx 60°$) and (3) kinetic for large arcs. It was found that the beam-arc plasma instability shows new characteristics that are different from those of the beam-plasma [*Gaffey*, 1976] and ring-plasma [*Tataronis and Crawford*, 1970; *Lee and Birdsall*, 1979] instabilities. In particular, for arcs close to but not greater than the critical arc (in the second regime) the Doppler-shifted growth rate spectrum of the instability is much broader and peaks near the lower hybrid frequency. The critical arc was found to increase with the water ion to electron density ratio.

The results of the linear analysis show that the beam-arc plasma instability has unique characteristics that can explain most details of the PDP wave spectrum detected within 10 meters of the shuttle. Various other properties of the observed waves were also found to be consistent with those predicted by the linear theory of the beam-arc plasma instability. However, a nonlinear analysis of the instability was still necessary to validate important assumptions made in the PDP data interpretation (using the linear theory) and to explain various features of the data that required a knowledge of the nonlinear evolution of the instability. Therefore, in Chapter 5 a PIC code simulation study of the beam-arc plasma instability was performed. Then, in Chapter 6 the PDP data interpretation using the linear theory was confirmed and further extended by using the simulations results.

7.4 Simulation of the Beam-Arc Plasma Instability

7.4.1 The Nonlinear Theory

In Chapter 5, we have made a nonlinear analysis of the beam-arc plasma instability by first examining the equations governing this instability and showing that these equations can be expressed in a normalized form which is independent of the ion to electron mass ratio. This was an important point in the numerical sense, since

it implied a mass ratio scaling for the nonlinear system, that is, that simulations performed with a reduced mass ratio can be used to determine the solution at a realistic mass ratio. Consequently, later in the simulations we have used a mass ratio of 512 for computational efficiency. We have also developed the quasilinear theory of the beam-arc plasma instability and calculated the quasilinear energy transfer rates in the hydrodynamic limit. These rates were confirmed later in the simulations but only for the initial small amplitude stage of the instability evolution where quasilinear theory was valid. In the kinetic limit, the quasilinear theory lead to a solution for the relaxed beam-arc distribution which predicted the formation of a plateau in the range of positive velocities smaller than the beam velocity. Another important result of the quasilinear theory was that the electrons should respond to the waves not as a highly magnetized low mass species but as an unmagnetized species with an effective mass of the order of to the ion mass. This is because the electrons are closely tied to the magnetic field lines which are nearly perpendicular to the wavevectors. Therefore, such results were consistent with our previous observation that the beam-arc plasma instability should be similar to the bump-on-tail instability (driving Langmuir waves). This observation was based on the fact that both instabilities have the same form of linear dispersion relation except that the magnetic field makes the natural frequency of oscillations of the former the lower hybrid frequency rather than the plasma frequency. Later in the simulations we have shown that, to some extent, this analogy between beam-arc plasma instability and the ordinary two-stream instability persists in the nonlinear regime.

7.4.2 The PIC code Simulation

The PIC code simulation design of the beam-arc plasma instability was aimed primarily to the determination of the wave electric field spectrum of the instability. Designing such simulation was a delicate task since for this instability the spectral field energy of the wave modes is a non-robust quantity. The total electrostatic field energy of the waves is only about 1 % of the thermal and drift energies of the particles. This is in contrast to the case of the (unmagnetized) bump-on-tail instability

246

where the field energies are of the order of 12% of the total energy. Therefore, in order to obtain reasonable results, our simulation design of the beam-arc plasma instability had to include the effects of resonant and non-resonant diffusion and the quasilinearlike feedback of wave-particle interaction. In particular, the modeling of the instability's transition to kinetic instability and subsequent quasi-linear evolution required closely spaced wave modes (i.e. very long simulation systems) for a proper evolution of the spectrum towards a quasi-steady state. For computational efficiency, we have designed the simulation by rescaling the beam-arc plasma instability after showing that the solutions of the linear dispersion relation, normalized by the natural frequency of oscillations, are independent of the m_O/m_e and ω_{pe}/ω_{ce} ratios.

We have performed 1d-3v PIC code simulations of the $X_p = 1$ and $X_p = 5$ beam-arc plasma instabilities for various propagation directions in the plane nearly perpendicular to the magnetic field. The output of the simulations show that in each propagation direction the instability evolution starts with an early stage of strong turbulence in which the beam-arc particles are strongly heated. As a result of the heating, the 1d beam-arc distributions of the various runs start resembling to each other long before saturation. Therefore, because of this resemblance in the early stage distributions, the results of the various runs for the different propagation directions are qualitatively the same. The major differences are in the magnitudes of the physical processes that occur in the nonlinear regime.

The instability evolution in any particular direction starts with the wave modes being destabilized by the reactive instability mechanism, from the bunching of the different species. At these early times the beam-arc particles are strongly heated but the instability continues to be dominated by the bunching mechanism of the linearly fastest growing modes. Then, the instability saturates by trapping of the beam-arc particles in the potential wells. Many modes are excited during saturation; there is no evidence for any especial nonlinear effect that would cause the dominance of a single mode. In phase space the usual vortices indicating trapping are seen. However, in contrast to simulations of other instabilities, for our long system, these structures are only seen when a section of the system is magnified.

Several lower hybrid periods after saturation, a transition from reactive to kinetic instability takes place which results from (1) the broadening of the space-averaged beam-arc distribution function by the sloshing motion of the particles in the vortices and (2) the randomization of the vortices, which increases significantly the number of beam-arc ions in the resonant region. Therefore, with a larger number of resonant ions the instability becomes kinetic and quasilinear theory and other turbulence theories are again expected to apply. In the kinetic stage, and even in the previous reactive stage, the feedback effect of the wave-particle interaction on the wave growth is important. Mode coupling effects are not prominent and thus unable to eventually prevent a plateau formation in the beam-arc distribution.

7.4.3 The Simulation Spectrum Analysis

Our analysis of the simulation wave modes spectrum and time history revealed various nonlinear processes. One of them, namely, competition between modes in the large k scale occurs because of the greater bunching ability of the linearly fastest growing modes. These fastest growing modes absorb some of the free energy that is initially available for the excitation of the other (i.e. linearly slower growing) modes and thus inhibit the low wavenumber modes from growing. Furthermore, with many modes present, the stochastic nature of turbulence is evident since the mode number spectrum shows a fine structure and individual wave modes show a rather erratic time dependence, unless there is some averaging. We have noted that the physical mechanism that produces the erratic fine structure of the mode number spectrum is related to the competition between modes in the small k scale. This involves some modes taking energy from, or preventing further growth of, their adjacent modes due to their greater bunching ability. This was found to be a result of the stochastic nature of the initial conditions of the simulation design such as the loading of the particles and the initial wave phases. The simulation spectrum analysis also showed that at the end of the run, in the quasi-steady state, the highest wave mode energies correspond to the modes that were initially the most linearly unstable and that those modes have frequencies near the lower hybrid frequency. However, the results also

show that larger and larger wavenumber modes are destabilized by the advance of a beam-arc distribution front to lower and lower velocities in connection to the wave-beam arc resonant particle interaction. This occurs in the early kinetic stage but the energy contained in these modes remains small (compared to that of the linearly most unstable modes). The rate of this process decreases until it terminates by the flattening of the bump in the total ion distribution. At that point, wave growth at larger and larger wavenumbers is arrested by landau damping from the background ions. Once a plateau is formed, in the quasi-steady state, changes in the total ion distribution and the spectrum remain very small.

7.5   Interpretation of the PDP Wave Data

In Chapter 6, we have put together all the theoretical pieces developed in the previous Chapters to give a fairly complete interpretation of the extensive PDP wave data. Our interpretation constitutes significant progress in the understanding of the nature of the shuttle environment waves. We have started the interpretation by making three important remarks. First, the simulation results show that the net effect of the beam-arc plasma instability is to excite lower hybrid waves (i.e. electrostatic waves with earth's frame frequencies near the lower hybrid frequency) in a wide range of propagation directions in the plane perpendicular to the magnetic field. Moreover, the amplitudes of the waves propagating in the various directions depend on the shape of the beam-arc. Second, the wavenumbers of these waves, predicted in the simulations, are consistent with those that could be detected by the PDP antenna. Third, for the interpretation of the PDP data the simulation results have to be Doppler shifted to the shuttle frame. This is because the simulation results were obtained by using the stationary ionospheric frame of reference (our so-called the earth's frame) whereas the PDP wave data was taken in the shuttle frame. Furthermore, we have noted that because of the Doppler shift, lower hybrid waves propagating in different directions perpendicular to the earth's frame magnetic field should be observed with different frequencies from the shuttle frame.

7.5.1 Interpretation of the PDP Wave Spectrum Observed in the Near Vicinity of the Shuttle

We have first interpreted the wave spectrum that was detected within 10 m. from the shuttle. This spectrum is composed of three components: a peak at low frequency ($\sim$ 200 Hz), another peak near the lower hybrid frequency ($\sim$ 10 kHz) and a uniform broadband component between the two peaks. The intensities of both peaks are only about twice that of the uniform component. The uniform component of the spectrum was interpreted in terms of waves propagating with $-15^o \leq \theta_{k_\perp} \leq 15^o$ and $\theta_{k_\perp} \approx 50^o$, where $\theta_{k_\perp}$ is approximately the angle between the propagation vector (which is always near the plane perpendicular to the magnetic field) and the orbital velocity vector. These waves are generated in the near vicinity of the shuttle and are driven by the local $X_p = 1$ beam-arc water ion distribution. The amplitudes and (Doppler shifted) frequencies of these waves predicted in the simulations agreed with those of the uniform component of the PDP spectrum.

The second component of the spectrum, the low frequency peak, was interpreted in terms of waves propagating with $\theta_{k_\perp} \approx 45^o$. These waves have the largest field energies, relative to those propagating in the other directions, in the initial growth stages of the instability and near saturation. This is because the reduced $X_p = 1$ beam-arc distribution that drives them has the largest free energy for the $\theta_{k_\perp} \approx 45^o$ propagation direction. The enhancements of the low frequency second component of the spectrum observed during water dumps and thruster firings were also explained in terms of waves propagating in the $\theta_{k_\perp} \approx 45^o$ direction. The amplitudes and (Doppler shifted) frequencies of these waves predicted in the simulations agreed with those of the second component of the PDP spectrum.

The simulation times used in the above interpretations were taken from those corresponding to the early stages, near saturation, of the fastest growing instabilities. This is because it was argued that the energy of the excited waves should radiate very rapidly away from the waves source regions, along the magnetic field lines. It was also noted that, although the simulations do not include the beam-arc regeneration effect from charge exchange reactions, this effect should not affect the early stages results

because the instability saturation time scales are at least two orders of magnitude smaller than the charge exchange time scales.

We have tried to explain the third component of the spectrum which is the peak near the lower hybrid frequency by assuming that, because of the plasma density gradients and warm plasma effects, some downstream convection of the (lower hybrid) waves would actually occur. The downstream convection of waves generated in the region upstream of the shuttle with propagation directions in the range $90^o \leq \theta_{k_\perp} \leq 270^o$ would correlate with high wave intensities near the lower hybrid (Doppler shifted) frequency. For these propagation directions, the waves generated upstream would have larger amplitudes than those generated in the near vicinity of the shuttle since the former would be driven by more ringlike distributions than the latter. We have shown that those waves generated upstream would have relatively large amplitudes by the time they would convect to the near shuttle region despite of the fact that they would be generated in regions of lower water ion density. However, we have found that the amplitudes of those waves would still be lower than that of the lower hybrid frequency peak of the near zone PDP spectrum. Further research is thus required to explain this peak.

7.5.2 Interpretation of the Mushroom Features of the Far Downstream Ion Trail Spectrum

Another important result of this thesis was the interpretation of the "mushroom" spectral features which characterize the PDP wave spectrum of the region far downstream from the shuttle. Feng et al. [1993] have shown that the wave spectrum of the region 250 m. directly downstream from the shuttle, for a time corresponding to the center of the mushroom, has two of the three components of the near shuttle region spectrum and within the same intensities. The far downstream spectrum has a peak near the lower hybrid frequency and a uniform component but does not have a peak at low frequencies. We have based our interpretation of this spectrum on our prediction that the source of waves observed in the downstream ion trail should be the local ion trail. This is because we have shown that the group velocities of

the lower hybrid waves excited in the ionosphere by the beam-arc plasma interaction should be very large and nearly parallel to the magnetic field. Therefore, the energy of the excited waves should radiate away from the wave source regions very rapidly along the magnetic field lines (that is, in the direction almost perpendicular to the orbital plane).

The peak near the lower hybrid frequency or top cap component of the mushroom spectrum was interpreted by considering the proposed wave source region, that is, the local water ion trail. In the downstream water ion trail, the rotating beamlike beam-arc distribution should excite the strongest waves with propagation directions in the local beam velocity direction. Therefore, these waves should have propagation directions in the range $90^o \leq \theta_{k_\perp} \leq 270^o$ because (1) the instability time scale is much smaller than the water ion cyclotron period and (2) the $E \times B$ cycloidal trajectories of the water ions (in the shuttle frame) have corresponding beam distribution velocities (in the earth frame) with negative $V_{X_{earth}}$ components along almost 90 % of the downstream water ion trail. We have shown that the Doppler shifted frequencies of these waves (with propagation directions in the range $90^o \leq \theta_{k_\perp} \leq 270^o$) are indeed near the lower hybrid frequency and the wave amplitudes, predicted in the simulations, match those of the peak of the downstream PDP spectrum. Furthermore, we have interpreted the PDP spectrum waves above the lower hybrid frequency as being produced by the nonlinear destabilization of large wavenumber modes with the advance of the beam-arc front observed in the simulations.

We have also shown that because the downstream beam-arc distribution is not simply a beam but has a finite effective arc, strong waves should also be excited with propagation directions within the ranges $-90^o \leq \theta_{k_\perp} \leq -50^o$ and $50^o \leq \theta_{k_\perp} \leq 90^o$. It was noted that the Doppler-shifted frequencies and amplitudes of these strong waves, predicted in the simulations, match those of the uniform component of the downstream PDP spectrum. Moreover, we have extended these arguments to predict that in the downstream ion trail the waves generated with propagation directions in the range $-50^o \leq \theta_{k_\perp} \leq 50^o$ should have relatively low amplitudes. This is because these waves would be generated in the directions opposite to the beam-arc (that is, in

directions almost always opposite to the beam velocity of the downstream beam-arc distribution). Since these waves would correspond to low Doppler-shifted frequencies, they could explain the lack of the low frequency peak (near 200 Hz) in the downstream ion trail spectrum.

The details of the mushroom spectral features were explained by extending Cairns and Gurnett's [1991b] theory relating the $| V_\parallel / V_T |$ effect. This involved two mutually compatible explanations for the wave intensity decreases with increases in $| V_\parallel / V_T |$: (1) larger values of $| V_\parallel / V_T |$ imply smaller $V_\perp$ values which in turn produce beam-arc distribution functions with arcs of smaller radius, or lower free energy, driving waves of lower amplitudes and (2) assuming that, because of the plasma density inhomogeneities and warm plasma effects, some downstream convection of the waves would occur, the different motions (parallel to the magnetic field) of the water ions driving the waves and the ionospheric plasma convecting the waves would imply that the waves would have a minimum (maximum) path length available for growth when $| V_\parallel / V_T |$ would be large (small), thereby explaining the differences in intensities. We have noted that the effect of reductions in the path lengths available for growth would be more important for waves propagating perpendicular to the ion trail (i.e. waves propagating to the right or to the left of the ion trail) because of the following two factors that would become more important as $| V_\parallel / V_T |$ would increase and the instability would become weaker (i) the finite cross section of the ion trail and (ii) the drift of the ion trail, in the direction parallel to the magnetic field, relative to the background ionospheric plasma. Therefore, for large $| V_\parallel / V_T |$ values only forward propagating waves (which would explain the foot of the mushroom) and backward propagating waves (which would explain the top cap of the mushroom) would have long enough path lengths for growth. This would be in agreement with the PDP wave data.

7.5.3 Interpretation of the Lower Hybrid Interference Patterns of the PDP Spectrograms

The above interpretation of the PDP spectra was confirmed by our analysis and interpretation of the lower hybrid interference patterns of the PDP spectrograms. Interference patterns indicate times when the PDP was in regions where waves with different wavelengths propagate in only one direction. Group 1 interference patterns are those that were observed in the shuttle wake region when the PDP was about 100 m or 250 m directly downstream from the shuttle. In contrast to Feng et al. [1993] interpretation of the interference patterns waves, we have shown that the source of the group 1 interference patterns waves should not be the downstream convection of waves from the region near the shuttle but the local ion trail. Therefore, the waves that form the group 1 interference patterns should be generated near the PDP, in the downstream region. Major evidence for this interpretation came from the remarkable agreement of the wave intensities and propagation directions inferred from the interference pattern data with those predicted from the characteristics of the rotating beam distribution of the downstream water ion trail, using the simulation results.

We have interpreted the strong waves observed along the magnetic field lines threading the shuttle as being primarily the energy of the waves generated near the shuttle being convected (i.e. radiated) along the magnetic field lines. This is because the group velocity of these lower hybrid waves is very large and almost parallel to the magnetic field. We have shown that the escape of wave energy along the magnetic field lines should tend to quench the instability near the shuttle. However, by the time that the water ions, driving the waves, should have convected to the regions far downstream of the shuttle, they should have already released most of their free energy through the strong waves generated in the near shuttle region. The water ions should then excite mostly weaker waves in the downstream water ion trail which should result in weaker wave intensities along the downstream magnetic field lines. This would be in agreement with the experimental data.

Our analysis of the interference pattern data correlating the different regions with

the different types of interference patterns observed showed that (1) inside the wake, in the region of the water ion trail, waves propagate mostly in one direction thus forming symmetric interference patterns, (2) near the edge of the wake, which should also be the region near the edge of the water ion trail, waves propagate in a small range of directions (e.g., less than 15°) near the plane perpendicular to the magnetic field thus forming tilted interference patterns and (3) outside of the water ion trail, far from the wake's edge, waves should propagate in various directions perpendicular to the magnetic field and thus cannot form interference patterns. We have noted that the source of the tilted interference pattern waves should also be the local ion trail.

Finally, we have seen that the dispersion relation predicted by the simulations agrees with that inferred from the interference pattern data. Both show that the highest wave energies are concentrated in waves with wavelengths in the range from 2 m. to 4 m. and frequencies slightly above the lower hybrid frequency. We have therefore concluded that the net effect of the beam-arc plasma instability on the shuttle environment is a perturbation which involves the excitation of the natural frequency modes of the ionospheric plasma, the lower hybrid modes.

7.6 Recommendations for Future Work

7.6.1 The Pickup Water Ion Distribution, the Water Ion Trail and the Shuttle's Wake

Various issues in our interpretation of the PDP wave data are based on the shapes and densities of the pickup water ion distribution predicted analytically. For the region upstream of the shuttle we have used the results of Cairns [1990] analysis which predict that the beam-arc distribution should change from a beamlike to a ringlike distribution with increasing upstream distance from the shuttle. There are no data available to verify these predictions. Therefore, in the future the real upstream pickup water ion densities and distribution shapes should be measured.

For the region far downstream of the shuttle, in the water ion trail, we have predicted that the pickup water ion distribution function should be a rotating symmetric beam-arc and that the gyrophase of this distribution should increase with increas-

ing downstream distance from the shuttle. Data analyses have not yet been made to verify these predictions. In the future it is crucial to make measurements and data analyses of the downstream pickup distribution to check our predictions and the corresponding wave data interpretation. Furthermore, it is also necessary to make measurements of the water ion densities (i.e. density profiles) of the water ion trail and verify the prediction that they should be fairly constant along the trail.

The characteristics and effects of the shuttle's wake region should also be measured and analyzed further. The wake of the shuttle should affect the assumed spherically symmetric spatial distribution of the charge exchange rates and thus the predicted symmetric shape of the far downstream pickup distribution function. It is necessary to determine to what extent the wake should affect the shape of the downstream distribution and the resulting instability. Furthermore, the polarization of the plasma cloud of the shuttle, predicted by Hastings and Gatsonis [1989], which affects the $E \times B$ drift of the particles should also be taken into account in future more elaborated predictions of the pickup ion distributions of the downstream ion trail.

Lastly, the simulations show that wave effects should dominate in the evolution of the pickup water ion distribution. Therefore, future predictions of this distribution should include wave effects.

7.6.2   Simulations in 2 or 3 Dimensions

The 1d-3v PIC code simulation studies showed that the beam-arc plasma instability excites primarily lower hybrid waves in a wide range of propagation directions in the plane perpendicular to the magnetic field. The results from the various runs for the different propagation directions turned out to be qualitatively the same because, in each case, the beam-arc particles were strongly heated in a very early stage of the instability evolution. The major differences in the results were in the magnitudes of the physical processes that occurred in the nonlinear regime. These magnitudes were found to be dependent on the shapes and densities of the beam-arcs, which implied our previous suggestion that more measurements of the beam-arc parameters are needed.

256

Furthermore, it is important that, in the future, our 1d simulation results be verified with simulations in 2 or 3 spatial dimensions. 2d simulations for planes almost perpendicular to the magnetic field must be performed. As in the 1d simulations, these 2d simulations should be designed such that the effect of mode discretization be negligible. This is because for this instability quasilinear effects have to be included in order to accurately model the spectrum. In particular, the modeling of the transition to kinetic instability and subsequent quasi-linear evolution requires closely spaced wave modes (i.e. large simulation system sizes) for a proper evolution of the spectrum towards a quasi-steady state. These 2d simulation designs, however, might be somewhat impractical due to computational time constraints.

Other type of 2d (or if possible 3d) simulations should be performed, ones with one dimension along the magnetic field and the other(s) perpendicular to the magnetic field. The escape of the wave energy along the magnetic field lines, and therefore the quenching of the instability growth should be studied with this type of simulations. Various runs should also be performed to examine the $| V_\parallel / V_T |$ effect. In particular, the effect of a plasma drift parallel to the magnetic field on the instability spectrum should be studied.

Future simulations should include the effect of charge exchange reactions; especially, for the cases of thruster firings and water releases. It is important to determine to what extent the beam-arc distribution regenerates itself and how this affects the wave spectrum. The running time for these simulations should be long, of the order of the ion cyclotron period. The ions should then be treated as magnetized and any additional effect due to the ion magnetization should be studied.

7.6.3 The Effects of the Density Inhomogeneities and the Lower Hybrid Frequency Peak of the Near Zone Spectrum.

Let us go back to the beam-arc plasma instability spectrum plots and note that, as shown in Figures 5-13 and B-6, long after plateau formation and saturation the spectrum develops a peak at low wavenumbers, usually at mode number 1 which is the

mode with the longest wavelength allowed in the (periodic) system. This peak is near the negative lower hybrid frequency, corresponding to waves propagating opposite to the beam-arc. Now, waves with small wave numbers are virtually (ion Landau) undamped, especially if propagating opposite to the beam-arc. Such waves thus could be easily excited by mode coupling. The possible mode coupling interactions are discussed in the paper by Dum and Sudan [1971]. For our case, scattering of primary waves off ions is the most likely process. Scattering of the primary wave spectrum by the ions produces then a secondary wave spectrum at smaller wave numbers, with propagation predominantly in the direction opposite to the beam.

This interpretation of the secondary spectrum is consistent with the results of recent simulations of the bump-on-tail instability [Dum, 1991a,b] which also reveal this type of mode coupling. As discussed in Chapters 4 and 5, the beam-arc plasma instability is somewhat analogous to the bump-on-tail instability, and Dum's [1991a,b] simulations of the latter also show that long after plateau formation the spectrum develops a peak at small wave numbers. The secondary spectrum consists largely of modes propagating opposite to the beam which are virtually undamped. As in the case of the beam-arc plasma instability, Dum's results show no extension of the secondary spectrum to short wavelengths thus indicating the impossibility of a "collapse" of the Langmuir spectrum and an avenue for damping, as predicted by strong turbulence theories [e.g. Goldman, 1984]. Dum [1991a,b] therefore identifies the secondary spectrum as the result of wave scattering by ions, which is consistent with his finding that mode coupling effects are negligible unless ions are modeled as discrete particles in the simulation. Furthermore, in Dum's results, the signatures of the mode coupling process are visible in the distribution functions. He claims that the physical ingredients for this process are an electron non-linearity for high-frequency oscillations (the ponderomotive force) and the low-frequency response of electron and ions, as in the strong turbulence models.

Now, going back to the case of the beam-arc plasma instability, let us note that the Doppler-shifted frequency of the secondary waves would fall near the lower hybrid frequency (i.e. the Doppler-shift in this case is negligible since these waves are low

wavenumber waves). Therefore, this process that generates the secondary spectrum could explain the peak near the lower hybrid frequency in the PDP Near Zone spectrum. However, there are two issues that must be studied further in the future in order to find more evidence for this correlation. (1) The first has to do with the fact that during the early stages of the instability, which are of interest for the PDP data interpretation (see Section 6.2.1), the energy of the secondary modes is small compared to that of the primary modes, with wave numbers in the linear instability range. The energy of the secondary modes becomes comparable to or greater than that of the primary modes only after the instability reaches the quasi-steady state, but these might be overestimates due to the introduction of numerical error from the scattering off the large masses of the macroparticles used in the simulations. Further analysis is necessary on these observations. (2) The second issue has to do with the following unsolved problem. In all of the runs, for the various simulation designs, we have found that the largest wave amplitude of the secondary waves always corresponds to mode 1 (the mode with wavelength equal to the system size), regardless of the system size used in the simulation (even in runs with system sizes of the order of 50 m., which correspond to the longest system sizes allowed by our computational constraints). Therefore, if these mode coupling effects would indeed be significant for the interpretation of the PDP spectrum of the near vicinity of the shuttle, they would be likely to be affected by the charged particle density gradients. This is because the secondary waves' wavelengths would be of the order of the water cloud radius (i.e. 100 m.). Unfortunately, there is no published data about the wavelength of the waves detected within 10 m. from the shuttle (except for the fact that they should be greater than or equal to 1.5 m., the PDP antenna length). Further research is required on these issues.

Lastly, let us also note that the charged particle density gradients in the environment around the shuttle could be sources of free energy that could modify the wave spectrum by coupling to the beam-arc plasma instability or by exciting new drift instabilities. Although the results of a preliminary linear analysis on the inhomogeneity effects indicate that there is no coupling and that any drift instability should have

growth rates much smaller than those of the beam-arc plasma instability, the effects of density gradients should be considered in future analyses of the shuttle environment waves. The peak near the lower hybrid frequency in the Near Zone spectrum may be a result of the density gradients effects.

7.7 Recommendations for Reducing the Background Electrostatic Noise in the Shuttle Environment

The results of this thesis's study of the shuttle environment waves are important for the design of future Low Earth Orbit missions involving orbital platforms subject to outgassing, such as the space shuttle or the proposed space station, which have a requirement that the background of plasma waves driven by outgassed pickup ions be minimized. This requirement for minimal levels of platform-associated plasma waves is a natural one for missions focused on either natural ionospheric plasma waves or active space plasma experiments involving plasma waves as either a diagnostic tool or the focus of the research. Cairns and Gurnett [1991a] have already given two suggestions on how to eliminate the shuttle environment waves based on their observational analysis of the PDP data. We have reconsidered their suggestions in light of our interpretation of the PDP data using simulations and we have found them valid. Therefore, we now merely confirm these two suggestions which are aside from the obvious comment that the potential sources of pick-up ions (e.g., outgassing from spacecraft surfaces, exhaust of thrusters, water dumps, etc.) should be minimized.

Cairns and Gurnett's [1991a] first suggestion which we now confirm is inferred from the the role of the quantity $|V_\parallel/V_T|$ in controlling the amplitude and spectral characteristics of shuttle environment waves. In particular, both plasma wave observations in the shuttle's outgas cloud, during the PDP free-flight mission [Cairns and Gurnett, 1990a] and in the near vicinity of the shuttle during the XPOP roll [Cairns and Gurnett, 1990b], show evidence of the $|V_\parallel/V_T|$ effect. Their first suggestion therefore applies to both platform-based (i.e., the shuttle's payload bay) and free-flying experiments: the primary implication of their observational research is that

260

the platform's orbit should be designed so that $\mid V_{\parallel} \mid \geq V_{\perp}$. Let us note that our theoretical and simulation interpretations also imply that large values of $\mid V_{\parallel}/V_T \mid$ should be pursued. This means that polar orbit are strongly favored, whereas equatorial orbits are contra-indicated. Cairns and Gurnett have noted, however, that a maximum value of $\mid V_{\parallel}/V_T \mid$ may exist: for $V_{\perp} = 0$ there is no convection electric field and the pickup ions and the background plasma once again move in the same plane, thereby again permitting more efficient growth. The beam-arc plasma instability has zero growth rate in this case; however, as Cairns and Gurnett [1991a] argued more familiar ion acoustic-type instabilities may grow in this case provided the temperature ratios T_e/T_O and T_O/T_w are sufficiently high. Therefore, in the absence of observational data with larger values of $\mid V_{\parallel}/V_T \mid$ than 0.95, their primary recommendation, which we now confirm, is for future missions with a requirement for low levels of plasma waves associated with the orbiting platform to have orbits with $0.7 \leq \mid V_{\parallel}/V_T \mid \leq 0.95$. These orbits are highly inclined with respect to Earth's equatorial plane.

Cairns and Gurnett's [1990a] secondary recommendation, which we now confirm, is that orbiter-based experiments involving plasma waves should be performed outside and upstream from the orbiter's water cloud and water ion trail so as to avoid confusion with the wide variety, large spectral width and significant levels of orbiter-associated plasma waves. A similar recommendation followed for other orbiting platforms, such as the proposed space station, which are inhabited or suffer significant outgassing. They noted that the PDP free-flight data and theoretical extent of the shuttle orbiter's water cloud [Paterson and Frank, 1989] indicate that upstream distances of at least 400 meters should be chosen, thereby arguing strongly for such research to be performed using independent, free-flying spacecraft.

Appendix A

Verification of the Simulation Design: Effect of Changing the PIC-code Computational Parameters

In Section 5.3 we have designed the simulation of the beam-arc plasma instability which involved choosing the values of the computational parameters (e.g., system length, time step, grid size and number of macroparticles). In this appendix we verify the accuracy of the computational parameter values chosen in that section. This is done by showing that the simulation results are independent from changes in these values within a reasonable range. Since we are interested in performing simulations for a wide variety of beam-arcs (e.g., some more beamlike and others more ringlike) and for various propagation directions (see Figures 5-3 and 5-5), it is necessary to make this verification in the more general cases. An appropriate way to do this verification efficiently is by considering the two extreme cases of the beam-arc plasma instability, namely, the beam plasma and ring plasma instabilities. The results of such verifications are shown in the figures of this appendix.

Let us recall that because of the periodic boundary conditions of the PIC code model, the number of wave modes in the simulation system can be increased by increasing the system length. In Section 5.3.3 we have discussed in great detail the criteria for determining the minimum number of modes required and the reader should refer to this section for details. Figures A-1 and A-2 show the effect of changing the

number of modes in the simulations of the beam plasma and ring plasma instabilities. It can be seen that the simulation results become independent of the number of modes in the simulation, within a reasonable margin of error, for $m_{\gamma_{max}}$ greater than 16, where $m_{\gamma_{max}}$ is the mode number of the linearly fastest growing mode. This therefore validates our choice of $m_{\gamma_{max}} = 40$ for the simulation of the beam-arc plasma instability.

It is interesting to note the field energy density oscillations with a period of $\sim \tau_{LH}/2$ in the case of the ring plasma instability. These oscillations are a result of the way that the PIC code computes the field energy, that is, as the product of the charge density times the potential (in Fourier space). In the case of the ring plasma instability the spectral amplitudes of both of these parameter properties are dominated by the $\cos(2\pi t/\tau_{LH})$ component such that the product of two of these cosines produces a $\cos(4\pi t/\tau_{LH})$ time variation.

In Sections 5.3.4 and 5.3.5 we have discussed in detail the criteria for choosing the grid size and the number of particles (i.e. macroparticles) in the simulation. We have noted that the number of particles should be as large as possible in order to reduce the computational noise and have a good statistical representation of the particle distributions in the important velocity space regions. Figures A-3 and A-4 show the effect of changing the number of particles of each species per cell in the simulations of the beam plasma and ring plasma instabilities. It can be seen that for our design criteria to be satisfied, the number of particle of each species per cell has to be greater than or equal to 64. This therefore validates our choice of 64 background ion particles per cell, 64 electron particles per cell and 128 beam-arc particles per cell for the simulation of the beam-arc plasma instability.

Lastly, in Section 5.3.4 we have shown that the most stringent condition for choosing the time step of the simulation is that the time step should be small enough to give a fairly accurate integration of the electron Larmor orbits. Figure A-5 and A-6 show the effect of changing the time step in the simulations of the beam plasma and ring plasma instabilities. It can be seen that the simulation results become independent of the time step, within a reasonable margin of error, for time steps equal to or smaller

than 0.2 (normalized by the electron plasma frequency). This therefore validates our choice of $\Delta t = 0.2$ (normalized by the electron plasma frequency) for the simulation of the beam-arc plasma instability.
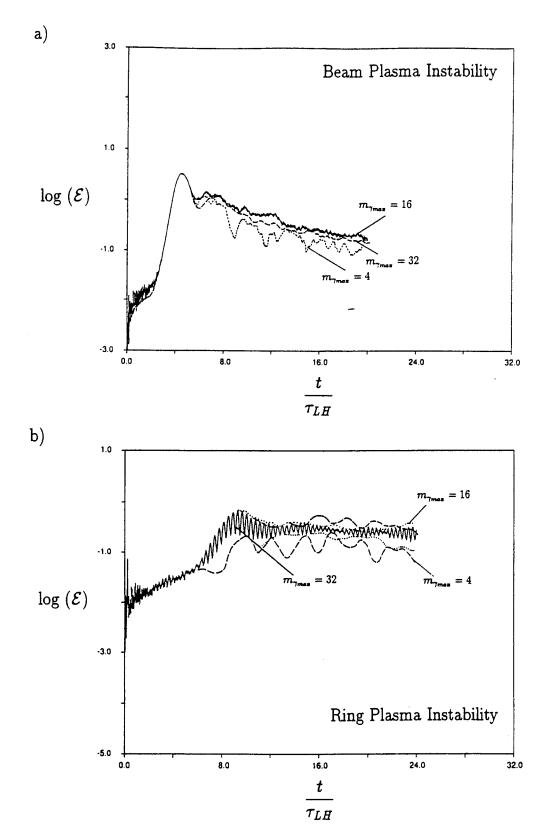
Figure A-1: Effect of changing the number of wave modes in the simulation system on the total electrostatic wave field energies of (a) the beam plasma instability and (b) the ring plasma instability. $m_{\gamma_{max}}$ denotes the mode number corresponding to the linearly fastest growing mode. In all these runs 64 particles per cell of each species were used and the time step was $\Delta t = 0.218082$ (normalized by the electron plasma frequency).

265

a)

Beam Plasma Instability

$\frac{1}{2} n_w m_w V_{Dw}^2$

$m_{\gamma_{max}} = 16$

$m_{\gamma_{max}} = 32$

$m_{\gamma_{max}} = 4$

$\dfrac{t}{\tau_{LH}}$

b)

$n_0 K T_0$

$m_{\gamma_{max}} = 16$

$m_{\gamma_{max}} = 32$

$m_{\gamma_{max}} = 4$

Ring Plasma Instability

$\dfrac{t}{\tau_{LH}}$
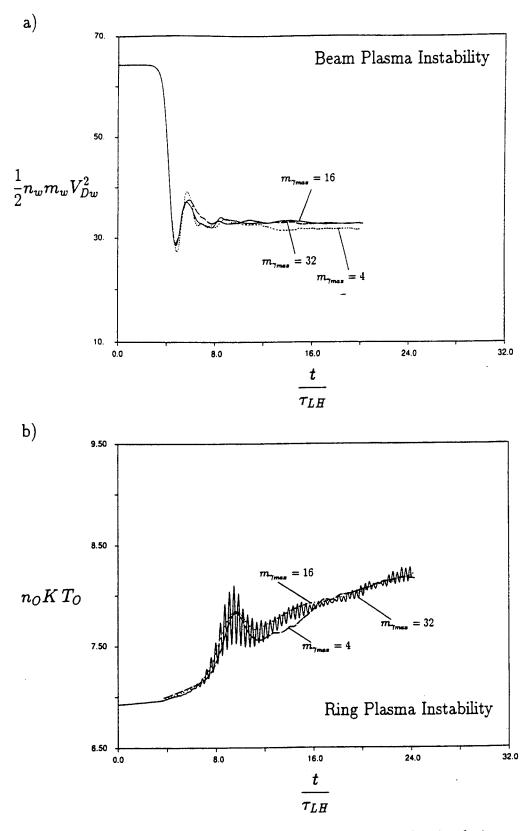
Figure A-2: Effect of changing the number of wave modes in the simulation system on the (a) beam drift energy of the beam plasma instability and (b) background ion thermal energy of the ring plasma instability. $m_{\gamma_{max}}$ denotes the mode number corresponding to the linearly fastest growing mode. In all these runs 64 particles per cell of each species were used and the time step was $\Delta t = 0.218082$ (normalized by the electron plasma frequency).

266
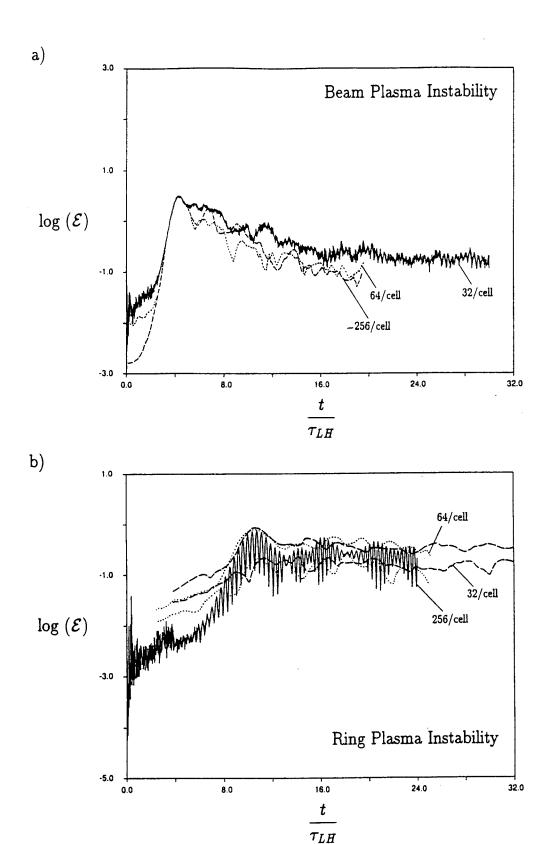
Figure A-3: Effect of changing the number of particles per cell of each species on the total electrostatic wave field energies of (a) the beam plasma instability and (b) the ring plasma instability. The number of particles per cell of each species used in the runs are indicated. In all these runs the time step was $\Delta t = 0.218082$ (normalized by the electron plasma frequency) and the system size was such that the linearly fastest growing mode was mode $m_{\gamma_{max}} = 4$.

a)

Beam Plasma Instability

$\frac{1}{2}n_w m_w V_{Dw}^2$

256/cell

64/cell

32/cell

70.

50.

30.

10.

0.0   8.0   16.0   24.0   32.0

$\dfrac{t}{\tau_{LH}}$

b)

$n_O K T_O$

9.50

8.50

7.50

6.50

32/cell

64/cell

256/cell

Ring Plasma Instability

0.0   8.0   16.0   24.0   32.0

$\dfrac{t}{\tau_{LH}}$
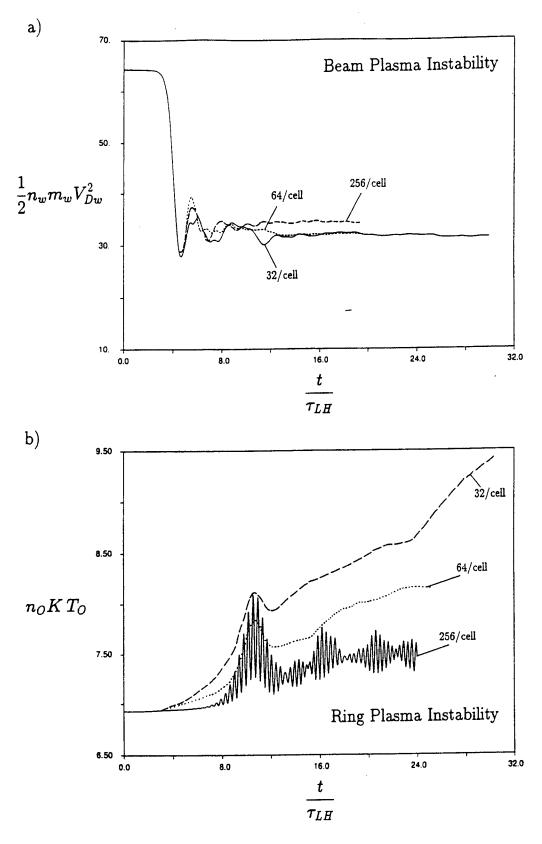
Figure A-4: Effect of changing the number of particles per cell of each species on the (a) beam drift energy of the beam plasma instability and (b) background ion thermal energy of the ring plasma instability. The number of particles per cell of each species used in the runs are indicated. In all these runs the time step was $\Delta t = 0.218082$ (normalized by the electron plasma frequency) and the system size was such that the linearly fastest growing mode was mode $m_{\gamma_{max}} = 4$.

a)

b)
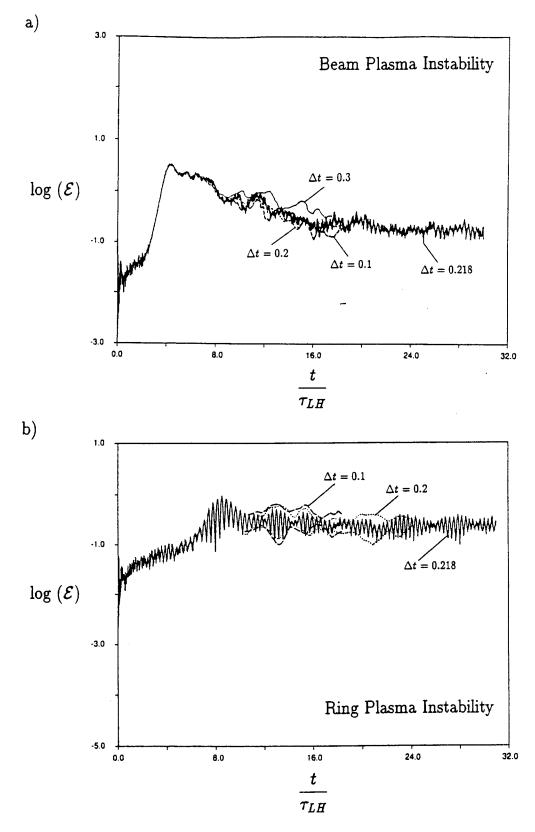
Figure A-5: Effect of changing the time step on the total electrostatic wave field energies of (a) the beam plasma instability and (b) the ring plasma instability. The time steps Δt (normalized by the electron plasma frequency) used in the runs are indicated. In all these runs 32 particles per cell of each species were used and the system size was such that the linearly fastest growing mode was mode $m_{\gamma_{max}} = 4$.

269

a)

b)
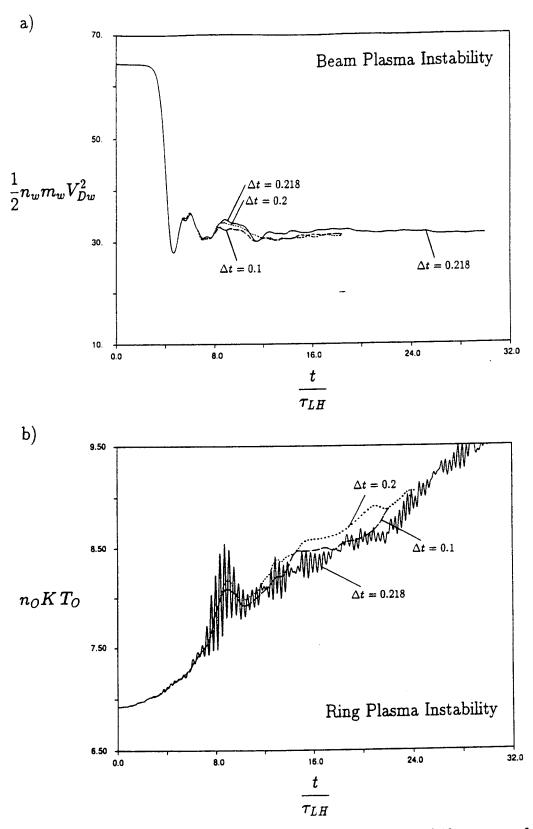
Figure A-6: Effect of changing the time step on the (a) beam drift energy of the beam plasma instability and (b) background ion thermal energy of the ring plasma instability. The time steps Δt (normalized by the electron plasma frequency) used in the runs are indicated. In all these runs 32 particles per cell of each species were used and the system size was such that the linearly fastest growing mode was mode $m_{\gamma_{max}} = 4$.

270

Appendix B

Simulation Results of the X5a135 Beam-Arc Plasma Instability

In Section 5.4, we present some of the 1d simulations results of the $X_p = 1$ and $X_p = 5$ beam-arc plasma instabilities for various propagation directions in the plane nearly perpendicular to the magnetic field. The output of the simulations show that in each propagation direction the instability evolution starts with an early stage of strong turbulence in which the beam-arc particles are strongly heated. As a result of the heating, the 1d beam-arc distributions of the various runs start resembling each other at early stages long before saturation. Furthermore, because of this resemblance in the early stages distributions, the results of the various runs for the different propagation directions turn out to be qualitatively the same. The major differences are in the magnitudes of the various effects of physical processes that occur in the nonlinear regime. In this appendix, we present the results of the X5a135 beam-arc plasma instability simulation (i.e. for the $X_p = 5$ beam-arc and in the $\theta_{k_\perp} = 135^o$ propagation direction) in order to show that they are indeed qualitatively the same as those of the X5a45 beam-arc plasma instability simulation, which are described in detail in Section 5.4.
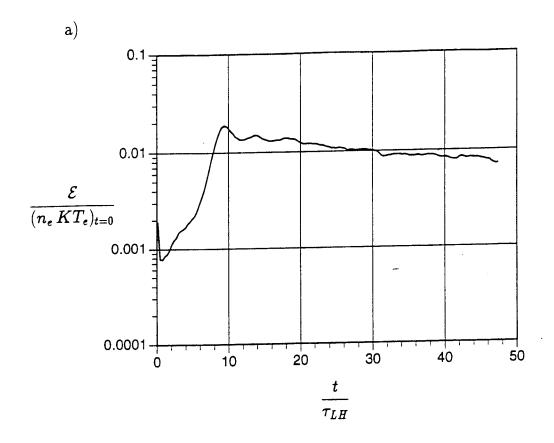
In what follows we summarize the results of the X5a135 beam-arc plasma instability simulation which are shown in the figures of this appendix. The reader should note that these results are qualitatively the same as those of the X5a45 beam-arc plasma instability simulation which are shown in Figures 5-8 to 5-13. The X5a135 instability evolution (see Figure B-1) starts with the wave modes being destabilized
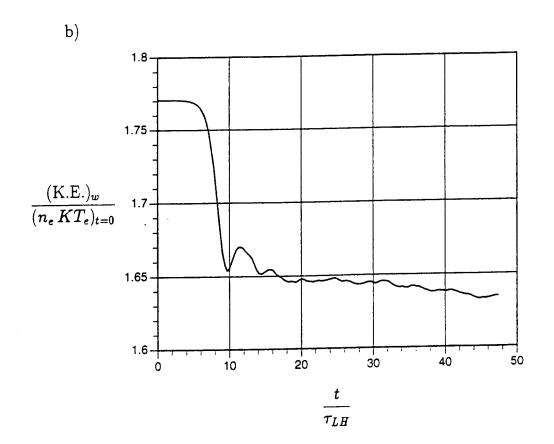
by the reactive instability mechanism, from the bunching of the different species. At these early times the beam-arc particles are strongly heated but the instability continues to be dominated by the bunching mechanism of the linearly fastest growing modes (see Figure B-2). Then, the instability saturates by trapping of the beam-arc particles in the potential wells. Many modes are excited during saturation; there is no evidence for any especial nonlinear effect that would cause the dominance of a single mode. In phase space the usual vortices indicating trapping are seen when a section of the system is magnified (see Figure B-3).
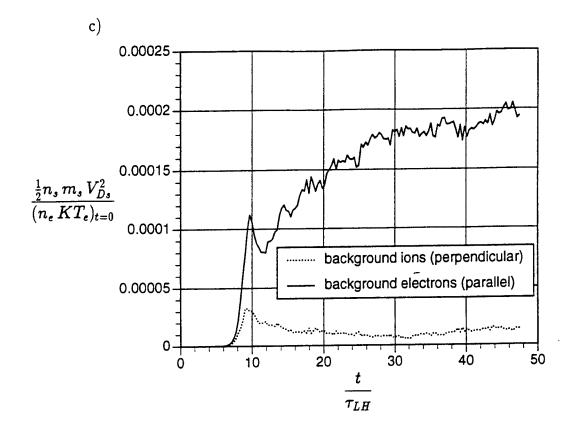
Several lower hybrid periods after saturation, a transition from reactive to kinetic instability takes place which results from (1) the broadening of the space-averaged beam-arc distribution function by the sloshing motion of the particles in the vortices and (2) the randomization of the vortices, which increase significantly the number of beam-arc ions in the resonant region. Therefore, with a larger number of resonant ions the instability becomes kinetic and quasilinear theory and other turbulence theories are again expected to apply. In this stage, and even in the previous stage of the extreme case of reactive instability, the feedback effect of the wave-particle interaction on the wave growth is important. Mode coupling effects are not prominent and thus unable to prevent plateau formation.
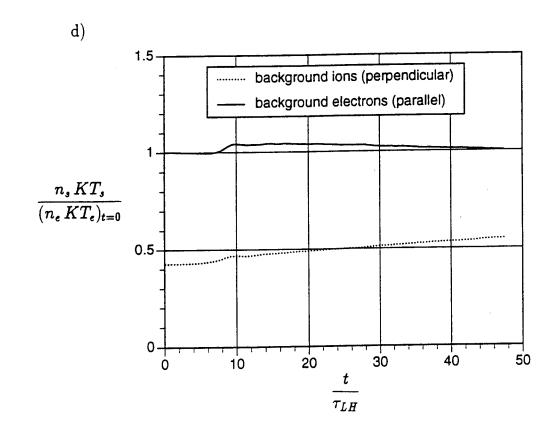
Lastly, our analysis of the wave modes spectrum and time history reveals various nonlinear processes. One of them, namely, competition between modes in the large k scale occurs because of the greater bunching ability of the linearly fastest growing modes (see Figure B-4). These fastest growing modes absorb some of the free energy that is initially available for the excitation of the other (i.e. linearly slower growing) modes and thus inhibit the low wavenumber modes from growing. Furthermore, with many modes present, the stochastic nature of turbulence is evident since the mode number spectrum shows a fine structure and individual wave modes show a rather erratic time dependence, unless there is some averaging (see Figure B-5). The physical mechanism that produces the erratic fine structure of the spectrum is related to the competition between modes in the small k scale. This involves some modes taking energy from, or preventing further growth of, their adjacent modes due to

their greater bunching ability. Therefore, this is a result of the stochastic nature of the initial conditions of the simulation design such as the loading of the particles and the initial wave phases. The simulation spectrum shows that at the end of the run, in the quasi-steady state, the highest wave mode energies correspond to the modes that are initially the most linearly unstable and that those modes have frequencies near the lower hybrid frequency (see Figure B-6). However, the results also show that larger and larger wavenumber modes are destabilized by the advance of a beam-arc distribution front to lower and lower velocities in connection to the wave-beam arc resonant particle interaction. This occurs in the early kinetic stage but the energy contained in these modes remains small (compared to that of the linearly most unstable modes). The rate of this process decreases until it terminates by the flattening of the bump in the total ion distribution. At this point, wave growth at larger and larger wave numbers is arrested by landau damping from the background ions. Once a plateau is formed in the quasi-steady state, changes in the total ion distribution and the spectrum remain very small.

a)

$$\frac{\mathcal{E}}{(n_e\,KT_e)_{t=0}}$$

$$\frac{t}{\tau_{LH}}$$

b)

$$\frac{(K.E.)_w}{(n_e\,KT_e)_{t=0}}$$

$$\frac{t}{\tau_{LH}}$$

274

c)

d)

e)

Figure B-1: Time history of energies for the X5a135 run. (a) Electric field energy. (b) Total (drift+thermal) energy of beam-arc water ions. (c) Drift energies of background ions and electrons. (d) Thermal energies of background ions and electrons. (e) Total (field+drift+thermal) energy in the simulation system.

a)

$\theta_{k_\perp} = 135^o$

$f_w(v)$

$\bar{t} = 0.0$
5.0
9.2
23.0

v

2400.

1600.

800.

0.

-0.40   -0.20   0.00   0.20   0.40

b)

c)
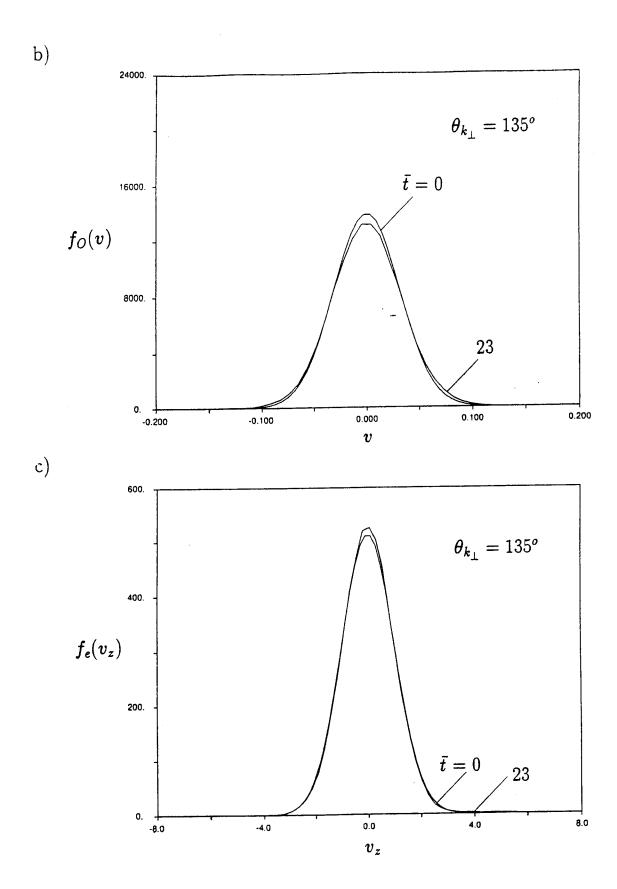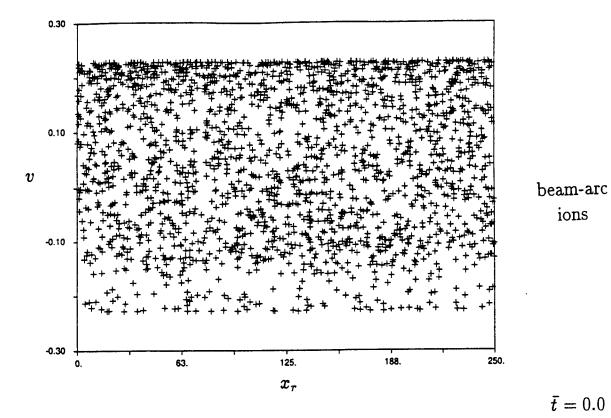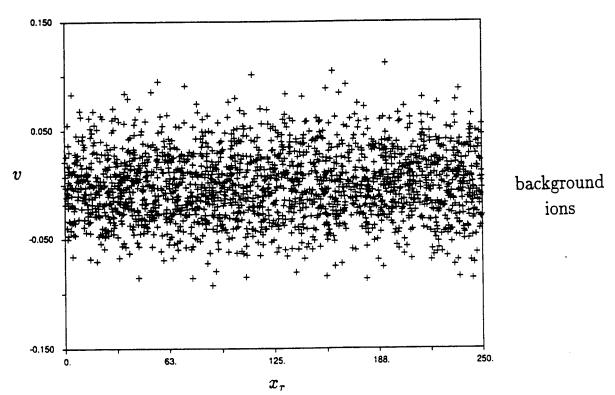
Figure B-2: Reduced distribution plots for the X5a135 run. (a) Evolution of the beam-arc ion distribution; the advance of the beam-arc front to lower velocities and the plateau formation are seen. (b) and (c) show the initial and quasi-steady state distributions of the background ions and electrons, respectively.
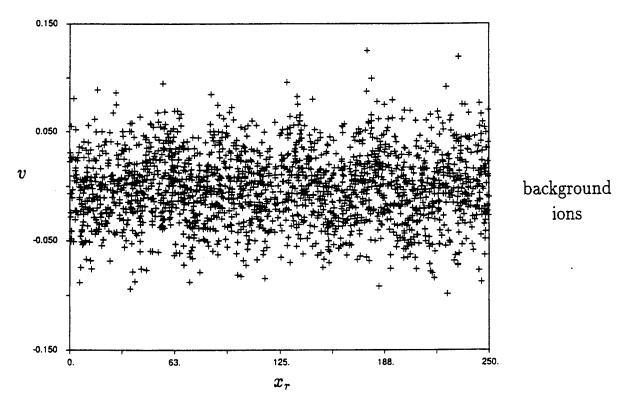
a)

beam-arc
ions

$\bar{t} = 0.0$

background
ions

$\bar{t} = 0.0$

electrons

b)

beam-arc
ions

$\bar{t} = 9.2$

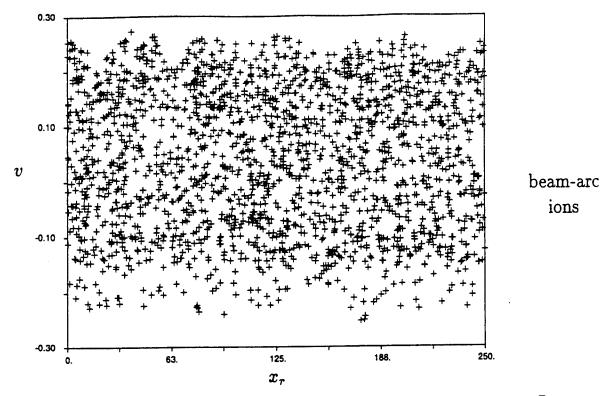background
ions

281

$\bar{t} = 9.2$

electrons

(parallel component)

$v_\parallel$

x_r

c)

beam-arc
ions

$\bar{t} = 13.7$

background
ions

283

$\bar{t} = 13.7$

electrons

$v_{\parallel}$ (parallel component)

x_τ

d)

beam-arc
ions

$\bar{t} = 23.0$

background
ions
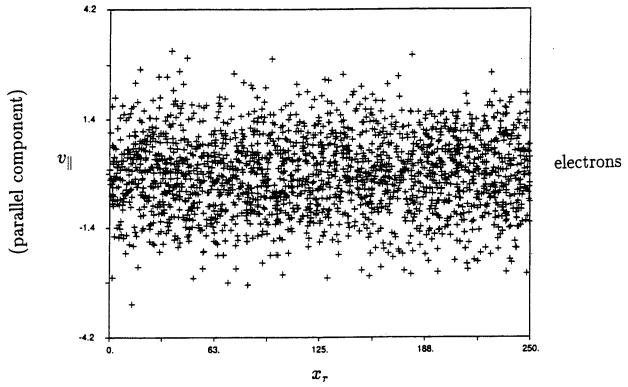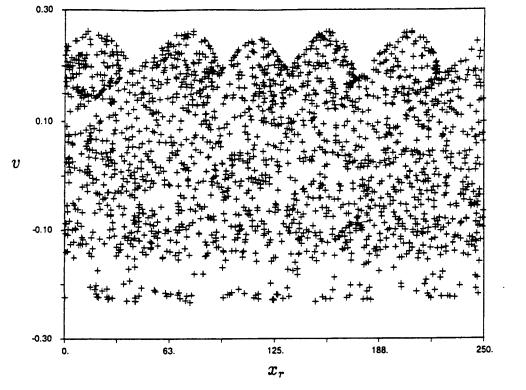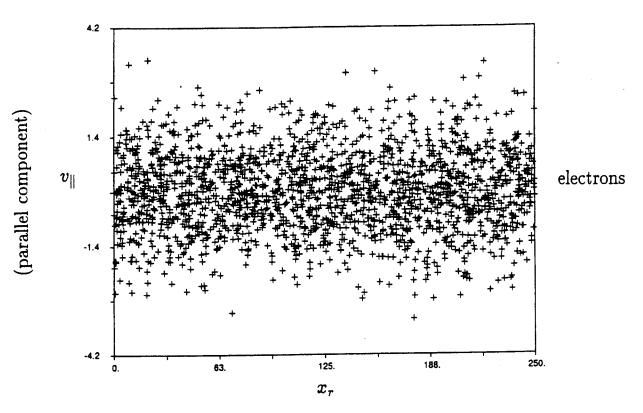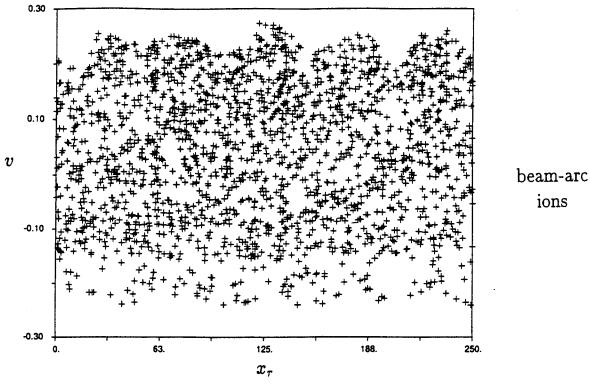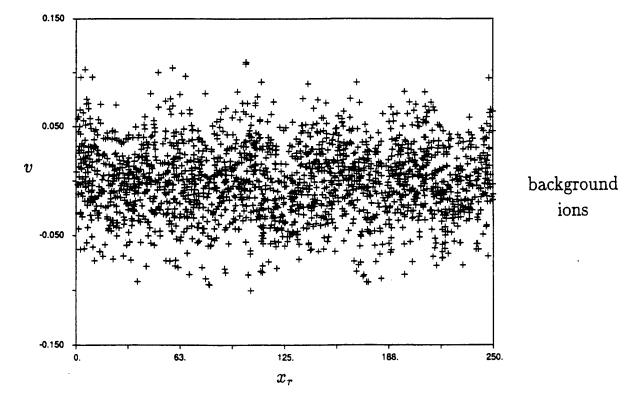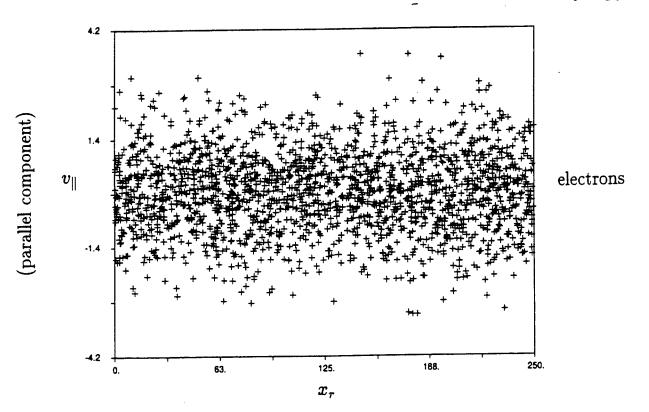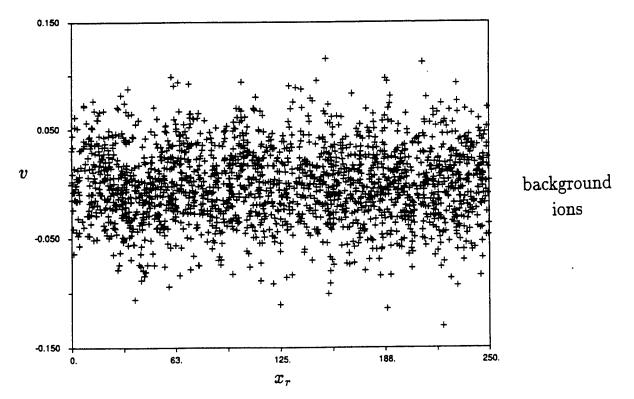
$\bar{t} = 23.0$
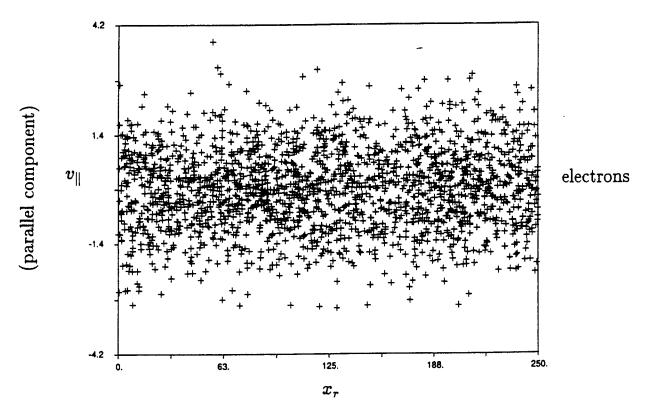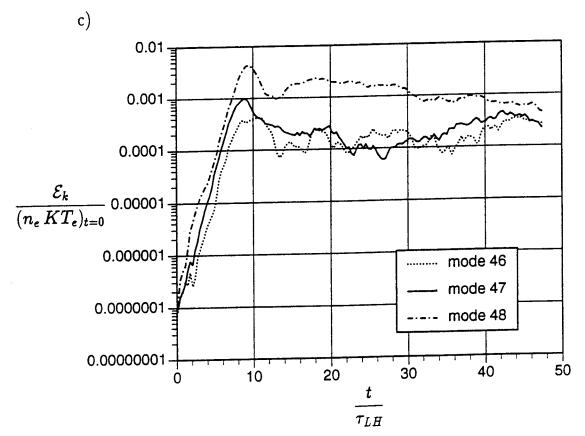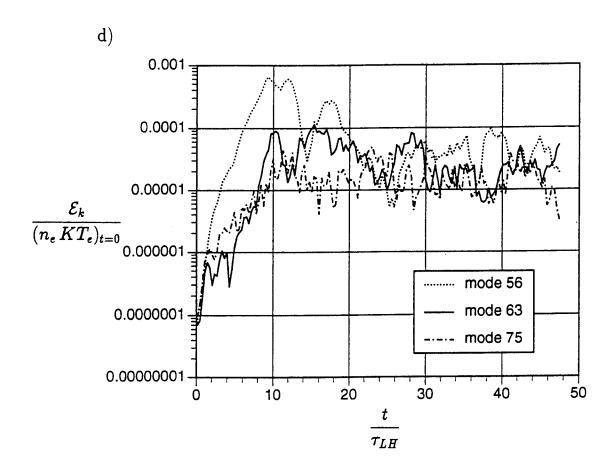
Figure B-3: Evolution of ions and electrons in phase space (only 1/8 of the system length and about 1% of the ions are shown). (a) At $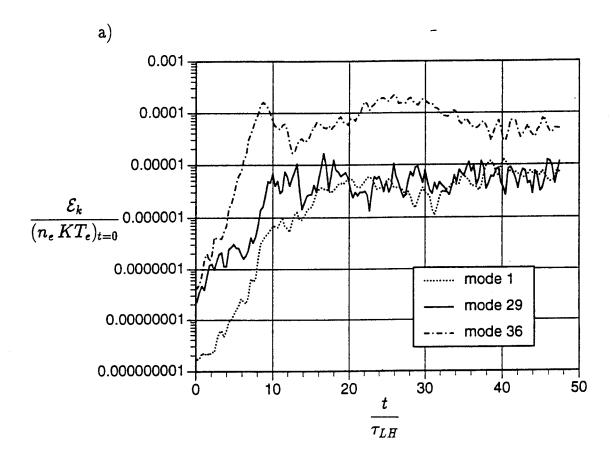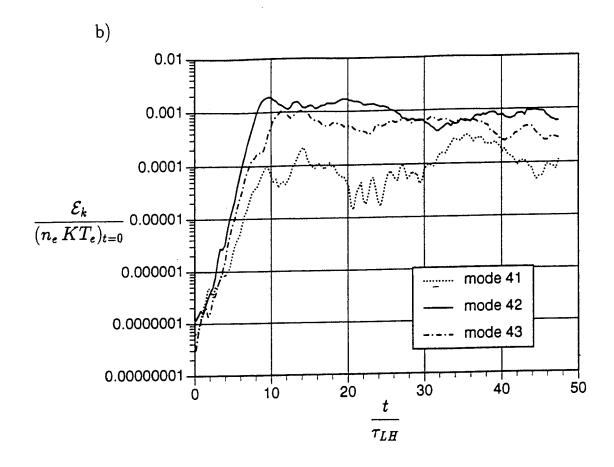\bar{t} = 0$. (b) Vortices indicating beam-arc ion trapping near saturation. (c) One bounce period after saturation. (d) In the quasi-steady state, vortices are smeared out by the randomization of the particles by the many modes.

a)

$$\frac{\mathcal{E}_k}{(n_e\,KT_e)_{t=0}}$$

....	mode 1
——	mode 29
—·—·—	mode 36

$$\frac{t}{\tau_{LH}}$$

b)

c)

d)
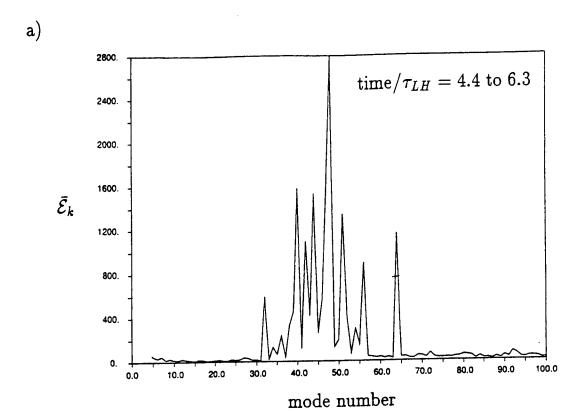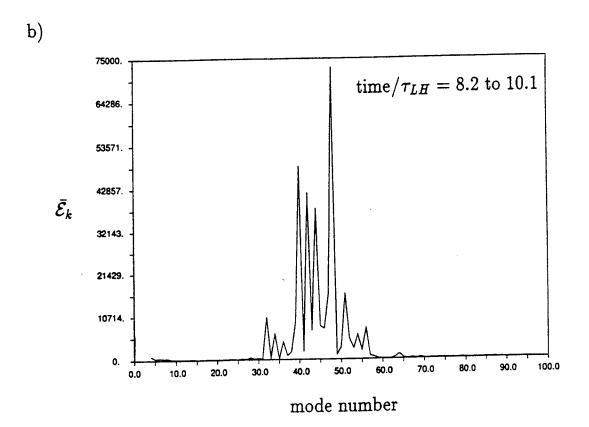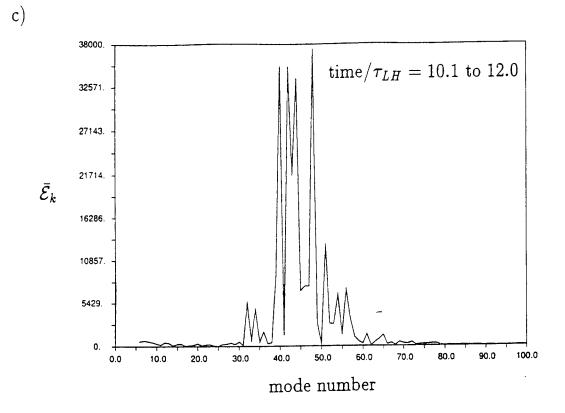
Figure B-4: Time history of mode energies. (a) Competition between modes (in the large k scale). The greater bunching ability of the most linearly unstable modes prevents the low wavenumber modes from growing. (b) and (c) Competition between modes (in the small k scale). Before saturation, modes with greater bunching ability prevent adjacent modes from growing. When many modes are present the stochastic nature of turbulence is evident: the mode number spectrum has a fine structure and individual wave modes show a rather erratic time dependence, unless there is some averaging. (d) Destabilization of large wavenumber modes. Linearly stable, large wavenumber modes are destabilized due to the advance of a beam-arc front to lower velocities.

a)

b)

c)

$$\text{time}/\tau_{LH} = 10.1 \text{ to } 12.0$$

$\bar{\mathcal{E}}_k$

mode number

d)

$$\text{time}/\tau_{LH} = 19.6 \text{ to } 21.5$$

$\bar{\mathcal{E}}_k$

mode number
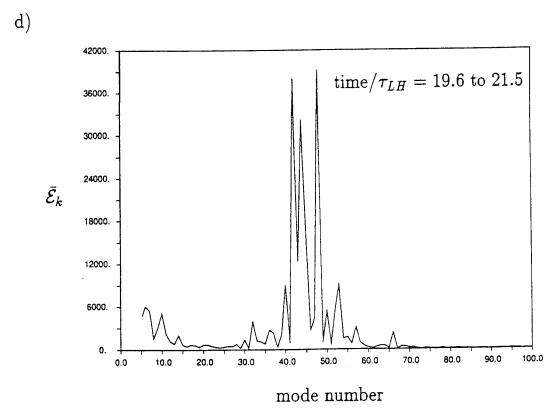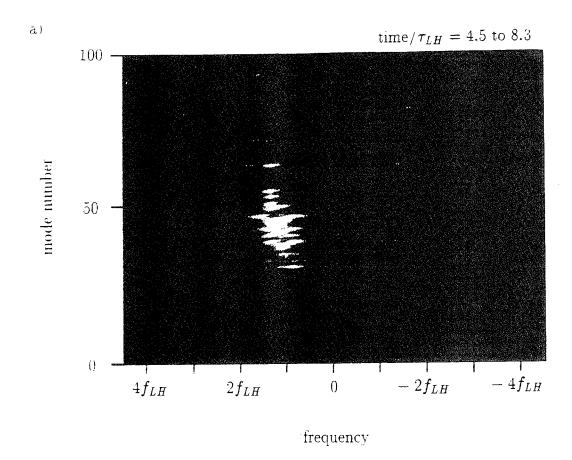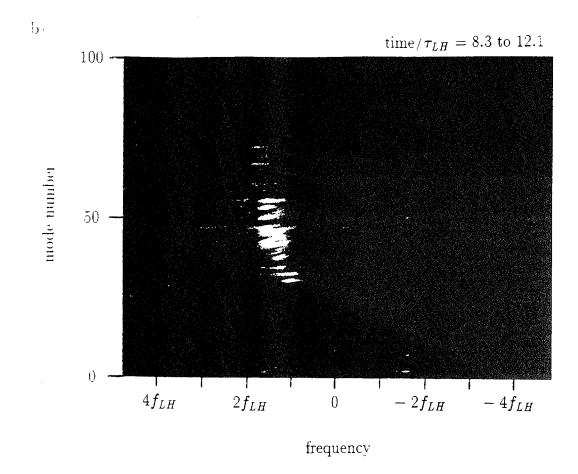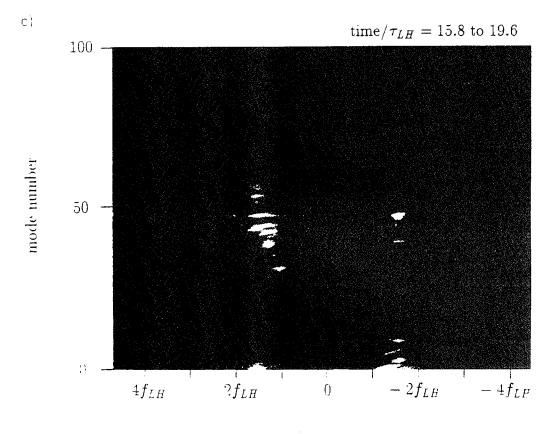
Figure B-5: Average mode number spectral field energies for various time periods. (a) In the linear regime, the spectrum is broad as predicted by the linear theory. (b) During saturation, the spectrum is broad but restricted to the range of most linearly unstable modes. (c) After saturation, large wavenumber modes are destabilized due to the advance of the beam-arc front to lower velocities. (d) The quasi-steady state spectrum.

a)

time/τ_{LH} = 4.5 to 8.3

mode number

100

50

0

4f_{LH} 2f_{LH} 0 −2f_{LH} −4f_{LH}

frequency

time/τ_{LH} = 8.3 to 12.1

100

mode number

50

0

4f_{LH} 2f_{LH} 0 $-2f_{LH}$ $-4f_{LH}$

frequency

c)

time/τ_{LH} = 15.8 to 19.6

100

mode number

50

0

4f_{LH} 2f_{LH} 0 $-2f_{LH}$ $-4f_{LH}$

frequency

d)   time/τ_{LH} = 19.6 to 23.4
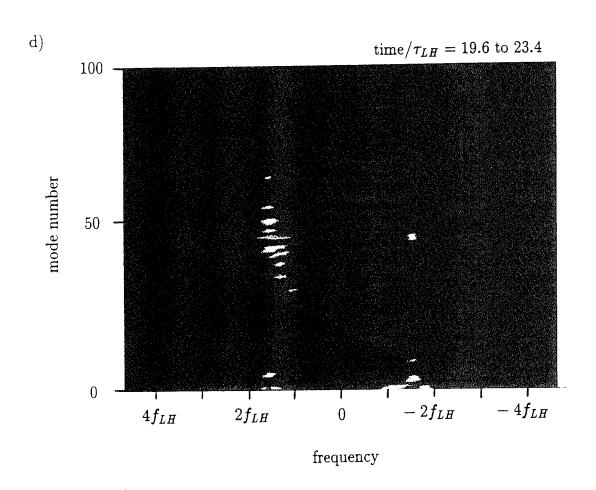
Figure B-6: Electric field energy density spectrum (frequency versus mode number) for various time periods. The color coded intensities decrease by about one order of magnitude in each color in the following order: red, yellow, green, light blue and dark blue. (a) Broad frequency spectrum in the reactive phase before saturation. (b) During saturation the frequency spectrum narrows. (c) After saturation and (d) in the quasi-steady state, the frequency spectrum remains narrow with $f \sim f_{LH}$ and concentrated near the linearly fastest growing modes.

Bibliography

[1] Adam, J. C. Laval, and D. Pesme, Importance of mode-coupling effects in quasi-linear theory, in *Proceedings of the 4th International Conference on Waves and Instabilities,* p. 298, Fusion Research Association of Japan, Nagoya, Japan, 1980.

[2] Alfven, H., *On the Origin of the Solar System,* Oxford University Press, New York, 1954.

[3] Anderson, R. R., G. K. Parks, T. E. Eastman, D. A. Gurnett, and L. A. Frank, Plasma waves associated with energetic particles streaming into the solar wind from the Earth's bow shock, *J. Geophys. Res., 86,* 4493-4510, 1981.

[4] Banks, P. M., P. R. Williiamson, and W. J. Raitt, Space shuttle glow observations, *Geophys. Res. Lett., 10,* 118-121, 1983.

[5] Berk, H.L., W. Horton, Jr., M.N. Rosenbluth, and P.H. Rutherford, Microinstability theory of two-energy-component toroidal systems, *Nucl. Fusion, 15,* 819, 1975.

[6] Biasca, R. J., Numerical simulation of the critical ionization velocity mechanism, *Ph. D. thesis, Massachusetts Institute of Technology,* 1992.

[7] Birdsall, C. K., and A. B. Langdon, *Plasma via Computer Simulation,* McGraw-Hill, New York, 1985.

[8] Biskamp, D., and H. Welter, On the validity of the quasi-linear approximation for turbulent plasmas, *Nucl. Fusion, 12,* 89-97, 1972.

[9] Bittencourt, J. A., *Fundamentals of Plasma Physics,* Pergamon Press, Oxford, 1986.

[10] Boutros-Ghali, T., and T. H. Dupree, Theory of two-point correlation function in a Vlasov plasma, *Phys. Fluids, 24,* 1839-1858, 1981.

[11] Cairns, I. H., and D. B. Melrose, A theory for the $2f_p$ radiation upstream of the Earth's bow shock, *J. Geophys. Res., 90,* 6637, 1985.

[12] Cairns, I. H., New waves at multiples of the plasma frequency upstream of the Earth's bow shock, *J. Geophys. Res.*, *91*, 2975, 1986.

[13] Cairns, I. H., The electron distribution function upstream from the Earth's bow shock, *J. Geophys. Res.*, *92*, 2315, 1987.

[14] Cairns, I. H., A semi-quantitative theory for the $2f_p$ radiation observed upstream from the Earth's bow shock, *J. Geophys. Res.*, *93*, 3958, 1988.

[15] Cairns, I. H., and K.-I. Nishikawa, Simulations relevant to the beam instability in the foreshock, *J. Geophys. Res.*, *94* 79, 1989.

[16] Cairns, I. H., Transition from ring to beam arc distributions of water ions near the space shuttle orbiter, *J. Geophys. Res.*, in press, 1990

[17] Cairns, I. H., Transition from ring to beam arc distribution functions of water ions with distance upstream from the space shuttle orbiter, *J. Geophys. Res.*, *95*, 15167, 1990.

[18] Cairns, I. H., and D. A. Gurnett, Control of plasma waves associated with the space shuttle by the angle between the orbiter's velocity vector and the magnetic field, *J. Geophys. Res.*, *96*, 7591, 1991a.

[19] Cairns, I. H., and D. A. Gurnett, Plasma waves observed in the near vicinity of the space shuttle, *J. Geophys. Res.*, *96*, 13913, 1991b.

[20] Cap, F.F., *Handbook of plasma instabilities, vol. 1*, Academic Press, Inc., New York, 1976.

[21] Chen, F.F, *Introduction to plasma physics and controlled fusion*, Plenum Press, New York, 1984.

[22] Cole, K. D., Atmospheric excitation and ionization by ions in strong auroral and man-made electric fields. *J. atmos. terr. Phys.*, 33, 1241-1249, 1971.

[23] Cordey, J.G., and M.J. Houghton, Problems associated with the injection of a high-energy neutral beam into a plasma, *Nucl. Fusion*, *13*, 215, 1973.

[24] Danielson, L., and N. Brenning, Experiment on the interaction between a plasma and a neutral gas, *Phys. Fluids*, *18*, 661-671, 1970.

[25] Davison, R. C., *Methods in Non-Linear Plasma Theory*, pp. 174-187, Academic, New York, 1972.

[26] Davidson, R. C., and J. M. Ogden, Electromagnetic ion cyclotron instability driven by ion energy anisotropy in high-beta plasmas, *Phys. Fluids*, *18*, 1045, 1975.

[27] Dawson, J., On Landau damping, *Phys. Fluids*, *4*, 869, 1961.

[28] Drummond, J. E., Basic microwave properties of hot magnetoplasmas, *Phys. Rev., 110*, 293, 1958.

[29] Drummond, W. E., J. H. Malmberg, T. M. O'Neil and J. R. Thompson, Nonlinear development of the beam-plasma instability, *Research Notes*, 2422-2425, 1970.

[30] Dum, C. T., Simulation studies of plasma waves in the electron foreshock: The generation of Langmuir waves by a gentle bump-on-tail electron distribution, *J. Geophys. Res., 95*, 8095, 1990a.

[31] Dum, C. T., Simulation studies of plasma waves in the electron foreshock: The transition from reactive to kinetic instability, *J. Geophys. Res., 95*, 8111, 1990b.

[32] Dum, C. T., Simulation of the plasma waves in the electron foreshock: The generation of downshifted oscillation, *J. Geophys. Res., 95*, 8123, 1990c.

[33] Dum, C. T., The electron beam instability and turbulence theories, in *Physics of Space Plasmas (1989), SPI Conference Proceedings and Reprints Series, No. 9*, ed. by T. Chang, G. B. Crew, and J. R. Jasperse, p. 67, Scientific Publishers, Inc., Cambridge, Mass., 1990d.

[34] Dunckel, N., Low-frequency radio emission from the Earth and Sun, Ph.D. thesis, 178 pp., Stanford Univ. Stanford, Calif., 1974.

[35] Elliot, D. F., and Rao, K. R., *Fast Transforms: Algorithms, Analyses, Applications*, Academic Press, New York, 1982.

[36] Farrell, W. M., D. A. Gurnett, P. M. Banks, R. I. Bush, and W. J. Raitt, An analysis of whistler mode radiation from the Spacelab-2 electron beam, *J. Geophys. Res., 93*, 153, 1988.

[37] Feng, W., D. A. Gurnett, and I. H. Cairns, Interference patterns in the Spacelab 2 plasma wave data: Lower hybrid waves driven by pickup ions, *J. Geophys. Res.*, in press, 1993.

[38] Feng, W., D. A. Gurnett, and I. H. Cairns, Interference patterns in the Spacelab 2 plasma wave data: Oblique electrstatic waves generated by the electron beam, *J. Geophys. Res., 97*, 17005, 1992.

[39] Formisano, V., A. A. Galeev, and R. Z. Sagdeev, The role of the critical ionization velocity phenomena in the production of inner coma cometary plasma, *Planet. Space Sci., 30*, 491-497, 1982.

[40] Fried, B.D., and S.D. Conte, *The plasma dispersion function*, Academic Press, Inc., New York,1961.

[41] Fried, B. D., and A. Y. Wong, Stability limits for longitudinal waves in ion beam-plasma interaction, *Phys. Fluids, 9*, 1084, 1966.

[42] Fuselier and D. A. Gurnett, Short wavelength ion waves upstream of the Earth's bow shock, *J. Geophys. Res., 89*, 91, 1984.

[43] Gaffey, J. D., Jr., Instability of energetic ion beam injection in tokamaks, *J. Plasma Phys., 16*, 171, 1976.

[44] Galeev, A. A., Quasilinear theory of the loss-cone instability, *J. Plasma Phys., 1.* 104, 1967.

[45] Gary, S. P., Electrostatic Instabilities in plasmas with two electron components, *J. Geophys. Res., 90*, 8213, 1985.

[46] Gatsonis, N. A., and D. E. Hastings, A three-dimentional model and initial time numerical simulation for an artificial plasma cloud in the ionosphere, *J. Geophys. Res., 96*, 7623, 1991.

[47] Ginzburg, V. L., and V. V. Zheleznyakov, On the possible mechanism of sporadic radio emission (radiation in an isotropic plasma), *Sov. Astron.*, Engl. Transl., 2, 653, 1959.

[48] Goldman, M. V., Strong turbulence of plasma waves, *Rev. Mod. Phys., 56*, 709, 1984.

[49] Grard, R., A. Pederson, J.-G. Trotignon, C. Beghin, M. Mogilevsky, Y. Mikhailov, O. Molchanov, and V. F. Formisano, Observations of waves and plasmas in the environment of comet Halley, *Nature, 321*, 290, 1986.

[50] Grebowsky, J.M., M.W. Pharo III, H.A. Taylor, Jr., and I.J. Eberstein, Measured thermal ion environment of STS-3, *AIAA pap., 83-2597*, 1983.

[51] Gurevich, A. V., *Nonlinear Phenomena in the Ionosphere*, p. 77, Springer-Verlag, New York, 1978.

[52] Gurnett, D. A., W. S. Kurth, and F. L. Scarf, Plasma waves near Saturn: initial results from Voyager 1, *Science, 212*, 239, 1981.

[53] Gurnett, D. A., R. R. Anderson, B. Hausler, G. Haerendel, O. H. Bauer, R. A. Treumann, H. C. Koons, R. Holzworth and H. Luhr, Plasma waves associated with the AMPTE artificial comet, *Geophys. Res. Lett., 12*, 851, 1985.

[54] Gurnett, D. A., T. Z. Ma, R. R. Anderson, O. H. Bauer, G. Haerendel, B. Hausler, G. Paschmann, R. A. Treumann, H. C. Koons, R. Holzworth and H. Luhr, Analysis and interpretation of the shocklike electrostatic noise observed during the AMPTE solar wind lithium releases, *J. Geophys. Res., 91*, 1301, 1986.

298

[55] Gurnett, D. A., W. S. Kurth, J. T. Steinberg, P. M. Banks, R. I. Bush and W. J. Raitt, Whistler-mode radiation from the Spacelab-2 electron beam, *Geophys. Res. Lett.*, *13*, 225, 1986.

[56] Gurnett, D. A., W. S. Kurth, J. T. Steinberg, and S. D. Shawhan, Plasma wave turbulence around the shuttle: Results from the Spacelab-2 flight, *Geophys. Res. Lett.*, *15*, 760, 1988.

[57] Haerendel, G., Alfven's critical velocity effect tested in space, *Z, Naturforsch.*, *379*, 728-734, 1982.

[58] Hastings, D. E., and N. A. Gatsonis, The motion of contaminant water plasma clouds about large active space structures, *J. Geophys. Res.*, *94*, 3729, 1989.

[59] Hildebrand, F. B., *Advanced Calculus for Applications.*, p. 150. Prentice-Hall, Englewood Cliffs, N.J, 1964.

[60] Hoang, S., J. Fainberg, J. L. Steinberg, R. G. Stone, and R. H. Zwickl, The $2f_p$ circumterrestrial radio emission as seen from ISSE 3, *J. Geophys. Res.*, *86*, 4531, 1981.

[61] Hoffman, R. J., and M. A. Hetreck, Jr., Plume contamination effects prediction: Contam III Computer Program, Tech. Rep. AFRPL TR82-033, Air Force Rocket Propul. lab., Edwards AFB, Calif., 1982.

[62] Hunton, D. E., and J. M. Calo, Low energy ions in the shuttle environment: Evidence for strong ambient-contaminant interactions, *Planet. Space Sci.*, *33*, 945, 1985.

[63] Hwang, K. S., N. H. Stone, K. H. Wright, Jr., and U. Samir, The emissions of broadband electrostatic noise in the near vicinity of the shuttle orbiter, *Planet. Space Sci.*, *35*, 1373, 1987.

[64] Ichimaru, S., Basic principles of plasma physics (a statistical approach), Addison-Wesley Publishing Company, Inc., 1973.

[65] Kairner, S., J. Dawson, and R. Shanny, Interaction of a highly energetic beam with a dense plasma, *Phys. Fluids*, *15*, 493, 1972.

[66] Kintner, P. M., M. C. Kelley, G. Holmgren, and R. Bostrom, The observations and production of ion acoustic waves during the trigger experiment, *J. Geophys. Res.*, *85*, 5071, 1980.

[67] Klimas, A. J., A mechanism for the plasma waves at harmonics of the plasma frequency in the electron foreshock boundary, *J. Geophys. Res.*, *88*, 9081, 1983.

[68] Klimas, A. J., Trapping saturation of the bump-on-tail instability and electro-static harmonic excitation in Earth's foreshock, *J. Geophys. Res.*, *95*, 14905, 1990.

[69] Klimas, A. J., and R. J. Fitzenreiter, On the persistence of unstable bump-on-tail electron velocity distribution in the Earth's foreshock, *J. Geophys. Res., 93*, 9628, 1988.

[70] Koons, H. C., J. L. Roeder, O. H. Bauer, G, Haerendel, R. Treumann, R. R. Anderson, D. A. Gurnett, and R. H. Holzworth, Observations of nonlinear wave decay processes in the solar wind by the AMPTE IRM plasma wave experiment, *J. Geophys. Res., 92*, 5865. 1987.

[71] Krall, N.A., and A.W. Trivelpiece, Principles of Plasma Physics, *San Francisco Press*, CA, 1986.

[72] Krall, N.A., and P.C. Liewer, Turbulent heating and resistivity in cool-electron θ-pinches, *Phys. Fluids, 15*, 1166, 1972.

[73] Krauss-Varban, D., The beam instability of the Z-mode in the solar wind, *J. Geophys. Res., 94*, 3527, 1989.

[74] Kurth, W. S., and L. A. Frank, The Spacelab-2 Plasma Diagnostics Package, *J. Spacecraft Rockets, 27*, 70-75, 1990.

[75] Lacombe, C., A. Mangeney, C. C. Harvey, and J. D. Scudder, Electron plasma waves upstream of the Earth's bow shock, *J. Geophys. Res., 90*, 73, 1985.

[76] Lee, J. K., and C. K. Birdsall, Velocity space ring-plasma instability, magnetized, Part I: Theory, *Phys. Fluids, 22*, 1306, 1979.

[77] Lin, C. S., and D. Winske, Simulation of the electron acoustic instability for a finite-size electron beam system, *J. Geophys. Res., 92*, 7569, 1987.

[78] Machuzak, J. S., W. J. Burke, J. M. Retterer, D. E. Hunton, J. R. Jasperse and M. Smiddy, Effects of thruster firings on the shuttle's plasma electric field environment, *J. Geophys. Res., 98*, 1513, 1993.

[79] Marsh, E., Beam-driven electron acoustic waves upstream of the Earth's bow shock,*J. Geophys. Res., 90,* 6327, 1985.

[80] Martinez-Sanchez, M., Private Communication, Department of Aeronautics and Astronautics, Massachusetts Institute of Technology, 1993.

[81] McBride, J.B., E. Ott, J.P. Boris, and J.H. Orens, Theory and simulation of turbulent heating by the modified two-stream instability, *Phys. Fluids, 15*, 2367, 1972.

[82] Mclean, D. J., and N. R. Labrum, *Solar Radiophysics*, Cambridge University Press, New York, 1985.

[83] Melrose, D. B., *Instabilities in Space and Laboratory Plasma*, Cambridge University Press, New York, 1986.

[84] Mende, S. B., O. K. Garriot, and P. M. Banks, Observations of optical emissions on STS-4, *Geophys. Res. Lett., 10,* 122-125, 1983.

[85] Mikhailovskii, A.B., and V.S. Tsypin, High-frequency instability of a plasma in a radial electric and longitudinal magnetic field, *JETP Letters, 3,* 158, 1966.

[86] Miyamoto, K., *Plasma Physics for Nuclear Fusion,* MIT Press, Cambridge, Mass, 1980.

[87] Moses, S. L., F. V. Coroniti, C. F. Kennel, and F. L. Scarf, Strong electron heat flux modes in Jupiter's foreshock, *Geophys. Res. Lett., 11,* 869, 1984.

[88] Murphy, G. B., S. D. Shawhan, L. A. Frank, N. D'Angelo, D. A. Gurnett, J. M. Grebowsky, D. L. Reasoner and N. Stone, Interaction of the space shuttle orbiter with the ionospheric plasma,*Spacecraft/Plasma Interactions and their Influence on Field and Particle Measurements,* ESA SP-189, 73, 1983.

[89] Murphy, G. B., J. S. Pickett, N. D'Angelo, and W. S. Kurth, Measurements of the plasma parameters in the vicinity of the space shuttle, *Planet. Space Sci., 34,* 993, 1986.

[90] Muschietti, L., and C. T. Dum, Nonlinear wave scattering and electron beam relaxation, *Phys. Fluids B, 3,* 1968, 1991.

[91] Mynick, H.E., M.J. Gerver, and C.K. Birdsall, Stability regions and growth rates for a two-ion component plasma, unmagnetized, *Phys. Fluids, 20,* 606, 1977.

[92] Narcisi, R., E. Trzcinski, G. Federico, L. Wlodyka, and D. Delorey, The gaseous and plasma environment around space shuttle, *AIAA Pap., 83-2659,* 1983.

[93] Nishikawa, K.-I., L. A. Frank, and C. Y. Huang, Simulation of electrostatic turbulence in plasma sheet boundary layer with electron current and beam-shaped ion beans, *J. Geophys. Res., 93,* 5929, 1988.

[94] Nishikawa, K.-I. and I. H. Cairns, Simulation of the nonlinear evolution of electron plasma waves, *J. Geophys. Res., 96,* 19343-19351, 1991.

[95] O'Neil, T. M., and J. H. Malmberg, Transition of the dispersion roots from beam-type to Landau-type solutions, *Phys. Fluids, 11,* 1754-1760, 1968.

[96] O'Neil, T., Probability distribution for Fourier components of the electric field in weak plasma turbulence theory, *Phys. Fluids, 17,* 2249-2254, 1974.

[97] Ott, E., and D. T. Farley, Microinstabilities and the production of short-wavelength irregularities in the auroral F region, *J. Geophys. Res., 80,* 4599, 1975.

[98] Papadopoulos, K., M. Goldstein, and R. Smith, Stabilization of electron streams in type III solar bursts, *Astrophys. J., 190,* 175-185, 1974.

[99] Papadopoulos, K., The theory of the beam plasma discharge, in *Artificial Particle Beams in Space*, edited by B. Grandal, pp. 505-524, Plenum, New York, 1981.

[100] Papadopoulos, K. D., On the shuttle glow (the plasma alternative), *Radio Science, 19*, 571, 1984.

[101] Paterson, W. R., and L. A. Frank, Hot ion plasmas from the cloud of neutral gases surrounding the space shuttle, *J. Geophys. Res., 94*, 3721, 1989.

[102] Pickett, J. S., G. B. Murphy, W. S. Kurth, C. K. Goertz and S. D. Shawhan, Effects of chemical releases by the STS 3 orbiter on the ionosphere, *J. Geophys. Res., 90*, 3487, 1985.

[103] Pickett, J. S., N. D'Angelo, and W. S. Kurth, Plasma density fluctuations observed during space shuttle orbiter water releases, *J. Geophys. Res., 94*, 12081, 1989.

[104] Raadu, M. A., The role of electrostatic instabilities in the critical ionization velocity mechanism, *Astrophys. Space Sci., 55*, 125-138, 1978.

[105] Reasoner, D. L., S. D. Shawhan, and G. Murphy, Plasma diagnostics package measurements of ionospheric ions and shuttle-induced perturbations, *J. Geophys. Res., 91*, 13463, 1986.

[106] Rivas, D.R., and D.E. Hastings, Theoretical interpretation of the electrostatic waves in the space shuttle induced plasma environment, *J. Geophys. Res. 97*, 17097, 1992.

[107] Robinson, P. A., and D. L. Newman, Quasiperiodic behavior in beam-driven strong Langmuir turbulence, *Phys. Fluids B, 1*, 2319, 1989.

[108] Rodriguez, P., and D. A. Gurnett, Electrostatic and electromagnetic turbulence associated with the earth's bow shock, *J. Geophys. Res. 80*, 19, 1975.

[109] Scarf, F. L., F. V. Coroniti, C. F. Kennel, D. A. Gurnett, W-H Ip and E. J. Smith, Plasma wave observations at comet Giacobini-Zinner, *Science, 232*, 377, 1986.

[110] Seiler, S., M. Yamada, and H. Ikezi, Lower Hybrid instability driven by a spiraling ion beam, *Phys. Rev. Lett., 13*, 700,1976.

[111] Shapiro, V. D., Nonlinear theory of the interaction of a monoenergetic beam with a plasma, *Sov. Phys. JETP, Engl. Transl., 17*, 416, 1963.

[112] Shawhan, S. D., Description of the Plasma Diagnostics Package (PDP) for the OSS-1 shuttle mission and JSC chamber test in conjunction with the fast pulse electron gun (FPEG), in *Artificial Particle Beams in Space Plasma Studies*, edited by B. Grandel, p.419, Plenum, New York, 1982.

[113] Shawhan, S., and G. Murphy, Plasma diagnostic package assessment of the STS-3 orbiter environment and system for science, *Rep. AIAA-83-0253*, Am. Inst. of Aeronaut. and Astronaut., New York, 1983.

[114] Shawhan, S.D., G.B. Murphy, and J. S. Pickett, Plasma Diagnostic Package initial assessment of the shuttle orbiter plasma environment, *J. Spacecr. Rockets*, *21*, 387,1984.

[115] Siskind, D. E., W. T. Raitt, P. M. Banks and P. R. Williamson, Interaction between the orbiting space shuttle and the ionosphere, *Planet. Space Sci.*, *32*, 881, 1984.

[116] Slanger, T. G., Conjectures on the origin of the surface glow of space vehicules, *Geophys. Res. Lett.*, *10*, 130-132, 1983.

[117] Stix, T.H., *The theory of plasma waves*, McGraw-Hill, New York, 1963.

[118] ST-Maurice, J.-P. and Schunk, R. W., Auroral ion velocity dristributions using a relaxation model. *Plamet. Space Sci.*, 21, 1115-1130, 1973.

[119] ST-Maurice, J.-P. and Schunk, R. W., Behavior of ion velocity distributions for a simple collision model. *Plamet. Space Sci.*, 22, 1-18, 1974.

[120] Stone, N. H., U. Samir, K. H. Wright, Jr., D. L. Reasoner, and S. D. Shawhan, Multiple ion streams in the near vicinity of the space shuttle, *Geophys. Res. Lett.*, *10*, 1215, 1983.

[121] Stone, N. H., K. H. Wright (Jr.), K. S. Hwang, U. Samir, G. B. Murphy and S. D. Shawhan, Further observations of space shuttle plasma-electrodynamic effects from OSS-1/STS-3, *Geophys. Res. Lett.*, *13*, 217, 1986.

[122] Tanenbaum, B. S., *Plasma Physics.*, McGraw-Hill, New York, 1967.

[123] Tataronis, J. A., and F. W. Crawford, Cyclotron harmonic wave propagation and instabilities I. perpendicular propagation, *J. Plasma Phys.*, *4*, 231, 1970.

[124] Temerin, M., Doppler shift effects on double-probe measured electric field power spectra, *J. Geophys. Res.*, *84*, 5929, 1979.

[125] Theilhaber, K., G. Laval, and D. Pesme, Numerical simulations of turbulent trapping in the weak beam-plasma instability, *Phys. Fluids, 30*, 3129-3149, 1987.

[126] Torr, M. R., Optical emissions induced by spacecraft-atmosphere interactions, *Geophys. Res. Lett.*, *10*, 114-117, 1983.

[127] Tribble, A. C., J. S. Pickett, N. D'Angelo, and G. B. Murphy, Plasma density, temperature, and turbulence in the wake of the shuttle orbiter, *Planet. Space Sci.*, *37*, 1001, 1989.

303

[128] Tsunoda, S. I., F. Doveil, and J. H. Malmberg, Experimental test of the quasilinear theory of the interaction between a weak warm electron beam and a spectrum of waves, *Phys. Rev. Lett.*, *58*, 1112-1115, 1987.

[129] Welch, P. D., Use of fast Fourier transform for the estimation of power spectra: A method based on time averaging over short, modified periodograms, *IEEE Trans. Audio and Electroacoust.*, *AU-15*, 70-73, 1967.

[130] White, S. M., D. B. Melrose, and G. A. Dulk, Electron cyclotron masers following a solar flare, *Proc. Astrom. Soc. Aust.*, *5*, 188, 1983.

[131] Wu, C. S., and R. C. Davidson, Electromagnetic instabilities produced by neutral-particle ionization in interplanetary space, *J. Geophys. Res.*, *77*, 5399, 1972.

[132] Yee, J. H., and V. J. Abreu, Visible glow induced by spacecraft-environment interaction, *Geophys. Res. Lett.*, *10*, 126-129, 1983.

[133] Zakharov, V. E., Collapse of Langmuir waves, *Zh. Eksp. Teor. Fiz.*, *62*, 1745-1759, 1972. (*Sov. Phys. JETP.* Engl. Transl., *35*, 908-914, 1972.)